

## CONTENTS

### LETTER FROM THE EDITOR

### HYDROCARBONS

Study of distribution of remaining oil in West Block of the Third District in North Saertu  
*Huabin Weila, Huanlai Zhu, Shangming Shi, Xinliang Yang, Jingjun Zhang, Jian Wang, Muhammad Aqeel Ashraf*.....A1-A4

Experimental study of petrophysical properties of a tight formation by considering the clay minerals and flow sensitivities  
*Guangfeng Liu, Shoujun Li, Daihong Gu, Yang Lu and Emmanuel Asamoah* .....B1-B5

### HYDROGEOLOGY

Mapping of Underwater Seabed Morphology of the Gaza Strip Coastal Zone Using Remote sensing technique  
*Khalidoun Abualhin*.....C1-C7

### HYDROLOGY

Water temperature prediction in a subtropical subalpine lake using soft computing techniques  
*Saeed Samadianfard, Honeyeh Kazemi, Ozgur Kisi, Wen-Cheng Liu*.....D1-D11

### NATURAL HAZARDS

Case Study of the Characteristics and Dynamic Process of July 10, 2013, Catastrophic Debris Flows in Wenchuan County, China  
*Gui-Sheng Hu, Ning-Sheng Chen, Javed Iqbal Tanoli, Yong You and Jun Li*.....E1-E13

Potential Settlement Due to Seismic Effects in the Residential Area of Ilgin (Konya, Turkey)  
*Adnan Ozdemir and M. Tahir Nalbantcilar*.....F1-F9

### GEOMORPHOLOGY

An algorithm for generation of DEMs from contour lines considering geomorphic features  
*Xiao-Ping Rui, Xue-Tao Yu, Jin Lu, Muhammad Aqeel Ashraf, Xian-Feng Song*.....G1-G9

### METEOROLOGY

Temporal-spatial distribution of oceanic vertical deflections determined by TOPEX/Poseidon and Jason-1/2 missions  
*Jin Yun Guo, Yi Shen, Kaihua Zhang, Xin Liu, Qiaoli Kong, Feifei Xie* .....H1-H5

### PALEONTOLOGY

Compaction and Collapse Characteristics of Dune Sand Stabilized with Lime-Silica Fume Mix  
*Mohammed Y. Fattah, Hasan H. Joni and Ahmed S. A. Al-Dulaimy*.....I1-I8

### GEOCHEMISTRY

Classification of cut slopes in weathered meta-sedimentary bedrocks  
*Johnbosco Ikenna Nkpadobi, John Kuna Raj and Tham Fatt Ng*.....J1-J9



Letter from the editor

Dear readers. The Earth Sciences Research Journal has been recently flooded with dozens of good papers expecting to be published. Thanks to you, readers, reviewers, authors for your trust. We are continuously working to improve our editorial processes.

The trend topics of those papers go from gas and petroleum exploitation, land use, geological hazards, to sustainable development, environmental protection and optimization of operation techniques. Without forgetting the basic research. All those subjects are welcome in Earth Sciences Research Journal. Proudly, we remark our journal, your journal, as the natural stage for the debate between economic development and sustainable development. There is no a better referee for this discussion than education entities. If your manuscript put lights on this important subjects, do not hesitate to submit it.

Is this not a minor topic! Nowadays, every political decision, every policy designed, every industrial and human activity are seen through the lens of the Environmental Awareness. We can not quit on this responsibility. As an example of how important those topics are, during the coming days, US President Barack Obama is going to enact a law expanding the protection areas in Hawaii in close four times the current size. It means longlines fishing operators will not be permitted in the 582581 square miles; neither the seabed mining in a region with rich deposits of manganese, nickel, zinc, cobalt, and titanium.

Similar decisions have been taken in Chile and Costa Rica, this last one with a 26% of its land territory protected as a natural park. Just talking about some cases in this side of the world, where we are more familiar with. The next meeting of Geological Society of America, taking place in Denver, on September, will hand on this same topics. Are the extracting and exploitation of resource prohibitions the solution to environmentalism? Welcome all your papers cracking this nut.

Carlos Alberto Vargas Jiménez.

Editor in Chief,

Earth Sciences Research Journal





## Study of distribution of remaining oil in West Block of the Third District in North Saertu

Huabin Wei<sup>1a</sup>, Huanlai Zhu<sup>1</sup>, Shangming Shi<sup>1</sup>, Xinliang Yang<sup>2</sup>, Jingjun Zhang<sup>1</sup>, Jian Wang<sup>3</sup>, Muhammad Aqeel Ashraf<sup>4</sup>

<sup>1</sup>Geoscience College of Northeast Petroleum University;

<sup>2</sup>School of Petroleum Engineering of Northeast Petroleum University;

<sup>3</sup>Daqing China National United Oil Corporation Eighth Oil Production Plant;

<sup>4</sup>Faculty of Science and Natural Resources, University Malaysia Sabah 88400 Kota Kinabalu, Sabah, Malaysia

<sup>a</sup>whbinemail@163.com

### ABSTRACT

Identifying remaining oil distribution is an essential study at the Third District in North Saertu of the West Block in Daqing Oilfield. This field is known as a flooding fine potential tapping demonstration zone, characterized by a long-developing history and complex well history. Based on tectonic features and sedimentary characteristics of the study area, the methods of facies controlled reservoir 3D geological modeling and numerical simulation are used in the process of establishing the geological 3D static model. In this paper, we summarized the causes and distribution law of remaining oil in the study area by using the method of fine reservoir numerical simulation to provide a reliable basis for the development and adjustment of the oil field. In combination with fine exploration such as water drive fracturing, water plugging, reperforating and injection-production segment, the recoverable reserves recovery rate could be effectively increased.

*Keywords: Remaining oil distribution, 3D geological modeling, Numerical reservoir simulation, Sedimentary microfacies, North Saertu.*

## Estudio de la distribución del remanente de petróleo en el bloque oriental del tercer distrito, en el norte de Sartu, China

### RESUMEN

La identificación de la distribución del remanente de petróleo es un estudio esencial en el tercer distrito del norte de Sartu, que corresponde al bloque occidental del campo petrolífero de Daqing. Este campo es conocido como una zona ejemplar para aprovechar el potencial de explotación por inundación y que se caracteriza por una historia compleja y de largo desarrollo de sus pozos. Con base a las características tectónicas y sedimentarias del área de estudio se utilizaron los métodos de modelado geológico 3D en depósitos con facies controladas y la simulación numérica en el proceso de establecer el modelo geológico 3D estático. En este artículo se establecen las causas y la ley distributiva del remanente de petróleo en el área de estudio a través del método de simulación numérica de depósitos de alta resolución que provea una base fiable para el desarrollo y ajuste del campo petrolero. Con la combinación de métodos de exploración como la fractura dirigida con agua, taponamiento acuático, reperforación y segmentos de inyección-producción, el índice de recuperación de reservas podría incrementar efectivamente.

*Palabras clave: Distribución del remanente de petróleo, modelado geológico 3D, simulación numérica de depósitos, microfacies sedimentarias, norte de Sartu.*

### Record

Manuscript received: 10/04/2016

Accepted for publication: 29/07/2016

### How to cite item

Wei, H., Zhu, H., Shi, S., Yang, X., Zhang, J., Wang, J., & Ashraf, M. A. (2016). Study of distribution of remaining oil in West Block of the Third District in North Saertu. *Earth Sciences Research Journal*, 20(2), A1-A4. doi:<http://dx.doi.org/10.15446/esrj.v20n2.55167>

1. Introduction

The West Block of the Third District in North Saertu water flooding fine potential tapping study area is located in the west of the pure oil of Saertu oilfield of Daqing placanticline and belongs to the delta facies lithologic-structural reservoir (Yang, 2004). Saertu, Putaohua, and Gaotaizi reservoirs developed in the study area (Tong et al., 2014). Since 1964, the District has experienced some major adjustments: the implementation of the fracturing, fill holes, water shutoff, subdivision injection production and other essential measures. Because of the long development time and complex well history conditions, it is not very clear for the remaining oil distribution law to find the appropriate area of remaining oil (Sun et al., 2011), the distribution of the remaining oil in the study area and the cause of formation. Those factors were quantitatively studied in this work.

2. Study area survey

West Block of the Third District in North Saertu Study zone is located at the west end of the anticlinal structures and having area of 18.5km<sup>2</sup> and it is in the northern part of Saertu oil field. The structure is gentle, with a 2~3 degrees formation dip. The average altitude of the ground is about 150m. There are 625 water-drive oil & water wells in the study area. Well density is 33.8 well/km<sup>2</sup>, the injection production ratio is 1.47, the average thickness of sandstone is 21.6m. So far, three types of subfacies developed in the study are have been seen: SI group, SII group, SIII group. PII group formation belongs to delta distributary plain subfacies and delta front subfacies sedimentary facies, and below G19 oil layer in Gaotaizi, all belong to the sand body deposition in the outer edge of the delta front except GII1+2b, GII12+13 (Wang et al. 2007).

3. 3D facies controlled geological modeling

Due to the heterogeneity of Saertu, Putaohua, and Gaotaizi reservoirs at the West Block of the Third District in North Saertu (Han, 2010), it was established the use of the static three-dimensional geological model of the software PETREL 2009 to control the morphology of the geological body, ensuring the accuracy of modeling, the thickness of stratum and well pattern density (Guo et al., 2015). The plane grid spacing was set to be 20m×20m to characterize the reservoir plane distribution characteristics (Zhang et al., 2010). The vertical average is a grid for each 0.5m, and the minimum is 0.25m, which is used to meet the requirement of resolving the thinner layer (Fig. 1). The sedimentary facies modeling is based on construction model (Li et al., 2013), under the guidance of sedimentary model, using the theory of Assign to closest point to plane interpolation for phase data, and take the result of interpolation as constraints to establish sedimentary microfacies model (Chong et al., 2011).

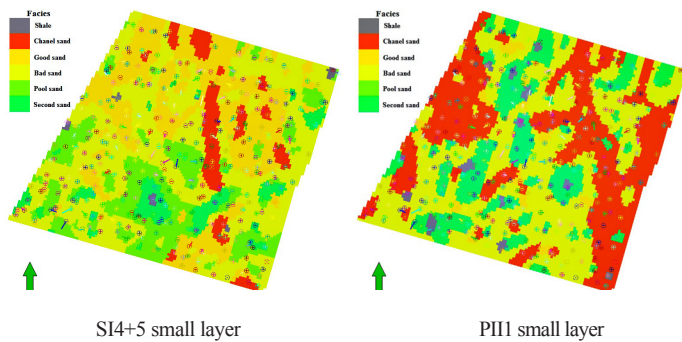


Figure 1. Microfacies model of reservoir sedimentary facies in the West Block of the Third District in North Saertu study zone

4. Numerical reservoir simulation

There is no visible crack in the study area, and the in-place oil is a conventional heavy oil. That is, the reservoir does not have an anti-coagulation phenomenon (Guo et al., 2013). It combines the actual situation in the study area to follow the first overall, after the local; the first principle of the block and single well numerical simulation to carry out the numerical simulation (Yang et al., 2011). Among 379 production wells in the region, the number of wells which have statistical production of single well fluid volume fitting relative error less than 20% is more than 65% of the total number of wells (Hu, 2012), the oil production fitting rate could reach to 100%, and the fitting accuracy of the study area is relatively high to meet the requirement of single well-fitting index (Fig. 2).

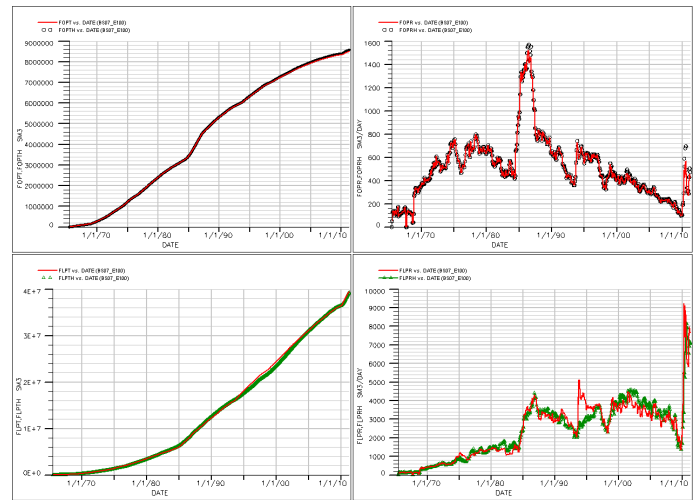


Figure 2. The fitting curve of generating oil and fluid in the West Block of the Third District in North Saertu Study zone

5. Residual oil analysis

5.1 Remaining oil distribution law.

The numerical simulation results were carried out, the remaining oil saturation were subtracted from the residual oil saturation (Fu et al., 2010), and the residual oil reserves were calculated using the formula of reserves calculation (Fig. 3).

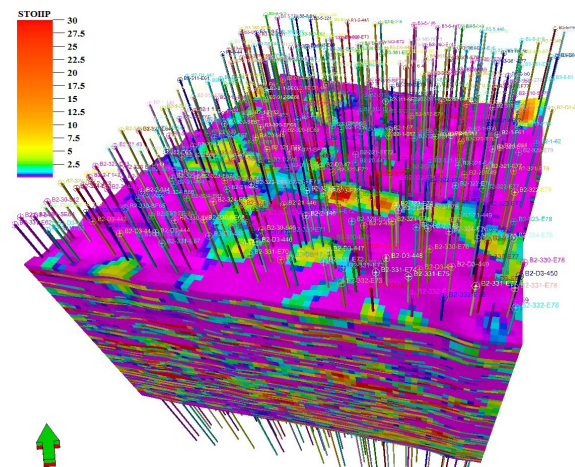


Figure 3. Movable remaining oil abundance distribution in West Block of the Third District in North Saertu Study zone

The distribution of remaining oil in the reservoir of Saertu oil layer is relatively uniform, and the remaining oil reserves are moderate, in the  $20\sim 50\times 10^4\text{t}/\text{km}^2$ , which are distributed in the North and South area. Putaohua reservoir movable remaining oil reserves abundance high-value area is not relatively wealthy, with the moving remaining oil reserves abundance between  $10\sim 50\times 10^4\text{t}/\text{km}^2$ . The high-value areas are in south and northeast. Gaotaizi reservoir remaining oil reserves plenty are between  $5\sim 50\times 10^4\text{t}/\text{km}^2$ ; the high-value area concentrated in the southern half of area. The potential of the remaining oil is mainly accumulated in the non- principal parts of  $<1.0\text{m}$ , by using the existing well nets to do the injection-production relationship, adjust layer, water blocking and other measures, the estimated total remaining recoverable reserves are expected to reach  $113.1\times 10^4$  tons, the ultimate recovery rate could be 49.8%.

**5.2 Analysis of the causes of the remaining oil.**

The formation of the remaining oil is influenced by the reservoir heterogeneity and the mining condition (Li et al., 2011; Wei et al., 2008). In this paper, the structure of the remaining oil in the block are affected by the following factors:

**The pattern can not control it.**

This kind of remaining oil is in the original well network, while drilling but not perforated, or original well pattern not being drilled and new infill wells drilled encountered reservoir is formed. Alternatively, is due to the relatively narrow oil-bearing sand body, passes through the middle of the two wells, due to well away from the Ohara pattern did not hold and the formation of remaining oil (Fig. 4).

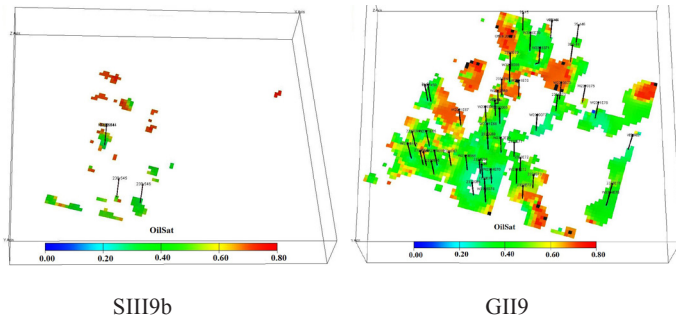


Figure 4. Remaining oil formation (well pattern can not control)

**The type whose injection production is not perfect.**

Such residual oil is only well drilling encountered or only wells drilled, or oil wells drilling met for interlayer, the cementing quality and the same layer and water control, water and other aspects of the reasons and no perforation of remaining oil (Fig. 5). Injection production system adjustment can improve this potential, well network encryption and hole filling and so on, which are used to raise the level of use.

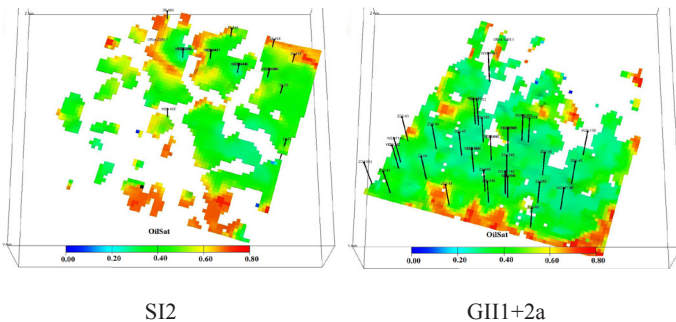


Figure 5. Remaining oil formation (the type whose injection production is not perfect)

**The kind of detention area.**

The remaining oil is formed by the pressure balance between adjacent wells, which is a certain proportion in the thick layer and thin layer, but its distribution area is relatively small. The encryption can be used to improve the injection production relationship (Fig. 6).

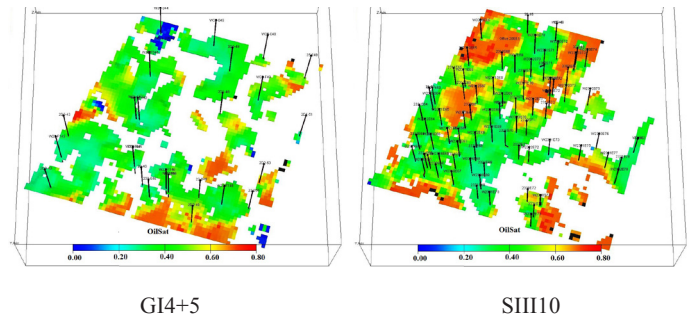


Figure 6. Remaining oil formation (the type of detention area)

**The kind of poor reservoir.**

The of this kind of residual oil is mainly due to the thin reservoir, poor physical properties, the original well pattern and well spacing conditions not established an effective drive system or the plane and inter layer interference. One is a thin layer with large distribution area, and the other is the area with poor physical properties in the side of the river. The remaining oil must be adjusted by the well network encryption and fracturing and other measures to improve the use of the situation (Fig. 7).

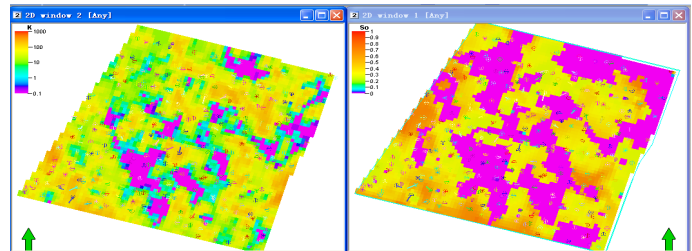


Figure 7. GI11+12 Comparison of permeability and residual oil saturation of the type of poor reservoir

**The Relationship between residual oil and sedimentary microfacies.**

With good physical properties of the channel sand reservoir, in the case of injection production, the water channeling occurred along the high permeability channel in the injection-production well, the water flooded in the first place, the formation of high permeability channel, and its adjacent non-main channel sand, front sand and other physical properties of the reservoir with low oil saturation, low level of reserves, the formation of the remaining oil enrichment (Fig. 8).

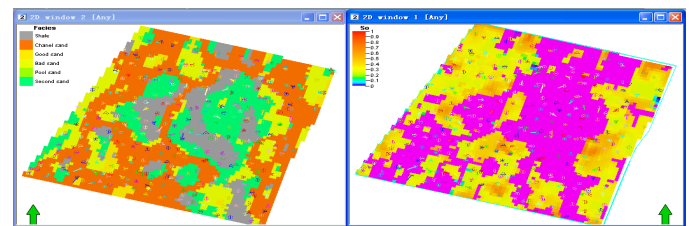


Figure 8. SIII12 The contrast between sedimentary microfacies and remaining oil saturation

### ***No water flooded type in the layer.***

This kind of remaining oil mainly exists in the thick oil layer. Because of the good heterogeneity of the layers, good physical properties, high permeability of the site development effect is good, while the physical properties of poor, low permeability of the part because of the high permeability of the impact of the use of poor or non-use of the remaining oil, the use of the well network encryption and injection production system adjustment can be improved. The remaining oil is mainly the third times such polymer flooding oil potential object.

### **6. Conclusion**

(1) Based on the geological modeling and numerical simulation, it was established that the remaining oil potential in West Block of the Third District in North Saertu Study zone is large, and Saertu oil reservoir remaining oil is mainly distributed in the area to the north and south; relatively few in the center. Residual oil of Putaohua reservoir is in the South and Northeast area. Gaotaizi reservoir remaining oil is concentrated in the southern half of area.

(2) The remaining oil potential in West Block of the Third District in North Saertu Study zone is concentrated in the non-main parts below 1.0m, the residual oil potential distribution is not balanced, and the local area has the encryption adjustment condition. It needs to use the existing well pattern and make the injection production relationship, adjustment layer, water shutoff and so on. The final recovery rate can reach 49.8%. Combined with water flooding fine exploration the recoverable reserves recovery rate could increase 1.1%.

### **Acknowledgments**

The authors would like to thank Shi Shangming for supporting the publication of this work and Zhu Huanlai for supporting the shale-gas reservoir modeling studies. The authors would also like to acknowledge Yang Xinliang, Zhang Jingjun and Wang Jian for his many contributions to shale-gas reservoir modeling that were instrumental in this work. This paper is supported by the state key laboratory breeding base co-constructed by unconventional oil and gas accumulation & development province department, and it is funded by the National Natural Science Foundation of China (Fund number: 41302210) and the Research Fund for young teachers of Northeast Petroleum University (Fund number: 2013NQ136).

### **References**

- Chong, R.J., & YU, X.H. (2011). The Keys to Quality Control of 3D Reservoir Modelling. *Marine Geology Frontiers*, pp. 64-69.
- Fu, Y.X, Feng, M.F., Liu, H. Bi, X.F. & Wang, S.Q. (2010). Analysis of Residual Oil Distribution Rules and Controlling Factors in Kumkol Oilfield. *Drilling & Production Technology*, pp. 61-63, 77.
- Guo, X., Wang X.B., Guo M., Liu P., & Zhou X.M. (2013). Application of 3D Geological Modeling in Reservoir Description - A Case Study of Block T in Daqing Oilfield. *Sino-Global Energy*, pp.48-52.
- Guo, Z., Sun, L.D., Jia A.I. & Lu T. (2015). 3D Geological Modeling for Tight Sand Gas Reservoir of Braided River Facies. *Petroleum Exploration and Development*, pp. 76-83.
- Han, M. (2010). Research on Three-dimensional Modeling and Numerical Simulation in Shuyi District Du 84 Block SAGD. *Petroleum Geology and Engineering*, pp. 43-45.
- Hu, H.F. (2012). Quality Evaluation Method on History Matching of Reservoir Numerical Simulation. *Fault-Block Oil & Gas Field*, pp. 354-358.
- Li, S.H., Liu, X.T., Wang, J., Gong, W.Q., & Lu, W.T. (2013). Improvement of the Alluvsim Algorithm Modeling Based on Depositional Processes. *Acta Petrolei Sinica*, pp. 140-144.
- Li, Y., Wang, X.H., Jin, S.S., Cai, S. Y., & Wang S. Q. (2011). The Rules of Remaining Oil Distribution and Measures for Potential Tapping in Wangji Oilfield. *Journal of Oil and Gas Technology (JJPI)*, pp. 294-296.
- Sun, Y. Ma, S.Z., Jiang, H.F., Liu, Y.Y., Liu, Z.B., & Yu, L.M. (2011). Distribution Characteristics and Controlling Factors for Reservoirs of Putaohua Oil Layer in Sanzhao Sag of Songliao Basin. *Journal of Central South University (Science and Technology)*, pp. 2387-2393 □
- Tong, S.Q., Li, B., Luo, Q. & Wang, H.J. (2014). Single-sandstone-layer Sedimentary Microfacies and Favorable Sandbody Prediction of Putaohua Reservoir in South Gulong Sag, Songliao Basin. *Oil & Gas Geology*, pp. 517-525.
- Wang, J.G., Wang, T.Q., Wei, P.S., Liang, S.J., & Han, X.Q. (2007). Sedimentary Mode of Shallow Lacustrine Delta of Large Continental Basin - An Example From Putaohua Formation in Northern Songliao Basin. *Lithologic Reservoirs*, pp. 28-34 □
- Wei, Z.L., & Huang, S.J. (2008). Reservoir Numerical Simulation Technology and Methods in High Water Cut Period. *Journal of Southwest Petroleum University (Science & Technology Edition)*, pp. 103-106.
- Yang, F. Wang, X.H. & Liu, H. (2011). Evaluation on Remaining Oil Distribution Law and Adjustment at High Water-cut Stage - An Example from Gasikule Gas Reservoir. *Journal of Oil and Gas Technology (JJPI)*, pp. 129-132.
- Yang, Y.F (2004). Formation Conditions and Distribution of Lithologic Pools in Songliao Basin. *Oil & Gas Geology*, pp. 393-399.
- Zhang, Y., Zheng, Z.J., Lu, G.X., Wang, H.X. & Pu, H.Q. (2010). Application of Three-dimensional Geological Modeling and Numerical Simulation in Exploitation of Fractured Water-Gas Reservoir. *Natural Gas Geoscience*, 21(5), pp. 863-867.



## Experimental study of petrophysical properties of a tight formation by considering the clay minerals and flow sensitivities

Guangfeng Liu<sup>1</sup>, Shoujun Li<sup>1\*</sup>, Daihong Gu<sup>1</sup>, Yang Lu<sup>2</sup> and Emmanuel Asamoah<sup>1</sup>

<sup>1</sup>CMOE Key Laboratory of Petroleum Engineering, China University of Petroleum, 18 Fuxue Road, Changping, Beijing, 102249, China

<sup>2</sup> China University of Geosciences, Beijing, 29 Xueyuan Road, Haidian, Beijing, 100083, China

### ABSTRACT

Quantitative X-ray diffraction analysis of rock, X-ray diffraction analysis of clay minerals types and components, Field Emission Scanning Electron Microscope (FESEM) and sensitivity flow experiments methods were used to research the effects of clay minerals on the porosity and permeability of Ordos Basin's tight Chang 7 reservoir (Zhenbei area). These methods were also used to analyze the type, degree, and factors affecting reservoir sensitivity. The research showed that the reservoir possessed poor water, salt, and alkali sensitivity, poor to strong acid sensitivity and none to poor velocity sensitivity. Acid sensitivity among them had comparatively large differences, mainly because acid sensitivity was not only affected by chlorite but also by components of carbonate minerals. Stress sensitivity experiment results showed that the maximum degree of permeability damage in the rocks of this reservoir was median to very strong; irreversible damage level was weak to strong. Consequently, the experimental studies are favorable to not only determine the factor dominating the petrophysical properties of the tight formation, but also to optimize the follow-up development strategies, e.g. injection schedule and hydraulic fracturing implement.

*Keywords: Analysis of clay minerals, porosity, permeability, sensitivity experiments, formation damage.*

## Estudio Experimental de las propiedades petrofísicas de una formación compacta al considerar las arcillas minerales y las respuestas de flujo

### RESUMEN

Este trabajo utilizó análisis cuantitativos de rocas por difracción de rayos X, análisis de los tipos y componentes de arcillas minerales por difracción de rayos X, análisis con el microscopio electrónico de efecto de campo (FESEM, del inglés Field Emission Scanning Electron Microscope) y ensayos de respuesta de flujo para investigar los efectos de las arcillas minerales en la porosidad y permeabilidad del depósito Chang 7, en la cuenca del Ordos (región Zhenbei). Estos métodos también se utilizaron para analizar el tipo, el grado y los factores que afectan la respuesta del depósito. La investigación demuestra que el depósito posee poca agua, sal y respuesta alcalina, baja a fuerte respuesta de acidez, y ninguna a baja respuesta de velocidad. Entre estas características, la respuesta de acidez presentó grandes diferencias comparativas debido a que está afectada tanto por el clorito como por los componentes de minerales carbonatos. Los resultados de los ensayos de respuesta de tensión muestran que el máximo grado de daño por permeabilidad en las rocas del depósito es de mediano a muy fuerte; el nivel de daño irreversible va de débil hasta fuerte. Por lo tanto los estudios experimentales son favorables no solo para determinar el factor dominante en las propiedades petrofísicas de la formación compacta sino también para optimizar las futuras estrategias de desarrollo, como una programación de las tareas de inyección y la implementación de la fractura hidráulica.

*Palabras clave: Análisis de arcilla mineral, porosidad, permeabilidad, ensayos de respuesta, daños de la formación.*

*Record*

Manuscript received: 02/12/2015

Accepted for publication: 27/05/2016

*How to cite item*

Liu, G., Li, S., Gu, D., Lu, Y., & Asamoah, E. (2016). Experimental study of petrophysical properties of a tight formation by considering the clay minerals and flow sensitivities. *Earth Sciences Research Journal*, 20 (2), B1-B6. doi:<http://dx.doi.org/10.15446/esrj.v20n2.54508>

## 1. Introduction

Clay minerals in tight reservoirs have a significant impact on its physical properties. Reservoir sensitivity analyses have theoretical and practical significance for the prevention and treatment of tight sandstone reservoirs. Since the 1960s, experts had noticed that formation damage is caused by clay mineral (Hewitt, 1963). Hower (1974) studied the distribution of clay minerals in the United States Gulf Coast and pointed out that the formation damage degree depended on the contents, types of clay mineral and their position in the rock. Krueger (1986), Amaerule, Kersey, Norman, and Shannon. (1988), Porter (1989) and Reed (1989) comprehensively reviewed the research of formation damage, which reflected the achievements of the 80s. Aase, Bjorkum and Nadeau (1996) and Pittman, Larese, and Heald (1992) studied the influence of different types and occurrences of clay on the formation and protection of secondary porosity. Baker, Uwins, and Mackinnon (1993a, 1993b, 1994) used Environment Scanning Electron Microscope (ESEM) to research the sensitivity of clay minerals. 'Clay Mineral Cements in Sandstones,' by Worden and Morad (2003), described the relationship between clay minerals and sandstone reservoir properties and looked to the future research direction of clay minerals.

Ordos Basin is located at the western margin of North China, with an area of  $25 \times 10^4 \text{ km}^2$ . It is a large cratonic basin of a multi-configuration system and multicycle evolution (Zhao, Liu, Yu, and Wang, 2008; Feng, Huang S., Huang P., Zou and Wu, 2009; Wang et al., 2010). Zhenbei area is a typical sandstone reservoir, situated at the north-western part of the basin. It possesses closed sediment supply and fast deposition rate. Chang 7 reservoir of this region is located in the southwest lake basin, mainly affected by the Northwest provenance. Chang 7 reservoir is a deep-water turbidite fan sedimentary system with developed turbidite sand body; it is the central horizon of the Zhenbei area (Lu et al., 2011; Cui, Feng, Qin, and Peng, 2013). In this article, X-ray diffraction analysis, FESEM and sensitivity flow experiments were used to research and evaluate the clay mineral features of the Zhenbei area's Chang 7 reservoir.

## 2. Analysis of Reservoir Minerals

The X-ray of whole rock analysis is usually adopted in laboratories for the quantitative analysis of rocks to get the clay mineral contents and X-ray diffraction analysis of clay minerals. Thus obtaining the corresponding contents of each type of clay mineral in the reservoir. The porosity and permeability of rocks can be gotten through gas logging porosity and permeability experiment. Through those experimentations carried out on ten wells of Zhenbei area, the results were as shown in Table 1 and Table 2.

**Table 1.** Analysis of Reservoir Rock Minerals

Well	Rock mineral content (%)				Clay mineral content (%)	Porosity (%)	Permeability ( $10^{-3} \mu\text{m}^2$ )
	Quartz	Feldspar	Plagioclase	Calcite			
Z-1	36	6	14	25	19	10.23	0.385
Z-2	38	5	17	18	22	7.84	0.184
Z-3	43	4	16	17	20	9.13	0.327
Z-4	30	7	16	22	25	6.637	0.121
Z-5	42	6	18	12	22	7.06	0.149
Z-6	45	7	14	13	21	8.46	0.251
Z-7	36	8	15	18	23	8.06	0.214
Z-8	42	5	14	20	19	9.85	0.352
Z-9	36	7	18	15	24	6.837	0.132
Z-10	40	5	15	17	23	7.11	0.163

**Table 2.** Analysis of Clay Minerals

Well	Clay mineral relative content (%)					
	K	C	I	S	I/S	%S
Z-1	13	45	11	/	31	18
Z-2	8	39	12	/	41	22
Z-3	14	43	10	/	33	17
Z-4	6	27	18	/	49	22
Z-5	10	35	12	/	43	20
Z-6	11	33	9	/	47	18
Z-7	8	34	15	/	43	15
Z-8	16	40	8	/	36	19
Z-9	2	28	14	/	56	20
Z-10	14	34	8	/	44	16

\*Note: K-Kaolinite, C-Chlorite, I-Illite, S-Smectite, I/S-illite smectite mixed layer, %S-the content of smectite in mixed-layer minerals of illite and smectite.

The data in Table 1 showed that the content of clay minerals in Zhenbei area's Chang 7 reservoir was high, the reservoir had a small porosity and ultra-low permeability. From Table 2 it could see that the main contents of clay minerals in the reservoir were the illite-smectite mixed layer, followed by illite and kaolinite; smectite was not independently developed but occupied a slight proportion in the illite-smectite mixed layer. FESEM photographs showed that kaolinite in Chang 7 reservoir often filled in the porosity with booklet shapes (as shown in Figure 1a); chlorite was usually distributed on the surfaces of particles with leaf shapes (Figure 1b) and the form of the illite and the illite-smectite mixed layer were flocculent structure (Figure 1c and Figure 1d).

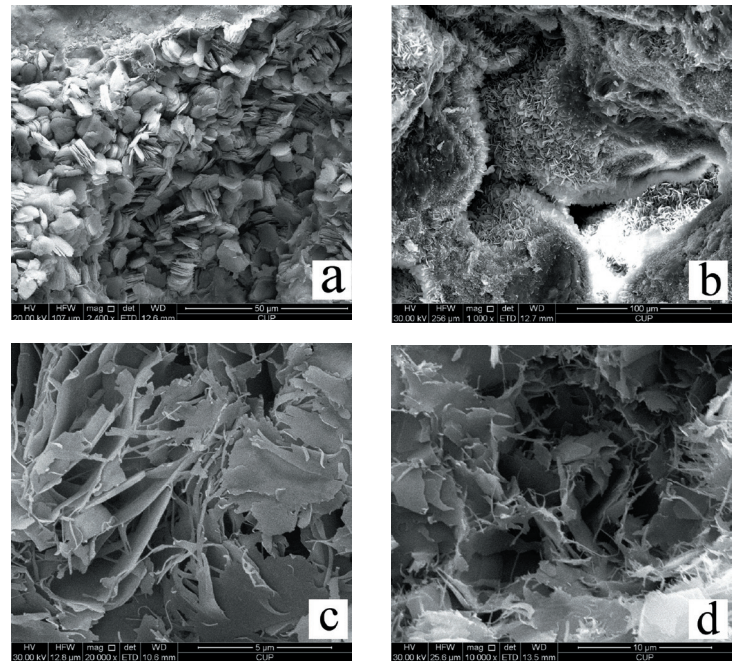


**Figure 1.** FESEM photographs of Zhenbei area Chang 7 reservoir.

## 3. Influence of clay minerals on the reservoir properties

The total content of clay minerals and types of clay minerals affected the properties of the reservoir. As shown in Figure 2, rock mineral components formed an inversely proportional relationship with both porosity and permeability. As fewer mineral content in the rock, the higher porosity and permeable the reservoir would be.

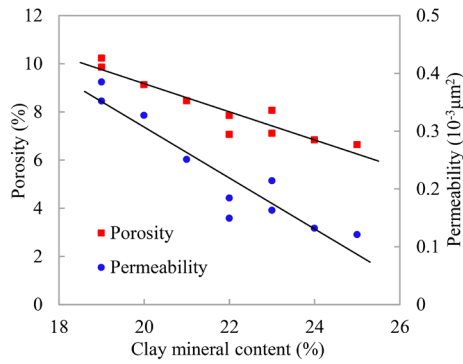


Figure 2. Influence of clay mineral content on porosity and permeability.

3.1 Influence of authigenic kaolinite on the reservoir properties

Authigenic kaolinite was the primary dissolution product of the feldspar (Huang et al., 2009), so the content change of authigenic kaolinite was closely related to the feldspar content in the sandstone reservoir. As shown in Figure 3, authigenic kaolinite and detrital feldspar had a significant negative correlation; it could be seen that authigenic kaolinite content increase with the decrease of feldspar. The content of authigenic kaolinite in Chang 7 reservoir was small and usually filled in the pores and throats. The kaolinite dissolution from feldspar grew much mineral intracrystal porosity, which had a positive effect on the reservoir property. As shown in Figure 4, as higher the content of kaolinite, higher the porosity and permeability.

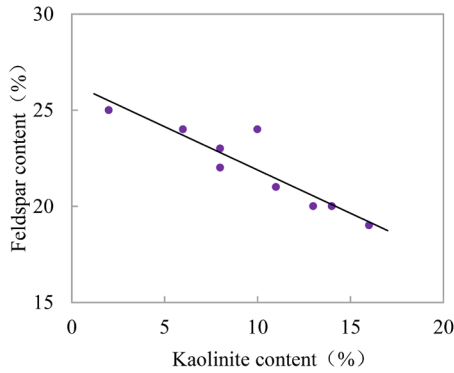


Figure 3. Relationship between authigenic kaolinite content and feldspar content.

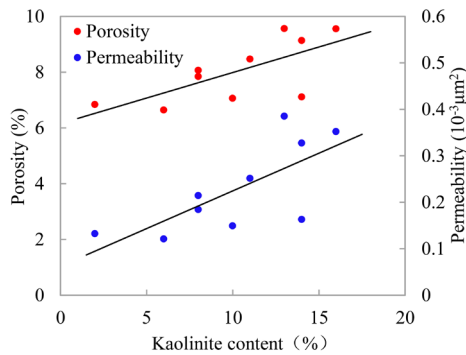


Figure 4. Influence of authigenic kaolinite content on porosity and permeability.

3.2 Influence of authigenic chlorite on the reservoir properties

The formation of chlorite membrane was suitable for the reservoir (Ehrenberg, 1993; Hurst & Nadeau, 1995; He, 2010): (1) Chlorite membrane could increase the mechanical strength of rock and resist the compaction to some extent, thus making the primary intergranular pore unable diminish further by compaction. (2) Feldspar could even be dissolved and formed a moldic pore, but the chlorite membrane would remain. If the chlorite rims had sufficient strength, they could support themselves and protect the secondary porosity formed by dissolution. (3) Quartz secondary enlargement caused porosity loss, but the chlorite film could prevent authigenic quartz cement from nucleating on the surface of detrital quartz by dividing pore water from quartz particle surface (4) Authigenic chlorite transformed part of the intergranular pores it occupied to intercrystalline pores, some of which might be effective for reservoir spaces. Therefore, the development of authigenic chlorite was favorable for reservoir physical property. As shown in Figure 5, the porosity and permeability were positively associated with the content of authigenic chlorite.

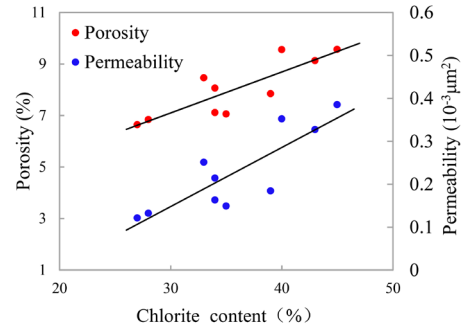


Figure 5. Influence of authigenic chlorite content on porosity and permeability.

3.3 Influence of authigenic illite and illite-smectite mixed layer on the reservoir properties

Common forms of authigenic illite are hair-like, fibrous and bridging. They often cut lots of pores and pore throats into micro bound pore and reduce the effective radius (Liu, Qu, Sun, Yue & Zhu, 1998, Lander & Bonnell, 2010). Zhenbei area Chang 7 reservoir has a high content of illite-smectite mixed layer whose main constituent is illite and FESEM showed that the attitude of the illite-smectite mixed layer was similar to illite, so the influence of it on the reservoir was also similar to that of illite. As shown in Figure 6, as higher the contents of illite and illite-smectite mixed layer, the lower the porosity, and permeability.

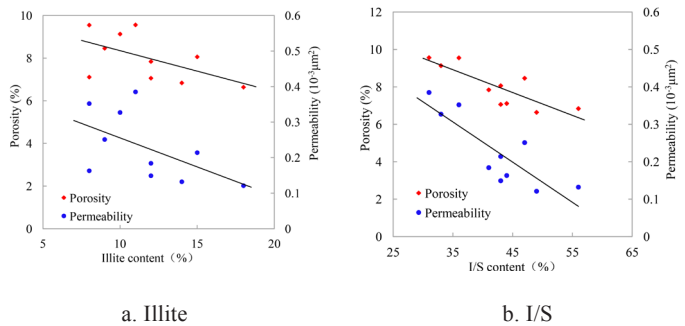
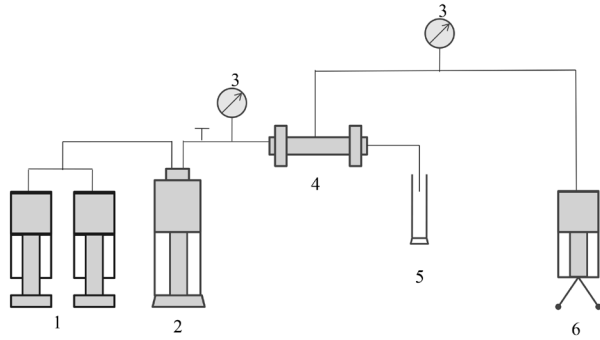


Figure 6. Influence of authigenic illite and I-S content on porosity and permeability.

4. Sensitivity Evaluation

Reservoir sensitivity is referred to the degree of change in reservoir permeability caused by the physicochemical interactions between the reservoir and fluid. Tight sandstone reservoir is different from the conventional low permeability reservoir, so its experimental methods require more precise and complex (Zhang, Chen, & Yan, 2006; Ju, Fan & Wan, 2007; Wu, Wang, Cui, Zhang, 2013). This experiment used cores in six wells to make systematic sensitivity evaluation for Chang 7 reservoir. The device schematic diagram is as shown in Figure 7.



\*Note: 1-Pump. 2-Intermediate container. 3-Pressure gage. 4-Core holder. 5-Measuring cylinder. 6-Confining pressure pump.

Figure 7. Experiment device schematic diagram.

4.1 Water and Salt Sensitivity Evaluation

Among reservoir clay minerals, montmorillonite has the strongest effect on water sensitivity; even a tiny amount of montmorillonite caused very strong sensitivity. Secondly, the illite-smectite mixed layer could also cause water sensitivity. The expansion of illite and chlorite upon contacted with water was feeble, and kaolinite was not easily hydrated (Cui, D. L. Liu, Tao, Li, & Y. B. Liu, 2004) The water sensitivity experiment results of Zhenbei area Chang 7 reservoir were as shown in Table 3; results of salt sensitivity were as illustrated in Figure 8.

Table 3. Results of Water Sensitivity Experiment on Zhenbei area's Chang 7 Reservoir.

Well	Permeability ratio of different fluids:			Water sensitivity damage rate (%)
	Kn/Ki (%)			
	8% standard saline	4% standard saline	Distilled water	
Z-1	100%	94.35	72.69	27.3
Z-2	100%	97.95	92.44	7.5
Z-3	100%	94.43	78.97	21
Z-4	100%	86.25	76.68	23.3
Z-5	100%	88.54	82.49	17.5
Z-6	100%	91.24	86.71	13.3

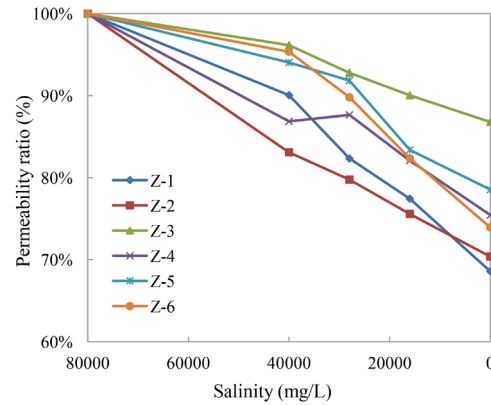


Figure 8. Salt sensitivity experiment results.

It could be seen from Table 3 that the region had weak water sensitivity. The salt sensitivity analysis results of Figure 8 shows that when formation salinity declines, the change in permeability was not obvious and had no critical salinity. The content of I-S in Zhenbei area Chang 7 reservoir was high, but the montmorillonite only took a slight percentage (less than 25%). It was close to the end-member composition of illite. The conversion content of montmorillonite was less than 10%, so the water and salt sensitivity was weak in this reservoir.

4.2 Acid Sensitivity Evaluation

In the process of water injection, tight oil reservoirs were prone to be blocked up. Therefore, acid fluids were to be infused to broken down reservoir to improve its productivity. Acid fluids upon entering the reservoir could react with sensitive acid minerals to produce deposits and released microparticles and blocked the reservoir, causing a reduction in permeability. Acid-sensitive rocks in clay were mainly chlorite, which produced ferric hydroxide upon contact with acid causing blockage in the reservoir. The acid sensitivity experiment results of Zhenbei area's Chang 7 Reservoir were as shown in Table 4.

Table 4. Acid sensitivity test results of Zhenbei area's Chang 7 reservoir.

Well	Permeability before acid injection (10 <sup>-3</sup> μm <sup>2</sup> )	Permeability after acid injection (10 <sup>-3</sup> μm <sup>2</sup> )	Acid sensitivity damage ratio	Degree of acid sensitivity
Z-1	0.392	0.338	13.78%	Weak
Z-2	0.159	0.064	59.75%	Medium to strong
Z-3	0.331	0.105	68.28%	Medium to strong
Z-4	0.125	0.109	12.80%	Weak
Z-5	0.162	0.031	80.86%	Strong
Z-6	0.247	0.057	76.92%	Strong

Table 4 showed that the acid sensitivity of each well at the Zhenbei area's Chang 7 reservoir had great differences. From Table 2, it could be known that difference in the chlorite content of six wells was not big, but the difference in the degree of acid sensitivity was huge. Through analysis, it could be seen that the calcite content of each well at the Zhenbei area had a particular difference. Calcite was carbonate mineral which compared to chlorite readily reacted with hydrochloric acid (Tian, Q. Guo, Y. Li, Y. Guo, & Y. Z. Li, 2009). Through X-Ray analysis, it could be seen that the contents of calcite in Z-1, Z-4 were large. Z-5, Z-6 only had small quantities of calcite and the contents of calcite in Z-2, Z-3 were between them (as illustrated in Table 1). Therefore, the acid sensitivities were different.

### 4.3 Alkaline Sensitivity Evaluation

During comparatively low temperatures,  $Ca^{2+}$ ,  $Mg^{2+}$  on the surface of clay minerals exchanged with other alkaline minerals to produce hydroxide precipitation and the calcium ions coverage was reduced. Then the surface of clay minerals was easier to expand or to be released from the sand surface (Li, Gao, Yang & Hua, 2012). Also, under high temperature and  $pH > 9$  conditions, it reacted kaolinite to form montmorillonite and caused further damage of the reservoir. The alkaline sensitivity experiment results of Zhenbei area's Chang 7 reservoir was as shown in Figure 9.

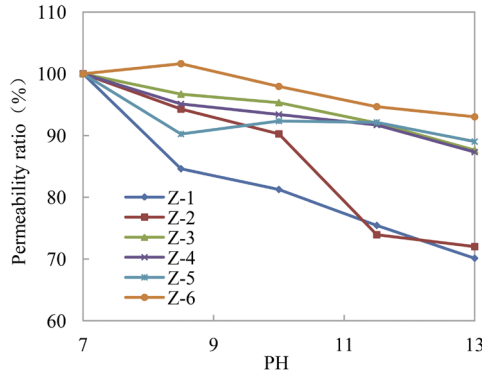


Figure 9. Alkaline sensitivity experiment results.

The results in Figure 9 revealed that Chang 7 reservoir had weak alkaline sensitivity. Data demonstrated that critical PH of Z-1 well is 7, critical PH of Z-2 well is 10 and other wells did not possess critical data.

### 4.4 Speed Sensitive Evaluation

Kaolinite was the clay mineral that most likely caused speed-sensitivity, and the second was hair-like illite. Results of a speed-sensitive experiment on Zhenbei area's Chang 7 reservoir were as showed in Figure 10.

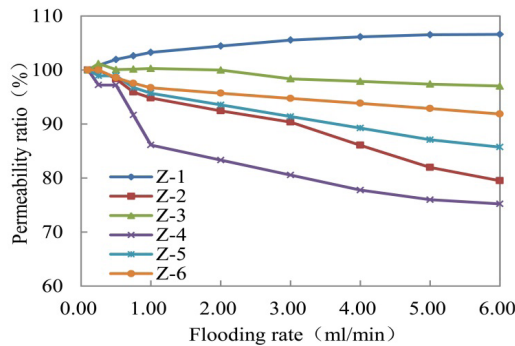


Figure 10. Speed sensitive test results.

Figure 10 showed that the speed-sensitivity of Chang 7 reservoir was none to poor and permeability of Z-1 was even improved. This phenomenon was due to different particle sizes were scoured by the fluid when the flow velocity got increased. When the particle size was greater than the pore throat radius, particles washed down by fluid would accumulate in the throats and form a 'bridge', which made the reservoir permeability decline (Yang & Wei, 2004). However, if particles size were less than the pore throat radius, particles would be carried out with fluid and the pore radius would increase, thereby the permeability of the reservoir got improved. Also, indoor experiment samples were too little, particles might be washed out of the experimental model, but these particles in the reservoir would still stay in it and block the throats. So the results gotten from the laboratory were less than that in the actual reservoir.

### 4.5 Stress Sensitive Evaluation

During reservoir development, with the output of the internal fluid, the pore pressure became decreasing, and the original force balance of the rocks got changed. That led to elastic-plastic deformation of the rocks and the changing of reservoir pore structure and permeability (Zhao, Yue, & Lv, 2009; Feng, Huang, Chen, Wang, Che, 2010; Ru, Liu, Fan, Li, Yu, 2011; Sun, Yang, Li, 2011). The experiment used a variable confining pressure to test the stress-sensitivity of three samples with different permeability. The trial included both ascending and descending net confining pressure processes. The results were as shown in Figure 11.

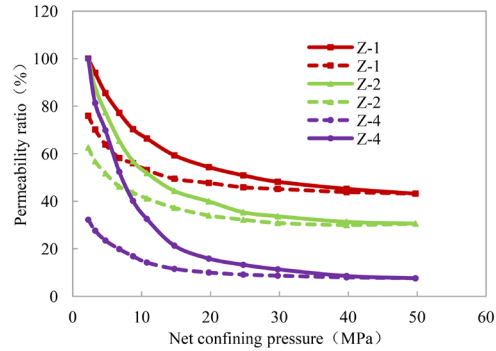


Figure 11. Stress sensitive experiment results.

As shown in the figure above, the solid lines represented ascending net confining pressure processes, and dotted lines indicated the descending net confining pressure processes. It could be seen the stress-sensitivity features of the reservoir were as below.

(1) During the ascending net confining pressure process, with the increasing of confining pressure, the core permeability reduced dramatically at first and then it slowed down to a modest pace. The smaller the core permeability was, the faster it declined and the greater the degree of permeability lost. (2) Part of the reservoir permeability loss would be restored in the process of descending net confining pressure, but it could not be returned to its initial state. So the permeability loss caused by stress-sensitivity was irreversible. The core with smaller permeability would have a greater irreversible permeability loss. (3) The content of clay mineral in Z-1, Z-2 and Z-3 are 15%, 22%, and 26% respectively (as shown in Table 1). The results showed that the higher content of clay mineral meant a higher stress sensitivity.

In general, the maximum degree of permeability damage in the rocks of this reservoir was median to very strong and irreversible damage level was weak to strong.

### 5. Results and Conclusions

(1) Chang 7 reservoir in the Zhenbei area had high contents of clay minerals; the main compositions of these were illite-smectite mixed layer and chlorite, illite and kaolinite only took up a small proportion of them.

(2) The reservoir porosity and permeability were negatively correlated to the total content of clay minerals. Kaolinite and chlorite were advantageous to reservoir porosity and permeability, illite and I-S were not good for them.

(3) The water, salt, alkali, speed sensitive were weak in Chang 7 reservoir in the Zhenbei area, and acid sensitive was weak to strong; the maximum degree of permeability damage in the rocks of this reservoir was median to very strong and irreversible damage degree was weak to strong.

(4) Since the reservoir heterogeneity, sensitivities of each well might be different in Chang 7 reservoir of the Zhenbei area. So it should be treated separately for each well when implementing acidification or other technological measures. Taking all sensitives into consideration, water with low salinity or high alkaline did not have severe impacts on permeability but acid fluid might

change it significantly, so weak alkaline substance could be added to protect the reservoir when fluids are injected for some technological measures. In the course of water flooding, considering the ability of wellhead pressure bearing and the formation fracture pressure, it could properly use a high injection rate. During production, it should select a consistent production pressure and control the bottom-hole pressure so that the damage degree of the stress-sensitivity to the reservoir would be reduced and the oil production would be kept.

### Acknowledgement

The work and results reported here were part of Project 51404282, supported by National Natural Science Foundation of China, Project 2014D-5006-0215, funded by PetroChina Innovation Foundation, and Project 2462015YQ0217, backed by Science Foundation of China University of Petroleum, Beijing.

### References:

- Aase, N. E., Bjorkum, P. A., & Nadeau, P. H. (1996). The effect of grain-coating microquartz on preservation of reservoir porosity. *AAPG Bulletin*, 80(10): 1654-1673.
- Amaerule, J. O., Kersey, D. G., Norman, D. K., & Shannon P. M. (1988). Annual Technical Meeting, June 12 - 16, Calgary, Alberta. DOI: <http://dx.doi.org/10.2118/88-39-65>
- Baker, J. C., Uwins, D. J. R., & Mackinnon, I. D. R. (1993a). ESEM study of authigenic chlorite acid sensitivity in sandstone reservoirs. *Journal of Petroleum Science and Engineering*, 8(4), 269-277. DOI: 10.1016/0920-4105(93)90004-X
- Baker, J. C., Uwins, D. J. R., & Mackinnon, I. D. R. (1993b). ESEM study of illite/smectite freshwater sensitivity in sandstone reservoirs. *Journal of Petroleum Science and Engineering*, 9(2), 83-94. DOI: 10.1016/0920-4105(93)90069-Q
- Baker, J. C., Uwins, D. J. R., & Mackinnon, I. D. R. (1994). Freshwater sensitivity of corrensite and chlorite/smectite in hydrocarbon reservoirs - an ESEM study. *Journal of Petroleum Science and Engineering*, 11(3), 241-247. DOI: 10.1016/0920-4105(94)90043-4
- Cui, L. T., Feng, D., Qin, Y. Q., & Peng, Y. D. (2013). Palaeogeomorphology reconstruction and sand body distribution of Chang 7 reservoir in Zhenbei area, Ordos Basin. *Lithologic Reservoirs*, 25(5), 65-69.
- Cui, W. J., Liu, D. L., Tao, J., Li, M., & Liu, Y. B. (2004) Reservoir sensitivity evaluation of block Cao 104 in Le'an Oilfield. *Oil Drilling & Production Technology*, 26(4), 46-48.
- Ehrenberg, S. N. (1993). Preservation of anomalously high porosity in deeply buried sandstones by grain-coating chlorite: Examples from the Norwegian Continental shelf. *AAPG Bulletin*, 77 (7), 1260-128. DOI: 10.1306/BDF8E5C-1718-11D7-8645000102C1865D
- Feng, H. X., Huang, X. W., Chen, J. B., Wang, H. F., & Che, K. D. (2010). Research on pressure sensitivity of fractured sandstone reservoir with low permeability in Wenliu Oilfield. *Fault-block Oil & Gas Field*, 17(5), 599-601.
- Feng, W. L., Huang, S. J., Huang, P. P., Zou, M. L. & Wu, M. (2009) Sand stone reservoir characteristics of Taiyuan Formation in northeastern Ordos Basin. *Lithologic Reservoirs*, 21(1), 89-93.
- He, Y. X. (2010). The Effects of Clay Minerals on Production Capacity of the Chang-8 Formation Sandstone Reservoirs in Jiyuan-Haqing Area. B.S. Dissertation, Chengdu University of Technology, China.
- Hewitt, C. H. (1963). Analytical techniques for recognizing water-sensitive reservoir rocks. *Journal of Petroleum Technology*, 15(8), 813-818. DOI: 10.2118/594-PA
- Hower, W. F. (1974). Influence of clays on the production of hydrocarbons. SPE Symposium on Formation Damage Control, 30 January-2 February, New Orleans, Louisiana, USA. DOI: <http://dx.doi.org/10.2118/4785-MS>
- Huang, S. J., Huang, K. K., Feng, W. L., Tong, H. P., Liu, L. H., & Zhang, X. H. (2009) Mass exchanges among feldspar, kaolinite and illite and their influences porosity formation in clastic diagenesis—A case study on the Upper on secondary Paleozoic Ordos Basin and Xujiache Formation, Western Sichuan Depression. *Geochimica*, 38(5), 498-506.
- Hurst, A. & Nadeau, P. H. (1995). Clay microporosity in reservoir sandstones: an application of quantitative electron microscopy in petrophysical evaluation. *AAPG Bulletin*, 79(4), 563-573.
- Ju, B. S., Fan, T. L., & Wang, X.D. (2007). A new practical method to quantitatively evaluate the changes in formation permeability during production. The SPE Europe/EAGE Annual Conference, 11-14 June London, United Kingdom. DOI: <http://dx.doi.org/10.2118/107026-MS>
- Krueger, R. F. (1986). An overview of formation damage and well productivity in oil field operations. *Journal of Petroleum Technology*, 38(2), 131-152. DOI: <http://dx.doi.org/10.2118/10029-PA>
- Lander, R. H., & Bonnell, L. M. (2010). A model for fibrous illite nucleation and growth in sandstones. *AAPG Bulletin*, 94(8), 1161-1187. DOI: 10.1306/04211009121
- Li, F. F., Gao, W. L., Yang, S. L., & Hua, X. W. (2012). Study on reservoir sensitivity for low permeability reservoirs in the Gao 52 block of Ansai oilfield. *Special Oil & Gas Reservoirs* 19(4), 126-129.
- Liu, L. Y., Qu, Z. H., Sun, W., Yue, L. P., & Zhu, Y. S. (1998). Properties of Clay Mineral of Clastic Rock in Shanshan Oil Field, Xinjiang. *Journal of Northwest University (Natural Science Edition)*, 28(5), 443-446.
- Lu, C. F., Fu, S. Y., Li, X. F., Li, W., Li, C., Du, G. C. & Chen, J. (2011). Diagenetic facies and high quality reservoir distribution of Chang 8 sandstones in Zhenbei Area of Ordos Basin. *Journal of Oil and Gas Technology*, 33(7), 1-6.
- Pittman, E. D., Larese, R. E., & Heald, M. T. (1992). Clay coats: Occurrence and relevance to preservation of porosity in sandstones. In Houseknecht, D. W., & Pittman, E. D. (Eds.) *Origin, diagenesis, and petrophysics of clay minerals in sandstones* (pp.107-123). Vol. 47.
- Porter, K. E. (1989). An overview of formation damage. *Journal of Petroleum Technology*, 41(08), 780-786. DOI: <http://dx.doi.org/10.2118/19894-PA>
- Reed, M. G. (1989). Formation damage prevention during drilling and completion. Centennial Symposium Petroleum Technology into the Second Century at New Mexico Tech. DOI: <http://dx.doi.org/10.2118/20149-MS>
- Ru, T., Liu, Y. F., Fan, Y., Li, B. G., & Yu, J. Z. (2011). Pressure-sensitive effect in development of low permeability sandstone gas reservoir. *Fault-block Oil & Gas Field*, 18(1), 94-96.
- Sun, X. X., Yang, S. L., & Li, W. G. (2011). Establishment of productivity equation for ultra-deep gas reservoirs considering threshold pressure gradient and pressure-sensitive effect. *Fault-block Oil & Gas Field*, 18(3), 360-362.
- Tian, Y., Guo, Q., Li, Y. Guo, Y. P. & Li, Y. Z. (2009). Acid sensitivity evaluation at Chang8 reservoir in Xifeng Oilfield. *Fault-block Oil & Gas Field*, 16(4), 108-110.
- Wang, C. Y., Zheng, R. C., Li, S. X., Han, Y. L., Shi, J. N., & Zhou, Q. (2010). Early tectonic evolution and sedimentary response of Ordos basin: A case study of Interval 8-Interval 6 oil layers of Yanchang Formation in Jiyuan area. *Geology in China*, 37(1), 134-143.
- Worden, R. H., & Morad, S. (2003). *Clay mineral cements in sandstones*. Blackwell Science Ltd.
- Wu, X. B., Wang, Z. F., Cui, Z. L., & Zhang, Y. T. (2013). Sensitivity evaluation and mechanism discussion on ultra-low permeability reservoir in Zhenbei Area. *Fault-block Oil & Gas Field*, 20(2), 4-8.
- Yang, S. L., & Wei, J. Z. (2004). *Petrophysics*. 1rd. Ed. Beijing Petroleum industry press, 166-170.
- Zhang, G. L., Chen, S. Y., & Yan J. H. (2006). Characteristics of clay minerals and their effects on formation sensitivity in Sha-1 member in Zhengjia-Wangzhuang area. *Acta Mineralogica Sinica*, 26(1), 99-106.
- Zhao, C. P., Yue, X. A., & Lv, C. Y. (2009). Experimental study on creep deformation of pressure sensibility for ultra-low permeability reservoir. *Fault-block Oil & Gas Field*, 16(2), 101-102.
- Zhao, J. F., Liu, C. Y., Yu, L., & Wang, X. M. (2008). The transfer of depocenters and accumulation centers of Ordos Basin in Mesozoic and its meaning. *Acta Geologica Sinica*, 82(4), 540-549.



## Mapping of Underwater Seabed Morphology of the Gaza Strip Coastal Zone Using Remote sensing technique

Khaldoun Abualhin

Al-Azhar University-Gaza, Gaza, Gaza Strip, P.O. Box 1277, Palestine, khaldon@alazhar.edu.ps

### ABSTRACT

The study investigated the feasibility of applying the depth-invariant index algorithm to delineate the shallow underwater geomorphological features using QuickBird imagery. Although the technical procedures of the depth-invariant index are already demonstrated in the professional literature, the algorithm needs to be applied and tested in several coastal regions with different seawater conditions and properties. Some of the geomorphological features in the coastal zone of the Gaza Strip are seasonal features such as underwater sand bars. However, since these features are non-permanent and dynamic, it would be useful to utilize satellite data to detect changes in both locations and depth, and also to monitor this feature in shallow coastal water. The importance of identifying the underwater sand bars in the coastal zone can be significant in the case of rip currents, and swimming conditions. Additionally, using satellite imagery for detecting dynamic underwater coastal morphologies may enable local authorities to adopt such an algorithm with a combination of satellite imagery for fast, efficient and extensive coverage mapping. While information about seafloor features can be obtained using active satellite data such as RADAR or LiDAR imagery, active satellite data are not available and require advanced processing and logistical resources, which are difficult to obtain in the case of the Gaza Strip. The study instead used passive QuickBird satellite imagery to map and delineate the seabed morphologies through the calculating the depth-invariant index for the spectral bands. By using the depth-invariant index, it was possible to distinguish and delineate the major underwater sand bars within the entire coastal zone of the Gaza Strip. Also, the spectral and spatial resolution of QuickBird imagery exhibited a substantial capability in mapping and delineating the underwater seabed morphologies.

*Keywords: Remote sensing, seabed morphology, depth-invariant index, Gaza Strip, Palestine.*

### Mapeo de la morfología del suelo oceánico en la zona costera de la Franja de Gaza a través de la técnica de detección remota

### RESUMEN

El estudio investigó la factibilidad de aplicar el algoritmo Índice de Profundidad Invariante para delinear las características geomorfológicas del suelo bajo el agua a través de las imágenes QuickBird. A pesar de que los procedimientos técnicos del Índice de Profundidad Invariante se han demostrado ampliamente en la literatura profesional, el algoritmo debe ser aplicado y verificado en varias regiones costeras con diferentes condiciones y propiedades del agua marina. Algunas de las condiciones geomorfológicas en la zona costera de la Franja de Gaza dependen de las estaciones, como las barreras de arena bajo el agua. Sin embargo, como estas condiciones son dinámicas, sería útil usar la información satelital para detectar cambios en las locaciones y en la profundidad, y para vigilar estas condiciones en el agua costera poco profunda. La importancia de identificar las barreras de arena en la zona costera puede ser determinante en el caso de corrientes violentas o para las condiciones de inmersión. Adicionalmente, el uso de imágenes satelitales para determinar las dinámicas morfológicas costeras bajo el agua podría permitir a las autoridades locales adoptar un algoritmo que combinado con dichas imágenes presente un mapeo más rápido, más eficiente y de mayor cobertura. Si bien la información sobre las características del suelo oceánico pueden obtenerse con información satelital activa como las imágenes de RADAR o LiDAR, la información no está disponible, además de requerir un procesamiento avanzado y recursos logísticos, que son difíciles de obtener en el caso de la Franja de Gaza. Este estudio, por su parte, utiliza imágenes satelitales pasivas de QuickBird para mapear y delinear las morfologías del lecho del mar a través de calcular el Índice de Profundidad Invariante para las bandas espectrales. Al utilizar el Índice de Profundidad Invariante fue posible determinar y delinear las mayores barreras de arena en toda la costa de la Franja de Gaza. La resolución espacial y espectral de las imágenes de QuickBird mostraron una capacidad sustancial en el mapeo y delimitamiento de las morfologías del lecho marino

*Palabras clave: Teledetección, morfología del suelo marino, índice de profundidad no variable, Franja de Gaza, Palestina.*

*Record*

Manuscript received: 19/04/2015

Accepted for publication: 26/04/2016

*How to cite item*

Abualhin, K. (2016). Mapping of Underwater Seabed Morphology of the Gaza Strip Coastal Zone Using Remote sensing technique. *Earth Sciences Research Journal*, 20(2), C1-C7.

doi:<http://dx.doi.org/10.15446/esrj.v20n2.50256>

## Introduction

Several techniques and algorithms have been developed to use satellite imagery for environmental monitoring and coastal habitats mapping. The mapping of underwater seabed morphologies includes several features such as massive valleys, canyons, rocky outcrops, geomorphological features, and sand bars [Goudie, 2004; Pavlopoulos et al., 2009]. Seabed morphologies are an important element of coastal protection and planning elements and also in mapping marine habitats and their management. Accordingly, it is necessary for the researcher to get detailed information about seabed morphology and habitats in the nearshore coastal zone. Recently, modern methods of marine surveying such as echo sounder and active satellite sensors like LiDAR data are used for scanning the seabed. The advantages of these modern techniques of mapping are on the accuracy and also a full range of depth coverage. On the other hand, these methods of seabed mapping are expensive, time-consuming, and difficult to process. In contrast, passive remotely sensed data have been shown to offer a reasonable alternative in providing reliable and low-cost information about coastal habitats and morphologies [Mumby and Edwards, 2002; Mumby et al., 2004]. Different passive satellite imagery has been used in studying coral reef and classification, benthic habitats classification, sand bottoms delineation and in other studies [Ahmad and Neil, 1994; Andréfou t et al., 2003; Edwards et al., 1999; Green et al., 2000; Hochberg and Atkinson, 2003; Michalek et al., 1993; Mishra et al., 2006; Mumby et al., 1998; Mumby and Edwards, 2002; Mumby and Harborne, 1999; Mumby et al., 2004; Ong et al., 1998; Pasqualini et al., 2005; Stumpf et al., 2003; Vanderstraete et al., 2003]. Mishra et al. (2006) utilized QuickBird multispectral data for identifying and classifying tropical-marine benthic habitats. In 1998, Ong and Hick combined spectral data and digital bathymetry to auto-classify larger benthic habitats. Pasqualini et al., (2005) used SPOT5 satellite imagery to map seagrasses. Mumby et al., (1997a,b, 1998) compared the descriptive resolutions of various remote sensing methods for mapping coral reef habitats of the Turks and Caicos Islands. Other researchers simulated IKONOS data for different seabeds and coral reef habitat mapping [Andréfouet et al., 2003; Hochberg and Atkinson, 2003].

Mumby et al., (2004) provided a general review of what can and cannot be mapped using passive remote sensing data and summarized the capacity of various methods to predict and derive bathymetry from different types of optical imagery [Jupp, 1988; Stumpf et al., 2003]. In terms of satellite spectral and spatial resolutions, multispectral imagery with coarse and medium spatial resolution, Landsat TM, Landsat ETM+, ASTER, and IKONOS satellite data are considered useful tools for monitoring the spatial dynamics of habitats [Mumby and Edwards, 2002; Mumby and Harborne, 1999]. However, taking into consideration the similarity in spectral resolution and the width of the spectral band between QuickBird and IKONOS sensors, the ability of QuickBird data to discriminate seabed morphology in the shallow coastal region is comparable to IKONOS data.

In this study, QuickBird satellite imagery was used to delineate the seabed morphology of sand bars mainly in the nearshore of the Gaza Strip coastal zone. In addition to oceanographic factors, the coastal region of the Gaza Strip suffers from intensive anthropogenic pollution and other manmade interventions along the entire coastal zone. Moreover, as a result of Israel's blockade of the Gaza Strip and the subsequent limitation on resources, it is not always possible to use the most recent technologies and tools for mapping and monitoring the coastal zone, including the mapping of underwater morphologies. As it is important to get up-to-date information about seabed morphologies for monitoring the changing conditions of the coastal zone, a QuickBird satellite image was used to extrapolate the underwater morphology of sand bars along the coastal zone of the Gaza Strip. Underwater bars can be defined as an aggregation of ridges of sediments whose formation, morphology and behavior were determined by interactions between waves, currents, tides, local slope and grain size. Bowman and Goldsmith (1983) delineated a wide

range of nearshore sand bars and shoal patterns along the Southeastern Mediterranean coastline. Their study identified three major types of sand bars: non-rhythmic parallel-meandering bar; inner single-crescentic bars; and, double-crescentic bars [Bowman and Goldsmith, 1983].

## Study area

The Gaza Strip is a part of historical Palestine and is located on the south eastern Mediterranean coast and bordered by Sinai from the south and the Negev desert from the east (Figure 1). The current area of the Gaza Strip is 360 km<sup>2</sup> with an estimated human population density of 4167 per km<sup>2</sup>. The geographic coordinates of the Lower Left and Upper Right corners of the Gaza Strip are 31.31 N, 34.2 E; and 31.53 N, 34.56 E. The shoreline of the Gaza Strip is a smooth line that extends 42 km. The coastal zone includes sand dunes in the south and north, coastal cliffs, and the Wadi Gaza mouth area. Wadi Gaza is the main seasonal river in the Gaza Strip and influence the biodiversity in the Gaza Strip than it does today.

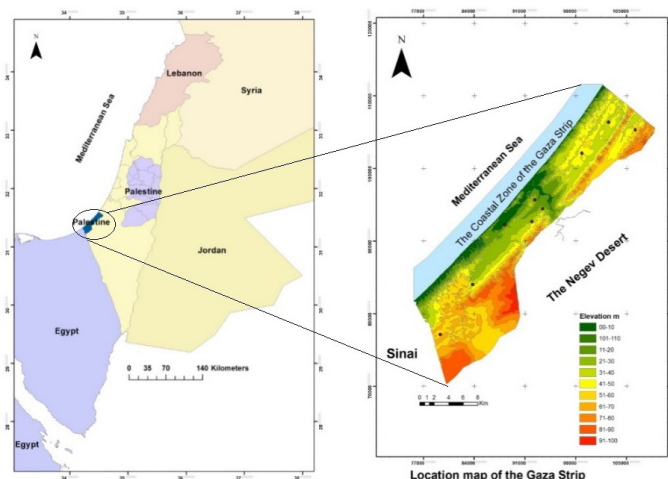


Figure 1. Map of the Gaza Strip, Palestine

## Methodology

Seabed feature and underwater patterns can be mapped from passive remote sensing imagery if the influence of the water column was removed. The implementation of the physical relation between spectral reflectance and light attenuation is the base of extracting information from multispectral satellite imagery over water bodies. The incident radiation on the water column is absorbed and scattered or reflected unequally. The attenuation influence can be estimated over the entire multispectral image by getting water depth at several pixels in the image [Lyzena, 1981]. However, to neutralize the influence of seawater on the reflected signal, an attenuation coefficient must be calculated at each pixel in the image [Green et al., 2000]. Lyzena (1978, 1981) proposed a simple image-based technique to combine the information in various spectral wavelengths to produce the depth-invariant index. In this method, the ratio of water attenuation coefficients are required and optical properties considered uniform.

## Depth-Invariant Index

The concept of extracting bottom-type information in shallow water depends on the fact that the reflected seabed-radiance is a linear function of bottom reflectance and an exponential function of water depth [Lyzena, 1978]. The technique to calculate depth-invariant index involves three main steps: (1) generate a linear relationship between depth and radiance; (2) calculate the ratio of attenuation coefficients of band pairs; and, (3) calculate the depth-invariant index of bottom type (Figure 2).

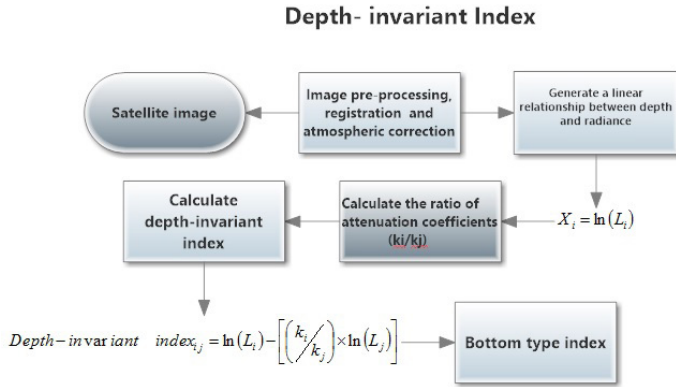


**Figure 2.** Flow chart for generating depth-invariant index

Since the relationship between the depth and reflected radiance over water bodies is an exponential relation, this relationship can be transformed using a natural logarithm (Equation 1) to become a linear relationship. For a given bottom type, the transformed radiance in bands (i) and (j) is linearly (Figure 3). The transformed radiance will attenuate linearly with increasing water depth.

$$X_i = \ln(L_i) \quad (1)$$

where  $X_i$  has transformed reflectance in the band (i).  $L_i$  has atmospherically corrected radiance in the band (i).  $L_n$  is the natural logarithm.

Accordingly, the transformed radiance in the band (i) is plotted versus the transformed radiance in the band (j) at variable depth and constant bottom type (Figure 3). The result falls along a straight line. Consequently, different bottom types should provide different parallel lines [Lyzenga, 1981]. The slope of the lines represents the ratio of attenuation coefficients for each spectral band (Figure 4 and Figure 5).

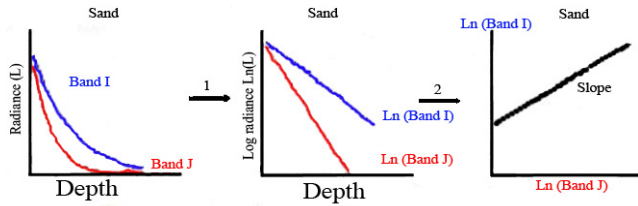


**Figure 3.** Linear exponential relationship between reflected radiance and depth using natural logarithms. The gradient of the line represents the ratio of attenuation coefficient. (Band i has a shorter wavelength, and, therefore, attenuates less rapidly, than band j)

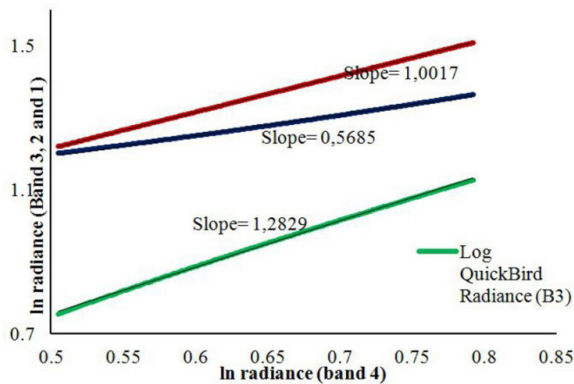


**Figure 4.** Scatter plot of the natural logarithm (log) of QuickBird radiance. QuickBird band 4 was plotted versus band 3, 2 and 1. (The DN values were obtained from 257 pixels over sandy bottom-type at varying depths in the coastal zone of the Gaza Strip.)

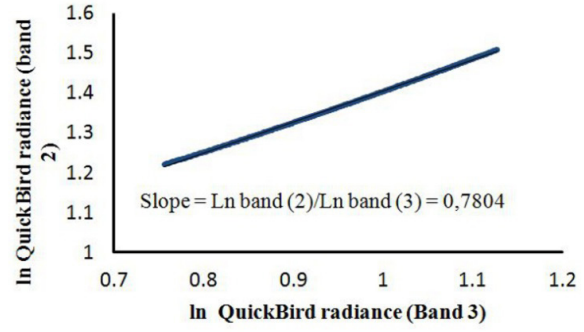


**Figure 5.** Scatter plot of the natural logarithm of QuickBird radiance in the band (3) versus radiance in the band (4) (The QuickBird image for the Gaza coastal zone was acquired on 21 January 2009)

The ratios of the attenuation coefficients of the spectral bands were derived from the scattering bi-plot. The slope of the scatter plot trend line represents the ratio of attenuation coefficients (Figure 5). The slope of the trend line will depend on the variable chosen to be the dependant variable. Accordingly, using Equation 2, the ratio of attenuation coefficients ( $k_i/k_j$ ) will not depend on the order the variable.

$$k_i/k_j = a + \sqrt{a^2 + 1}$$

where,  $a = (\sigma_{ii} - \sigma_{jj})/2\sigma_{ij}$  (2)

$$\sigma_{ij} = \overline{X_i X_j} - \overline{X_i} \overline{X_j}$$

where  $\sigma_{ii}$  and  $\sigma_{jj}$  are the variances for  $i$  and  $j$  measurements respectively, and  $\sigma_{ij}$  is the covariance between  $i$  and  $j$  bands.

Once the ratios of attenuation coefficients are calculated, the depth-invariant indexes can be calculated using Equation 3 for the entire image. Each pair of spectral bands produces a single depth-invariant index for the bottom type.

$$Depth-invariant\ index_j = \ln(L_i) - \left[ \left( \frac{k_i}{k_j} \right) \times \ln(L_j) \right] \quad (3)$$

#### Implementation of Depth-Invariant Index Algorithm on QuickBird Image

A QuickBird satellite image acquired on 21 January 2009 at 08:35 GMT was used to calculate the depth-invariant indices and then to map the seabed morphology along the coastal zone of the Gaza Strip. The QuickBird image was radiometrically and geometrically corrected. The image was registered to the topographic map with RMS less than 0.4 pixels (Table 1). The atmospheric correction was then performed using the ENVI FLAASH module. The homogeneous regions in the satellite image with a uniform bottom reflectance were selected to be used for attenuation coefficient calculation. The ratio of attenuation coefficients was calculated based on the equation 2. Table 2 shows the calculated attenuation coefficients ratios ( $k_i/k_j$ ) for each pair of spectral bands.

**Table 1.** Satellite data characteristics

Satellite Imagery	Date dd-mm-yy	Spatial resolution (m)	Spectral resolution	RMS pixel
QuickBird	21.01.2009	2.4	4 bands	0.39

**Table 2.** The calculated variance ( $\sigma_{ii}$ ,  $\sigma_{jj}$ ), covariance ( $\sigma_{ij}$ ) and the ratio of attenuation coefficients ( $k_i/k_j$ ) for each pair of logarithmic transformed QuickBird bands

	$\ln(b1)$	$\ln(b2)$	$\ln(b3)$	$\ln(b4)$		
Variance ( $\sigma_{ii}$ )	0.0022	0.0068	0.011	0.0068		
	<i>B1-B2</i>	<i>B1-B3</i>	<i>B1-B4</i>	<i>B2-B3</i>	<i>B2-B4</i>	<i>B3-B4</i>
Covariance ( $\sigma_{ij}$ )	0.00386	0.00494	0.00385	0.0087	0.00679	0.0087
<i>a</i>	-0.06	-0.9	-0.6	-0.25	0.0017	0.25
Attenuation Co. ( $k_i/k_j$ )	1.1	0.445	0.566	0.78	1.0	1.28

**Results and discussion**

Several depth-invariant indices were calculated from QuickBird imagery for the coastal zone of the Gaza Strip, portraying different abilities to recognize seabed morphology. For example the calculated index from band 1 and band 3 demonstrated the ability to map features in shallow depth up to 10 m. The index derived from band 2 and band 3 showed the feasibility of mapping features at shallow water depth. The index of band 2 and band 4 as well as an index of the band 3 and band 4 obtained reasonable results in mapping the very shallow coastal bars at depth varying from 0.0 -1.5 m. These bars welded to the coastline. Accordingly, different types of seabed bars were clearly observed and delineated at different locations in the entire coastal zone and nearshore zone of the Gaza Strip. Types of bars are often distinguished based on their shape and orientation about the shoreline. They may be linear, sinuous or crescentic, or they may consist of alternating transverse bars, which are welded to the shoreline and are separated by channels occupied by rip currents, as seen in Figure 6 [Goudie, 2004].

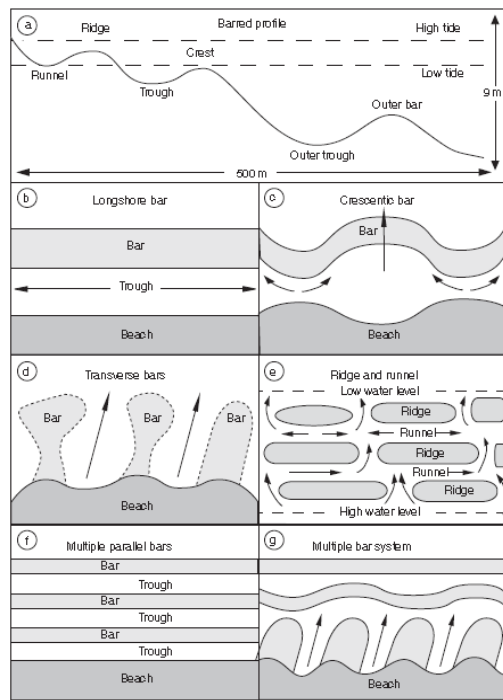


**Figure 6.** Idealized cross-shore barred profile (a) and some examples of bar types [Goudie, 2004].

The mapped sand bars in the coastal zone of the Gaza Strip were similar to those observed by [Almagor and Hall, 1984; Bowman and Goldsmith, 1983; Goldsmith et al., 1982], in the South-eastern Mediterranean coast. Some of these sand bars are seasonal occurrences while others occur throughout the year.

The delineated underwater sand bars in the Gaza Strip coastal zone were as follows: single-crescentic bars; anvil-shaped transverse bars, oblique transverse bars, initial crescentic bars, double crescentic bars and triple crescentic bars. Figure 7 shows the different types of underwater sand bars delineated in the

nearshore of the Gaza Strip. As mentioned above, depth-invariant indices demonstrated disparities in their sensitivity to mapping seabed features in the shallow coastal region. For instance, double and triple crescentic bar systems can be delineated using the ratio index of band 1 and band 2. The ratio of band 2 and band 3 achieved a respectable result in mapping different sand bar systems at different locations. The indices of band 2 and band 4 and of band 3 and band 4 showed less capability in mapping sand bar features.

In addition, the calculated depth-invariant indices provided a dimensionless bottom relief in the nearshore zone of the Gaza Strip. Several bottom relief profiles were generated perpendicular to the coastline (Figure 7 and Figure 8). Figure 8 shows a variation in the seabed relief on both sides of the fishing port. This variation may be the result of sediments being transported from the Nile Delta to the Southeastern Mediterranean nearshore shelf by northward longshore currents [Rohrlicht and Goldsmith, 1984; Zviely et al., 2007]. Since the sediments are trapped and accumulated at the southern side of the fishing port, the sand supply to the northern side of the fishing port has decreased. Two sandbars appeared at the southern side of the fishing port and located at a distance of 100 m up to 400 m from the coastline. Figure 9 illustrates the bottom relief of the general morphology and distribution of the underwater sand bars.

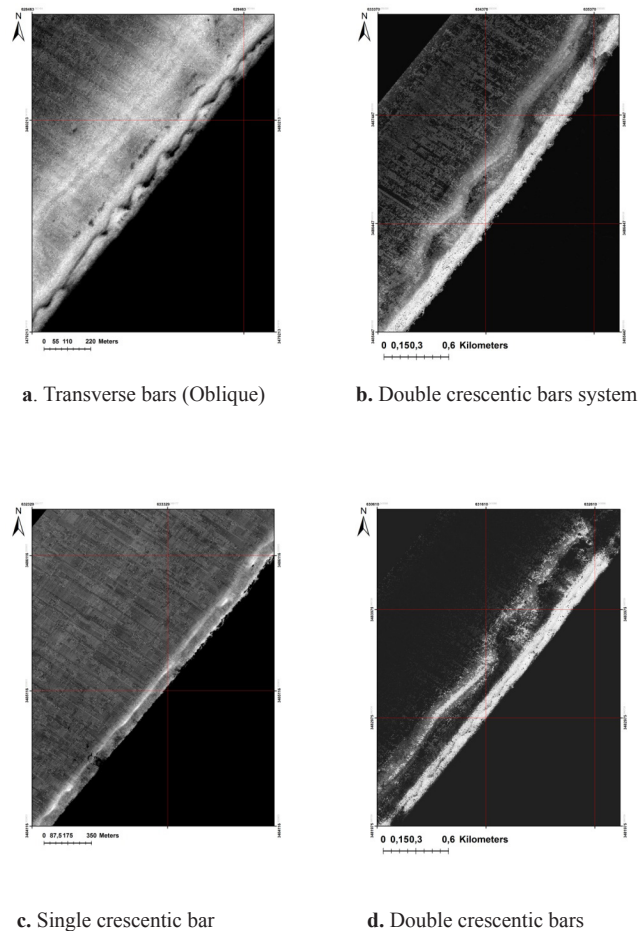


**Figure 7.** Example of sand bars observed along the coastal zone of the Gaza strip. (The bars were extracted from QuickBird imagery using depth-invariant index technique [Lyzenga, 1981])

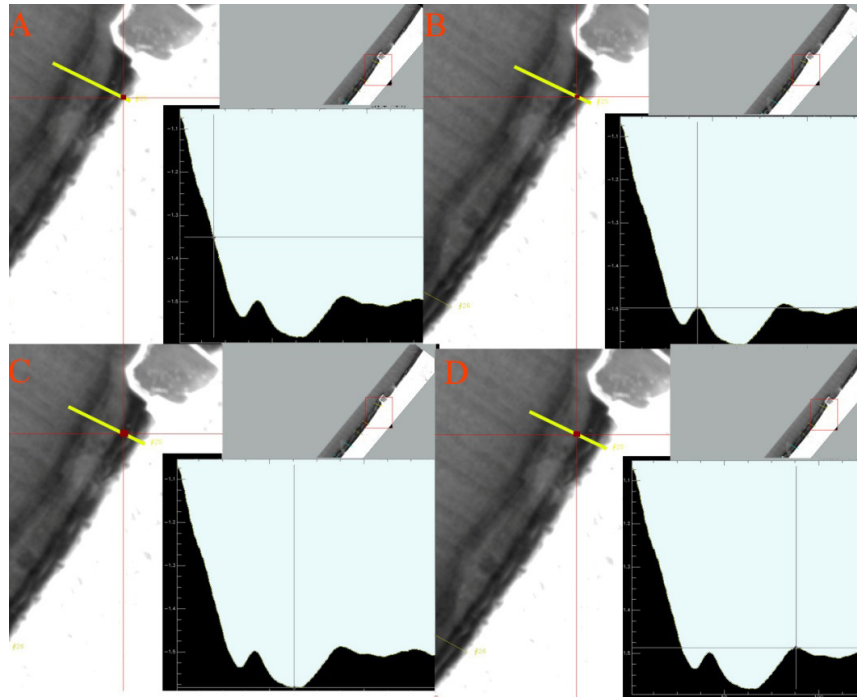


Figure 8. The bottom relief on the southern side of the Seaport and up to 400m seaward. (The figure reveals the bars crest and trough about the distance of 500 m from the shoreline. The profile was obtained from the calculated depth-invariant index for QuickBird imagery.)

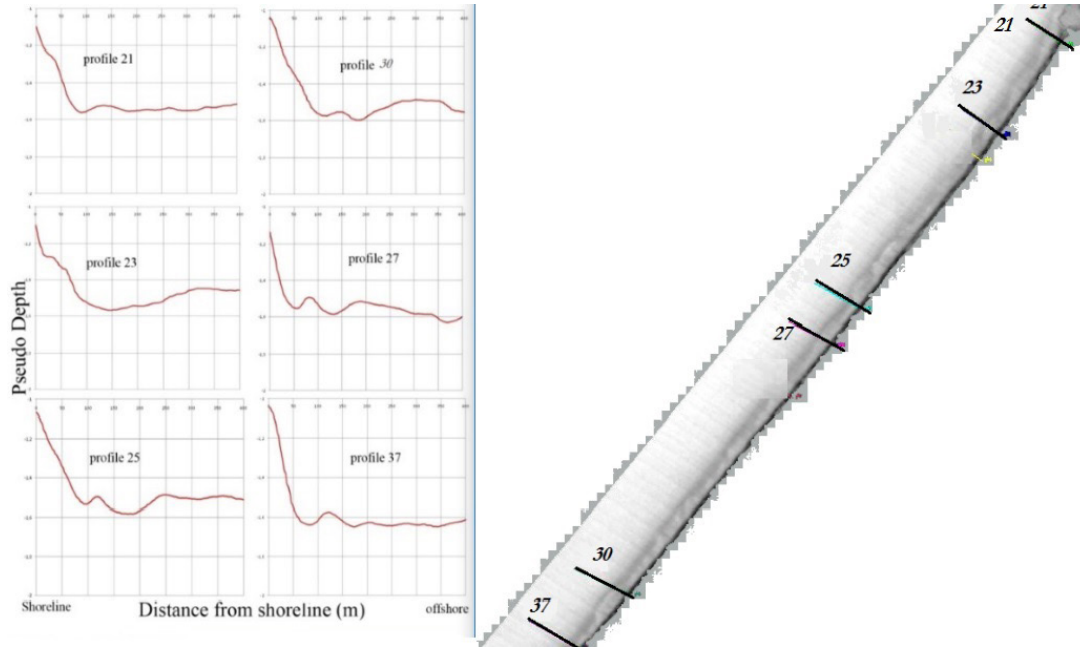
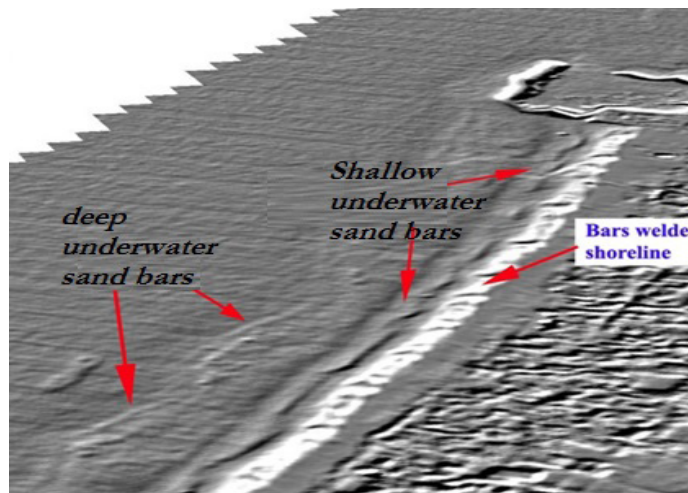


Figure 9. Bottom relief profiles. (The profiles were extracted from the calculated depth-invariant index for QuickBird band 2 and band3. The horizontal component of the patterns was relatively accurate where the vertical component is pseudo-depth.)

Utilizing the ENVI Topographic Modelling tool, the slope, the aspect and the shaded relief image were derived from the seabed indices (Figure 10). Index from band 1 and band b3 demonstrated a slope gradient of the Gaza Strip coastal zone ranging from  $0.57^\circ$  to  $0.41^\circ$  at a distance of 50 m to 100 m from the coastline.



**Figure 10.** Shaded relief surface generated from the depth-invariant index of QuickBird band 2 and band 3. (The sand bars appear in three sets: the first one attached to the coastline, the second located within a very shallow water from 2-4 m, and the third located at 200-400 m distance from the coast at a depth of 7-10 m.)

### Conclusion

Gathering Information about seabed morphology and bottom profiles requires advanced instruments and sometimes it is a time-consuming process. Data collection may also be complicated by challenging field and logistical circumstances beyond the control of researchers, as has been the case in the Gaza Strip. Nevertheless, remotely sensed imagery has provided an alternative method for generating bathymetric maps with reasonable accuracy. In particular, the utilization of the depth-invariant index to map and delineate underwater seabed morphology has proven effective. The study confirmed the possibility of deriving underwater seabed morphology in shallow water. The calculated indices provided interesting results on mapping seabed morphology such as sand bars and bottom profile. The method enables mapping and delineates the major underwater sand bars along the entire coastal zone of the Gaza Strip. Importantly, various types of seabed morphologies were clearly observed and defined at different regions and depths in the Gaza Strip coastal zone such as crescentic bars, single-crescentic bars, double-crescentic bars, triple crescentic bars and transverse bars. Some bar systems were located onshore and attached to the shoreline at a very shallow depth of up to 2 meters, as was the case for transverse bars, which then moved offshore to form crescent bars. Consequently double crescent bars are formed at a deeper depth and distance from 150 up to 400 meters offshore.

Finally, as the nearshore region of the Gaza Strip is homogeneous and consists mainly of sandy sediments, the spectral and spatial resolution of QuickBird imagery were useful in distinguishing natural variations and contrasts due to optical physical properties of coastal habitats. QuickBird imagery exhibited a substantial capacity to delineate underwater seabed morphology by using depth-invariant index technique. The achieved findings were quite satisfying and consistent with published information on the region.

### Acknowledgment

Special gratitude is extended to the DAAD (German Exchange Service) for funding support and the purchase the QuickBird image.

### References

- Ahmad, W., & Neil, D. (1994). An evaluation of Landsat Thematic Mapper (TM) digital data for discriminating coral reef zonation: Heron Reef (GBR). *International Journal of Remote Sensing*, 15, 2583-2597.
- Almagor, G., Gill, D., & Perath, I. (2000). Marine sand resources offshore Israel. *Marine Georesources and Geotechnology*, 18, 1-42.
- Almagor, G., & Hall, J. (1984). Morphology and bathymetry of the Mediterranean Continental margin of Israel. *Geological Survey of Israel Bulletin*, 77.
- Andréfouet, S., Kramer, P., Torres-Pulliza, D., Joyce, K., Hochberg, E., Garza-Pérez, R., Mumby, P., Riegl, B., Yamano, H., & White, W. (2003). Multi-site evaluation of IKONOS data for classification of tropical coral reef environments. *Remote Sensing of Environment*, 88, 128-143.
- Bowman, D., & Goldsmith, V. (1983). Bar morphology of dissipative beaches: an empirical model. *Marine Geology*, 51, 15-33.
- Edwards, A., Mumby, P., Green, E., & Clark, C. (1999). *Applications of Satellite and Airborne Image Data to Coastal Management: Seventh Computer-Based Learning Module (BILKO for Windows)*. Paris: UNESCO.
- Goldsmith, V., Bowman, D., & Kiley, K. (1982). Sequential stage development of crescentic bars: HaHoterim Beach, Southeastern Mediterranean. *Journal of Sedimentary Petrology*, 52, 233-249.
- Goudie, A. (2004). *Encyclopedia of geomorphology*. New York: Routledge Ltd.
- Green, E., Mumby, P., Clark, C., & Edwards, T. (2000). *Remote sensing handbook for tropical coastal management*. Paris: UNESCO.
- Green, E., Mumby, P., Edwards, A., & Clark, C. (1996). A review of remote sensing for the assessment and management of tropical coastal resources. *Coastal Management*, 24, 1-40.
- Hochberg, E., & Atkinson, M. (2003). Capabilities of remote sensors to classify coral, algae, and sand as pure and mixed spectra. *Remote Sensing of Environment*, 85, 174-189.
- Huston, M. (1994). *Biological Diversity: The Coexistence of Species*. Cambridge: Cambridge University Press.
- Jupp, D. (1988). Background and extension to depth of penetration (DOP) mapping in shallow coastal waters. In *Proceedings of the Symposium on Remote Sensing of the Coastal Zone*. Gold Coast, Queensland.
- Lyzenga, D. (1978). Passive remote sensing techniques for mapping water depth and bottom features. *Appl. Opt.*, 17, 379-383.
- Lyzenga, D. (1981). Remote sensing of bottom reflectance and water attenuation parameters in shallow water using aircraft and Landsat data. *International Journal of Remote Sensing*, 2, 71-82.
- Michalek, J., Wagner, T., Luczkovich, J., & Stoffle, R. (1993). Multispectral change vector analysis for monitoring coastal marine environments. *Photogrammetric engineering and remote sensing*, 59, 381-384.
- Mishra, D., Narumalani, S., Rundquist, D., & Lawson, M. (2006). Benthic habitat mapping in tropical marine environments using QuickBird multispectral data. *Photogrammetric engineering and remote sensing*, 72, 1037.
- Mumby, P. J., Green, E. P., Edwards, A. J., & Clark, C. D. (1997). Coral reef habitat mapping: how much detail can remote sensing provide?. *Marine Biology*, 130(2), 193-202.
- Mumby, P. J., Green, E. P., Clark, C. D., & Edwards, A. J. (1997). Reefal habitat assessment using (CASI) airborne remote sensing. In *Proc 8th Int Coral Reef Symp (Vol. 2, pp. 1499-1502)*.
- Mumby, P., Clark, C., Green, E., & Edwards, A. (1998). Benefits of water column correction and contextual editing for mapping coral reefs. *International Journal of Remote Sensing*, 19, 203-210.
- Mumby, P., & Edwards, A. (2002). Mapping marine environments with IKONOS imagery: enhanced spatial resolution can deliver greater thematic accuracy. *Remote Sensing of Environment*, 82, 248-257.
- Mumby, P., & Harborne, A. (1999). Development of a systematic classification scheme of marine habitats to facilitate regional management and mapping of Caribbean coral reefs. *Biological Conservation*, 88, 155-163.
- Mumby, P., Skirving, W., Strong, A., Hardy, J., LeDrew, E., Hochberg, E., Stumpf, R., & David, L. (2004). Remote sensing of coral reefs and their physical environment. *Marine pollution bulletin*, 48, 219-228.

- Ong, C., Hick, P., Burt, J., & Wyllie, A. (1998). Marine habitat mapping using data from the Geoscan airborne multi-spectral scanner. *Geocarto International*, 13, 27 - 34.
- Pasqualini, V., Pergent-Martini, C., Pergent, G., Agreil, M., Skoufas, G., Sourbes, L., & Tsirika, A. (2005). Use of SPOT 5 for mapping seagrasses: an application to *Posidonia Oceanica*. *Remote Sensing of Environment*, 94, 39-45.
- Pavlopoulos, K., Evelpidou, N., & Vassilopoulos, A. (2009). *Mapping Geomorphological Environments*. Berlin: Springer Verlag.
- Rohrlicht, V., & Goldsmith, V. (1984). Sediment Transport along the Southeast Mediterranean: A geological perspective. *Geo-Marine Letters*, 4, 99-103.
- Stumpf, R., Holderied, K., & Sinclair, M. (2003). Determination of water depth with high-resolution satellite imagery over variable bottom types. *Limnology and Oceanography*, 48, 547-556.
- Vanderstraete, T., Goossens, R., & Ghabour, T. (2003). Can ASTER-data be used for bathymetric mapping of coral reefs in the Red Sea using digital photogrammetry? In, *Proceedings of the Second Workshop of the EARSeL Special Interest Group on Remote Sensing for Developing Countries* (pp. 212-218). Bonn, Germany.
- Zviely, D., Kit, E., & Klein, M. (2007). Longshore sand transport estimates along the Mediterranean coast of Israel in the Holocene. *Marine Geology*, 238, 61-73.





## Water temperature prediction in a subtropical subalpine lake using soft computing techniques

Saeed Samadianfard<sup>1,\*</sup>, Honeyeh Kazemi<sup>1</sup>, Ozgur Kisi<sup>2</sup>, Wen-Cheng Liu<sup>3</sup>

<sup>1</sup>Department of Water Engineering, University of Tabriz, Tabriz, Iran (\*corresponding author, e-mail: s.samadian@tabrizu.ac.ir, Tel: +989141101845, Fax: +984113356007)

<sup>2</sup>Department of Civil Engineering, Canik Basari University, Samsun, Turkey

<sup>3</sup>Department of Civil and Disaster Prevention Engineering, National United University, Miao-Li, Taiwan

### ABSTRACT

Lake water temperature is one of the key parameters in determining the ecological conditions within a lake, as it influences both chemical and biological processes. Therefore, accurate prediction of water temperature is crucially important for lake management. In this paper, the performance of soft computing techniques including gene expression programming (GEP), which is a variant of genetic programming (GP), adaptive neuro fuzzy inference system (ANFIS) and artificial neural networks (ANNs) to predict hourly water temperature at a buoy station in the Yuan-Yang Lake (YYL) in north-central Taiwan at various measured depths was evaluated. To evaluate the performance of the soft computing techniques, three different statistical indicators were used, including the root mean squared error (RMSE), the mean absolute error (MAE), and the coefficient of correlation (R). Results showed that the GEP had the best performances among other studied methods in the prediction of hourly water temperature at 0, 2 and 3 meter depths below water surface, but there was a different trend in the 1 meter depth below water surface. In this depth, the ANN had better accuracy than the GEP and ANFIS. Despite the error (RMSE value) is smaller in ANN than GEP, there is an upper bound in scatter plot of ANN that imposes a constant value, which is not suitable for predictive purposes. As a conclusion, results from the current study demonstrated that GEP provided moderately reasonable trends for the prediction of hourly water temperature in different depths.

*Keywords: Soft computing techniques, statistical indicators, subalpine lake, water temperature.*

### RESUMEN

La temperatura del agua es uno de los parámetros básicos para determinar las condiciones ecológicas de un lago, ya que está influenciada por procesos químicos y biológicos. Además, la exactitud en la predicción de la temperatura del agua es esencial para el manejo del lago. En este artículo se evalúa el desempeño de técnicas de soft computing como la Programación de Expresiones de Genes (PEG), que es una variante de la Programación Genética (PG), el Sistema Neuro-fuzzy de Inferencia Adaptativa (Anfis, en inglés) y las Redes Neuronales Artificiales (RNA) para predecir la temperatura del agua en diferentes niveles de una estación flotante del lago Yuan-Yang (YYL), en el centro-norte de Taiwán. Se utilizaron tres indicadores estadísticos, el Error Cuadrático Medio (ECM), el Error Absoluto Medio (MAE, en inglés) y el Coeficiente de Correlación (R) para evaluar el desempeño de las técnicas de computación. Los resultados muestran que la PEG es más exacta en la predicción de la temperatura del agua entre 0,2 y 3 metros de profundidad. Sin embargo, se evidencia una tendencia diferente a partir del metro de profundidad. A esta distancia de la superficie, las RNA son más exactas que la PEG y el Anfis. Los resultados de este estudio probaron claramente la usabilidad del PEG y las RNA en la predicción de la temperatura del agua a diferentes profundidades.

*Palabras clave: Técnicas soft computing, indicadores estadísticos, lago subalpino, temperatura del agua.*

### Record

Manuscript received: 29/04/2014

Accepted for publication: 26/02/2016

### How to cite item

Samadianfard, S., Kazemi, H., Kisi, O., & Liu W. C. (2016). Water temperature prediction in a subtropical subalpine lake using soft computing techniques. *Earth Sciences Research Journal*, 20(2), D1-D11. doi:<http://dx.doi.org/10.15446/esrj.v20n2.43199>

## 1. Introduction

Water temperature is a fundamental physical property with a direct impact on all organisms inhabiting the aquatic environment (Webb et al., 2008). Because predicting the water temperature is important for maintaining water quality and for ecosystem management, several authors have investigated methods for simulating water temperature of lakes (Lawrence et al., 2002; Lee et al., 2009; Schwab et al., 2009). Hondzo and Stefan (1996) simulated daily water temperature and dissolved oxygen profiles in Minnesota lakes by deterministic process-based water quality models with daily meteorological conditions as input. Derived empirical formulas for lake water quality and stratification indicators from the simulation results gave good predictions of temperature and dissolved oxygen characteristics estimated from measurements in seven Minnesota lakes. Fang and Stefan (1996) substantially modified a water temperature and ice cover model for freshwater lakes and combined it with a summer model to simulate water temperature structures and ice thickness in two small lakes in the north central US. The best value of volume averaged water temperature for the two studied small lakes was higher than was previously found for a larger lake. Benyahya et al. (2007) provided an overview of the existing statistical water temperature models. They categorized them in two major groups: deterministic and statistical/stochastic models. They stated that the deterministic models require numerous input data and they are appropriate for analyzing different impact scenarios, but the main advantage of the statistical models is their relative simplicity and relative minimal data requirement. Sharma et al. (2008) developed models to predict annual maximum near-surface lake water temperatures for lakes across Canada using four statistical approaches: multiple regression, regression tree, artificial neural networks and Bayesian multiple regression. Although artificial neural networks were marginally better for three of the four data sets, multiple regression was considered to provide the best solution based on the combination of model performance and computational complexity. Trumpickas et al. (2009) tried to construct empirical relationships between surface water temperatures and local air temperatures that could be used to estimate future water temperatures using future air temperatures generated by global climate models. Zhao et al. (2011) calculated the surface water temperature, deep water temperature and mean annual epilimnetic temperature and compared the obtained values with empirical data in Lake Taihu by using the dynamic water temperature model. The simulated values were consistent with empirical data. Results showed that this model could be used for the temperature simulation in the studied lake. Thiery et al. (2014) evaluated a set of one dimensional lake models for Lake Kivu, East Africa. In this study, meteorological observations from two automatic weather stations were used to drive the models, whereas a unique dataset, containing over 150 temperature profiles recorded since 2002, was used to assess the model's performance. Simulations were performed over the freshwater layer only (60 m) and over the average lake depth (240 m). The good agreement between the deep simulations and the observed meromictic stratification also showed that a subset of models was able to account for the salinity- and geothermal induced effects upon deep-water stratification.

Also, some attempts have been made to relate lake water temperature to meteorological parameters such as air temperature. In this context, Piccolroaz et al. (2013) developed Air2Water, a simple physically based model to relate the temperature of the Lake Superior (USA–Canada), considering a 27 years record of measurements, to air temperature only. The results proved that their model was suitable to be applied over long timescales (from monthly to interannual), and could be easily used to predict the response of a lake to climate change, since projected air temperatures were usually available by large-scale global circulation models. Toffolon et al. (2014) reconstructed temperature of the surface layer of temperate lakes by means of a simplified model on the basis of air temperature alone. The comparison between calculated and observed data showed a remarkable agreement for all 14 lakes investigated (Mara, Sparkling, Superior, Michigan, Huron, Erie, Ontario, Biel, Zurich, Constance, Garda, Neusiedl, Balaton, and Baikal, in west-to-east order), which presented a wide range of morphological and hydrological characteristics.

Given the significant impact of lakes on surface atmosphere interactions, the need for an accurate simulations of lake temperatures at different depths arises. For this purpose, soft computing techniques such as gene expression programming (GEP), adaptive neuro fuzzy inference system (ANFIS) and artificial neural networks (ANN) can play undeniable roles in mentioned simulations.

Gene expression programming (GEP) has been applied to a wide range of problems in artificial intelligence, artificial life, engineering and science. GEP can be successively applied to areas where (i) the interrelationships among the relevant variables are poorly understood (or where it is suspected that the current understanding may well be wrong), (ii) finding the size and shape of the ultimate solution is difficult, (iii) conventional mathematical analysis does not, or cannot, provide analytical solutions, (iv) an approximate solution is acceptable (or is the only result that is ever likely to be obtained), (v) small improvements in performance are routinely measured (or easily measurable) and highly prized, (vi) there is a large amount of data in computer readable form, that requires examination, classification, and integration, e.g., molecular biology for protein and DNA sequences, astronomical data, satellite observation data, financial data, marketing transaction data, or data on the World Wide Web (Banzhaf et al. 1998). During the last decade, genetic programming has been used as a viable alternative approach to physical models. Aytekin and Kisi (2008) applied GP to suspended sediment transport, and found it to perform better than conventional rating curve and multi-linear regression techniques. Shiri and Kisi (2011) compared GEP and ANFIS methods for predicting groundwater table depth fluctuations and found GEP to be better than ANFIS in this regard. Samadianfard (2012) examined the potential of the GEP technique in estimating flow friction factor in comparison with the most currently available explicit alternatives to the Colebrook–White equation. Results revealed that by using GEP, the friction factor could be identified precisely. Samadianfard et al. (2012) studied the capabilities of the GP in simulating the wetting patterns of drip irrigation. Results showed that the GP method had good agreement with the results of HYDRUS 2D software considering the full set of operators in estimation of radius and depth of wetting patterns. Also results obtained from field experimental in a sandy loam soil showed reasonable agreement with the GP results. Results of the study demonstrated the usefulness of the GP method for estimating wetting patterns of drip irrigation.

ANFIS is a neuro-fuzzy system, which uses a feed-forward network to search for fuzzy decision rules that perform well on a given task. Using a given input/output data set, ANFIS creates a fuzzy inference system whose membership function parameters are adjusted using a back-propagation algorithm alone or a combination of a back-propagation algorithm with a least mean square method. This allows the fuzzy systems to learn from the data being modeled. Kisi (2006) investigated the ability of ANFIS technique to improve the accuracy of daily evaporation estimation. Based on his results, the ANFIS computing technique could be used successfully in modeling evaporation process from the available climatic data. Shiri et al. (2011) compared ANFIS to ANN to estimate daily pan evaporation values from climatic data and found ANFIS to be better than ANN.

The artificial neural network (ANN) approach provides a viable solution to the environmental problems because it is based on training not on analytical models or statistical assumptions. ANN models can be trained to predict results from examples and once trained; they can perform predictions at very high speed (Mellit et al., 2006). ANN is an intelligent data-driven modeling tool that is able to capture and represent complex and non-linear input/output relationships. ANNs are massively parallel, distributed processing systems that can continuously improve their performance via dynamic learning. Moghaddamnia et al. (2009) explored evaporation estimation methods based on ANN and ANFIS techniques. They found that ANN and ANFIS techniques had much better performances than the empirical formulas. Zaier et al. (2010) developed ANN ensemble models to improve the results of single artificial neural network (single ANN) for the estimation of the ice thickness in a number of selected Canadian lakes during the early winter ice growth period. ANN ensemble models for the estimation of ice thickness proved to be more accurate than single ANN models. Kisi et al. (2012) applied three artificial intelligence approaches,

namely ANNs, ANFIS and GEP to forecast daily lake-level variations of Lake Iznik in Turkey. The results obtained by the GEP approach indicated that it performed better than ANFIS and ANNs in predicting lake-level variations. Liu and Chen (2012) compared the performance of the ANN technique with a physically based three-dimensional circulation model for prediction of water temperature at a buoy station in the Yuan-Yang Lake in north-central Taiwan at various measured depths. The simulated results revealed that the accuracy of the three-dimensional circulation model was better than the ANN model. Fallah-Mehdipour et al. (2013) investigated the capability of ANFIS and GP as two artificial intelligence tools to predict and simulate groundwater levels in three observation wells in the Karaj plain, Iran. Results indicated that GP yielded more appropriate results than ANFIS when different combinations of input data were employed in both prediction and simulation processes.

The main objective of this paper is to investigate the accuracy of soft computing techniques such as gene expression programming, adaptive neuro fuzzy inference system and artificial neural network methods for the prediction of hourly water temperature in a lake at different measured depths. Some statistical parameters for error estimation are used herein as comparing criteria for the evaluation of the performance of the studied models.

## 2. Material and Methods

### 2.1. Study site and data collection

Yuan-Yang Lake (YYL, 24°34'60.00"N, 121°24'0.00"E, area=  $3.7 \times 10^4$  m<sup>2</sup>; maximum depth= 4.5 m) in north-central Taiwan is a subtropical, humid lake in the Cilian National Forest Preserve (Figure 1). Figure 2 shows the bathymetry of the YYL (contours in m). Also, YYL is a subalpine lake situated in a natural reserve area that has been virtually undisturbed by human activity for a long time (Chen and Wu, 1999). It is surrounded by a cloud belt forest of Taiwan yellow cypress, an important timber tree and a relic species. The lake is located 1670 m above the mean sea level which is at the subalpine region. The geography of the drainage basin allows large quantities of terrestrial runoff from the surrounding mountains to enter the YYL (Wu et al., 2001). The mean annual air temperature is approximately 13°C (monthly averages range from -5 to 15°C), and annual precipitation can exceed 4000 mm. Wind speed over the lake, which was measured 1 m above the lake by an anemometer, (between 0 to 4.220 m.s<sup>-1</sup>) is relatively weak. The dominant wind directions are from the east and the south west because of the V-shaped valley facing east to west. Concerns about the water quality in YYL, have been rapidly increasing recently due to the natural and anthropogenic pollution. In order to understand the underlying physical and chemical processes as well as their associated spatial distribution in YYL, Liu et al. (2011) analyzed fourteen physico-chemical water quality parameters recorded at the eight sampling stations by using multivariate statistical techniques and a geostatistical method. Their results showed that four principal components i.e., nitrogen nutrients, meteorological factor, turbidity and nitrate factors, account for 65.52% of the total variance among the water quality parameters. The spatial distribution of principal components further confirmed that nitrogen sources constitute an important pollutant contribution in the YYL. Since April 2004, the deepest point of YYL (approximately 4.5 m) was instrumented with a buoy that measures environmental parameters every 10 min (see Figure 2); these data are accessible at the Global Ecological Lakes Observatory Network (GLEON) website. All data from the instrumented buoy and associated meteorological variables were downloaded from the GLEON publicly accessible database. The YYL buoy measured surface dissolved oxygen, wind speed, wind direction, water temperature profiles, and air temperature. A weather station approximately 1 km from the lake also measured rainfall, humidity, and soil temperature. High-resolution water temperature profiles collected from the buoy were used for the training and validation of the studied models. Also meteorological variables given in Table 1 were used to develop the soft computing techniques.

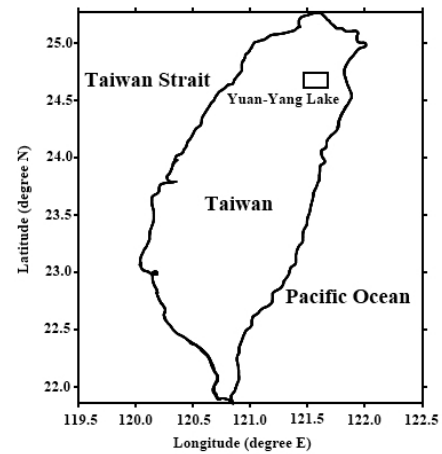


Figure 1. Location of Yuan-Yang Lake in Taiwan

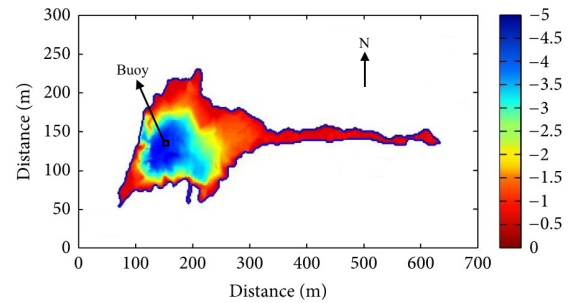


Figure 2. The bathymetry of the YYL (contours in m)

Table 1. Meteorological variables used to develop the models

Variables	Notation
Solar radiation (W.m <sup>-2</sup> )	SR
Air pressure (h.pa)	AP
Relative humidity (%)	RH
Rainfall (mm)	RA
Wind speed (m.s <sup>-1</sup> )	WS
Soil temperature (°C)	ST
Air temperature (°C)	AT
Water temperature at surface (°C)	WT0
Water temperature at 1 m below surface (°C)	WT1
Water temperature at 2 m below surface (°C)	WT2
Water temperature at 3 m below surface (°C)	WT3

Table 2 represents the hourly statistical parameters of the applied variables. In this table, the terms  $X_{mean}$ ,  $X_{min}$ ,  $X_{max}$ ,  $S_p$ ,  $C_v$ , and  $C_{sk}$  denote the mean, minimum, maximum, standard deviation, coefficient of variation and skewness coefficient, respectively. As can be seen clearly, rainfall has the maximum skewness. Solar radiation and relative humidity also indicate a skewed distribution. Air pressure, soil temperature and air temperature show normal distributions because they have significantly low skewness values. Table 3 shows the correlations between the meteorological and hourly water temperature parameters. As can be seen from the table, the soil temperature has the highest correlations with hourly water temperatures in all depths. Air temperature also has higher correlations than the other variables. Time variation graphs of the meteorological variables used as inputs to the GEP, ANFIS and ANN models are illustrated in Figure 3.

**Table 2.** Hourly statistical parameters of the observed data.

Variables	Notation
Solar radiation (W.m <sup>-2</sup> )	SR
Air pressure (h.pa)	AP
Relative humidity (%)	RH
Rainfall (mm)	RA
Wind speed (m.s <sup>-1</sup> )	WS
Soil temperature (°C)	ST
Air temperature (°C)	AT
Water temperature at surface (°C)	WT0
Water temperature at 1 m below surface (°C)	WT1
Water temperature at 2 m below surface (°C)	WT2
Water temperature at 3 m below surface (°C)	WT3

**Table 3.** Correlations between meteorological and hourly water temperature parameters.

	SR	AP	RH	RA	WS	ST	AT	WT0	WT1	WT2	WT
SR	1.00										
AP	0.43	1.00									
RH	-0.53	-0.11	1.00								
RA	-0.11	-0.14	0.07	1.00							
WS	0.61	0.14	-0.33	0.06	1.00						
ST	0.09	0.18	0.03	0.01	0.01	1.00					
AT	0.66	0.42	-0.43	-0.04	0.51	0.35	1.00				
WT0	0.11	0.45	-0.05	-0.03	0.13	0.59	0.66	1.00			
WT1	0.05	0.35	0.03	0.04	0.08	0.77	0.35	0.72	1.00		
WT2	0.06	0.14	0.06	0.04	0.03	0.92	0.26	0.44	0.70	1.00	
WT3	0.06	-0.11	0.05	0.05	0.03	0.83	0.22	0.25	0.44	0.90	1.00

Note: the terms  $X_{mean}$ ,  $X_{min}$ ,  $X_{max}$ ,  $S_x$ ,  $C_v$  and  $C_{sk}$  denote the mean, minimum, maximum, standard deviation, coefficient of variation and skewness, respectively.

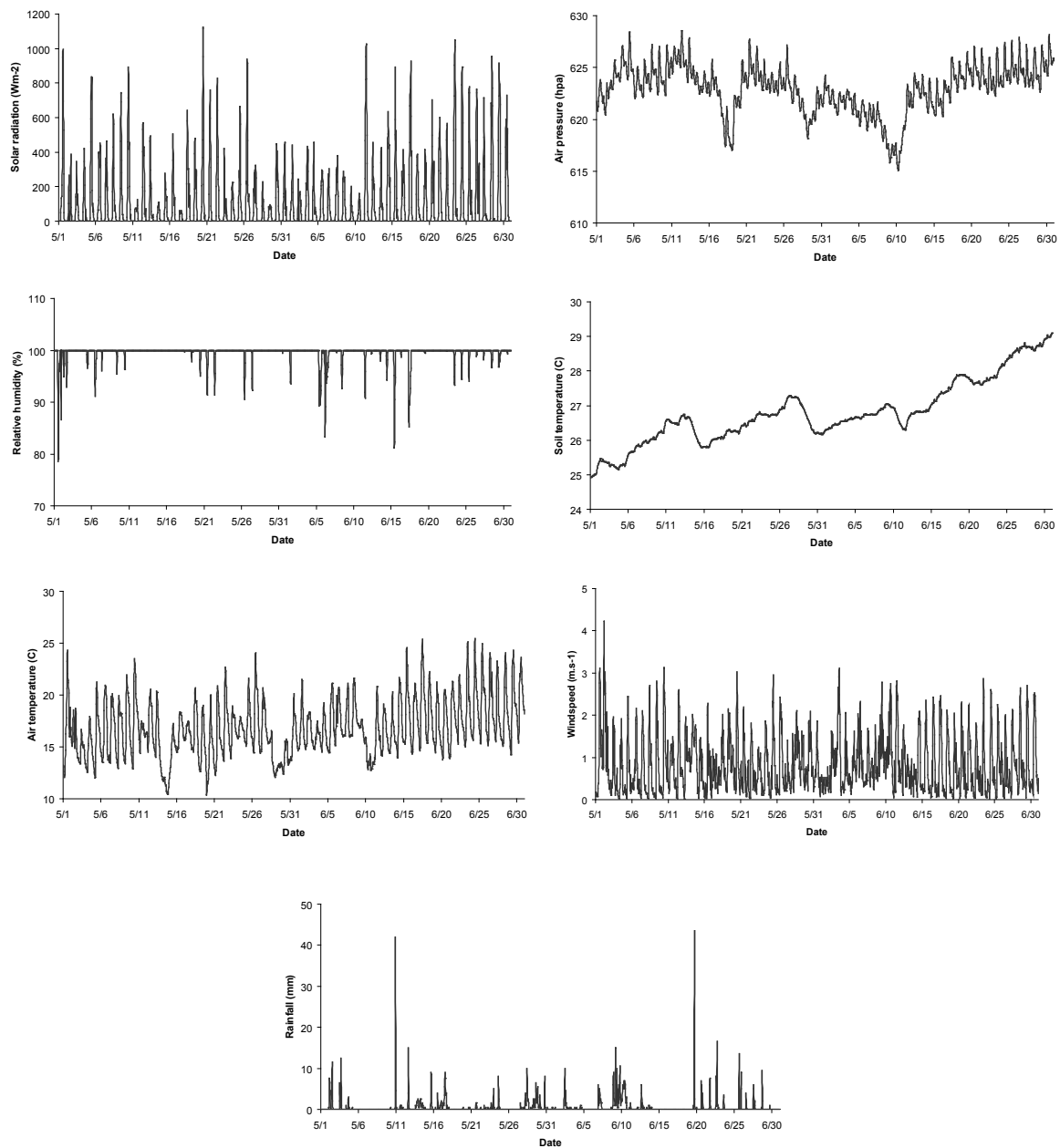


**Figure 3.** Time variation graphs of the meteorological conditions.

## 2.2 General overview of genetic programming

In this section, a brief overview of the GP and GEP is given. Detailed explanations of GP and GEP are provided by Koza (1992) and Ferreira (2006), respectively. GP was first proposed by Koza (1992). It is a generalization of genetic algorithms (GAs) (Goldberg, 1989). The fundamental difference between GA, GP, and GEP is due to the nature of the individuals. In the GA, the individuals are linear strings of fixed length (chromosomes). In the GP, the individuals are nonlinear entities of different sizes and shapes (parse trees), and in GEP the individuals are encoded as linear strings of fixed length (the genome or chromosomes), which are afterwards expressed as nonlinear entities of different sizes and shapes (Ferreira, 2001 a,b). GP is a search technique that allows the solution of problems by automatically generating algorithms and expressions. These expressions are coded or represented as a tree structure with its terminals (leaves) and nodes (functions). GP applies GAs to a “population” of programs, typically encoded as tree-structures. Trial programs are evaluated against a “fitness function” then the best solutions are selected for modification and re-evaluation. This modification-evaluation cycle is repeated until a “correct” program is produced.

There are five major preliminary steps for solving a problem by using GEP. These are the determination of (i) the set of terminals, (ii) the set of functions, (iii) the fitness measure, (iv) the values of the numerical parameters and qualitative variables for controlling the run, and (v) the criterion for designating a result and terminating a run (Koza, 1992). A GEP flowchart is presented in Figure 4.

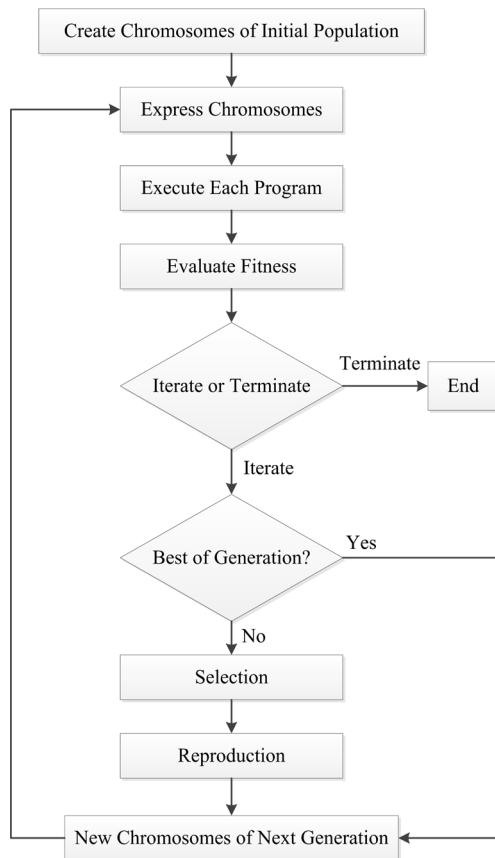


Figure 4. GEP flowchart

There are five major steps in preparing to use GEP of which the first is to choose the fitness function. The fitness of an individual program  $i$  for fitness case  $j$  is evaluated by Ferreira (2006) using:

$$\text{If } E(i, j) \leq p, \text{ then } f_{(ij)} = 1; \text{ else } f_{(ij)} = 0 \quad (1)$$

Where  $p$  is the precision and  $E(i, j)$  is the error of an individual program  $i$  for fitness case  $j$ . For the absolute error, this is expressed by:

$$E(i, j) = |P_{(i,j)} - T_j| \quad (2)$$

Where  $P(i, j)$  is the value predicted by the individual program  $i$  for fitness case  $j$  (out of  $n$  fitness cases) and  $T_j$  is the target value for fitness case  $j$ . Again for the absolute error, the fitness  $f_i$  of an individual program  $i$  is expressed by:

$$f_i = \sum_{j=1}^n (R - |P_{(i,j)} - T_j|) \quad (3)$$

Where  $R$  is the selection range. The second major step consists of choosing the set of terminals  $T$  and the set of functions  $F$  to create the chromosomes. For this study, the function set consists of 7 functions including four basic arithmetic operators, i.e., (+, -, ×, /) and some basic mathematical functions, i.e., ( $\sqrt{\quad}$ ,  $\ln(x)$ ,  $exp$ ) selected among all the available functions in GEP. The function selection was based on simplicity and its relevance to the nature of the problem thus ensuring a simple and efficient final GEP model. The third major step is to choose the chromosomal architecture, i.e., the length of the head and the number of genes. Values of the length of the head,  $h = 10$ , and six genes per chromosome were employed based on the discussion in Ferreira (2001b). The fourth major step is to choose the linking function. In this study, the sub-programs were linked by addition on the basis of recommendations made by Ferreira (2001a) and findings of other studies (e.g. Guven and Aytek, 2009). Finally, the fifth major step is to choose the set of genetic operators that cause variation along with their rates. A combination of all genetic operators, i.e., mutation, transposition and recombination, was used for this purpose.

The parameters of the training of the GEP are given in Table 4.

Table 4. Parameters of the GEP model

Parameter	Value
Function set	+, -, ×, /, $\sqrt{\quad}$ , $\ln(x)$ , $exp$
Chromosomes	30
Head size	10
Number of Genes	6
Linking Function	Addition (+)
Mutation Rate	0.044
Inversion Rate	0.1
One-Point Recombination Rate	0.3
Two-Point Recombination Rate	0.3
Gene Recombination Rate	0.1
Gene Transposition Rate	0.1

## 2.3. General overview of adaptive neuro-fuzzy inference system (ANFIS)

ANFIS (Jang, 1993), using a given input/output data set, constructs a fuzzy inference system (FIS) whose membership function parameters are tuned (adjusted) using either a back propagation algorithm alone or in combination with a least squares type of method. This adjustment allows fuzzy systems to learn from the data set. Figure 5 shows the ANFIS structure for a fuzzy inference system with two inputs.

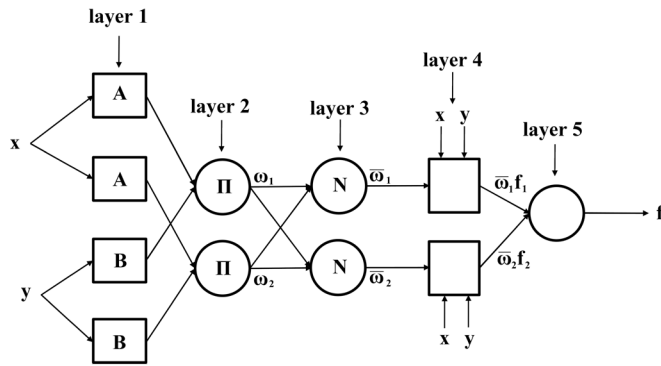


Figure 5. ANFIS structure

Firstly, the FIS type should be selected. In this regard, the Sugeno method was selected for the present study (Ozger, 2009; Ullah and Choudhury, 2013). To train a FIS, a training data set that contains the desired input/output data of the system to be modeled must be loaded. Before training, an initial FIS model structure must be specified:

(1) Hybrid algorithm was selected as the optimization method. The optimization methods train the membership function parameters to emulate the training data.

(2) The number of training Epochs and the training Error Tolerance were selected. These values are entered to set the stopping criteria for training. The training process stops whenever the maximum epoch number is reached or the training error goal is achieved. To validate the trained FIS, after loading the test data, the number of membership functions (MFs) and the type of input and output membership functions were selected. There are only two choices for the output membership function: constant and linear. This limitation of output membership function choices is because ANFIS only operates on Sugeno-type systems (Jang, 1993). The Built-in membership function composed of difference between two sigmoidal membership functions (dsigmf) and the constant membership function were selected as the input and output membership functions, respectively. The number of MFs assigned to each input was three. It should be noted that there is no basic rule for selecting the optimization method and determining the optimal number and type of MFs and they are usually considered by trial and error. Nevertheless, it should be taken into consideration that large numbers of MFs will increase the calculation time and efforts (Keskin et al., 2004). The values assigned to each parameter for the ANFIS model are given in Table 5.

Table 5. Parameters for the ANFIS model

Parameter	Value
FIS type	Sugeno
Optimization method	Hybrid algorithm
Number of MFs	3
Input MF type	Dsigmf
Output MF type	Constant

#### 2.4. General overview of artificial neural networks (ANNs)

The Qnet neural network development system which is a complete solution for back propagation neural network modeling (Qnet, 2000) was used for the present study. Back propagation type neural networks process information in interconnecting processing elements termed nodes. These nodes are organized into groups termed layers. There are three distinct types of layers in a back propagation neural network: the input layer, the hidden layer(s) and the output layer. A network consists of one input layer, one or more hidden layers and one output layer. Connections exist between the nodes of adjacent layers to relay the output signals from one layer to the next. Information enters

a network through the nodes of the input layer. The input layer nodes are unique in that their sole purpose is to distribute the input information to the next processing layer (i.e., the first hidden layer). Figure 6 shows the structure of the ANNs with one hidden layer including three nodes.

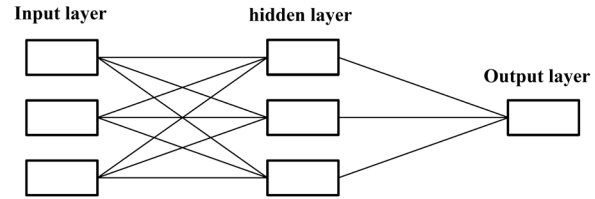


Figure 6. The structure of the artificial neural networks

To design the neural network, the modeler must specify the layer and node quantities, transfer functions and network connections. Including the input layer, one hidden layer and the output layer, the specified number of the layers for the network was three. The number of nodes in the input layer will be equal to the number of input data values in the model. According to table 1, it was specified seven for the prediction of hourly water temperature for the present study. The number of output nodes for the network must correspond to the number of outputs in the network. It was one because we only had one output. Choosing the number of hidden layers and the number of hidden nodes in each layer is not so trivial. The construction of the hidden processing structure of the network is arbitrary. Generally, it is best to start with simple network designs that use relatively few hidden layers and processing nodes. However, in practice, it is usually better to employ multiple hidden layers for solving complex problems. A single hidden layer including three single nodes was specified herein to avoid an unnecessary large and complex model. The sigmoid function is Qnet's default transfer function and it is the most widely used function for back propagation neural networks. Another network design consideration concerns how to control the network's connections. While the connection editor gives the modeler almost unlimited flexibility in designing a network, the fact is that the vast majority of designs work best fully connected. Qnet's connection editor is best suited for highly advanced models that require groups of input data to be processed through separate network pathways. The default fully connected configuration was used for the present study. The values assigned to each parameter for the ANN model are given in Table 6. As it is explained above, Qnet has a high and intelligent ability to simulate complex networks easily while preparing a code for these networks could be excruciating. For practical problems, using an easy method, which is usable for different cases, is more acceptable than sophisticated methods. In summary, Qnet is professional user friendly software and it has been used for simulating different complex problems (Kuo et al. 2004, Yang et al. 2009) and that is why it was used in this research.

Table 6. Parameters for the ANN model

Parameter	Value
Transfer function	Sigmoid
Number of layers	3
Number of hidden layer(s)	1
Number of hidden node(s)	3
Maximum iterations	10000

The performance of three soft computing techniques, namely GEP, ANFIS and ANN to predict the hourly water temperature at YYL at various measured depths was compared. Hourly water temperature data from May 1 to June 11, 2008 were taken as the training data set, while the measured

data from June 12 to 30, 2008 served as the validation data set. Furthermore, time-series meteorological conditions served as inputs for the studied models for data from May 1 to June 30, 2008 (Figure 3).

### 2.5. Evaluation parameters

Several parameters can be considered for the evaluation of the model-predicted values of hourly water temperature in the YYL Lake. In this study, root mean squared error (RMSE), mean absolute error (MAE) and correlation coefficient (R) were used as the evaluation criteria and they can be computed as follows (Liu and Chen, 2012):

$$RMSE = \sqrt{\frac{1}{n} \sum_{i=1}^n (T_p(i) - T_o(i))^2} \quad (4)$$

$$MAE = \frac{1}{n} \sum_{i=1}^n |T_p(i) - T_o(i)| \quad (5)$$

$$R = \frac{(1/N) \sum_{i=1}^n (T_p(i) - \bar{T}_p)(T_o(i) - \bar{T}_o)}{\sqrt{(1/N) \sum_{i=1}^n (T_p(i) - \bar{T}_p)^2} \times \sqrt{(1/N) \sum_{i=1}^n (T_o(i) - \bar{T}_o)^2}} \quad (6)$$

where  $T_p(i)$  and  $T_o(i)$  represent the model-predicted and the observed water temperature, respectively, and  $n$  is the number of observations.

### 3. Results and discussion

A comprehensive comparison was made to compare the accuracy of GEP, ANFIS and ANN methods for the prediction of hourly water temperature in different depths in the YYL. RMSE, MAE and R values of each model for the prediction of hourly water temperature at different depths are shown in Table 7. It is clear from the table that in the case of surface water temperature, the GEP model has the lowest RMSE (1.49 °C), MAE (1.21 °C) and the highest R (0.73) values. The ANN model seems to be the second best from the RMSE and MAE viewpoints. Also, in the case of 1 meter depth, the ANN model shows better accuracy than the GEP and ANFIS models. ANFIS model is ranked as the second best. Despite the error (RMSE value) is smaller in ANN than GEP, there is an upper bound in scatter plot of ANN (see figure 7.e) that imposes a constant value, which is not suitable for predictive purposes. Furthermore, at the 2 meter depth below water surface, the GEP model has the lowest RMSE (0.35 °C) and MAE (0.24 °C) values. Also, the ANN model has a better accuracy than the ANFIS. Finally, at the 3 meter depth below water surface, the superiority of the GEP model over the other models is clearly seen from Table 7. The ANN model seems to be the second best from the RMSE, MAE and R viewpoints.

Figure 7 shows the observed (x-axis) and predicted (y-axis) hourly water temperature values in different depths and in validation period in the form of scatter plots. GEP model seems to be better than the other soft computing techniques. In the case of surface water temperature, the estimates of GEP model seem to be closer to the exact line than those of the ANN and ANFIS models. The ANFIS model's estimates are also less scattered than the ANN. In the case of 1 meter depth, although the ANN model has the least scattered estimates, but there is an upper bound in scatter plot of ANN that imposes a constant value, which will make additional problems in future predictions. So, GEP model having less scattered estimations seems to be the best.

**Table 7.** Performance assessment of different models for predicting hourly water temperature at different depths

Depth	Model	Statistical parameters		
		RMSE (°C)	MAE (°C)	R
0	GEP	1.49	1.21	0.73
	ANN	1.64	1.32	0.64
	ANFIS	1.77	1.34	0.63
1	GEP	0.68	0.57	0.64
	ANN	0.44	0.35	0.80
	ANFIS	0.64	0.51	0.41
2	GEP	0.35	0.24	0.82
	ANN	0.40	0.31	0.84
	ANFIS	0.81	0.67	0.59
3	GEP	0.32	0.25	0.78
	ANN	0.55	0.44	0.75
	ANFIS	0.68	0.58	0.52

At the 2 meter depth below water surface, the estimates of the GEP model closer to the exact line than those of the other models. The ANN and ANFIS models underestimate all the high values (>13.5 °C). The ANN model has a better accuracy than the ANFIS because ANFIS model significantly underestimates high values (>13 °C). It is clear from the figure, at the 3 meter depth below water surface, the estimates of the GEP model are closer to the ideal line than those of the other models. The ANN model's estimates seem to be less scattered than the ANFIS model.

It should be noted that actual physical processes of the lakes such as vertical mixing, which controls the vertical distribution of temperature, have undeniable roles in changing water temperatures at different depths. Vertical mixing, in small, seasonally stratified lakes such as YYL, might result in partial or complete mixing of the water column, depending on the thermal conditions of the lake and the strength of meteorological forces driving the mixing process. Due to the fact that the purpose of the current research is statistical investigation of the effects of metrological parameters in predicting hourly water temperatures of YYL, the roles of physical phenomena including vertical mixing and phase lag between the sub-daily variations of the variables, affecting the heat flux, have been ignored. So, ignoring the physical factors might be one of the sources, which increased the error parameters of the predictions.

Figure 8 shows the observed and predicted values as time series plot in the validation period. From the figure, it can be said that the GEP model is generally more successful than the ANN and ANFIS model especially for the high water temperature values. One of the advantages of GEP in comparison to the other theories is its ability in producing analytical formula for determination of output parameters. Table 8 summarizes the GEP mathematical equations for the prediction of hourly water temperature in different depths. From the table, the  $AP$  seems to be not effective variable on the water temperature in the case of 2- and 3-meter depth below water surface. It can be said that the  $AP$  has a more effect on  $WT_0$  than the  $WT_1$ . Decreasing  $AP$  effect by increasing depth is clearly seen from the table.

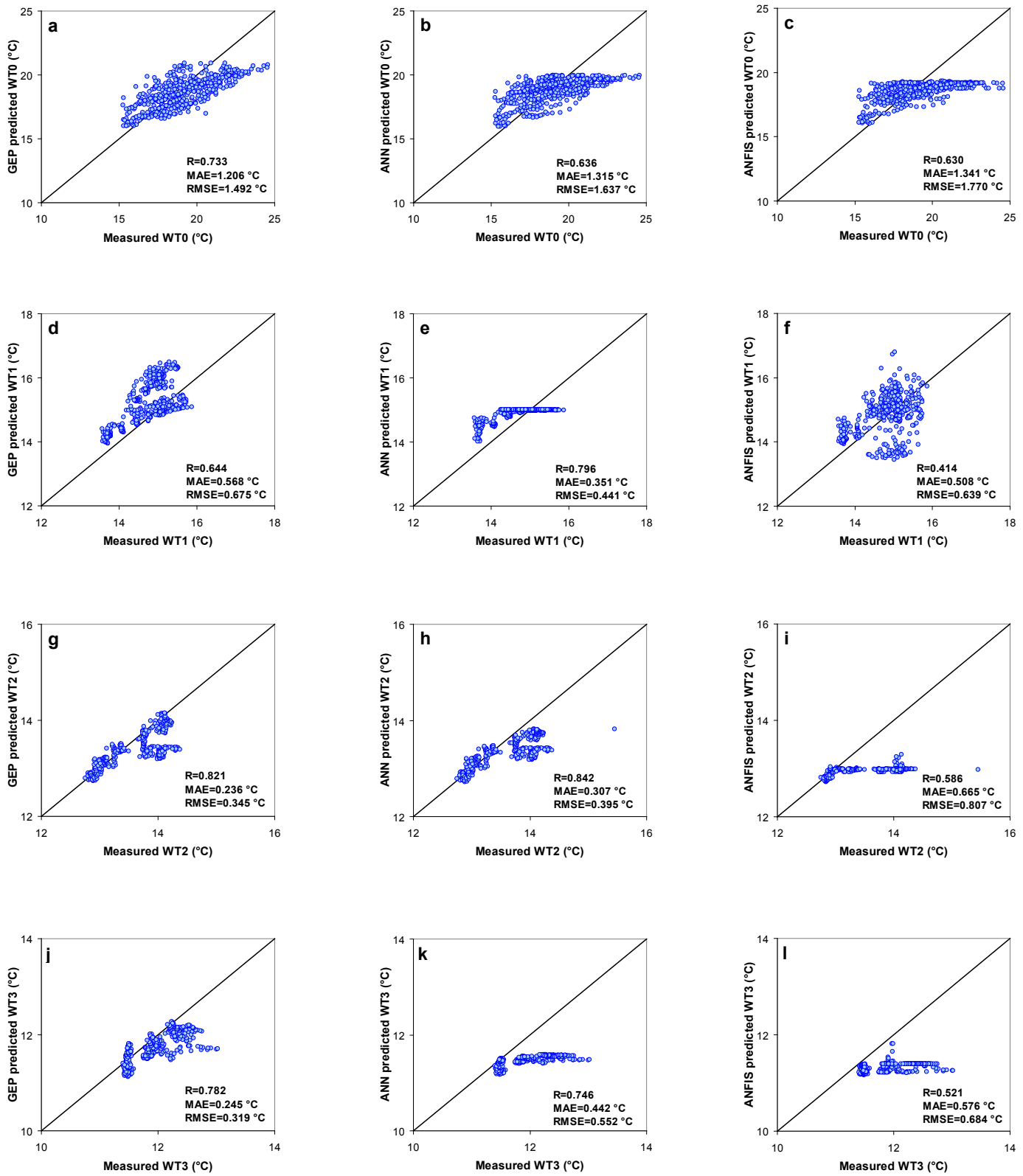


Figure 7. Scatter plots of observed (x-axis) and predicted values (y-axis) of hourly water temperature in different depths.

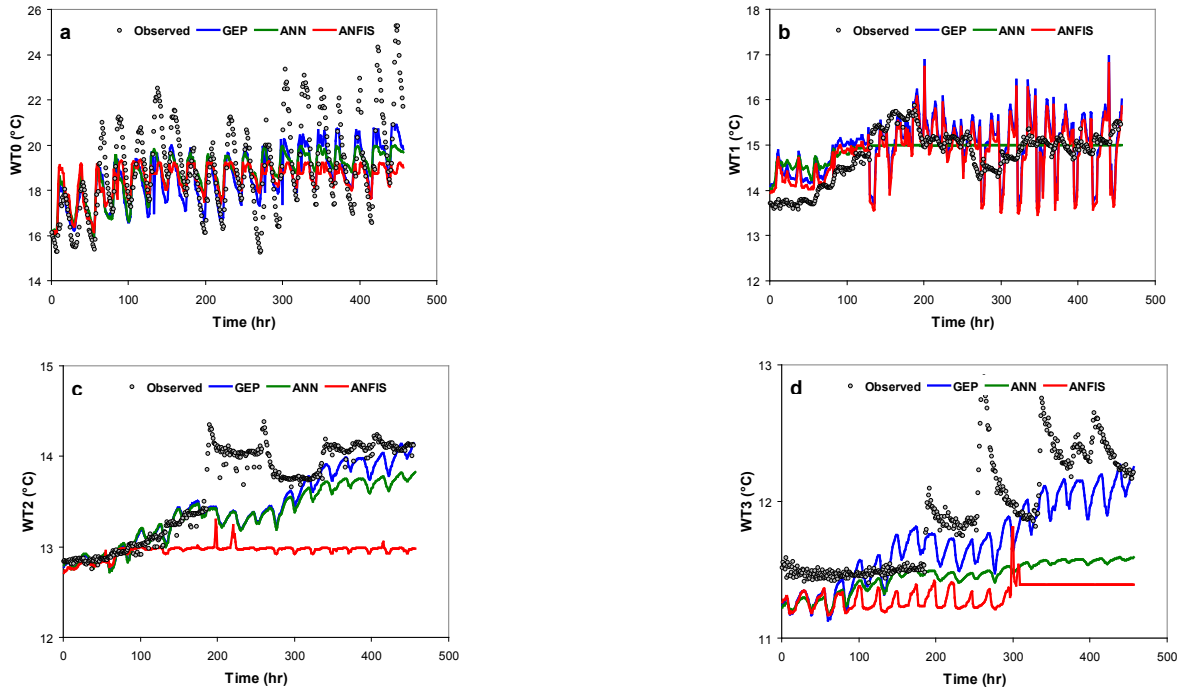


Figure 8. Time series plots of observed and predicted values of hourly water temperature in different depths.

Table 8. Mathematical expressions of GEP model.

Predicted	Mathematical Expression of the model
WT0	$-21.906 - \frac{1.57009 \times \text{Exp}[0.798065AT]}{AP^3} + 3.30075(AT(3.30075 + AT) - 3 \times ST)^{1/4} -$ $\frac{6.77805(9.72513 - AT) + ST}{2.27471 + AT^2} + ST + \text{Exp}[-AT] \times (-AT \times ST - 3.64459ST(ST - AP)) +$ $\frac{4.83991ST + ST(AT + ST)}{6.62537 - AP + ST} + \frac{ST}{\text{Ln}[\text{Exp}[ST] - AP] - \text{Ln}[2AP]}$
WT1	$-15.6273 + 0.0253065AT + 2.8006\sqrt{ST} - \frac{AT \times ST}{2AP} + \frac{AT \times ST}{2AT(AP + AT) - 3AP} -$ $\frac{4.42575ST(ST - 8.32956)}{AT - 8.32956ST} + \text{Exp}[-AT] \times (AT \times ST^2 - 9.59219) \times \text{Ln}[2.31732 + AT] +$ $0.00227366AP \times \text{Ln}[ST]$
WT2	$-3.42694 - 8.38251(1.03943 - 0.000228836(AT - ST)) - \sqrt{ST} + 0.97287ST +$ $\frac{132.822 - AT + 4.88901 \times \text{Ln}[AT]}{ST} + \text{Exp}[-0.286869ST] \times (9.95398AT + ST^2 + \sqrt{AT \times ST}) +$ $(AT - 7.30499) \times \text{Exp}[3.63193 - AT] \times (AT + ST) \times \text{Ln}[AT] + \text{Ln}\left[\frac{8.28603}{ST}\right]$
WT3	$-15.2691 - \text{Exp}\left[-\frac{2.27249(-7.40158 + AT) \times AT^2}{ST^2}\right] +$ $\sqrt{\frac{5.5354 + 0.548691ST}{1 + 5.5354AT} + \frac{6.48978(5.4389 + AT + ST)}{ST^2}} +$ $\sqrt{\frac{AT}{(-1.49371 - AT) \times (8.11706 - 0.669473AT)ST}} + ST +$ $\sqrt{8.66666ST - 0.807352AT} + \sqrt{5.13181 + ST}$

As a conclusion, output results showed that GEP provided reasonable and moderately accurate trends for the prediction of hourly water temperature in different depths.

#### 4. Conclusion

In the present study, the performance of some soft computing techniques, namely gene expression programming, adaptive neuro fuzzy inference system and artificial neural network to predict hourly water temperatures at different layers of the Yuan-Yang Lake in north-central Taiwan has been compared. A time-series set of data for the hourly water temperature at different measured depths from May 1 to June 11, 2008 was taken as training dataset, while the data measured from June 12 to June 30, 2008 were served as a validation dataset for the studied models. The relative performances of these models were comprehensively evaluated using various statistical indices including RMSE, MAE and R coefficients. Results showed that the GEP had the best performances in predicting hourly water temperatures at the surface and both 2 and 3 meter depths below water surface, whereas, a different trend was seen for the 1 meter depth below water surface. In this depth, in spite of smaller error in ANN than GEP, there is an upper bound in scatter plot of ANN that imposes a constant value, which is not appropriate for predictive purposes. Conclusively, results obtained from this study showed that GEP can provide reasonable trends for the prediction of hourly water temperature in different depths especially in shallow waters.

#### Acknowledgments

Sincere thanks are given to the two anonymous reviewers for their invaluable and constructive comments and suggestions for improving the paper quality.

#### References

- Aytac, A. & Kisi, O. (2008). A genetic programming approach to suspended sediment modelling. *Journal of Hydrology*, 351, 288-298.
- Banzhaf, W., Nordin, P., Keller, R. E. & Francone, F. D. (1998). Genetic programming. Morgan Kaufmann, San Francisco, CA.
- Benyahya, L., Caissie, D., St-Hilaire, A., Ouarda, T.B.M.J. & Bobee, B. (2007). A review of statistical water temperature models. *Canadian Water Resource Journal*, 32(3), 179-192.
- Chen, S.H. & Wu, J.T. (1999). Paleolimnological environment indicated by the diatom and pollen assemblages in an alpine lake of Taiwan. *Journal of Paleolimnology*, 22, 149-158.
- Fallah-Mehdipour, E., Borzorg Haddad, O. & Marino, M.A., (2013). Prediction and simulation of monthly groundwater levels by genetic programming. *Journal of Hydro-environment Research*, 7(4), 253-260.
- Fang, X., & Stefan, H.G. (1996). Long-term lake water temperature and ice cover simulations/measurements. *Cold Regions Science and Technology*, 24, 289-304.
- Ferreira, C., (2001a). Gene expression programming in problem solving. 6th Online World Conf. on Soft Computing in Industrial Applications (invited tutorial).
- Ferreira, C., (2001b). Gene expression programming, A new adaptive algorithm for solving problems. *Complex Systems*, 13 (2), 87.
- Ferreira, C., (2006). Gene expression programming: mathematical modeling by an artificial intelligence. Springer, Berlin 2006, p. 478.
- GLEON, Global Lake Ecological Observatory Network. <http://gleon.org/>.
- Goldberg, D.E. (1989). Genetic algorithms in search, optimization, and machine learning. Addison-Wesley, Reading, MA.
- Guyen, A., & Aytek, A. (2009). New approach for stage-discharge relationship: gene expression programming. *Journal of Hydrologic Engineering*, 14, 812-820.
- Hondzo, M., & Stefan, H.G. (1996). Long-term lake water quality predictors. *Water research*, 30(12), 2835-2852.
- Jang, R. (1993). ANFIS: adaptive network-based fuzzy inference system. *IEEE Transactions on Systems, Man, and Cybernetics*, 23, 665-685.
- Keskin, M.E., Terzi, O., & Taylan, D. (2004). Fuzzy logic model approaches to daily pan evaporation estimation in Western Turkey. *Hydrological Sciences Journal*, 49 (6), 1001-1010.
- Kisi, O. (2006). Daily pan evaporation modeling using a neuro-fuzzy computing technique. *Journal of hydrology*, 329, 636-646.
- Kisi, O., Shiri, J., & Nikoofar, B. (2012). Forecasting daily lake levels using artificial intelligence approaches. *Computers & Geosciences*, 41, 169-180.
- Koza, J.R. (1992). Genetic programming, on the programming of computers by means of natural selection. MIT Press, Cambridge, MA, ISBN 0-262-11170-5.
- Kuo, Y. M., Liu, C. W. & Lin, K.H., (2004). Evaluation of the ability of an artificial neural network model to assess the variation of groundwater quality in an area of blackfoot disease in Taiwan. *Water Research*, 38 (1), 148-158.
- Lawrence, S.P., Hogeboom, K., & Le Core, H. L. (2002). A three-dimensional general circulation model of the surface layer of Lake Baikal. *Hydrobiologia*, 487 (1), 95-110.
- Lee, H.S., Yamashita, T., & Haggag, M. (2009). Modelling hydrodynamic in Yachiyo Lake using a non-hydrostatic general circulation model with spatially and temporally varying meteorological conditions. *Hydrological Processes*, 23 (14), 1973-1987.
- Liu, W. C., & Chen, W. B. (2012). Prediction of water temperature in a subtropical subalpine lake using an artificial neural network and three-dimensional circulation models. *Computers & Geosciences*, 45, 13-25.
- Liu, W. C., Yu, H.L., & Chung, C. E. (2011). Assessment of Water Quality in a Subtropical Alpine Lake Using Multivariate Statistical Techniques and Geostatistical Mapping: A Case Study. *International Journal of Environmental Research and Public Health*, 8, 1126-1140.
- Mellit, A., Benghanen, M., & Kalogirou, S.A. (2006). An adaptive wavelet network model for forecasting daily total solar radiation. *Applied Energy*, 83, 705-722.
- Moghaddammia, A., Ghafari Gousheh, M., Piri, J., Amin, S., & Han, D. (2009). Evaporation estimation using artificial neural networks and adaptive neuro-fuzzy inference system techniques. *Advances in Water Resources*, 32, 88-97.
- Ozger, M. (2009). Comparison of fuzzy inference systems for streamflow prediction. *Hydrological Sciences Journal*, 54(2), 261-273.
- Piccolroaz, S., Toffolon, M., & Majone, B. (2013). A simple lumped model to convert air temperature into surface water temperature in lakes. *Hydrology and Earth System Sciences*, 17, 3323-3338.
- Qnet (2000). Qnet 2000 Neural Network Modelling for Windows 95/98/NT, QnetToll User's Guide and Datapro User's Guide. Vesta Services, Incorporated, USA.
- Samadianfard, S. (2012). Gene expression programming analysis of implicit Colebrook-White equation in turbulent flow friction factor calculation. *Journal of Petroleum Science and Engineering*, 92-93, 48-55.
- Samadianfard, S., Sadraddini, A. A., Nazemi, A. H., Provenzano, G., & Kisi, O. (2012). Estimating soil wetting patterns for drip irrigation using genetic programming. *Spanish Journal of Agricultural Research*, 10(4), 1155-1166.
- Schwab, D. J., Beletsky, D., DePinto, J., & Dolan, D. M. (2009). A hydrodynamic approach to modeling phosphorus distribution in Lake Erie. *Journal of Great Lakes Research*, 35 (1), 50-60.
- Sharma, S., Walker, S. C., & Jackson, D.A. (2008). Empirical modelling of lake water-temperature relationships: a comparison of approaches. *Freshwater Biology*, 53, 897-911.
- Shiri, J., & Kisi, O. (2011). Comparison of genetic programming with neuro-fuzzy systems for predicting short-term water table depth fluctuations. *Computers & Geosciences*, 37 (10), 1692-1701.
- Shiri, J., Dierickx, W., Pour-Ali Baba, A., Nemat, S., & Ghorbani, M. A. (2011). Estimating daily pan evaporation from climatic data of the state of Illinois, USA using adaptive neuro-fuzzy inference system and artificial neural network. *Hydrological research*, 42 (6), 491-502.

- Thiery, W., Stepanenko, V. M., Fang, X., Johnk, K. D., Li, Z., Martynov, A., ... Lipzig, N. P. M. V. (2014). LakeMIP Kivu: evaluating the representation of a large, deep tropical lake by a set of one-dimensional lake models. *Tellus A*, 66, 21390. <http://dx.doi.org/10.3402/tellusa.v66.21390>
- Toffolon, M., Piccolroaz, S., Majone, B., Soja, A.M., Peeters, F., Schmid, M., & Wuest, A. (2014). Prediction of surface temperature in lakes with different morphology using air temperature. *Limnology and Oceanography*, 59 (6), 2185-2202.
- Trumpickas, J., Shuter, B. J., & Minns, C. K. (2009). Forecasting impacts of climate change on Great Lakes surface water temperatures. *Journal of Great Lakes Research*, 35, 454-463.
- Ullah, N. & Choudhury, M. (2013). Flood Flow Modeling in a River System Using Adaptive Neuro-Fuzzy Inference System. *Environmental Management and Sustainable Development*, 2(2), 54-68.
- Webb, B. W., Hannah, D. M., Moore, R. D., Brown, L. E., & Nobilis, F. (2008). Recent advances in stream and river temperature research. *Hydrological Processes*, 22, 902-918.
- Wu, J. T., Chang, S. C., Wang, Y. S., Wang, Y. F. & Hsu, M.K. (2001). Characteristics of the acidic environment of the Yuan yang Lake (Taiwan). *Botanical Bulletin of Academia Sinica*, 42, 17-22.
- Yang, C. T., Marsooli, R. & Aalami, M. T. (2009). Evaluation of Total Load Sediment Transport Formulas Using ANN. *International Journal of Sediment Research*, 24(3), 274-286.
- Zaier, I., Shu, C., Ouarda, T. B. M. J., Seidou, O. & Chebana, F. (2010). Estimation of ice thickness on lakes using artificial neural network ensembles. *Journal of Hydrology*, 383, 330-340.
- Zhao, L., Yu, Z., & Acharya, K. (2011). Modeling water temperature of Lake Taihu. American Geophysical Union, Fall meeting.





## Case Study of the Characteristics and Dynamic Process of July 10, 2013, Catastrophic Debris Flows in Wenchuan County, China

Gui-Sheng Hu<sup>1</sup>, Ning-Sheng Chen<sup>1\*</sup>, Javed Iqbal Tanoli<sup>1,2</sup>, Yong You<sup>1</sup> and Jun Li<sup>1</sup>

<sup>1</sup> Key Lab of Mountain Hazards and Surface Processes, Institute of Mountain Hazards and Environment, Chinese Academy of Sciences, 610041, Chengdu, China. Tel: +86-18683259117. Email: huguisheng@imde.ac.cn.

<sup>2</sup>Department of Earth Sciences, COMSATS Institute of Information Technology, Abbottabad, 22060, Pakistan

\*Corresponding author: chennsh@imde.ac.cn

### ABSTRACT

The Wenchuan earthquake of May 12, 2008, generated a significant amount of loose solid material that can produce devastating debris flows. In the five years since the earthquake, there have been many large-scale individual and group catastrophic debris flows that have caused lots of damage to the resettled population and the reconstruction efforts. The reconstructed towns of Yingxiu, Yixing and Miansi have suffered debris flows and other secondary disasters in the past five years and are still not out of danger in the future. A debris-flow catastrophic event hit four towns of Wenchuan County along the Duwen Highway, part of China's National Highway 213, at midnight on July 10, 2013, following a local extreme rainfall of 176.2mm 24h-1. The debris flows occurred simultaneously along seven gullies. A total of 15000 people were affected due to the destruction of resettlement areas, factories, power stations, and houses. Because of this devastating event, traffic along the Duwen highway was completely disrupted during the disaster and recovery period. The present study focuses on the Lianshan Bridge debris flow gully; the disaster characteristics and cause of the debris flow were analyzed based on field investigations, remote sensing interpretation, and laboratory experiments. The particular dynamic parameters of the debris flow were calculated and analyzed including density, velocity, discharge, total volume and impact force. Also, the dynamic processes and changes that occurred in the debris flow were examined, and the block and burst characteristics of debris flow were studied based on statistical calculation and analysis dynamic characteristic parameters of debris flow. Finally, a program to prevent further debris flow was proposed according to the on-site investigation and based on the analysis of the features and dynamic processes of the debris flow.

*Keywords: Debris flow, dynamic process, the block and burst characteristics, prevention and cure measures.*

## Características y procesos dinámicos de los catastróficos movimientos de detritos en el condado de Wenchuan, China, el 10 de julio de 2013 - Caso de estudio

### RESUMEN

El terremoto de Wenchuan, el 12 de mayo de 2008, generó una gran cantidad de material sólido suelto que puede producir flujos de detritos devastadores. En los años posteriores al terremoto han ocurrido deslizamientos a gran escala individuales y simultáneos que han causado daño a los habitantes reubicados y a los esfuerzos de reconstrucción. Las ciudades reconstruidas de Yingxiu, Yixing y Miansi han sufrido flujos de detritos y otros desastres secundarios desde el terremoto, y no están exentas de eventos futuros. Un evento simultáneo de flujo de detritos afectó a cuatro localidades del condado de Wenchuan, a lo largo de la autopista de Duwen, parte de la carretera nacional 213, en la medianoche del 10 de julio de 2013, después de una lluvia extrema de 176,2 mm 24h-1. Los movimientos de detritos ocurrieron en siete pendientes. Un total de 1500 personas resultaron afectadas debido a la destrucción en áreas de reasentamiento, fábricas, estaciones eléctricas y viviendas. Debido a este devastador hecho, el tráfico de la autopista Duwen estuvo interrumpido durante el período del desastre y mientras se recuperaba la zona. Este estudio se enfoca en el deslizamiento del Puente Lianshan, donde se analizaron las características y las causas del flujo de detritos basados en investigaciones de campo, interpretación de detección remota y experimentos de laboratorio. Se calcularon y analizaron los parámetros dinámicos particulares del flujo de detritos como la densidad, velocidad, descarga, volumen total y fuerza de impacto. También se analizaron los procesos dinámicos y los cambios que ocurrieron en el flujo de detritos, al igual que se estudiaron las características de bloqueo y ruptura del flujo con base en cálculos estadísticos y análisis de los parámetros dinámicos característicos. Finalmente, se propone un programa para prevenir mayores movimientos de detritos de acuerdo con la investigación de campo y basado en los análisis de las características y procesos dinámicos del flujo de material sólido suelto.

*Palabras clave: Flujo de detritos, procesos dinámicos, características de bloqueo y ruptura, medidas de prevención.*

### Record

Manuscript received: 23/12/2014

Accepted for publication: 13/05/2016

### How to cite item

Hu, G. S., Chen, N. S., Tanoli, J. I., You, Y., & Li, J. (2016). Case Study of the Characteristics and Dynamic Process of July 10, 2013, Catastrophic Debris Flows in Wenchuan County, China. *Earth Sciences Research Journal*, 20(2), E1-E13. doi:<http://dx.doi.org/10.15446/esrj.v20n2.48026>

## 1. Introduction

Numerous landslides have been triggered in earthquake-affected areas and the largest ones have been located close to the rupture faults (Chen et al. 2009; Huang et al. 2012). Abundant loose solid erodible material from co-seismic rock falls and landslides are then deposited in gullies, which form the source material for debris flows (Shieh et al. 2009). Numerous debris flows have been triggered during the rainy season in the years following an earthquake (Yu et al. 2014). The frequency and magnitude of debris flows were thus increased significantly after the Wenchuan earthquake of 2008 (Cui et al. 2011; Chen et al. 2013); during the rainy seasons in the past five years, over 800 debris flows have occurred and this has caused great damage to the resettled population and the reconstruction efforts (Zhang et al. 2013). Although mitigation measures were constructed in a few gullies such as the Wenjia and Bayi Gullies, disastrous debris flows still occurred; in some small gullies the mitigation measures installed proved to be inadequate and incomplete (Wang et al. 2012, 2013). For example, a catastrophic debris-flow event hit four towns in Wenchuan County along the Duwen highway,

part of the China National Highway G213, at midnight on July 10, 2013; this event broke out simultaneously in seven debris flow gullies. A total of 15000 people were affected; 18 people were reported dead or missing and there was significant destruction of resettlement areas, factories, power stations and houses (Table 1). These debris-flow gullies located along the Duwen highway have seen reoccurring debris flow disasters in the geological history, and it is likely that some part of these gullies will have another debris flow disaster in the near future. Debris flow activity of these small gullies is still very active and poses a serious threat to the local population, property, traffic safety, and the development of the local social economy. Thus, debris flow mitigation measures should be installed in a timely fashion (Xu et al. 2012). Using the Lianshan Bridge debris flow gully as an example, an analysis was performed on the disaster characteristics, cause of the debris flow, the dynamic processes and the changes in the debris flow through field measurements, remote sensing interpretation, and laboratory experiments. It is essential to provide a comprehensive debris flow control scheme which will lay the foundation for future research on regional debris flows.

**Table 1.** Summary of destruction caused by a Group of Catastrophic Debris Flows that occurred on July 10, 2013.

No.	Gully name	Site	Disaster losses
1	Xingfu Gully	Gengda town, Wenchuan	Reconstructed Housing and the Giant Panda Research Center were destroyed
2	Qipan Gully	Weizhou town, Wenchuan	15 people were dead or missing, 350 houses were destroyed
3	Yangdian Gully	Miansi town, Wenchuan	part of G213 and 100 houses were destroyed
4	Chutou Gully	Miansi town, Wenchuan	3 people were reported dead, part of G213 were destroyed
5	Taoguan Gully	Yinxing town, Wenchuan	8 factories and 2 power stations were destroyed
6	Wayao Gully	Miansi town, Wenchuan	30 houses and motorway service were destroyed,
7	Lianshan Bridge Gully	Yinxing town, Wenchuan	part of G213 was destroyed, Minjiang River deposition 2-3m

## 2. Study area

### 2.1 Location of the study area

The Lianshan Bridge debris flow gully is located in Yinxing Town, Wenchuan County, Sichuan Province of China. It is the first order and left branch of the Minjiang River (Figure 1), with coordinates 103°29'49"E, 31°11'24"N at the gully mouth. The catchment covers an area of 0.7 km<sup>2</sup> and the main channel is 1.34km long with a 48.3% longitudinal slope. The flow direction of the gully is from west to east. The dimensions of the watershed from east to west and south to north approximately 3.0 and 4.0 km, respectively. The gully is accessible to traffic via the Duwen highway that passes through its deposition area.

### 2.2 Landform conditions

The study area, located on the eastern edge of the Qinghai–Tibetan Plateau, has a complex terrain characterized by considerable elevation differences and steep slopes (Zhang et al. 2006). High mountains, deep-cut rivers, and steep slopes are the main landform characteristics of this area. The elevation difference of the gully is 1159 m from the maximum elevation of 2184m in the west of the catchment to the minimum elevation of 1025 m at the gully mouth.

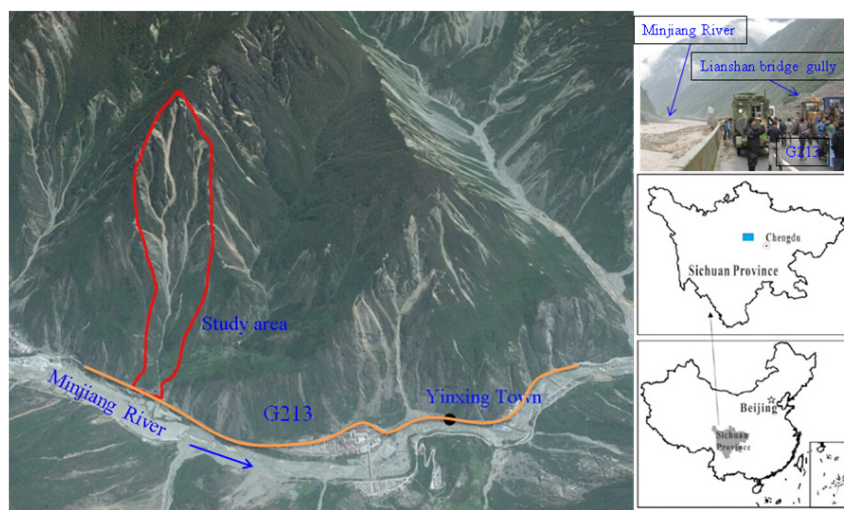


**Figure 1.** Location of the study area.

### 2.3 Geological conditions

The geological conditions of the study area are complex; earthquakes occur frequently and cause significant destruction to mountain surface. The “5.12” Wenchuan earthquake that occurred in this area was due to the Longmen Mountain Fault zone. The gully is in the Cathaysian tectonic belt, very close to the deep fracture zone of the Maoxian-Wenchuan reverse fault (Longmen Mountain Fault zone), which lies in the southwest to northeast direction (Zhou et al. 2000). The strata exposed in the gully include diorite ( $\delta 23$ ) in the upper reaches, plagioclase granite ( $\gamma 24$ ) in the middle reaches, and granodiorite ( $\gamma \delta 23$ ) in the lower reaches. The rock mass of the study area belongs to the magmatic rock formed in the Jinning-Chengjing Period with structural characteristics of high strength, joint fissures, and strongly weathered layers at the surface. Consequently, it is prone to instability, collapse and landslides.

The Lianshan Bridge Gully is located in the area of the active fault. Furthermore, the gully is situated about 5 km from the epicenter of the Wenchuan earthquake. The earthquake caused widespread destruction in the catchment of Lianshan Bridge Gully and formed a large number of landslips and landslides, providing a rich source of loose solid material for the debris flows. Based on “the ground motion parameter zoning map of the Wenchuan earthquake” (GB18306-2001), the study area belongs to the high-intensity seismic region (VIII degrees) with peak ground acceleration of 0.2 g and characteristic period of seismic response spectrum of 0.35 s.

### 2.4. Rainfall

The study area is in the subtropical humid monsoon climate zone of the Sichuan Basin border and it is situated within the rainstorm center of the west Sichuan region. According to the observation data from the Wenchuan meteorological station, the average annual rainfall is 932.6mm, and the maximum and the minimum annual rainfalls are 1277 and 754 mm, occurring in 1992 and 1998, respectively. The maximum daily rainfall can be up to 166.7mm mm. Precipitation over the year is unevenly distributed, concentrated mainly in the period May to September (Figure 2), which accounts for 79% of the annual rainfall. This period usually has a large number of collapses, landslides, debris flows, and other geological disasters (Liu et al. 2010). In short, the water source condition is favorable to the formation of debris flows in the Lianshan Bridge Gully.

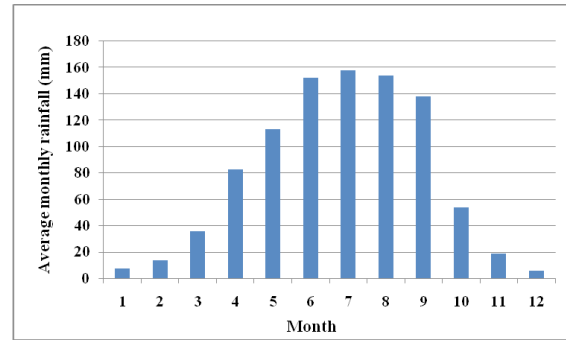


Figure 2. The average monthly rainfall of Yinxiang Town, Wenchuan (Data from 1990 to 2010).

### 3. Methodology

#### 3.1 Field investigations

This research used field investigations, remote sensing interpretation and model calculation to determine the dynamic characteristics of the debris flow. The steps taken to collect and analyze the data are shown in Figure 3. Field work was conducted from July 12 to August 28, 2013, by interviewing local residents to ascertain the debris flow history in Lianshan Bridge gully (We will visit and inquiry many local residents of different ages in near Lianshan Bridge gully. Some older local residents can remember their grandparents, parents who tell them the history of debris flow disasters. We ascertain the frequency of the debris flow disasters based on investigative information) and show that the “7.10” debris flow was the largest debris flow in the past century in this gully. A 1:1000 topography map of the deposition area and a 1:200 cross-section map of the downstream channels are given in Figure 4A and B. As shown in Figure 4, nine test pits in the downstream channel and debris flow samples at six sites (S1–S6) from the downstream channel and debris fan were collected for sieving and particle gradation analysis (Figure 4A and C). Field and laboratory dry sieving tests were conducted following the British Standards (Chen et al. 2012). The seven materials identified (smaller than 2 mm diameter) were tested further using laboratory dry sieving tests. Grain sizes were determined by using field weighing and laboratory particle size analysis techniques, from which the debris flow bulk density was then obtained.

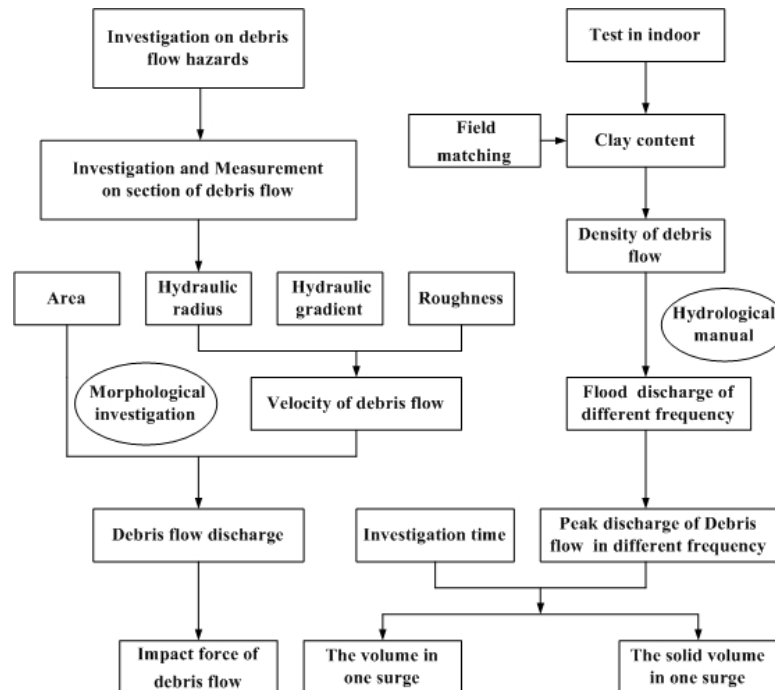


Figure 3. Schematics of investigation methods for debris flow dynamic characteristics

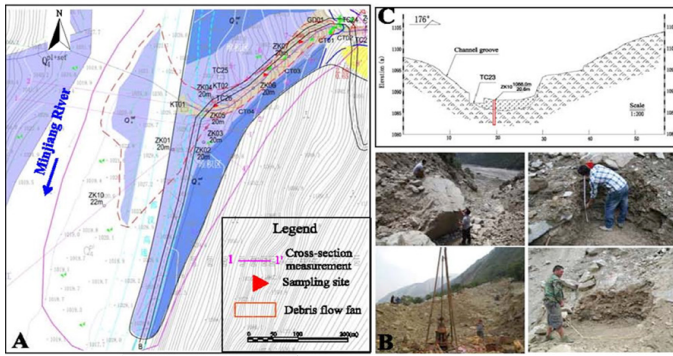


Figure 4. Field investigation methods of debris flow gully.

### 3.2 Parameter calculating

#### 3.2.1 Density of debris flow

Density of debris flow was calculated using field matching and statistical analysis methods.

##### a. The field matching method

In the field matching method, first of all, we measured the size of bucket before sampling, and then we can calculate the volume of samples. Secondly, soil samples were uniformly mixed in the field in order to help local residents to compare it with 7.10 debris flow (Figure 5). Finally, we got the weight of the soil samples, and at the same time we can use these data to calculate the mean value of debris flow density. We select five soil samples to calculate debris flow density; the results of debris flow density are shown in table 2.



Figure 5. The field weighing of debris flow density.

Table 2. The calculation results of debris flow density.

No.	Weight (kg)	Volume ( $10^{-3}\text{m}^3$ )	Density ( $\text{kg}/\text{m}^3$ )	No.	Weight (kg)	Volume ( $10^{-3}\text{m}^3$ )	Density ( $\text{kg}/\text{m}^3$ )
1	10.2	5.2	1962	4	9.4	4.9	1918
2	10.2	5.2	1962	5	9.4	4.9	1918
3	9.8	5.1	1922	Mean value of debris flow density			1936

##### b. The statistical analysis method.

The density of debris flow was calculated using the Formula 1 (Chen et al. 2003). This formula was obtained from data collected from a large number of debris flow gullies located in the southwest region of China; this reflected the relationship between the percentage of clay particles in the debris flow ( $< 0.005\text{mm}$ ) and the density of the debris flow.

$$\gamma_c = -1.32 \times 10^3 x^7 - 5.13 \times 10^2 x^6 + 8.91 \times 10^2 x^5 - 55x^4 + 34.6x^3 - 67x^2 + 12.5x + 1.55 \quad (1)$$

where  $\gamma_c$  is the density of the debris flow ( $\text{kg}/\text{m}^3$ ), and  $x$  is the percentage of clay particles in the debris flow. Formula 1 is mainly suitable for the calculation of the viscous debris flow density that clay content of debris flow is less than 10%.

The percentage of debris flow clay particles was obtained by particle size analysis tests conducted in the laboratory, and the results of debris flow density with clay content are shown in table 3.

The debris flow density of Lianshan Bridge debris flow gully is  $1940\text{kg}/\text{m}^3$  according to the calculation results of the above two methods.

Table 3. The results of debris flow density with clay content.

No.	Site	Percentage of clay	Density ( $\text{kg}/\text{m}^3$ )
1	N31°11'25", E103°29'48"	3.89	1940
2	N31°11'44", E103°30'08"	3.34	1943

#### 3.2.2 Velocity of debris flow

The velocity of the viscous debris flow was calculated using the experiential Formula 2 (Chen et al. 2011a), which was obtained from statistical data of a large number of debris flow gullies located in the southwest region of China.

$$V_c = (1/n_c) H_c^{2/3} I_c^{1/2} \quad (2)$$

where  $V_c$  is velocity of the viscous debris flow ( $\text{m}/\text{s}$ );  $n_c$  is the roughness values of debris flow gully, the  $n_c$  is empirical coefficient that it was determined by the hydraulic radius of the debris flow;  $H_c$  is the hydraulic radius of the debris flow ( $\text{m}$ );  $I_c$  is the longitudinal gradient of debris flow gully bed (%). The hydraulic radius and longitudinal slope of 10 debris flow sections were measured from the top of gully to the gully mouth (Figure 6). The velocity of 10 debris flow sections were calculated through these acquired parameters, and the results are showed on the Table 4.

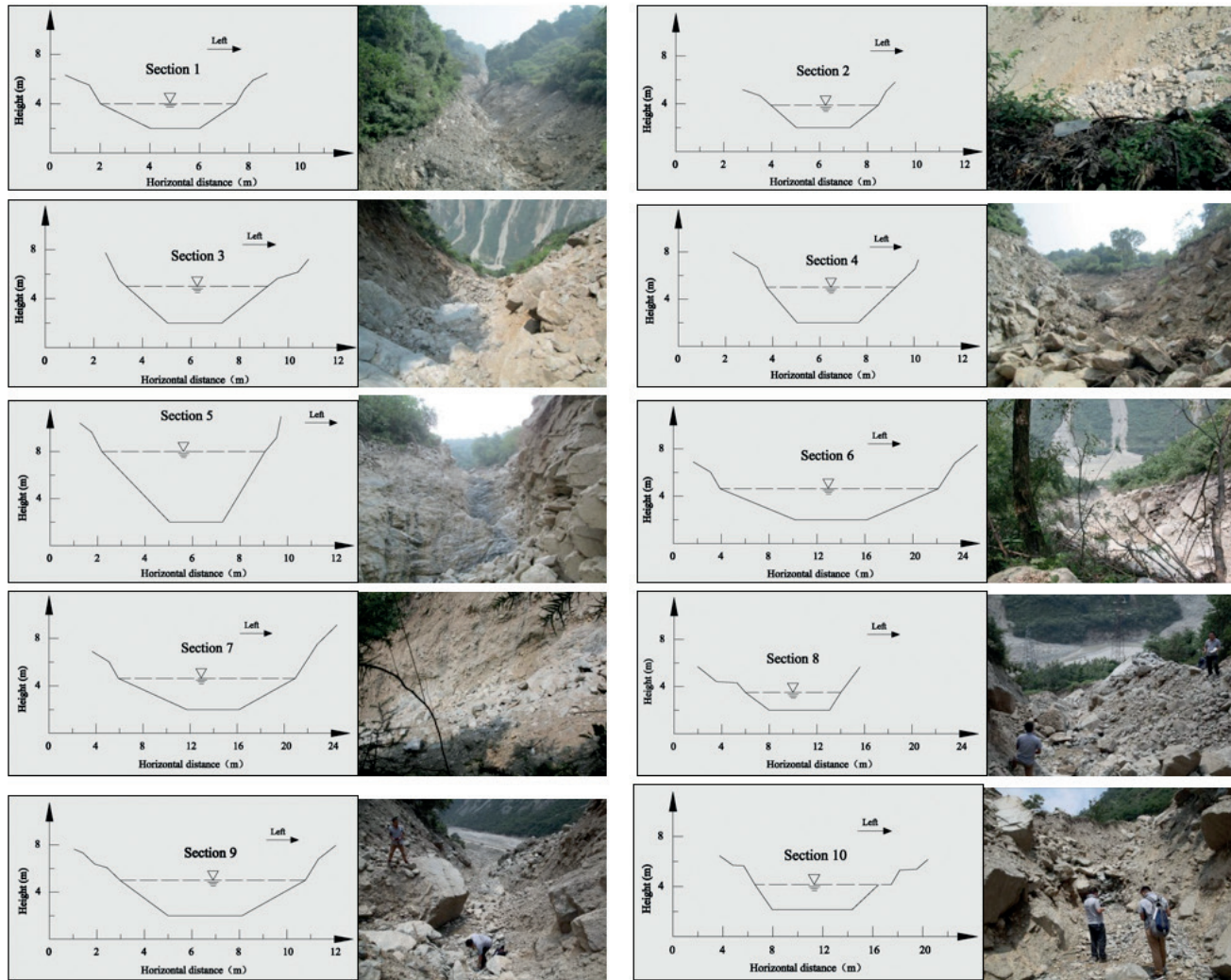


Figure 6. The field investigation of debris flow section.

Table 4. The calculation of debris flow velocity.

No.	Section site	$I_c$ (‰)	$H_c$ (m)	$1/n_c$	$V_c$ (m/s)	No.	Section site	$I_c$ (‰)	$H_c$ (m)	$1/n_c$	$V_c$ (m/s)
1	N31°11'21.57" E103°30'55.8" H:1560.4m	560	2.0	4.0	3.0	6	N31°11'20.26" E103°30'1.96" H:1218.4m	430	2.0	7.0	7.3
2	N31°11'21.56" E103°30'54.8" H:1538m	530	2.0	5.5	4.2	7	N31°11'20.11" E103°29'59.87" H:1173.1m	330	2.3	8.0	8.0
3	N31°11'21.43" E103°30'42.7" H:1440.3m	510	3.0	3.5	5.2	8	N31°11'21.99" E103°29'54.22" H:1102.5m	269	2.9	8.0	8.4
4	N31°11'21.31" E103°30'32.4" H:1335.8m	550	3.0	4.0	6.1	9	N31°11'20.94" E103°29'57.34" H:1058.7m	300	3.6	7.0	9.0
5	N31°11'21.16" E103°30'17.6" H:1248.1m	610	3.5	3.0	7.7	10	N31°11'20.59" E103°29'50.41" H:1052.1m	320	2.1	10.0	9.3

### 3.2.3 The discharge of debris flow

The peak discharge of debris flow  $Q_c$  was calculated by both the morphological investigation method and the hydrological manual method.

#### a. The morphological investigation method

The discharge of debris flow based on the morphological investigation method was calculated using the area of each debris flow section and the corresponding velocity of debris flow. The results are showed in Table 5.

**Table 5** The calculation of discharge using the morphological investigation method

Section No.	Area of Section (m <sup>2</sup> )	$V_c$ (m/s)	$Q_c$ (m <sup>3</sup> /s)	Section No.	Area of Section (m <sup>2</sup> )	$V_c$ (m/s)	$Q_c$ (m <sup>3</sup> /s)
1	7.0	3.0	21.0	6	22.1	7.3	161.3
2	8.0	4.2	33.6	7	21.3	8.0	170.4
3	12.0	5.2	62.4	8	21.0	8.4	176.4
4	12.0	6.1	73.2	9	20.9	9.0	188.1
5	20.5	7.7	157.8	10	21.3	9.3	198.1

#### b. The hydrological manual method.

Firstly, the flood peak discharge ( $Q_p$ ) of Lianshan Bridge gully was determined in order to calculate the debris flow peak discharge ( $Q_c$ ). The flood peak discharge ( $Q_p$ ) can be calculated by Formula 3 that the flood peak discharge calculated from this formula is more suitable for the southwest region of China (Ni et al. 2012), and the results are given in Table 6.

$$Q_p = 0.278\psi \frac{S}{\tau^n} A \quad (3)$$

where  $A$  is the watershed area of debris flow gully;  $\psi$  is the runoff coefficient of the flood peak;  $S$  is the rainfall intensity;  $\tau$  is the runoff confluence time of the rainstorm, and  $n$  is the attenuation index of the rainstorm;  $L$  is the length of debris flow gully;  $J$  is the mean gradient of debris flow gully bed;  $P$  is the rainstorm frequency, for example,  $P=1\%$  means that the rainstorm was a once-in-a-century.

**Table 6.** The calculation of the flood peak discharge.

Section No.	$A$ (km <sup>2</sup> )	$L$ (km)	$J$ (‰)	$D_U$	Flood peak discharge				Debris flow peak discharge			
					$Q_p$ (m <sup>3</sup> /s)				$Q_c$ (m <sup>3</sup> /s)			
					P=1%	P=2%	P=5%	P=10%	P=1%	P=2%	P=5%	P=10%
10	0.7	1.34	483	3	5.49	4.65	3.52	2.66	41.80	31.54	20.51	14.16
8	0.65	1.16	625	3	5.08	4.12	3.08	2.13	38.57	28.13	18.09	10.79
2	0.44	0.4	849	2	3.61	2.93	2.25	1.69	25.48	17.87	11.12	6.99
1	0.1	0.35	601	2	0.91	0.72	0.57	0.44	6.57	4.56	2.98	1.84

The debris flow peak discharge ( $Q_c$ ) can be calculated using the Formula 4.

$$Q_c = (1 + \varphi)Q_p \cdot D_U \quad (4)$$

where  $D_U$  is the blockage coefficient in the debris flow gully. Usually, the degree of blockage is classified as very serious blockage ( $D_U=3.0-2.5$ ), serious blockage ( $D_U=2.5-2.0$ ), normal blockage ( $D_U=2.0-1.5$ ) and minor blockage ( $D_U=1.5-1.0$ ). For the situation in the Wenchuan earthquake area, the values were calculated to be 5.5-4.5, 4.5-3.5, 3.5-2.5 and 2.5-1 (You et al. 2012). Based on the field investigation and the channel blockage as identified from aerial photography, the blockage coefficient for the Lianshan Bridge gully is considered to be 2 and 3. is the increase coefficient of debris flow peak discharge, which can be calculated (Formula 5) as follows.

$$\varphi = (\gamma_c - \gamma_w) / (\gamma_s - \gamma_c) \quad (5)$$

where  $\gamma_w$  is the density of water (kg/m<sup>3</sup>), usually determined as 1000 kg/m<sup>3</sup>;  $\gamma_s$  is the density of the solid material (kg/m<sup>3</sup>), usually determined as 2650kg/m<sup>3</sup>, and  $\gamma_c$  is the density of debris flow (kg/m<sup>3</sup>).

### 3.2.4 The total and solid volume of debris flow

The total and solid volumes of debris flow were calculated using the experiential Formulae 6 and 7(Chen et al. 2011b). The results are given in Table 7.

$$W_c = \frac{19T_c Q_c}{72} = 0.264T_c Q_c \quad (6)$$

$$W_s = (\gamma_c - \gamma_w)W_c / (\gamma_s - \gamma_w) \quad (7)$$

where  $W_c$  is the total volume of debris flow (m<sup>3</sup>);  $T_c$  is duration of the debris flow (s);  $Q_c$  is the debris flow peak discharge (m<sup>3</sup>/s);  $\gamma_w$  is the density of water (kg/m<sup>3</sup>);  $\gamma_c$  is the density of the debris flow (kg/m<sup>3</sup>);  $\gamma_s$  is the density of the solid material (kg/m<sup>3</sup>); is the solid volume of the debris flow.

**Table 7.** The total volume of debris flow in different frequency.m

P (%)	Density	T(s)	$Q_c$ (m <sup>3</sup> /s)	$W_c$ (10 <sup>4</sup> m <sup>3</sup> )	$W_s$ (10 <sup>4</sup> m <sup>3</sup> )
1	1.9	600	41.8	0.662	0.361
2	1.82	600	31.54	0.500	0.248
5	1.7	600	20.51	0.325	0.138
10	1.62	600	14.16	0.225	0.085

### 3.2.5 The impact force of the debris flow

The impact force of debris flow is an important parameter in debris flow control engineering design that includes the impact force of the debris flow due to the dynamic pressure and the maximum stone size.

#### a. The impact force of debris flow dynamic pressure

The impact force of the debris flow due to the dynamic pressure was calculated using the Formula 8 (He and Wu 2009). The results are shown in Table 8.

$$\sigma = \lambda \frac{\gamma_c}{g} V_c^2 \sin \alpha \quad (8)$$

where  $\sigma$  is the impact force of the debris flow due to the dynamic pressure (kg/m<sup>2</sup>);  $\gamma_c$  is the density of the debris flow (kg/m<sup>3</sup>);  $\lambda$  is the building shape coefficient, usually determined as 1.33 when the building is rectangular;  $V_c$  is velocity of debris flow (m/s);  $\alpha$  is the angle between the buildings and the stress surface pressure direction, which is usually determined as 90°.

**Table 8.** The results of the impact of the debris flow.

No.	$\gamma_c$ (kg/m <sup>3</sup> )	$V_c$ (m/s)	$\sigma$ (kg/m <sup>2</sup> )	No.	$\gamma_c$ (kg/m <sup>3</sup> )	$V_c$ (m/s)	$\sigma$ (kg/m <sup>2</sup> )
1	1600	3.0	1954	6	1940	7.3	14030
2	1700	4.2	4070	7	1940	8.0	16850
3	1940	5.2	7119	8	1940	8.4	18577
4	1940	6.1	9797	9	1940	9.0	21326
5	1940	7.7	15610	10	1940	9.3	22772

**b. The impact force of the maximum stone size**

The impact force of debris flow dynamic pressure resulting from the maximum size of individual stones was calculated by the Formula 9 (He and Wu, 2009). The results are shown in the Table 9.

$$F = K_c n a^{2/3} \tag{9}$$

$$n = \left[ \frac{16R_2}{9\pi^2(k_1 + k_2)^2} \right]^{1/2}; a = \left( \frac{5V^2}{4nn_1} \right)^{2/5}; k_1 = (1 - \nu_1^2)/(\pi E_1); k_2 = (1 - \nu_2^2)/(\pi E_2); n_1 = 1/m_2$$

where  $F$  is the impact force of the maximum article size in the debris flow (kN);  $K_c$  is the correction coefficient and usually determined as 0.1;  $R_2$  is the radius of the maximum stone size and determined as 2.9m;  $\nu_1$  is the Poisson's ratio of material and  $\nu_2$  is Poisson's ratio for the maximum stone size;  $m_2$  is quality of the maximum stone (kg) in the gully;  $V$  is relative velocity of the stones (m/s) and determined as the 70% of  $V_c$ ;  $E$  is the modulus of elasticity of binding material and  $E_2$  is modulus of elasticity of the maximum stones (kg/m<sup>2</sup>).

**Table 9.** The impact of debris flow calculated using the elastic impact method.

Material	Poisson ratio	$E$ (kg/m <sup>2</sup> )	$F$ (kN)
Concrete	0.167	200000000	4955
Wood	0.1	80000000	823
Mortar	0.2	180000000	1458
Rubber	0.47	6820000	167

**4. Disaster characteristics**

**4.1 Triggering rainfall**

**4.1.1 The previous rainfall amount**

The previous rainfall amount is a very important factor in calculating potential debris flow. The daily precipitation from July 5 to July 10, 2013 at the Lianshan Bridge debris flow gully was collected through the Taoguan Village meteorological station (E103°29'13", N31°15'05", H: 1113m) located 100m upstream of the gully and the Dongjielaonao Village

meteorological station (E103°29'13", N31°15'05", H: 955m) located 50m downstream of the gully. The previous rainfall amounts are given in Table 10. There has been rainfall within 3 days before debris flow triggered. Taoguan Village meteorological station showed that maximum daily rainfall is up to 57.5 mm and the cumulative rainfall is 102.5mm within 3 days before debris flow triggered, the Dongjielaonao Village meteorological station showed that maximum daily rainfall is up to 185.5mm and the cumulative rainfall is 240.9 mm within 3 days before debris flow occurred.

**Table 10.** Daily rainfall occurring before July 10, 2013 (mm).

Stations	Date					Cumulative rainfall
	July 5	July 6	July 7	July 8	July 9	
Taoguan	0	0	0.2	44.8	57.5	102.5
Dongjielaonao	0	0	0	55.4	185.5	240.9

**4.1.2 Characteristics of 24 hour rainfall**

24 hour rainfall data from July 5th to July 10th were collected from Taoguan and Dongjielaonao Village meteorological stations. (Table 11 and Figure 7). Table 11 indicates that from 1hr to 5hr, rainfall has a maximum intensity which reaches up to 88.1mm. The maximum 1 hour rainfall is 21mm on July 10th and Lianshan Bridge debris flow triggered at the same time around 3 am.

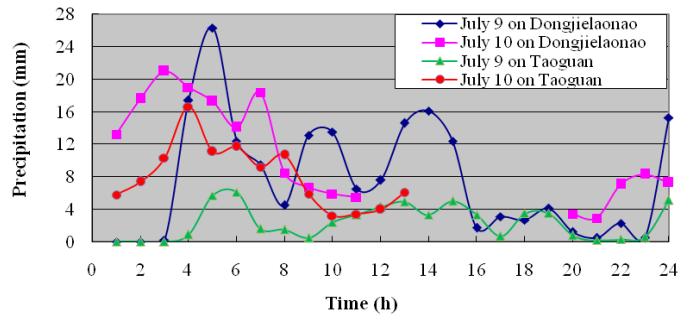


**Figure 7.** 24 hour rainfall curve.

**Table 11.** 24 hour rainfall data from July 5 to 10.

Time (hr)	Date											
	5	6	7	8	9	10	5	6	7	8	9	10
	Taoguan station (mm)					Dongjielaonao station (mm)						
1	0	0	0	0	0	5.8	0	0	0	0	0	13.2
2	0	0	0	0.3	0	7.4	0	0	0	1	0	17.6
3	0	0	0	0.8	0	10.3	0	0	0	0.3	0.2	21
4	0	0	0	1.2	0.9	16.6	0	0	0	3.8	17.4	19
5	0	0	0	4	5.7	11.1	0	0	0	13.1	26.3	17.3
6	0	0	0	13.1	6.1	11.7	0	0	0	17	12.4	14.1
7	0	0	0	17	1.6	9.2	0	0	0	9.6	9.5	18.4
8	0	0	0	1.7	1.5	10.7	0	0	0	1.1	4.5	8.5
9	0	0	0	0.1	0.5	5.9	0	0	0	0.3	13.1	6.7
10	0	0	0	0	2.4	3.2	0	0	0	0	13.5	5.9
11	0	0	0	0	3.3	3.4	0	0	0	0	6.5	5.5
12	0	0	0	1.1	4.3	4	0	0	0	0.3	7.6	0
13	0	0	0.2	0.2	4.9	6.1	0	0	0	1.9	14.6	0
14	0	0	0	2.6	3.3	0	0	0	0	5.4	16.1	0
15	0	0	0	2.7	5	0	0	0	0	0.4	12.4	0
16	0	0	0	0	3.3	0	0	0	0	0	1.7	0
17	0	0	0	0	0.7	0	0	0	0	0	3.1	0
18	0	0	0	0	3.5	0	0	0	0	0	2.7	0
19	0	0	0	0	3.5	0	0	0	0	0	4.1	0
20	0	0	0	0	0.8	0	0	0	0	0	1.2	3.4
21	0	0	0	0	0.2	0	0	0	0	0	0.5	2.9
22	0	0	0	0	0.3	0	0	0	0	1.2	2.3	7.1
23	0	0	0	0	0.6	0	0	0	0	0	0.5	8.3
24	0	0	0	0	5.1	0	0	0	0	0	15.3	7.3

## 4.2 The loose solid material

The Wenchuan earthquake of May 12, 2008 produced a great deal of loose solid material that can lead to the development of devastating debris flows (Tang et al. 2009, 2011). Shieh et al (2009) pointed out that the loose sediments, deposited by the co-seismic landslides, were the main reason for a lowering of the meteorological thresholds for debris flows. The debris flow activity in these earthquake-affected areas is very high in the first 5–10 years after an earthquake, while the total period with an increased potential for debris flow activity can last 20 to 40 years (Tang et al. 2012). The distribution of loose solid materials in Lianshan Bridge debris flow gully was mapped through post-disaster field investigations and remote sensing interpretation (Figure 8). Pit tests were used to determine the thickness of solid materials, and the total volume of loose solid materials was calculated through field measurements. Radar mapping was used to determine the thickness of the solid materials in some areas of the gully bed where pit tests were difficult to undertake, and the volume of solid materials calculated (Figure 9). The area and thickness of old debris flow deposits and landslide deposits were obtained by remote sensing, which measured the area of colluvial deposits; the function (Guzzetti et al. 2008) was used to calculate the volume of the colluvial deposits. The loose solid material in the Lianshan Bridge debris flow gully was  $140.5 \times 10^4 \text{ m}^3$  based on the field investigation and remote sensing interpretation, including collapse sediments  $197,000 \text{ m}^3$ , landslide  $721,000 \text{ m}^3$ , bed sediments  $57,000 \text{ m}^3$ , slope erosion loose solid materials  $325,000 \text{ m}^3$ , old debris flow sediments  $105,000 \text{ m}^3$ . Such abundant loose solid material provided source conditions for the large-scale debris flow outbreak.

**Figure 8.** Field measurement and radar test.

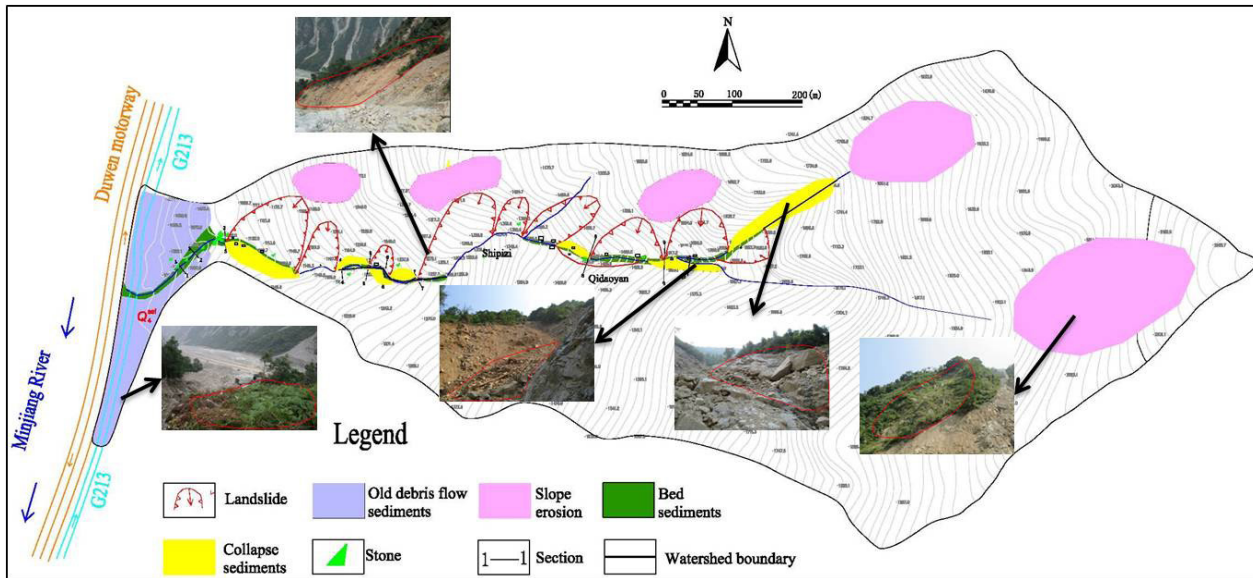


Figure 9. The distribution map of loose solid materials.

### 4.3 Deposition characteristics

#### 4.3.1 The characteristics of particle size along the gully

The gully is divided into 6 parts based on the changes in the particle size characteristics (Figure 10). These are: (a) From the top of gully to Qidaoyan, the particle size is mostly gravel-cobble, containing angular diorite and granite, without sorting. The gravel size is generally in the 3-10cm range, and the gravel content is 40-50%. The stone size is generally 20-40cm, and the content is about 30%. The largest stone size is up to 3m. (b) From the right branch ditch to the entrance of the main gully, the particle distribution is mostly stone, containing angular diorite and granite, without sorting. The gravel size is generally in the 5-15cm range, and the gravel content is 30-40%. The sizes of the stones are generally in the 30-60cm range, and the stone content is approximately 40%, with the largest stone size up to 2.5m. (c) From Qidaoyan to Shipizi, the particles are mostly stone and soil; the stone is angular diorite and granite, without

sorting. The gravel size is 6-16cm, and the gravel content is 20-30%. The stone size is generally in the 20-60cm range, and the stone content is about 50%. The largest stones are up to 2m. (d) In the Shipizi gully, the characteristic particle size shows mostly gravel and soil, containing angular diorite and granite, without sorting. The gravel size is generally 5-15cm, and the gravel content is 40-50%. The stone size is mostly in the 20-40cm range, and the content of stone is about 25%; the stone size can be up to 4m. (e) From Shipizi to an altitude of 1100m, the particles are mostly gravel and soil; the gravel is angular diorite and granite, without sorting. The gravel size is 5-20cm, and the content is 30-40%. The stone size is in the 20-60cm range, and the stone content makes up about 20%, with the largest stones up to 2m. (f) From an altitude 1100m to the mouth of gully, the particles are mostly gravel and soil; the gravel is angular diorite and granite, without sorting. The gravel size is generally in the 5-15cm range making up 10-15% of the whole. The stone size is mostly 20-60cm, and the stone content is about 5%; the largest stones can be up to 1.5m.

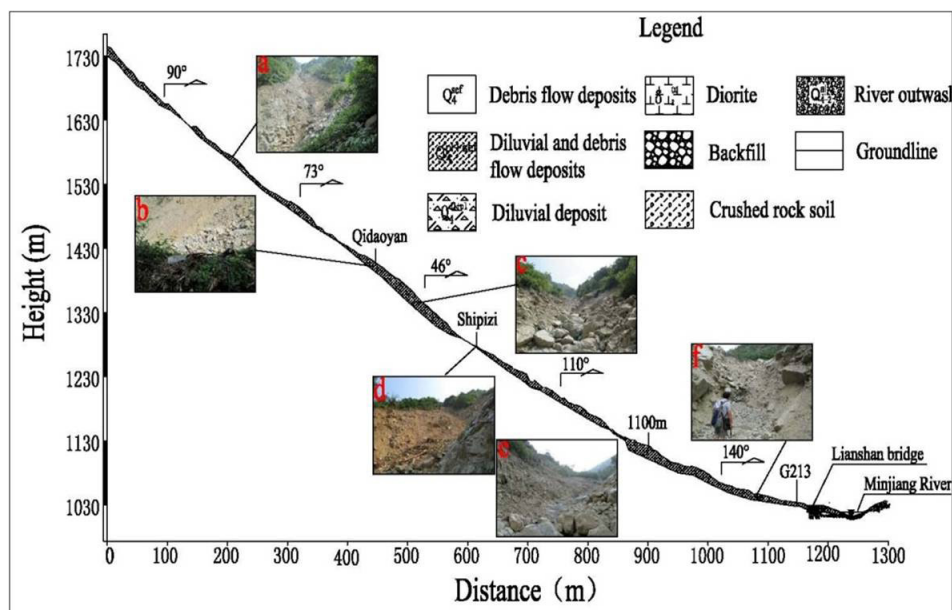


Figure 10. The changed characteristics of particle size along the gully.

#### 4.3.2 The particle characteristics on debris flow deposition

The debris flow partition accumulation characteristic of the gully is significant because of the gradient of the gully. The debris flow deposition is mainly distributed on the lower slopes and wider regions

of gully downstream. From the field investigation, it was found that the composition of the material has a wide grading of soil, and the clay fraction is less. The majority of the stone is angular, and the stone content is about 50-60%. Lithology varies between mostly anorthosite and granodiorite (Table 12).

**Table 12.** Statistics of particle survey on the gully mouth (site: N31°11'26.2"E103°29'57.5" H:1068m) .

No.	Particle size (cm)	Lithology	Psephicity	No.	Particle size (cm)	Lithology	Psephicity
1	55×50×23	plagioclasite	subangular	31	36×20×10	plagioclasite	subangular
2	60×30×24	plagioclasite	angular	32	<2	\	\
3	45×33×26	diorite	subangular	33	<2	\	\
4	<2	\	\	34	60×30×27	plagioclasite	subangular
5	20×5×3	plagioclasite	subangular	35	40×40×30	diorite	subangular
6	26×22×9	plagioclasite	subangular	36	120×70×50	plagioclasite	subangular
7	18×14×12	diorite	subangular	37	<2	\	\
8	16×9×5	plagioclasite	subangular	38	<2	\	\
9	<2	\	\	39	10×10×8	plagioclasite	subangular
10	<2	\	\	40	120×90×40	diorite	subangular
11	35×15×9	plagioclasite	subangular	41	<2	\	\
12	25×20×7	plagioclasite	subangular	42	<2	\	\
13	22×13×7	plagioclasite	subangular	43	16×10×8	plagioclasite	subangular
14	9×6×3	plagioclasite	subangular	44	45×40×20	plagioclasite	subangular
15	50×34×15	plagioclasite	subangular	45	47×35×20	plagioclasite	subangular
16	12×9×7	plagioclasite	subangular	46	<2	\	\
17	12×5×3	granite	subangular	47	17×15×9	plagioclasite	subangular
18	18×16×5	plagioclasite	subangular	48	<2	\	\
19	<2	\	\	49	<2	\	\
20	76×50×14	plagioclasite	subangular	50	13×10×7	granite	subangular
21	<2	\	\	51	<2	\	\
22	<2	\	\	52	<2	\	\
23	26×10×7	diorite	subangular	53	30×10×7	plagioclasite	subangular
24	<2	\	\	54	<2	\	\
25	<2	\	\	55	<2	\	\
26	13×9×4	diorite	subangular	56	30×19×7	plagioclasite	subangular
27	34×15×13	plagioclasite	subangular	57	<2	\	\
28	<2	\	\	58	16×9×5	granite	subangular
29	30×13×9	diorite	subangular	59	25×20×8	plagioclasite	subangular
30	14×12×10	plagioclasite	subangular	60	<2	\	\

#### 5. The block and burst characteristics of a debris flow gully

It is unusual that such a large-scale debris flow outbreak should occur in such a small debris flow gully. Blockage of debris flow gully is the main reason for large-scale debris flow outbreaks in small debris flow gullies in earthquake-affected areas. In Lianshan Bridge debris flow discharge case, it

was found that there were two discharge alteration points, in section No. 2 to No. 3 (the discharge increased from 33.6m<sup>3</sup>/s to 62.4m<sup>3</sup>/s, an increase of nearly 100%) and in section No. 4 to No. 5, where the discharge increased from 73.2m<sup>3</sup>/s to 157.8m<sup>3</sup>/s, a discharge increase of over 100% (Figure 11).

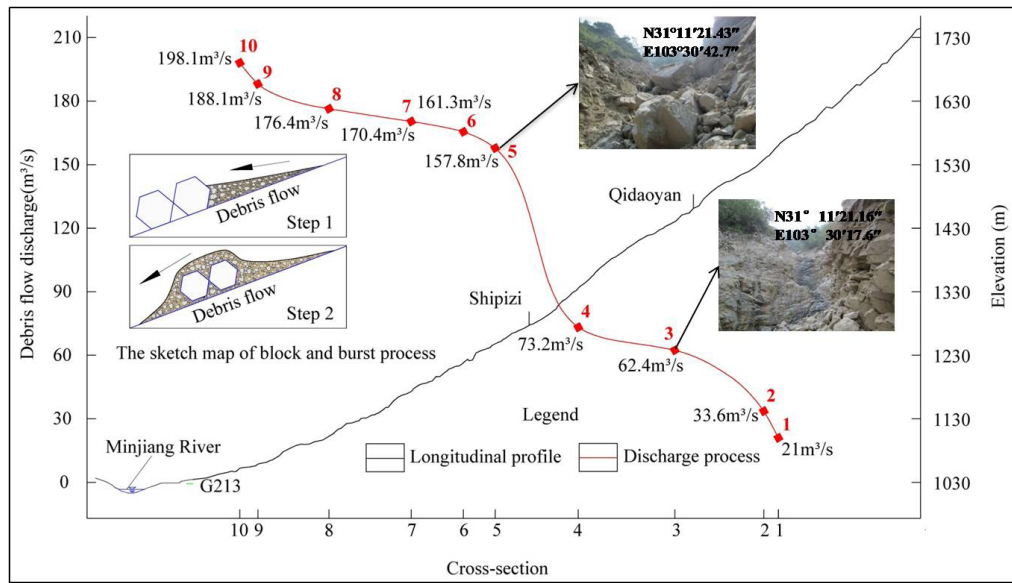


Figure 11. The block and burst characteristics of debris flow gully.

Site investigations make it apparent that large stones (greater than 1.5m in length) in the Lianshan Bridge channel were considered to have a statistical effect on the debris flow discharge (Table 13). Because the shape of large stone is irregular, the volume of stone is calculated based on the cuboids, and multiplied by the experiential coefficient 0.7 for China’s western mountains (Hu et al.2011; Chen et al. 2005).

The channel distribution of these large stones is shown in Figure 9 and 11. The main reason for the change in debris flow discharge is these large landslides and massive stones. Two sections 3 and 5 block the movement of debris flow. Because of higher hydraulic gradient and strong impact of landslide around this section, it offers more resistance as compared to section 3 (Figure 11 and 12).

Table 13. Statistics of the large stones size on the channel (Units: m and m³).

Stone No.	Length	Width	Height	Volume	Stone No.	Length	Width	Height	Volume
1	2.3	1.7	1.5	4.1	16	2.3	1.6	1.3	3.4
2	1.8	1.5	1.3	2.5	17	1.7	1.4	0.8	1.3
3	2	1.6	1.4	3.2	18	2.2	1.8	1	2.8
4	4.5	3.8	3.1	37.1	19	2.8	2.2	2	8.6
5	3	2.4	2	10.1	20	2.2	1.8	1.2	3.4
6	2.4	2	1.5	5.0	21	1.8	1.3	1.2	2.0
7	4	2	1.8	10.1	22	2	1.7	1.4	3.4
8	3.8	3.2	2.6	22.1	23	1.7	1.5	1.3	2.3
9	4.2	2.3	2	13.5	24	2.1	1.9	1.2	3.4
10	4.3	3.7	3	33.4	25	3	2	1.3	5.5
11	2.5	2	1.7	6.0	26	2.4	1.8	1.5	4.6
12	2.8	2.4	2	9.4	27	2.3	2.1	1.7	5.7
13	2.8	2.4	2	9.4	28	1.9	1.6	1.4	3.0
14	4.6	4	2.8	36.1	29	1.8	1.6	1.3	2.6
15	1.7	1.5	1.2	2.2	30	2.2	1.7	1.4	3.6

6. Prevention and control measures

Strong earthquakes often induce a large number of collapses, landslides and unstable slopes and also generate abundant unconsolidated material that contributes to debris flow. Debris flows will be a major hazard in the Wenchuan earthquake area for many years (Cui et al. 2014). Characteristics of debris flow in the Wenchuan earthquake area compel us to take engineering measures before the active period of debris flows. New engineering structures are proposed in this paper to mitigate debris flow

hazards along some small gullies and slopes. The appropriate engineering measures include the buildup of one or more block dams, to stop the huge stones, and a fence wall to resist the loose solid materials to reach on the outside of gully. A block dam engineering measure has already been applied in the circulation area of debris flow which makes the steady flow of the loose solid materials. One horizontal grided dam was built in the accumulation area to intercept large stones. The debris flow will then be channeled into a drainage groove, and finally drained into the Minjiang River (Figure 12).



Figure 12. Aerial photograph of the Lianshan Bridge gully (A: shoot on August, 2013; B: November, 2014).

## 7. Summary

After the Wenchuan earthquake, debris flows from Yinxing to Miansi Town in Wenchuan County along the G213 road occurred often, resulting in frequent interruption of traffic on both the G213 road and Duwen highway. Using field investigations, remote sensing interpretation, laboratory experiments, model calculation and interviewing local residents, it was concluded that the factors influencing the debris flow were the formation processes and dynamic characteristics of “7.10” Lianshan Bridge debris flow. The following conclusions were drawn from the available information. (a) In areas with long term seismic activity, intense rainfall can easily induce debris flow. (b) Bank collapse and large rocks also contributed to an increase in debris flow scale and discharge, and eventually led to the “7.10” large scale debris flow in the Lianshan Bridge gully watershed. (c) Currently, there is still considerable loose solid material available for debris flow formation in these gullies. Landslide deposition, channel deposition, and soil erosion sediment are three kinds of sediment that supply material for debris flow formation. The total volume of loose solid material is  $140.5 \times 10^4 \text{ m}^3$ . Such large amounts of solid loose sediment could generate debris flows easily given adequate rainfall. (d) Reliable prevention and control measures should be put forward with the purpose of reducing debris flow disasters in these debris flow gullies (e) Monitoring and early warning systems should be set up and government should strengthen propaganda on disaster prevention and mitigation to improve residents’ consciousness of debris flow disasters, which could effectively reduce the human and infrastructure losses caused by debris flow hazards.

## Acknowledgements

This research was supported by the National Natural Science Foundation of China (Grant No. 41501012 and 41661134012) and Foundation for selected young scientists, Institute of Mountain Hazards and Environment, CAS (No.SDS-QN-1306, Y3L1340340, sds-135-1202-02).

## References

- Chen, H.X., Zhang, L.M., Chang, D.S., and Zhang, S. (2012). Mechanisms and runoff characteristics of the rainfall-triggered debris flow in Xiaojiagou in Sichuan Province, China, *Nat. Hazards*. 62 (3), 1037–1057.
- Chen, H.X., Zhang, L.M., Zhang, S., Xiang, B., and Wang, X.F. (2013). Hybrid simulation of the initiation and runoff characteristics of a catastrophic debris flow, *Journal of Mountain Science*. 10 (2), 219–232.
- Chen, N.S., Cui, P., Liu, Zh.G., and Wei, F.Q. (2003). Calculation of the debris flow concentration based on clay content, *Science in China Ser. E Technological Sciences*. 46, 163–174.
- Chen, N.S., Li, T. Ch., Gao, Y. Ch. (2005). A great disastrous debris flow on 11 July 2003 in Shuikazi valley, Danba County, western Sichuan, China, *Landslides*. 2:71–74.
- Chen, N.S., Hu, G.S., Deng, M.F., Zhou, W., Yang, C.L., Han, D., and Deng, J.H. (2011a). Impact of earthquake on debris flows—a case study on the Wenchuan earthquake, *J. Earthq. Tsunami*. 5 (5), 493–508.
- Chen, N.S., Yang, C.L., Zhou, W., Hu, G.S., Li, H., and Han, D. (2009). The critical rainfall characteristics for torrents and debris flows in the Wenchuan earthquake stricken area, *Journal of Mountain Science*. 6, 362–372.

- Chen, N.S., Yang, C.L., Zhou, W., Wei, F.Q., Li, Z.L., Han, D., and Hu, G.S. (2011b). A new total volume model of debris flows with intermittent surges: based on the observations at Jiangjia Valley, southwest China, *Nat Hazards*. 56, 37–57.
- Cui, P., Hu, K.H., Zhuang, J.Q., Yang, Y., and Zhang, J.Q. (2011). Prediction of debris-flow danger area by combining hydrological and inundation simulation methods. *Journal of Mountain Science*. 8, 1–9.
- Guzzetti, F., Peruccacci, S., Rossi, M., and Stark, C.P. (2008). The rainfall intensity–duration control of shallow landslides and debris flows: an update, *Landslides*. 5(1), 3–17.
- He, S.M., Wu, Y., and Shen, J. (2009). Simplified calculation of impact force massive stone in debris flow, *Journal of natural disasters*. 18(5), 51–56 (in Chinese with English abstract)
- Hu, G.S., Chen, N.S., Deng, M.F and Lu, Y. (2011). Analysis of the characteristics of impact force of massive stones of Sanyanyu debris flow gully in Zhouqu, Gansu province, *Earth and Environment*. 39(4), 478–484 (in Chinese with English abstract).
- Huang, R., Pei, X., and Fan, X. (2012). The characteristics and failure mechanism of the largest landslide triggered by the Wenchuan earthquake, May 12, 2008, China, *Landslides*. 9, 131–142.
- Liu, J.F., You, Y., and Chen, X.C. (2010). Identification of potential sites of debris flows in the upper Min river drainage, following environmental changes caused by the Wenchuan earthquake, *Journal of Mountain Science*. 7, 255–263.
- Ni, H., Zheng, W., Tie, Y., Su, P., Tang, Y., Xu, R., Wang, D., and Chen, X. (2012). Formation and characteristics of post-earthquake debris flow: a case study from Wenjia gully in Mianzhu, Sichuan, China, *Natural Hazards*. 61 (2), 317–335.
- Shieh, C.L., Chen, Y.S., Tsai, Y.J., and Wu, J.H. (2009). Variability in rainfall threshold for debris flow after the Chi-Chi earthquake in central Taiwan, China, *Int. J. Sediment Res.* 24, 177–188.
- Tang, C., Zhu, J., Li, W., and Liang, J. (2009). Rainfall-triggered debris flows following the Wenchuan earthquake, *Bulletin of Engineering Geology and the Environment*. 68 (2), 187–194.
- Tang, C., Zhu, J., and Ding, J. (2011). Catastrophic debris flows triggered by a 14 August 2010 rainfall at the epicentre of the Wenchuan earthquake, *Landslides*. 8, 485–497.
- Tang, C., Van, A.T., Chang, M., Chen, G., Zhao, X., and Huang, X. (2012). Catastrophic debris flows on 13 August 2010 in the Qingping area, southwestern China: The combined effects of a strong earthquake and subsequent rainstorms, *Geomorphology*. 139, 559–576.
- Wang, J.J., Zhao, D., Liang, Y., and Wen, H.B. (2013). Angle of repose of landslide debris deposits induced by 2008 Sichuan Earthquake, *Engineering Geology*. 156, 103–110.
- Wang, Z.Y., Qi, L.J., and Wang, X.Z. (2012). A prototype experiment of debris flow control with energy dissipation structures, *Nat. Hazards*. 60, 971–989.
- Xu, Q., Zhang, S., Li, W.L., Van A.T., and Tan, W.J. (2012). The 13 August 2010 catastrophic debris flows after the 2008 Wenchuan earthquake, China, *Nat. Hazards Earth Syst. Sci.* 12, 201–216.
- You, Y., Liu, J.F., and Chen, X.C. (2012). Design of Sluiceway channel in a landslide dam triggered by the Wenchuan earthquake, *Disaster Adv.* 5, 241–249.
- Yu, B., Wu, Y.F., and Chu, Sh.M. (2014). Preliminary study of the effect of earthquakes on the rainfall threshold of debris flows, *Engineering Geology*. 182, 130–135.
- Zhang, H.P., Yang, N., and Zhang, Y.Q. (2006). Geomorphology of the Minjiang drainage system (Sichuan, China) and its structural implications, *Quat. Sci.* 26, 126–135 (in Chinese with English abstract).
- Zhang, S., Zhang, L.M., Chen, H.X., Yuan, Q., and Pan, H. (2013). Changes in runoff distances of debris flows over time in the Wenchuan earthquake zone. *Journal of Mountain Science*. 10 (2), 281–292.
- Zhou, R.J., Pu, X.H., and He, Y.L. (2000). Recent activity of Minjiang fault zone, uplift of Minshan block and their relationship with seismicity of Sichuan, *Seismol. Geol.* 22, 285–294 (in Chinese with English abstract).





## Potential Settlement Due to Seismic Effects in the Residential Area of Ilgin (Konya, Turkey)

Adnan Ozdemir, Necmettin Erbakan University, Department of Civil Engineering, Konya, Turkey.

M. Tahir Nalbantçilar, Batman University, Department of Geological Engineering, Batman, Turkey.

### ABSTRACT

Ilgin lies on newly formed, loose, granular deposits, and there is substantial risk for surface liquefaction and foundation settlements due to the seismic effects resulting from groundwater close to the surface. This study evaluates potential settlement due to seismic effects in the residential areas of Ilgin using the Standard Penetration Test (SPT) performed on 45 geotechnical bores. In Turkey, where earthquakes occur frequently, the selection of residential areas is of great importance. In this research, the number of settlements was calculated considering an earthquake having a Local Magnitude of 6 (i.e.,  $ML \geq 6.0$  and  $a \geq 0.4g$ ) under a 0.4 g seismic force, and a potential settlement map of the residential area was prepared. The amount of settlement exceeds 20 cm at locations near Ilgin Lake and in the northern section of Ilgin residential areas; downtown, the settlement ranges from 10-20 cm. The settlements presented here exceed the allowable threshold limits for structures constructed using adobe and brick in this district. Thus, improvements to minimise earthquake-induced damages are required for structures in Ilgin. Moreover, the selection of new residential areas, along with the proper design of the structures before construction, should be examined further to avoid ground liquefaction and structure damage due to settlement.

*Keywords: Soil settlement, soil dynamic, liquefaction, earthquake, Ilgin.*

## Asentamiento potencial del suelo debido a efectos sísmicos en el área residencial de Ilgin (Konya, Turquía)

### RESUMEN

La localidad de Ilgin está ubicada sobre depósitos recién formados, granulares y no compactos, por lo que existe un riesgo sustancial de licuefacción de la superficie y la creación de asentamientos o deslizamientos debido a los efectos sísmicos resultantes del agua subterránea poco profunda. Este artículo evalúa el potencial de asentamiento debido a los efectos sísmicos en las áreas residenciales de Ilgin a través del Ensayo de Penetración Estándar (SPT, en inglés) realizado en 45 perforaciones geotécnicas. En Turquía, donde los terremotos ocurren frecuentemente, la selección de áreas residenciales es de gran importancia. En esta investigación, se calculó el número de asentamientos ante un terremoto con Magnitud Local (ML) de 6 y con una fuerza sísmica de 0.4 g para preparar un mapa de asentamientos en el área residencial. La cantidad de asentamientos supera los 20 centímetros en lugares cercanos al lago Ilgin y en la sección norte del área residencial; en el centro, los rangos de asentamiento van de 10 a 20 cm. Los asentamientos presentados exceden los límites de lo permitido para estructuras construidas en adobe y ladrillo en este distrito. Por esto, se requieren mejoras para minimizar los daños inducidos por terremotos en las estructuras de Ilgin. Además, la selección de nuevas áreas residenciales, junto con el diseño apropiado de las estructuras antes de la construcción, debe ser revisado atentamente para evitar la licuefacción del suelo y el daño de las estructuras debido al asentamiento.

*Palabras clave: Asentamiento del suelo, dinámica de suelos, licuefacción, terremoto, Ilgin.*

### Record

Manuscript received: 10/04/2015

Accepted for publication: 11/03/2016

### How to cite item

Ozdemir, A., & Nalbantçilar, M. H. (2016). Potential Settlement Due to Seismic Effects in the Residential Area of Ilgin (Konya, Turkey). *Earth Sciences Research Journal*, 20(2), F1-F9. doi:<http://dx.doi.org/10.15446/esrj.v20n2.50062>

## 1. Introduction

Ground oscillation, liquefaction, flows, slides, and settlements caused by seismic effects result in damage or destruction of transportation infrastructure, energy transmission lines, municipal water infrastructure, wastewater facilities, communication lines, and other engineered structures. Earthquakes can also lead to significant economic losses and loss of human lives (Bardet and Kapuskar, 1993; Clough et al., 1994; Kimura, 1996; Holzer, 1998). Displacements, which occur in various forms due to the variety of flows, slides, falls, precipitations, and settlements, may exceed 10 m at times (Zhang et al., 2004). Pore-water pressure, which appears to increase during seismic cycles in water-absorbable sandy soils, gradually dissipates after an earthquake, and the settlement, which is the vertical component of the volumetric deformations to the ground, can significantly damage nearby engineered structures. Settlements can even result in the destruction of structures. Furthermore, differential settlement caused by the nonuniformity of structures can result in increased structural damage.

Currently, the selection of residential areas and the implementation of earthquake-design constructions are of high importance. Recent studies have been focused on determining the most appropriate residential areas and designing earthquake-resistant structures (Bartlett and Youd, 1995; Hamada et al., 1996; Seed, 1979; Ishihara and Yoshimine, 1992; O'Rourke and Pease, 1992; Stewart et al., 2002; Stewart and Whang, 2003; Zhang et al., 2004; Kayabali and Beyaz, 2011). The selection of residential areas is particularly important in Turkey, where earthquakes occur frequently. Earthquake-induced damages can be devastating due to the limited number of earthquake-resistant structures that can tolerate both seismic settlements and differential ground settlements. (Kayabali, 1997; Ulusay et al., 2000; Cetin et al., 2002; Mollamahmutoglu et al., 2003). Thus, some researchers have investigated liquefaction and shear failures in soils. Zhang et al. (2002) examined the estimation of liquefaction-induced ground settlements from CPT data, while Andrus et al. (2004) compared the liquefaction evaluation methods using the penetration-Vs relations. Tatsuoka et al. (1987) observed settlement in saturated sand due to cyclic undrained simple shear. Yoshimine et al. (2006) showed the flow deformation of a liquefied sand layer under a constant shear load and analysed the slide flow of an infinite slope.

This study focuses on the determination of ground settlement potentials in the residential areas of Ilgin (Figure 1), which is located in the first-degree earthquake zone of the Region of Lakes (i.e., the central-southwest of Turkey). In situ test data were obtained by the Standard Penetration Test (SPT). Although there is much interest, previous studies have not studied ground settlement due to seismic effects. Generating fundamental data to inform the planning of residential areas (in both Ilgin and other regions) and the design of earthquake-resistant structures requires determining the ground deformations due to the seismic movements, as well as liquefaction susceptibility of medium-high and low resistance areas (Ozdemir and Ince, 2005). This particular study determines the level of the settlements in Ilgin and similar areas by performing a full evaluation of the morphology, geology, seismo-tectonics, and liquefaction potential of the residential areas in Ilgin. In the following sections of the study, the morphology, geology, and hydrogeology after seismo-tectonics, as well as the liquefaction potential of the study area, are examined. Furthermore, the calculation details for saturated and unsaturated soil settlements with seismic effects are given.

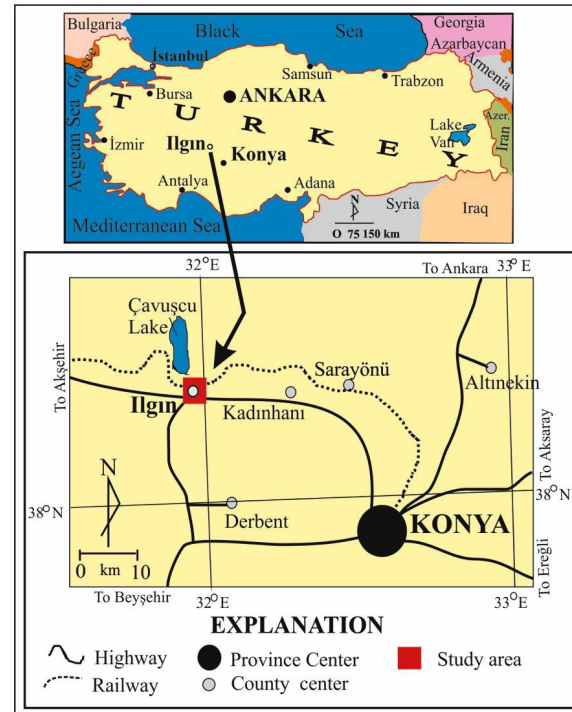


Figure 1. Map of the study area

## 2. Materials and methods

### 2.1 Location information, morphology, geology, and hydrogeology

Ilgin is located 90 km northwest of Konya in the south-central section of Central Anatolia (Figure 1). Ilgin is bordered by Hamam Sirti to the southwest and Sivri Tepe to the northeast. The town is located on a flat area, and the study area has an altitude between 1025–1035 m. Cavuşcu Lake is approximately 5 km northeast of Ilgin. The study area is located to the south and north of the central section, while the overall topographical inclination is from west to east due to the major hills in the region. The topographical inclination in the residential areas varies between 1 and 3%. There are irrigation canals in the western and northern sections that run from south to north and from west to east (Figures 1 & 2, respectively).

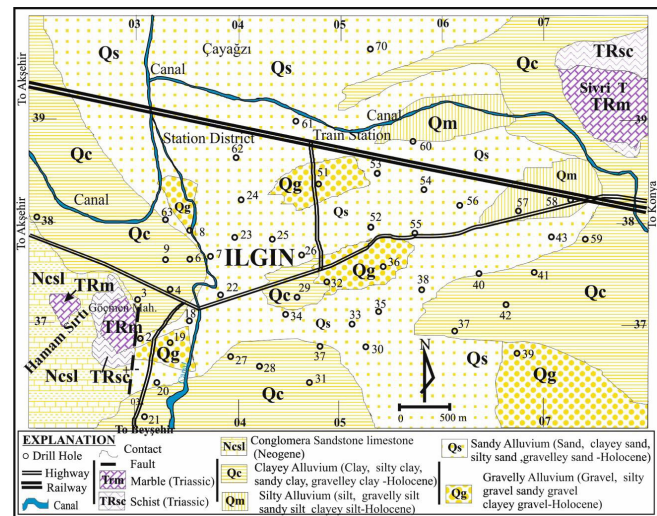


Figure 2. Geological map of the Ilgin residential area and vicinity (Ozdemir and Ince, 2005)

The geology and hydrogeology of Ilgin and its vicinity has been previously researched (Boray et al., 1985; Saroglu et al., 1987; Barka et al., 1995; Kocyigit et al., 2000; Canik, 1981). The regional geology, hydrogeology, tectonics, historical earthquakes, and potential for liquefaction of the study area has also been previously investigated in detail (Ozdemir and Ince, 2005). Data from previous studies that is relevant to this study is summarised in the next paragraph.

The region consists of Neogene and Pre-Neogene aged rock units along with Quaternary units. Triassic-aged marble ( $T_{RM}$ ) and schist ( $T_{RSC}$ ) are present in the region. These units do not show liquefaction-settlement potential resulting from seismic effects. Additionally, there are units such as Tertiary-aged conglomerate, limestone, sandstone, and marl (Nc-kg-s) that are not susceptible to liquefaction-induced settlement in the residential areas. Such units are unconformably overlain by Quaternary gravel (Qg), sand (Qs), silt (Qm), and clay (Qc).

**2.2 Tectonics, seismo-tectonic, and ground liquefaction potential**

The thicknesses of Quaternary-aged units, which have liquefaction and settlement potential, vary from 20-50 m and 0-20 m north of the selected study location and at the other locations, respectively. Vertical and lateral transitions at short distances are present within the Quaternary-aged units. Areas in Ilgin are underlain by loose Quaternary units, and liquefaction susceptibility of such loose precipitation is medium to high (Ozdemir and Ince, 2005). A groundwater map was drawn from data obtained by water depths measurements in 45 boreholes during July of 2000 (Figure 3). The groundwater table depth ranges from -2 m to -4 m.

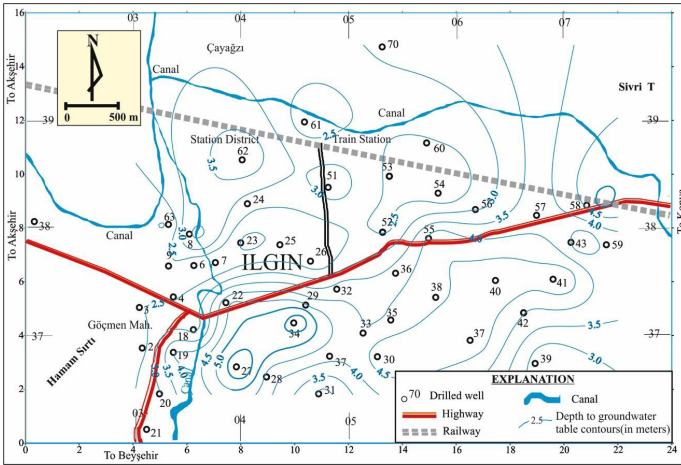


**Figure 3.** Locations and values of groundwater level measurements (Ozdemir and Ince, 2005)

Ilgin is located at the intersection of the following four active major faults: the southwest trending Sultandagi (Boray et al., 1985; Saroglu et al., 1987), the E-W trending Argithani fault (Kocyigit et al., 2000), the NNE-WWS trending Mecidiye fault, and the N-S trending Cavuscu fault. There are also numerous secondary faults in the region. Earthquakes ranging in magnitudes from 5.5-6.5 have been recorded. As Ilgin is located on recently formed and loose precipitations, there is a high potential for liquefaction following a seismic event (Figures 2 & 3).

**2.3 Ground settlement due to earthquakes**

Calculations of expected seismic settlements based on the unsaturated (i.e., dry) and/or saturated soil settlement resulting from seismic movements have been extensively investigated (Pyke et al., 1975; Tokimatsu and Seed, 1987; Ishihara and Yoshimine, 1992; Shamoto et al., 1998; Darendeli and Stokoe, 2001; Liu et

al., 2001; Seed et al., 2001; Stewart et al., 2001; Stewart et al., 2002). In this study, seismic settlements were calculated using the most commonly used method, the Standard Penetration Test (SPT), developed by Tokimatsu and Seed (1987). The SPT blow counts obtained from the 45 borehole logs were used for the calculations. The correction factor of transferred energy for the SPT test was taken as 0.75 (Seed et al., 1985), and the correction coefficient for the diameter of the borehole was taken as 1 (Robertson, 1994; Robertson and Fear, 1996) to obtain the corrected blow counts  $N_{i(60)}$  from the raw SPT blow counts (Equation 2.1). The correction factor for the effective overburden stress was determined according to Liao and Whitman (1986) (Equation 2.2). The cyclic stress ratio (CSR) was determined according to Seed and Idriss (1971) (Equation 2.3), and the stress reduction factor was determined according to NCEER (1997) (Equations, 2.4-2.7).

Where:  $(N_{i(60)})$  is the corrected SPT blow count,  $C_{ER}$  is the energy ratio

$$(N_{i(60)}) = C_{ER} C_N N \tag{2.1}$$

in percent, and  $C_N$  is the overburden stress correction factor (NCEER, 1997).

$$C_N = 1 / \sqrt{\sigma'_0} \tag{2.2}$$

Where:  $\sigma'_0$  is the effective vertical overburden stress and  $N$  is the raw SPT blow count.

Where: CSR is the cyclic stress ratio induced by a given earthquake,

$$CSR = 0.65 (\sigma_0 / \sigma'_0) a_{max} r_d \tag{2.3}$$

$\sigma_0$  is the total vertical overburden stress,  $\sigma'_0$  is the effective vertical overburden stress,  $a_{max}$  is the peak horizontal ground acceleration (PGA) in g, and  $r_d$  is an estimated stress reduction coefficient (NCEER, 1997).

$$r_d = 1 - 0.00765 z \quad \text{for } z \leq 9.15 \text{ m} \tag{2.4}$$

$$r_d = 1.174 - 0.00267 z \quad \text{for } 9.15 \text{ m} \leq z \leq 23 \text{ m} \tag{2.5}$$

$$r_d = 0.744 - 0.008 z \quad \text{for } 23 \text{ m} \leq z \leq 30 \text{ m} \tag{2.6}$$

$$r_d = 0.5 \quad \text{for } > 30 \text{ m} \tag{2.7}$$

The volumetric deformations were estimated according to the corrected SPT blow counts and the cyclic stress rates (CSR) using the curves given by Tokimatsu and Seed (1987) (Figure 4). The settlement ( $S_{SAT}$ ) of each layer (i) was calculated as the product of the volumetric deformation and the thickness ( $h_i$ ) of the layer (Equation 2.8; Tokimatsu and Seed, 1987).

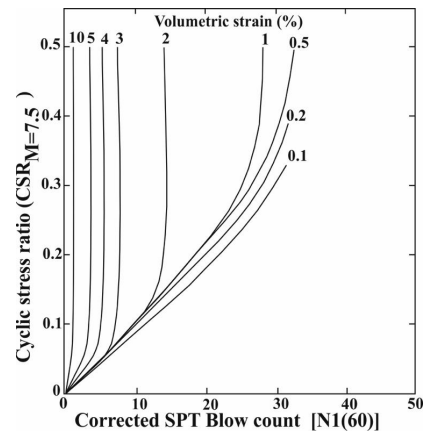


**Figure 4.** Volumetric strain versus corrected Standard Penetration blow count [(N1)60] and cyclic stress ratio (CSR) (Tokimatsu and Seed, 1987)

$$S_{sat} = \sum_{i=1}^n \left( \frac{\varepsilon_c}{100} \right) h_i \quad 2.8$$

Where:  $S_{sat}$  is the settlement of saturated soil;  $i$  is the number of layers;  $n$  is the total number of layers;  $\varepsilon_c$  is the volumetric deformation; and  $h_i$  is the thickness of layer  $i$ .

Because the minimum peak horizontal ground acceleration (PGA) of 0.4 g should be used when determining structural designs in Ilgin, which is located in the most dangerous first-degree earthquake zone (Aydinoglu, 1998), the PGA in this study was taken as 0.4 g when calculating the settlements.

The settlements on dry soil are calculated according to Tokimatsu and Seed (1987), using an estimated earthquake magnitude (Richter Magnitude,  $M_L$ ) of 6.

For dry soil settlement calculations, the procedure is the same but uses the corresponding SPT input data. The dry soil settlement is calculated by the following six steps:

i.  $G_{max}$ , the shear modulus of the soil at small strain, is estimated (Equation 2.9; Seed and Idriss, 1970).

$$G_{max} = 4400 [(N_1)_{60}]^{1/3} (\sigma_m)^{1/2} \quad 2.9$$

Where:  $(N_1)_{60}$  is the normalised SPT blow count (unitless) and  $\sigma_m$  is the mean normal total stress in kPa, which is approximated as 0.65  $\sigma_v$  ( $\sigma_v$  is vertical stress).

ii. Shear strain-modulus ratio,  $\gamma_{eff} (G_{eff}/G_{max})$  is determined to evaluate the cyclic shear strain (Equation 2.10) by the shear modulus,  $G_{max}$ :

$$\gamma_{eff} \frac{G_{eff}}{G_{max}} = 0.65 \frac{\sigma_0}{G_{max}} a_{max} r_d = CSR_{M=7.5} \frac{\sigma_0'}{G_{max}} \quad 2.10$$

Where:  $\gamma_{eff} (G_{eff}/G_{max})$  is a hypothetical effective shear strain-modulus ratio,  $a_{max}$  is the peak ground acceleration, and  $CSR_{M=7.5}$  is the cyclic stress ratio for an earthquake with a magnitude of 7.5.

iii. Effective shear strain ( $\gamma_{eff}$ ) is estimated using the previously calculated shear strain – shear modulus ratio (Figure 5).

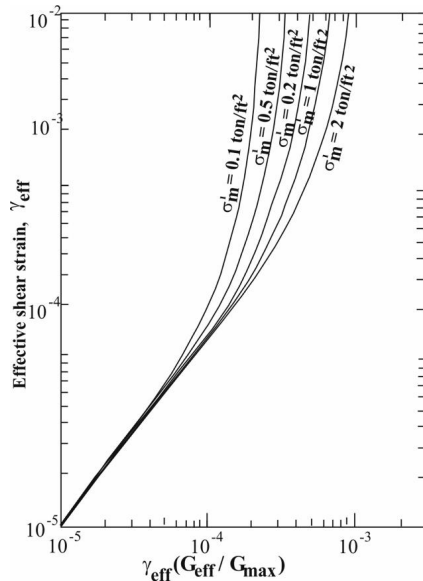


Figure 5. Plot for determining earthquake-induced effective shear strain in deposits (Tokimatsu and Seed, 1987)

iv. The volumetric strain due to compaction,  $\varepsilon_c$ , for an earthquake with a magnitude of 7.5 (15 cycles) is determined (Figure 6), and the shear strain is evaluated (Step 3; assuming that  $\gamma_{eff} \approx \gamma_c$  (cyclic shear strain)).

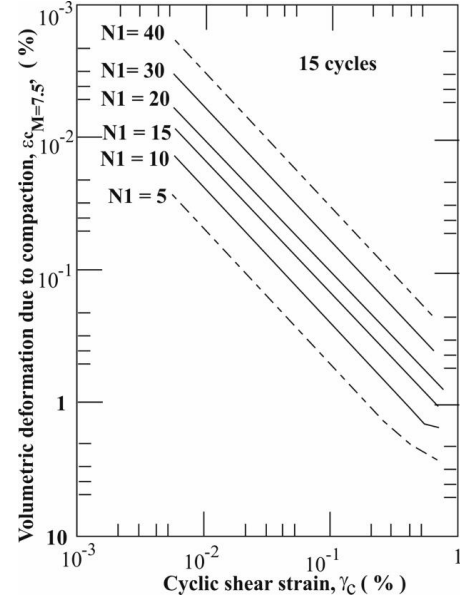


Figure 6. Relation between volumetric strain ( $\varepsilon_c$ ), cyclic shear strain ( $\gamma_c$ ), and corrected SPT blow count for  $(N_1)$  unsaturated sands (Tokimatsu and Seed, 1987)

v. Figure 6 corresponds to an earthquake with a magnitude of 7.5, with approximately 15 representative cycles. Magnitude correction of the volumetric strain was employed because the figures used above were developed for a magnitude 7.5 earthquake. For earthquakes with magnitudes other than 7.5, the volumetric strain ( $\varepsilon_c$ ) is obtained from the volumetric strain scaling factor  $r_m$  (Equation 2.11). Values for  $r_m$  are obtained from a plot of magnitude correction factor versus magnitude:

$$r_m = \frac{(\varepsilon_c)M}{(\varepsilon_c)_{M=7.5}} \quad 2.11$$

Where:  $\varepsilon_{c,M}$  is calculated by multiplying  $\varepsilon_{c, M=7.5}$  with the magnitude strain ratio ( $r_m$ ).

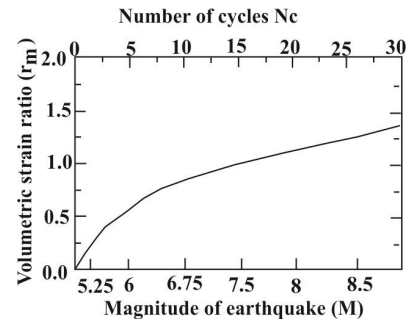


Figure 7. Magnitude correction factor versus magnitude (Tokimatsu and Seed, 1987)

vi. Dry soil settlement is calculated using the volumetric strain (Equation 2.1): 2.11

$$S_{dry} = \sum_{j=1}^n \frac{2(\varepsilon_{c,M})}{100} h_j \quad 2.12$$

Where:  $S_{dry}$  is the settlement of dry soil;  $\epsilon_{c,M}$  is the volumetric deformation [Magnitude ( $M_L$ ) = 6];  $h_j$  is the thickness of the unsaturated or dry soil layer  $j$ ; and  $n$  is the total number of soil layers.

Then, the total settlement ( $S_{total}$ ) at any specified depth,  $d$ , in the saturated and unsaturated ( $S_{sat}$ ) or in the dry soil ( $S_{dry}$ ) is determined (Equation 2.13):

$$S_{total} = \sum_{bottom}^{GWT} S_{sat} + \sum_{GWT}^d S_{dry} \tag{2.13}$$

Where:  $S_{total}$  is the earthquake induced total settlement at a certain depth ( $d$ ); GWT is the depth of groundwater level; and  $d$  is the certain depth.

The SPT blow counts used in this study, along with the other relevant data, are provided in Table 1. The settlements calculated for ground thicknesses of less than 10 m are presented in Table 2, and the map generated for the potential settlements according to the existing settlements at the depth of 2 m is shown in Figure 8.

**Table 1.** Data used for the calculation of seismically affected settlements (MERCAN-SU, 2000)

Borehole No	Depth to Groundwater (m)	Elevation of Groundwater Table (m)	Depth (m)	N <sub>SPT</sub>	Unit weight (kN/m <sup>3</sup> )	Fines Content (%)	Depth (m)	N <sub>SPT</sub>	Unit weight (kN/m <sup>3</sup> )	Fines Content (%)	Depth (m)	N <sub>SPT</sub>	Unit weight (kN/m <sup>3</sup> )	Fines Content (%)	Depth (m)	N <sub>SPT</sub>	Unit weight (kN/m <sup>3</sup> )	Fines Content (%)	Depth (m)	N <sub>SPT</sub>	Unit weight (kN/m <sup>3</sup> )	Fines Content (%)				
2	2	1035	2	7	19.6	55	3.0	3	20	55	8.0	24	19.6	55												
3	2.5	1032	2	6	19.6	1	3.0	11	19.6	1																
4	2.5	1031	2	5	18.7	16	5.0	8	18.7	16	7.0	13	16	10	11	18.7	99									
5	2	1031	2	11	18.7	16	5.0	8	18.7	16	8.0	8	18.7	16												
6	2	1031	2.5	7	19.6	41	5.0	10	18.8	41	8.0	10	18.7	41	10	7	18.7	99								
7	2	1031	2	5	19.6	28	5.0	8	18.7	28	7.0	9	18.7	52												
8	4.5	1030	2	2	18.7	87	5.0	7	18.7	87	8.0	8	18.7	40	10	50	18.7	99								
9	2,5	1030	2	5	18.5	7	4.0	7	18.5	7	7.0	9	18.5	7	10	50	27.0	99								
18	2.8	1034	2.5	17	18.5	2	7.0	6	18.5	2	10.0	20	18.5	2	12	50	27.0	99								
19	4.1	1036	2.5	5	17.6	48	5.0	4	17.6	48	8.0	4	17.6	47	10	7	17.6	48	12.0	50	27.0	99				
20	3	1035	2.5	7	17.6	35	5.0	3	17.6	35	7.5	10	17.6	35	10	9	17.6	35	12.0	11	17.6	35	15	13	17.6	35
22	4.6	1035	2.5	3	19.1	16	5.0	5	19.1	91	7.5	5	19.1	87	10	6	19.1	87	11.0	50	27.0	99				
23	1.8	1029	2.5	2	19.0	84	5.0	3	19.3	91	7.5	5	19.3	91	10	6	27.0	29	11.0	35	19.3	99	15	16	19.3	99
24	2.7	1029	2.5	2	18.6	83	5.0	8	18.6	77	7.5	11	18.6	77	10	12	18.6	77	12.0	8	27.0	99	14	50	27.0	99
25	2	1028	2	2	18.6	30	5.0	7	18.6	76	8.0	9	18.6	56	10	8	18.6	73	12.0	9	18.6	73	16	9	18.6	73
26	2	1028	2	7	18.5	93	5.0	8	18.5	90	8.0	11	18.8	81	10	12	18.8	81	13.0	19	18.8	81	16	19	18.8	81
27	6.1	1036	2.5	4	18.3	76	5.0	6	18.3	76	8.0	11	18.3	78	15	7	18.6	90	20.0	11	18.6	90				
28	4.2	1033	2.5	8	19.1	86	5.0	2	19.1	76	8.0	5	19.1	80	12	5	19.1	84	15.0	12	19.4	84	17	23	19.4	84
29	4.2	1033	3.0	40	18.6	21	5.0	5	18.6	77	8.0	5	19.3	77	10	10	19.3	77	13.0	10	19.3	77	16	16	19.3	77
30	5	1030	2.0	9	19.8	80	5.0	1	19.8	13	8.0	42	19.8	99	10	17	19.8	68	13.0	8	19.8	68	15	19	19.8	68
31	2.8	1031	2.0	8	18.8	78	5.0	8	18.8	88	8.0	34	19.1	88	10	17	19.1	88	13.0	11	19.1	88				
32	3.8	1032	2.0	5	19.6	46	5.0	5	19.6	88	8.0	6	19.6	88	10	7	20.6	88	13.0	14	20.6	88				

Table 2. Calculated settlements

Borehole No	Depth to Groundwater table (m)	Total Settlement (cm) for Depth			
		Depth = 2 m	Depth = 4 m	Depth = 6 m	Depth = 8 m
2	2.0	5.91	2.31	0.16	0
3	2.5	20.46	16.93	11.67	5.98
4	2.5	16.28	12.28	7.2	3.28
6	2.0	10.99	9.28	6.45	3.03
7	2.0	16.39	12.09	7.96	4.1
8	4.5	7.45	7.09	4.52	0.5
9	2.5	15.59	10.65	4.45	0
18	2.8	17.36	16.21	11	3.84
19	4.1	13.22	12.85	8.55	3.62
20	3.0	13.23	11.45	6.72	2.87
22	4.6	11.91	11.47	8.25	3.56
23	1.8	19.1	13.56	8.46	3.59
24	2.7	11.96	9.06	5.58	2.43
25	2.0	16.91	12.27	8.18	4.17
26	2.0	12.22	10.33	6.85	3.4
27	6.1	4.6	4.32	3.95	1.88
28	4.2	13.34	13.11	8.6	3.64
29	4.2	10.67	10.61	8.03	3.35
30	5.0	2.7	2.22	0	0
31	2.8	2.99	2.34	0.17	0.17
32	3.8	14.21	13.59	9.19	4.6
33	4.0	3.25	3	0.82	0.09
34	5.9	8.92	8.53	7.91	3.77
35	4.0	8.62	8.31	7.07	3.67
36	3.8	4.54	4.34	2.75	0.7
37	4.8	0.35	0.19	0	0
38	4.4	1.61	1.43	0.04	0
39	2.5	7.33	5.9	3.21	2.48
40	4.9	0.31	0.2	0.11	0.11
41	5.0	2.25	2.04	0.63	0.28
42	3.9	3.3	3.13	2.83	2.46
43	3.0	3.27	2.87	0.63	0.3
51	3.4	12.8	12.72	8.52	4.07
52	2.4	5.64	5.63	4.3	2.83
53	2.4	17.19	13.42	8.39	3.64
54	2.0	14.41	10.8	6.53	2.16
55	4.5	8.77	4.48	6.46	3.74
56	3.0	10.46	9.29	4.63	1.19
58	5.2	8.06	7.82	5.89	1.99
59	3.8	11.32	10.86	6.7	3.46
60	2.5	7.8	7.57	5.14	1.81
61	2.1	13.47	11.91	8.63	4.19
62	4.0	13.92	13.55	9.42	4.47
63	2.0	16.68	11.63	6.57	1.94
70	3.2	22.54	21.98	15.84	6.9

### 3. Results and Discussion

Ilgın and its vicinity are located in a first-degree earthquake zone; are at the intersection of the Argıthani, Mecidiye, and Cavuscu faults; are on the southeastern section of the active Sultandagi fault; and experience seismic movements in the range of  $5.5 \leq M \leq 6.5$ . Earthquakes that hit Sultandagi and Cay towns, which are 75 km to the northwest of the centre of Ilgın, between 2000-2003 were measured in the range of 6-6.2, based on Local Magnitude. They caused significant damage and deaths in the region.

However, it is well-known that seismic energy on the northeast section of the fault (i.e., Ilgın and its surroundings) has not yet been discharged (Kocıyigit et al., 2002). Studies indicate that there is a seismic gap around the Argıthani fault (Demirtas and Yilmaz, 1996). The extent of the damage to structures is moderate, and damage was observed in the centre of Ilgın due to the effects of the recent

earthquakes in Sultandagi and Cay towns. These data indicate that any future earthquake hitting the Ilgın epicentre or its proximity will cause considerable damage to structures, and the degree of damage largely depends on the settlements and ground liquefaction. Any earthquake of  $6.0 \leq M \leq 6.5$  would inevitably lead to fatal damage.

Pre-Quaternary rocky units and Quaternary-aged and loose deposits are present in the residential areas of Ilgın. There is a potential for liquefaction and settlement of the Quaternary units due to seismic effects. Quaternary-aged and loose precipitations not only have the potential for liquefaction but also the potential for settlement due to seismic effects. Ozdemir and Ince (2005) showed that the Ilgın soils have medium to high liquefaction potentials (i.e., 70-80%).

In general, the groundwater flows from the southwest to the northeast. The groundwater level depth is between 1.5 m to 6 m in most

sections except for Hamam Sirti and Sivri Tepe; however, in several sections the water level is as high as 2-4 m. Groundwater levels near the surface contribute to the risk of liquefaction and oversettlement of the ground (dependent on the degree of liquefaction).

Statistical analysis of the settlement potential for a ground thickness of 10 m under the seismic movement caused by an earthquake (6 on the Local Magnitude), examined using the results of the SPT test (Table 3), shows that the maximum settlement is 2 m. Settlement varies from 0-22.5 cm for different depths, with an average settlement of 10.3 cm. At a depth of 4 m, settlement ranges from 0-22 cm, with an average settlement of 9 cm. However, the standard deviations of settlements are large and reflect the complexity of the ground.

**Table 3.** Statistical analysis of the calculated settlements

	Settlement-induced earthquake (cm)			
	Depth = 2 m	Depth = 4 m	Depth = 6 m	Depth = 8 m
Maximum	22.54	21.98	15.84	6.9
Minimum	0.31	0.19	0	0
Mean	10.32	8.79	5.75	2.54
Standard Deviation	11.13	10.98	8.02	3.49

Settlements larger than 20 cm are found at borehole 70 to the north of Ilgin, near the region of the Ilgin Lake, and settlements between 15 cm and 20 cm are observed in the western, northern, and central sections of Ilgin (Figure 5); settlements are to the lower south of Ilgin. When settlements were evaluated in conjunction with the geological map, the maximum settlement is observed around the borehole number 70; settlements between 15 cm and 20 cm are found in the sandy alluvium area (Qs). South of Ilgin, where the potential for settlement is relatively low, gravel and clayish alluvium are found together with sandy alluvium. Sandy alluvium is between gravel and clayish alluvium, indicating that sandy alluvium is largely comprised of clay and gravel. In this particular section, the lower settlement is partially due to deeper groundwater levels than those found in other sections. When the geological, hydrogeological, and settlement maps are combined, it is clear that the groundwater level is in close proximity to the surface, and in sections containing sandy alluvium, intense settlements can follow an earthquake. The map showing the settlement potential indicates numerous areas with settlements in the range of 10-15 cm.

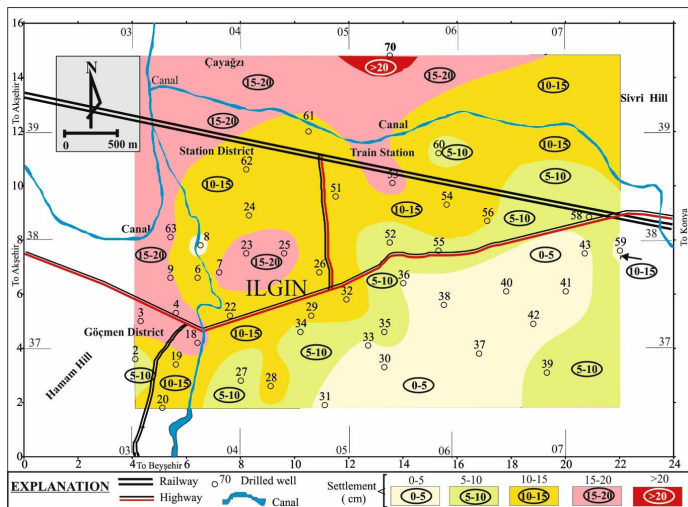


**Figure 8.** A map showing the settlement potential due to seismic effects in the residential area of Ilgin

The indications on the ground due to the settlement effect and their relation with the expected damage to the structures are presented in Table 4 (Ishihara and Yoshimine, 1992).

**Table 4.** Relation between settlement and degree of damage (Ishihara and Yoshimine, 1992)

Degree of Damage	Settlement in cm	Indications on the ground
Light–none	0-10	Small cracks
Medium	10-30	Small cracks, penetration of the sand
More	>30	Large cracks, sand gush, lateral movement

In general, the settlements due to seismic effects near Ilgin are between 10-20 cm. Small cracks and sand penetration to the surface of the earth can also be expected in conjunction with the medium-degree damage to structures.

It should be noted that the structures in Ilgin and the vicinity are in the form of heaps, and the major structural materials are adobe and briquettes. A few of these structures have had engineering services provided because their seismic resistance is quite low. Even an earthquake on the order of  $5 \leq M \leq 5.5$  in the region could cause substantial damage and a large loss of life due to the poor materials used in the structures.

The maximum allowable settlement for structures made of adobe and briquette is 8-10 cm (Whals, 1981). Settlements exceeding 10 cm were predicted in sections of Ilgin and the vicinity, indicating that settlements due to seismic effects have the potential to exceed the permissible threshold values for structures in the area. The settlements in the northern section of the Istasyon quarter of Ilgin (15 cm - 22.54 cm) exceed the maximum permissible limit for structural reinforced concrete (15.2 cm).

During the 2000 and 2003 earthquakes in Sultandagi and Afyon, respectively, cracks in Ilgin structures became visible, depending on the amount of the settlement. However, no systematical data were recorded for these settlements. Seismic activity above  $ML=6$  within 75 km of the centre of Ilgin would likely increase damage to a large extent due to settlement. To avoid damage, studies focused on earthquake damage minimisation should be conducted. In addition, recommendations of the best available planning/designing activities should be made and implemented for residential areas to avoid ground liquefaction and damage arising from settlement caused by earthquakes.

#### 4. Conclusion

The following conclusions are made based on the outcome of this research. (1) The expected settlements of the residential areas in Ilgin, which bear medium and high degrees of liquefaction potential, were determined to exceed the allowable settlement limits of the structures. (2) Settlements of 5 cm were observed to the south of Ilgin, while in the northern and north-eastern areas, the settlement amounts reached 15-20 cm. (3) North of the selected area, at the sections near the region of the Lake of Ilgin, the settlements were observed to be 23 cm. (4) The structures in the region are not earthquake-resistant structures. (5) Any earthquake measuring 6-6.5 on the Richter scale that hits the Ilgin district and is regarded as a seismic gap poses substantial risk for damage and deaths.

#### 5. References

- Andrus, D.A., Piratheepant, P., Ellis, B.S., Zhang, J., Juang, C.H., 2004. Comparing liquefaction evaluation methods using penetration-Vs relationships. *Soil Dynamics and Earthquake Engineering*, 24(9-10), 713-721.
- Aydinoglu, M.N., 1998. Afet Bolgelerinde Yapilacak Yapilar Hakkinda Yonetmelik. Ministry of Public Works and Settlement, The Republic of Turkey (in Turkish).
- Bardet, J.P., Kapuskar, M., 1993. Liquefaction sand boils in San Francisco during 1989 Loma Prieta earthquake. *Journal of Geotechnical Engineering*, ASCE, 119(3), 543-562.

- Barka, A., Reilinger, R., Saroglu, F., Sengor, A.M.C., 1995. The Isparta Angle: Its importance in the neotectonics of the Eastern Mediterranean Region: Proceedings of the International Earth Sciences Colloquium on the Aegean Region, 1, 3-18.
- Bartlett, S.F., Youd, T.L., 1995. Empirical predictions of liquefaction-induced lateral spread. *Journal of Geotechnical Engineering*, 121(4), 316-329.
- Boray, A., Saroglu, F., Emre, O., 1985. Isparta buklumunun kuzey kesiminde Dogu-Bati daralma icin bazi veriler. *Geological Engineering*, 23, 9-20 (in Turkish). <http://journals.tubitak.gov.tr/earth/issues/yer-03-12-1/yer-12-1-5-0301-4.pdf>
- Canik, B., 1981. Ilgin sicak su kaynaklarinin hidrojeoloji incelemesi. *Bulleten of Science Faculty of Selcuk University*, 1, 1-18 (in Turkish).
- Cetin, K.O., Youd, T.L., Seed, R.B., Bray, J.D., Sancio, R., Lettis, W., Yilmaz, M.T., Durgunoglu, H.T., 2002. Liquefaction-induced ground deformations at Hotel Sapanca during Kocaeli (Izmit), Turkey earthquake. *Soil Dynamics and Earthquake Engineering*, 22, 1083-1092.
- Clough, G.W., Martin, J.R., Chameau, J.L., 1994. The geotechnical aspects: Practical Lessons from the Loma Prieta Earthquake. National Research Council, National Academy Press, Washington D.C., pp. 29-63.
- Darendeli, M.B., Stokoe, K.H., 2001. Development of a new family of normalized modulus reduction and material damping curves: University of Texas, Geotechnical Engineering Report GD01-1.
- Demirtas, R., Yilmaz, R., 1996. Seismotectonics of Turkey: Preliminary approach to earthquake forecasting based on long-term variations in seismic activity and present seismicity. Republic of Turkey, Ministry of Public Works, General Directorate of Disaster Affairs, Earthquake Research Department, June 1996, 95p.
- Hamada, M., Wakamatsu, K., Ando, T., 1996. Liquefaction induced ground deformation and its caused damage during the 1995 Hyogoken-Nambu Earthquake: Proc. 6th Japan-U.S. Workshop on Earthquake resistant Design of Lifeline Facilities and Countermeasures Against Soil Liquefaction. In: Hamada M., O'Rourke T.D. (Eds.), Tech. Rep. NCEER-96-0012, September 11, 137-152, Utah.
- Holzer, T.L., 1998. Map showing Locations of ground-Failure and damage to Facilities on Treasure Island Attributed to the 1989 Loma Prieta Earthquake: The Loma Prieta California Earthquake of October 17 1989-Liquefaction, U.S. Geological Survey Profesional Paper 1551-B, U.S. Gov. Printing office, Washington, D.C., B1-B8.
- Ishihara, K., Yoshimine, M., 1992. Evaluation of settlements in sand deposits following liquefaction during earthquakes. *Soils and Foundations* 32(1), 173-188.
- Kayabali, K., 1997. The role of soil behavior on damage caused by the Dinar Earthquake (southwestern Turkey) of October 1, 1995. *Environmental and Engineering Geosciences*, 3(1), 111-121.
- Kayabali, K., Beyaz, T., 2011. Strong motion attenuation relationship for Turkey-a different perspective. *Bulletin of the Engineering Geology and Environment*, 70, 467-481.
- Kimura, M., 1996. Damage statistics. *Soils and Foundations: Special ISSUE on Geotechnical Aspects of the January 17, 1995, Hyogoken-Nambu Earthquake*. Japanese Geotechnical Society, 1-6.
- Kocyigit, A., Bozkurt, E., Kaymakci, N., Saroglu, F., 2002. 3 Şubat 2002 Cay (Afyon) depreminin kaynagi ve agir hasarin nedenleri: Aksehir fay Zonu (Jeolojik on rapor): ODTU Jeoloji Muhendisligi Bolumu Tektonik Arastirma Birimi, 17s. Ankara (in Turkish). <http://www.metu.edu.tr/~akoc/Afyon.pdf>
- Kocyigit, A., Unay E., Sarac, G., 2000. Episodic graben formation and extensional neotectonic regime in west Central Anatolia and Isparta Angle: a case study in the Aksehir-Afyon Graben, Turkey. In: Bozkurt, E., Winchester, J.A., Piper, J.D.A. (Eds.), *Tectonics and Magmatism in Turkey and the surrounding Area*, Geological Society London, Special Publications, 173, 405-421.
- Liao, S.S.C., Whitman, R.V., 1986. Catalogue of liquefaction and non-liquefaction occurrences during earthquakes: Res. Rep., Dept. of Civ. Engrg., Massachusetts Institute of Technology, Cambridge, Mass.
- Liu, A.H., Stewart J.P., Abrahamson N.A., Moriwaki, Y., 2001. Equivalent number of uniform stress cycles for soil liquefaction analysis. *J. Geotech. & Geoenv. Engrg.*, ASCE, 127(12), 1017-1026.
- MERCAN-SU, 2000. Konya Ili Ilgin Ilcesi ilce merkezi ve yakin dolayinin jeolojik etut raporu. Municipality of Ilgin Town, Turkey, 66p. (in Turkish).
- Mollamahmutoglu, M., Kayabali, K., Beyaz, T., Kolay, E., 2003. Liquefaction related building damage in Adapazari during the Turkey earthquake of August 17, 1999. *Engineering Geology*, 67, 297-307.
- NCEER, 1997. Proceedings of the NCEER Workshop on evaluation of Liquefaction Resistance of Soils: Edited by Youd, T.L., Idriss, I.M., Technical No. NCEER-97-0022, December 31, 1997.
- O'Rourke, T.D., Pease, J.W., 1992. Large ground deformations and their effects on lifeline facilities: 1989 Loma Prieta earthquake, Case study of Liquefaction and Lifeline Performance During Past Earthquakes, Volume 2: United States case Studies, Tech. Rep., NCEER-92-0002, O'Rourke, T.D., Hamada, M. (eds.), February 17, 85p.
- Ozdemir, A., Ince, I., 2005. Geology seismotectonics and soil liquefaction susceptibility of Ilgin (west-central part of Turkey) residential area. *Engineering Geol.*, 77, 169-188.
- Pyke R., Seed H.B., Chan C.K., 1975. Settlement of sands under multidirectional shaking. *J. Geotech. Engrg.*, ASCE, 101(4), 379-398.
- Robertson, P.K., Fear, C.E., 1996. Soil liquefaction and its evaluation based on SPT and CPT: Draft of paper presented at the NCEER Workshop on Evaluation of Liquefaction Resistance, Salt Lake City, Utah, January 4-5.
- Robertson, P.K., 1994. Design considerations for liquefaction: Proc., 13th int. Conf. Soil Mech. Found. Engrg., 5, 185-188, New Delhi, India.
- Saroglu, F., Emre, O., Boray A., 1987. Turkiyenin diri faylari ve deprenselligi: Mineral Research and Exploration Institute of Turkey, Report No: 8174, 394p. (In Turkish).
- Seed, H.B., Idriss, I.M., 1971. Simplified procedure for evaluating soil liquefaction potential. *Journal of the Soil Mechanics and Foundations Division*, ASCE 97 (SM 9), 1249-1273.
- Seed, H.B., Tokimatsu, K., Harder, L.F., Chung, R.M., 1985. The Influence of SPT procedures in soil liquefaction resistance evaluations. *J. Geotech. Eng.*, 111(12), 1425-1445.
- Seed, H.B., 1979. Soil liquefaction and cyclic mobility evaluation for level ground during earthquakes. *J. Geotech. Engrg. Div.*, ASCE 105(2), 201-255.
- Seed, R.B., Cetin, K.O., Moss, R.E.S., Kammerer, A.M., Wu, J., Pestana, J.M., Riemer, M.F., 2001. Recent advances in soil liquefaction engineering and seismic site response evaluation. Proc. 4th Int. Conf. on Recent Advances in Geotech. Eqk. Engrg. Soil Dyn., Paper No. SPL-2.
- Shamoto, Y., Zhang, J., Tokimatsu, K., 1998. New charts for predicting large residual post-liquefaction ground deformations. *Soil Dyn Earthquake Engrg.* 17: 427-438.
- Stewart, J.P., Bray, J.D., McMahon, D.J., Smith, P.M., Kropp, A.L., 2001. Seismic performance of hillside fills. *J. Geotech. & Geoenv. Eng.*, 127(11), 905-919.
- Stewart, J.P., Smith, P.M., Whang, D.H., Bray, J.D., 2002. Documentation and analysis of field case histories of seismic compression during the 1994 Northridge, California earthquake: Report No. PEER-2002/09, Pacific Earthquake Engineering Research Center, U.C. Berkeley, October.

- Stewart, J.P., Whang, D.H., 2003. Simplified procedure to estimate ground settlement from seismic compression in compacted soils: Proc. Of the 2003 Pacific conference on Earthquake Engineering, New Zealand Society for Earthquake Engrg., Paper No. 046.
- Tatsuoka, F., Sasaki, T., Yamada, S., 1984. Settlement in saturated sand induced by cyclic undrained simple shear. Proc. 8th World Conf. Earthquake Engineering, San Francisco, CA, 95-102.
- Tokimatsu, K., Seed, H.B., 1987. Evaluation of settlements in sands due to earthquake shaking. Journal of ASCE, 113(8), 861-878.
- Ulusay, R., Aydan, O., Kumsar, H., Sonmez, H., 2000. Engineering geological characteristic of the 1998 Adana Ceyhan Earthquake with particular emphasis on liquefaction phenomena and the role of soil behaviour. Bulletin of Engineering Geology and the Environment, 59(2), 99-118.
- Whals, H.E., 1981. Tolerable settlement of buildings. Journal of the Geotechnical Engineering Division, ASCE, 107(11), 1489-1504.
- Yoshimine, M., Nishizaki, H., Amano, K., Hosono, Y., 2006. Flow deformation of liquefied sand under constant shear load and its application to analysis of flow slide of infinite slope. Soil Dynamics and Earthquake Engineering, 26(2-4), 253-264.
- Zhang, G., Robertson, P.K., Brachman, R.W.I., 2002. Estimating liquefaction-induced ground settlements from CPT for level ground. Canadian Geotechnical Journal, 39, 1168-1180.
- Zhang, G., Robertson, P.K., ASCE, M., Brachman, R.W.I., 2004. Estimating Liquefaction-Induced Lateral Displacements Using the Standard Penetration Test or Cone Penetration Test. Journal of Geotechnical and Geoenvironmental Engineering, 130(8), 861-871.





## An algorithm for generation of DEMs from contour lines considering geomorphic features

Xiao-Ping Rui<sup>1</sup>, Xue-Tao Yu<sup>2,3</sup>, Jin Lu<sup>4</sup>, Muhammad Aqeel Ashraf<sup>5</sup>, Xian-Feng Song<sup>1\*</sup>

<sup>1</sup>College of Resources and Environment, University of Chinese Academy of Sciences, Beijing 100049, China;

<sup>2</sup>School of Traffic and Transportation, Shijiazhuang Tiedao University, Shijiazhuang 050043, China;

<sup>3</sup>Traffic Safety and Control Lab in Hebei Province, Shijiazhuang 050043, China;

<sup>4</sup>China Institute of Water Resources and Hydropower Research, Beijing 100038, China;

<sup>5</sup>Faculty of Science and Natural Resources, University Malaysia Sabah 88400 Kota Kinabalu, Sabah, Malaysia;

\* Corresponding author, email: song7537338@163.com

### ABSTRACT

Geomorphic information is omitted from many existing methods of generating gridded digital elevation models (DEMs) from contour lines, resulting in significant errors during interpolation. Here, we present an advanced schema for improvement of the comprehensive regionalized method of linear interpolation. This approach uses a moving fitting method for an interpolated point and selects elevation points that are representative of geomorphic features as a whole to improve interpolation quality. A total of 16 points are selected, according to certain criteria, in eight directions surrounding the interpolated point; thus, there are two points in each direction, which is sufficient to provide an accurate representation of the geomorphic features of the DEM. Our method introduces virtual control points to prevent sudden changes in the interpolation results, which helps to overcome problems related to the distortion of the local geospatial distribution in areas where feature geomorphic information is inadequate. We construct the spline interpolation function using intersection points and virtual control points, all of which are applied to compute the point elevation. Moreover, we index all elevation values and spatial points of linear features using the R-tree method to ensure that points related to an interpolated position can be retrieved as quickly as possible. Finally, we test our method using a coal mine elevation dataset. The results confirm that our proposed method can generate DEMs smoothly and, in particular, avoid problems related to local distortion.

*Keywords: Digital Elevation Models (DEM), interpolation points, contour lines map, geomorphic features.*

### Algoritmo para la generación de Modelos Digitales de Elevación considerando líneas de contorno y características geomórficas

### RESUMEN

La información geomórfica se omite en muchos de los métodos de generación de Modelos Digitales de Elevación (DEM, en inglés) que se elaboran a partir de líneas de contorno, lo que resulta en errores significativos durante la interpolación. En este trabajo se presenta un esquema avanzado para el mejoramiento del método comprensivo regionalizado de interpolación lineal. Esta aproximación utiliza un método de ajuste móvil para un punto interpolado y selecciona puntos de elevación representativos o características geomórficas como un todo para mejorar la calidad de la interpolación. Se seleccionaron 16 puntos de acuerdo con ciertos criterios, en ocho direcciones alrededor del punto interpolado; por lo tanto, hay dos puntos en cada dirección, lo que es suficiente para proveer una representación precisa de las características geomórficas del DEM. El método propuesto consta de puntos virtuales de control para prevenir cambios repentinos en los resultados de la interpolación, lo que ayuda a vencer los problemas relacionados a la distorsión de la distribución geoespacial local en áreas donde la información de las características geomórficas es inadecuada. Se utilizó una función de interpolación spline con puntos de intersección y puntos de control virtual, que fueron utilizados para calcular el punto de elevación. Además, se indexaron todos los valores de elevación y los puntos espaciales de las características lineales con el método de árbol-R para asegurar que los puntos relacionados a una posición interpolada pueden ser recuperados tan rápido como sea posible. Finalmente, el método fue evaluado con la configuración de elevación de una mina de carbón. Los resultados confirman que el método propuesto puede generar modelos sin problemas y, en particular, evitar complicaciones relacionadas a distorsión local.

*Palabras clave: Modelos de Evaluación Digital, puntos de interpolación, mapas lineales de contorno, características geomórficas.*

*Record*

Manuscript received: 25/01/2016

Accepted for publication: 15/07/2016

*How to cite item*

Rui, X. P., Yu, X. T., Lu, J., Ashraf, M. A., & Song, X. F. (2016). An algorithm for generation of DEMs from contour lines considering geomorphic features. *Earth Sciences Research Journal*, 20(2), G1-G9.

doi:<http://dx.doi.org/10.15446/esrj.v20n2.55348>

## 1. Introduction

Digital elevation models (DEMs) are imperative in the field of geosciences and have been used widely in the generation and display of three-dimensional terrain. For example, DEMs have been applied to investigate slope and aspect, construct terrain profiles between selected points, and delineate other significant surface features (Kweon and Kanade, 1994; Zhou and Liu, 2004; Zhou and Chen, 2011; Hickey et al., 1994; Jones, 1998; Oky et al., 2002). Many methods have been proposed to generate DEM data, including photogrammetry techniques, radar interferometry, laser altimetry, and interpolation (Wood and Fisher, 1993; Wood, 1994; Hearnshaw and Unwin, 1994). Although elevation mapping technology now allows production of DEMs directly from measured points, accurate interpolation from contours is still important in areas where high-resolution DEMs are not available (Taud et al., 1999; Werbrouck et al., 2011) or in cases where historical contour maps are used to evaluate topographic change (Carley et al., 2012). For the generation of regional or continental DEMs, interpolation methods using fine scale contours are useful owing to their low cost and the relative ease of obtaining contour maps in this way (Doytsher and Hall, 1997; Heritage et al., 2009; Wise, 2011).

Accordingly, various interpolation algorithms have been developed to generate DEMs from contours. The contours, which are in vector or raster format, consist of a large number of elevation points. Moreover, the shape of (and geometric relationships between) the contours can be indicative of certain geomorphic features. To determine the elevation at a given point, interpolation algorithms often adopt a sampling strategy that selects representative elevation points from contours in order to reduce computation time, subsequently conducting interpolation using functions such as the inverse distance weight function or surface spline function (Huang et al., 2011; Maekawa et al., 2007; Gofuku et al., 2009). Here, we describe several of the most popular interpolation algorithms.

The weighted moving average technique interpolates by making use of the geometric relationships between adjacent contour lines (Watson, 1992). For a given grid, the elevation at each cell is computed as follows. First, geometrical rays are drawn from the cell center following both cardinal and intermediate directions. Then, eight corresponding intersection points between those rays and their closest adjacent contour lines are identified, and the elevation value  $F(n)$  is computed from these intersection points using the inverse distance weight method (Figure 1) based on these eight crossing points (C1, C2... C8). However, this approach cannot reflect the topography of mountaintops and depressions with sufficient resolution for most purposes (Figure 2) (Rvachev et al., 2001; Dinis et al., 2007; Watson, 1999).

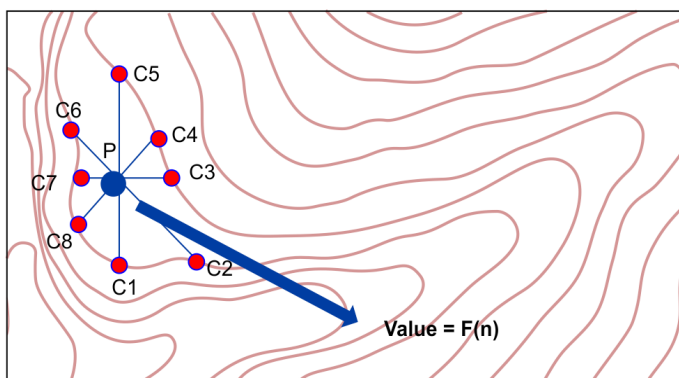


**Figure 1.** Weighted moving average technique. C1, C2, and so on are intersection points in eight directions; P is an interpolated grid point.  $F(n)$  is elevation computation function of point P.

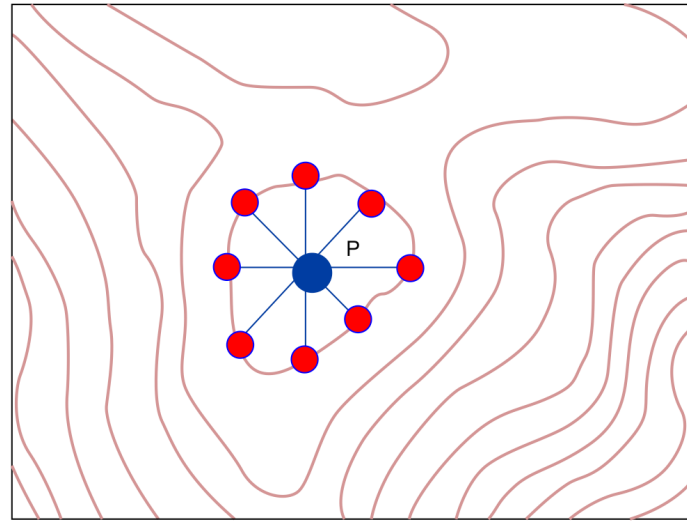


**Figure 2.** An example to illustrate the drawbacks of the weighted moving average technique: it is hard to determine whether P is in a valley or on top of a hill.

Taud et al. (1999) developed a raster-based interpolation method to generate digital elevation models through the dilation of contour lines stored in a raster grid. This method uses an iterative procedure to produce an extension of contour lines by applying alternate four- and eight-connected erosions of the background until the generated surfaces become contiguous. This process stops when no new contour lines can be generated. The contour line dilation algorithm can prevent any crossing, especially when the isoline contours are adjacent. This method is simple to apply and has a low computational cost (Oky et al., 2002; Gousie and Franklin, 2003). However, it is clear that, when the contour line is closed, the interpolated data in the inner exhibits the same elevation value as the closed contour line, which may result in error.

To insert the height of steep slope areas, Xie et al. (2003) developed a special kernel filter that can interpolate a grid cell through which multiple contour lines pass. The contour lines are first rasterized as a grid. Then, three cell types are defined concerning the relationships between contours and cells: no-value (NVC), single-value (SVC), and multi-value (MVC) cells, which indicate no contour lines, a single contour line, or multiple contour lines passing through the cell, respectively. The elevations of MVCs are computed using an MVC filter, whereas those of SVCs are directly assigned based on the appropriate contour elevation. The value of a given NVC is interpolated from its neighboring SVCs or MVCs in both the cardinal and intermediate directions. Wang et al. (2005) further improved the interpolation of the elevation of SVCs by considering the spatial relationship between SVC-associated contours and their neighboring contours. In this modified method, a triangulated irregular network is constructed using two adjacent contours; then, the triangle within which the SVC center falls is identified and its three vertices used to interpolate the elevation of the SVC.

Clarke et al. (1982) evaluated three interpolation methods: linear interpolation with four data points found in the grid axis directions (LIXY), linear interpolation between two data points found in the approximate direction of steepest slope (LISS), and cubic interpolation using four data points found in the approximate direction of steepest slope (CISS). Their results indicated that DEMs generated using methods that consider terrain features such as break lines, ridges, and spot heights are more accurate than those generated using methods that do not take such features into account. However, the methods introduced by Clarke et al. (1982) use only a few points to infer geomorphic trends; thus, they are successful in improving the quality of DEMs but are incapable of delineating specific patterns.

Skeleton lines (i.e., ridge and drainage lines) are essential for the description of terrain surfaces. Aumann et al. (1991) developed two methods to achieve automatic derivation of skeleton lines from digitized contours but were unable to apply their results to generate DEMs from contours. Conversely, a hydrologically correct grid of elevation can be produced using Hutchinson's algorithm, which takes into account information inherent to the contours and uses them to build a generalized drainage model. Then, this information can be applied to form constraints for the interpolation process to ensure that the output DEM displays appropriate hydrogeomorphic properties (Hutchinson 1988, 1996, 2008). Using this method, a network of streams and ridges can be built by identifying areas of local maximum curvature in each contour and, thus, the field of steepest slope. The interpolation procedure uses a discretized thin plate spline technique, where the roughness penalty has been modified to allow the fitted DEM to follow abrupt changes in terrain (e.g., streams and ridges). The method uses a maximum of 50 data points from these contours within each cell, which improves computational efficiency. This algorithm has a well-known implementation of TOPOGRID in ArcGIS, and the drainage conditions imposed by the algorithm produce higher accuracy surfaces with fewer input data (Peralvo and Maident, 2008; Binh and Thuy, 2008).

To enable interpolation in the regions surrounding mountaintops or depressions, Yu and Tan (2002) proposed a regionalized comprehensive interpolation method to produce DEMs using contour lines. Based on an interpolated point, geometrical rays in the horizontal and vertical directions are used to intersect with two neighboring contour lines, thus producing a total of eight intersection points in four directions (Figure 3). These intersection points are then used to calculate the point elevation using a surface spline function (Yu, 2001). This system represents a considerable advantage over the above methods, in that the method of Yu and Tan (2002) can predict the elevations of mountaintops or depressions using splines because the sample points along each ray direction have different height values. However, points obtained from only four fixed cardinal directions may not be representative; that is, the points on contour lines that are close to the interpolated cell may not be selected, but the points obtained from the intersection points between contour lines and rays that are far from the interpolated cell are selected (Figure 4). Thus, this method often leads to serious errors, particularly in narrow ridge or valley areas with steep slopes or cliffs.

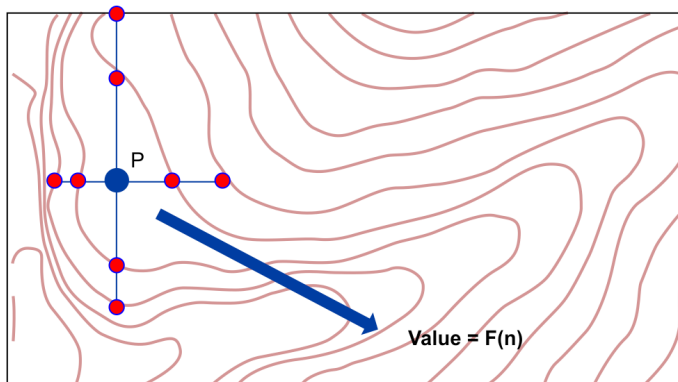


**Figure 3.** Regional interpolation. Red dots indicate eight intersection points from four directions; blue dot represents P;  $F(n)$  represents the elevation computation function of point P.

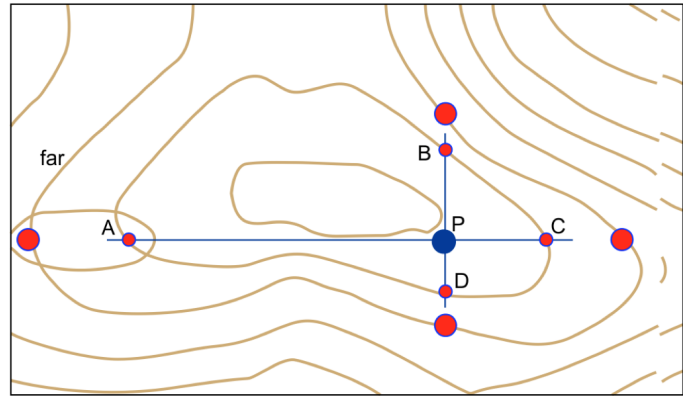


**Figure 4.** An example to illustrate the drawbacks of regional interpolation. Red dots represent eight virtual control points from four directions. The blue dot represents P. The intersection point A is far from the interpolated point P and the information on the adjacent contour line is not used.

The quality of the derived DEM depends greatly on the data source and interpolation technique used (Heritage et al., 2009; Bouillon et al., 2006; Wise, 2011, 2012). Vieux (1993) was the first to suggest that the Shannon–Weaver information statistic, often referred to as entropy, might offer potential as a measure of some characteristics of DEM error. Li (1994) and Carrara et al. (1997) evaluated the quality of DEM results derived from digital contour lines using different algorithms. However, their analysis evaluated errors primarily through comparison with the contour interval (CI), and they did not discuss the causes of errors introduced through the use of various algorithms.

In summary, it is clear that DEMs generated using methods that consider terrain features such as break lines, ridges, and spot heights are better than DEMs produced using methods that do not take such features into account. Moreover, of the methods that do consider all available geomorphic information, many are still unable to process cells in the region of mountaintops or depressions, which are often enclosed by only one contour line (Xiao and Liu, 2012; Xie et al., 2003). Although Hutchinson's algorithm works well in most cases, it may also introduce some errors in regions of complex geomorphology.

However, geomorphic information is included within existing contour maps, and information relating to mountaintops and depressions can be achieved by studying the contour lines of these maps. Using this information when interpolating gridded DEM data from contour lines can preserve the precision of the results (Bonin and Rousseaux, 2005). Therefore, this paper introduces a grid-based DEM interpolation method that considers the geomorphic information hidden in contour maps to avoid the interpolation error that typically occurs in traditional methods. It was achieved by adopting the positive aspects of both the weighted moving average technique and the comprehensive regionalized method. This approach utilizes eight-directional ray sampling method to obtain necessary geomorphic information from a contour map. For areas such as mountaintops, depressions, boundaries, or corners, some virtual control points to control the precision of interpolation were added. Then, the obtained results were compared with those obtained using the comprehensive regionalized method of Yu and Tan (2002) and associated ArcGIS functions.

$$W(x, y) = a_0 + a_1x + a_2y + \sum_{i=1}^n F_i r_i^2 \ln(r_i^2 + \epsilon) \quad (1)$$

## 2. An interpolation method considering geomorphic information

### 2.1. Basic premise

The fundamental step in this process is finding the contour line nearest to an interpolated point P and obtaining a perpendicular foot B from point P to this

contour line. Then, using P–B as the base direction, eight-half lines are drawn at intervals of 45° to produce rays in eight directions. These half lines intersect with two adjacent contour lines around P, resulting in a maximum of 16 intersection points denoted by P1, P2, P3, and so on. If the number of sample points,  $n$ , is less than 16, the results will reflect the geomorphic features of the terrain adequately. Conversely, if  $n > 16$ , the efficiency of the method will be impacted negatively. Figure 5 presents an example in which 16 intersection points are obtained for the interpolated P. We use a spline function to construct an interpolation function, as described by Curry and Schoenberg (1996) and Yu (2001):

where  $x$  and  $y$  are coordinates,  $w(x,y)$  is the elevation value of interpolated point P, and  $a_0, a_1, a_2$ , and  $F_i$  ( $i = 1, 2, \dots, n$ ) are undetermined coefficients, of which there are  $N + 3$  in total.  $r_i^2 = (x-x_i)^2 + (y-y_i)^2$  and  $\epsilon$  are empirical parameters that allow for the adjustment of surface curvature. For large (small) changes in the surface shape,  $\epsilon$  should be small (large); values of  $\epsilon$  range from  $10^{-2}$  to 1 for flat surfaces and  $10^{-6}$  to  $10^{-5}$  for singularity surfaces.

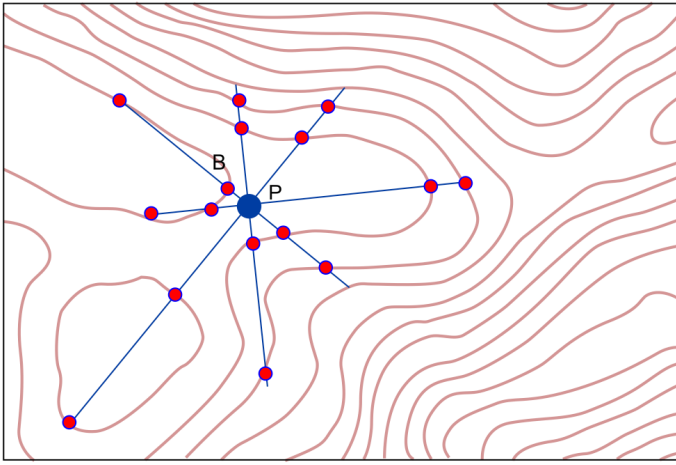


**Figure 5.** Using eight directions to obtain intersection points. Red dots indicate 16 intersection points from eight directions; blue dot represents P.

The  $N + 3$  unknowns are determined according to Equation 2.

$$\begin{cases} W_j = a_0 + a_1x_j + a_2y_j + \sum_{i=1}^n F_i r_{ij}^2 \ln(r_{ij}^2 + \epsilon) + c_j F_j \\ [j = 1, 2, \dots, n; r_{ij}^2 = (x_i - x_j)^2 + (y_i - y_j)^2] \\ \sum_{i=1}^n F_i = 0 \\ \sum_{i=1}^n x_i F_i = 0 \\ \sum_{i=1}^n y_i F_i = 0 \end{cases} \quad (2)$$

The coefficient  $c_j$ , which is in units of length squared, is equal to  $16\pi D/K_j$ , where  $D$  is the plate rigidity and  $K_j$  the spring constant associated with the  $j^{\text{th}}$  point. During interpolation,  $K_j = \infty$  and  $c_j = 0$ .

## 2.2. Introduction of virtual control points

To ensure that the interpolated results can be constrained by the values of the contour lines, virtual control points were added to control the precision of interpolation. It was designated  $E_n$  as the value of a point on the contour line near P and  $E_{ci}$  as the contour interval. From the features of the contour map, it is clear that, if P is located between two contour lines,

$w(x,y)$  should lie between the values of these two contour lines. Similarly, if P is within a closed contour line,  $w(x,y)$  should be less than  $E_n + E_{ci}$  or larger than  $E_n - E_{ci}$ . If not, then this may lead to wrong results. Therefore, to prevent sudden changes from occurring in complex areas, we add a virtual control point V for the four intersection points. Then, our algorithm calculates the elevation value at point V based on the heights of the four surrounding points, according to the following rules.

The elevation of V is  $Z_V$ , which is calculated according to Equation 3.

$$z_V = E_n + E_{ci} * \delta \quad \text{or} \quad z_V = E_n - E_{ci} * \delta \quad (3)$$

where  $\delta$  is a coefficient between 0 and 1 and is used to control the elevation of V. The adding and subtracting operations were used for DEMs covering mountaintops and depressions.

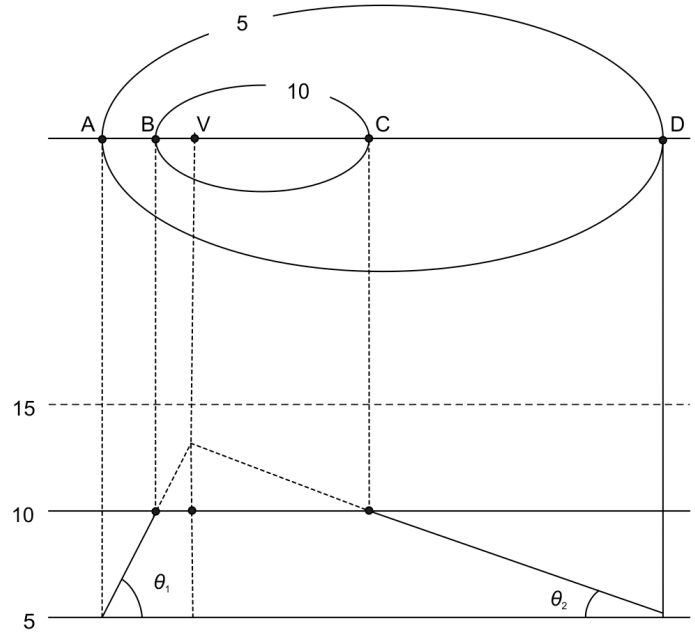


**Figure 6.** The procedure for adding a virtual control point. The top part of this figure illustrates two neighboring contour lines that indicate a mountaintop area; points A, B, C, and D are four intersection points on the contour line. The bottom of the figure illustrates the corresponding sections of lines AB and CD.

Figure 6 illustrates a typical example of the addition of a virtual control point in one direction for a case in which the interpolated point lies along an adjacent contour line. In this case, the elevation value of V should be larger than  $H_{BC}$  (where  $H_{BC}$  is the height of the contour line located using B and C) but lower than  $H_{BC} + \Delta h$  (where  $\Delta h$  is the interval of the contour lines).  $\theta_1$  and  $\theta_2$  denote the inclinations of lines AB and CD, respectively, and  $\delta$  can be set according to the geomorphic feature studied:

$$\delta = \frac{\min\{\sin(\theta_1), \sin(\theta_2)\}}{\max\{\sin(\theta_1), \sin(\theta_2)\}} \quad (4)$$

$\delta$  ranges from 0 to 1 and is equal to 1 when  $\theta_1 = \theta_2$ . Based on the features of the contour line map, it is clear that  $z_V$  should be less than  $H_{BC} + \Delta h$ ; however, when  $\delta = 1$ ,  $z_V$  will be equal to  $H_{BC} + \Delta h$ . To avoid  $z_V$  reaching this value, a small perturbation ( $\epsilon$ , equal to 0.01) is added to  $\delta$  such that  $\delta = 0.99$ . When  $\theta_1 \neq \theta_2$ ,  $\delta$  will be greater than 0 and less than 1 and Equation 3 can be rewritten as follows:

$$z_V = E_n \pm E_{ci} * \frac{\min\{\sin(\theta_1), \sin(\theta_2)\}}{\max\{\sin(\theta_1), \sin(\theta_2)\}} \quad (5)$$

Subsequently, the coordinates and elevation of the virtual control point can be determined. Here, E denotes the intersection of lines AB and CD, and its coordinates can be obtained by solving Equations 6 and 7.

$$\begin{cases} y = \frac{y_B - y_A}{x_B - x_A} x + \frac{x_B y_A - x_A y_B}{x_B - x_A} & \text{--- Line AB} \\ y = \frac{y_C - y_D}{x_C - x_D} x + \frac{x_C y_D - x_D y_C}{x_C - x_D} & \text{--- Line CD} \end{cases} \quad (6)$$

$$\begin{cases} x_V = x_E \\ y_V = y_E \end{cases} \quad (7)$$

Then, the value of  $\sin(\theta_i)$  can be obtained as follows.

$$\begin{cases} \tan(\theta_1) = \frac{y_B - y_A}{x_B - x_A} \\ \sin(\theta_1) = \frac{|\tan(\theta_1)|}{\sqrt{1 + \tan^2(\theta_1)}} = \frac{\tan(\theta_1)}{\sqrt{1 + \tan^2(\theta_1)}} \quad (\theta_1 \in [0, \frac{\pi}{2}]) \end{cases} \quad (8)$$

$\sin(\theta_2)$  can be calculated in a similar manner. Thus, when both  $\sin(\theta_1)$  and  $\sin(\theta_2)$  are known, the elevation of the virtual control point can be obtained from Equation 3.

As discussed above, rays in eight directions are used to query the intersections with the contour lines. However, two intersection points are not present in all directions, e.g., if the interpolated point is at a boundary or corner of the map. Therefore, geomorphic information is missing in such directions. Moreover, it is not necessary to add a virtual control point in cases where there are no intersection points in a particular direction because this virtual point may introduce obvious error. If there is only one intersection point in a particular direction, two intersection points are used on the symmetrical contour lines; this produces three crossing points in total, which is sufficient to determine whether a virtual control point is required based on the geomorphic trend inferred from the three points.

There are three possible situations in cases with three points (Figure 7).

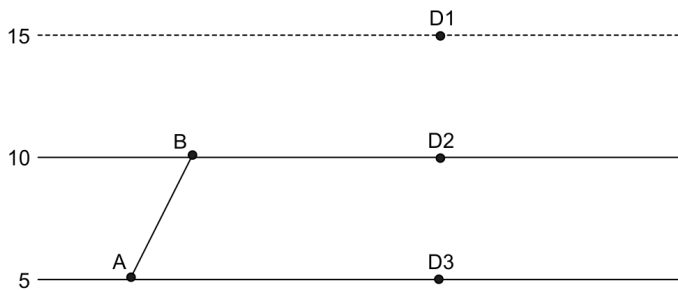


Figure 7. Three intersection points in one direction.

1) When the elevation of the intersection point is higher than that of either A or B (e.g., D1 in Figure 7), the geomorphic trend gets higher from A to D1, so the interpolated point is just between B and D1, and no virtual control point is required.

2) When the elevation of the intersection point is equal to that of A or B or lower than that of B (e.g., D2 in Figure 7), it can be assumed that the local maximum occurs at B (or in its vicinity) and that the elevation of the local maximum will never exceed  $HBC + \Delta h$ . A virtual control point must be added in such cases. For example, line AB could be extended to intersect the constraint contour (i.e., point C in Figure 8). Here, C acts to limit the elevation of the virtual control point. Then, the method described above can be applied to compute the coordinates and elevations of virtual points using the points A, B, C, and D.

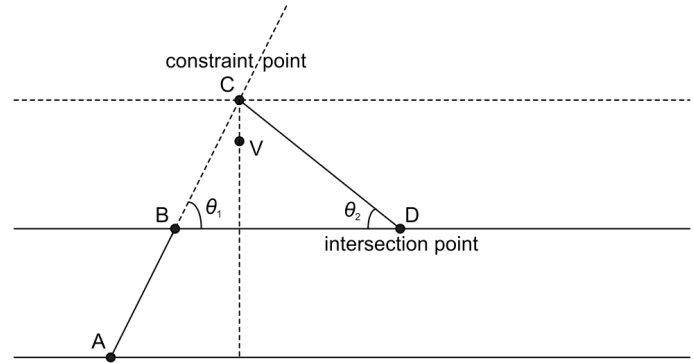


Figure 8. The procedure for adding a virtual control point for three intersection points.

3) When the height of the intersection is lower than that of B (e.g., D3 in Figure 7), it can be assumed that B represents the local maximum; in such cases, the geomorphic trend is clear, and no control point is required.

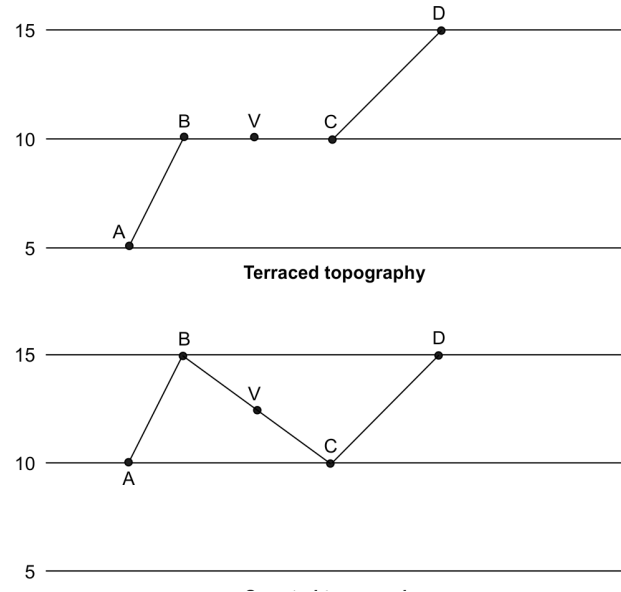


Figure 9. Other geomorphic features expressed in contour line maps.

In other cases, such as where the topography is terraced or serrated (Figure 9), the elevation and location of V reflect the average of the neighboring intersection points and the midpoint of line BC, respectively. The distances between all of the virtual control points were calculated adding and removing the control point if the distance is less than a threshold value. Then, all of the remaining distances between virtual control points are above the threshold value. Different threshold values were used to test the algorithm; according to the experimental results, the threshold value should be set to 2–3 times the interpolation accuracy. Finally, it was constructed the interpolation equation using all of the virtual control points and intersection points and calculate the value of point P based on the interpolation equation.

### 2.3. Algorithm workflow

Here, it was introduced an efficient algorithm that achieves the interpolation of DEMs from contour maps, as shown in Figure 10. The main steps in this algorithm workflow can be summarized as follows. First, the contour lines of the map were traversed and decomposed, before dividing them into line segments and saving them. This procedure allows obtaining the average length of the line segments. Then, the R-tree indexes for these line segments were built and stored the elevation in the R-tree (Huang, P. Lin and H. Lin, 2001; Corral

and Almendros-Jiménez, 2007; Zhu, Gong and Zhang, 2007). Finally, each interpolated point A was processed as follows. 1) The R-tree was used to query the closest line segment and point (i.e., B) to point A on the line segment. 2) A step K was set, whose value is equal to the average length of the line segments, and extend line AB in two directions at intervals of K. In this manner, it was assessed whether line AB intersects with the contour line, find the intersection points in both directions along line AB, and add a virtual control point if the interpolated position is on a closed contour line (Figure 11). 3) There were constructed eight lines at intervals of 45°, find

the associated intersection points, and add virtual control points where appropriate. 4) It was filtered the control points according to the distance between virtual control points based on a filtering rule, which states that the distances between the added virtual control points must be above a threshold value, i.e., 2–3 times the interpolation accuracy. 5) There were calculated the coefficients of the spline interpolation function, which are determined according to the control points, and calculated the interpolated point value based on the spline interpolation feature. (6) Finally, it was output the value of the interpolated point.

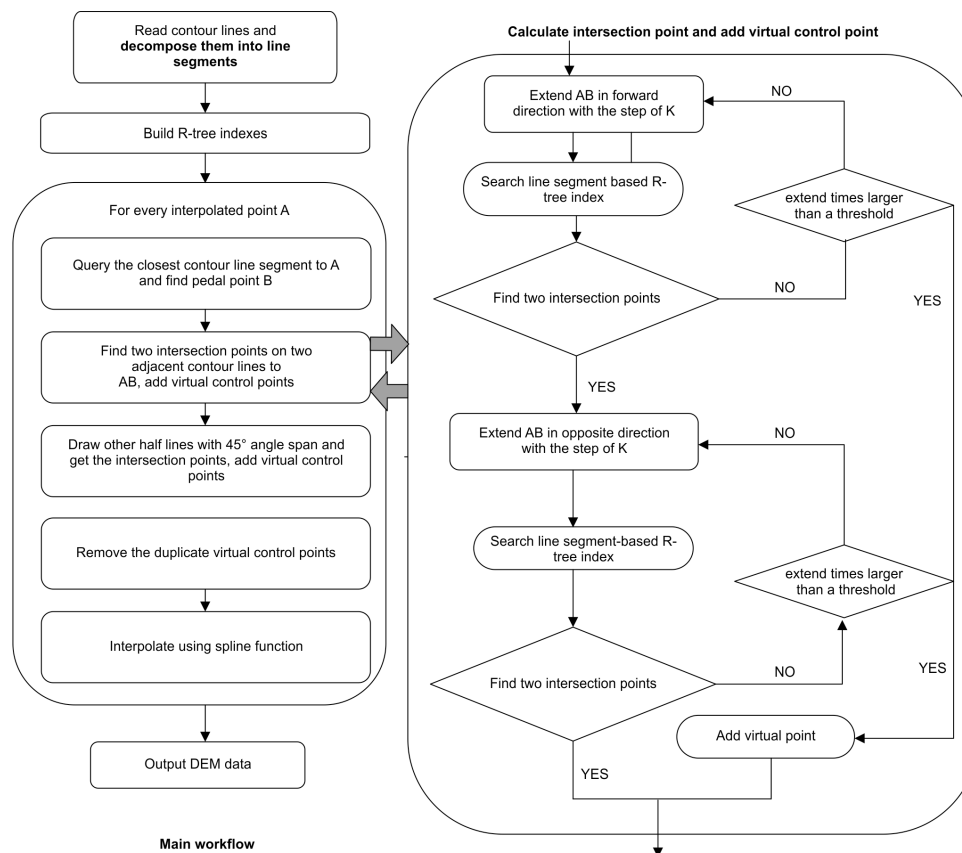


Figure 10. Flowchart illustrating the interpolation of DEM data.

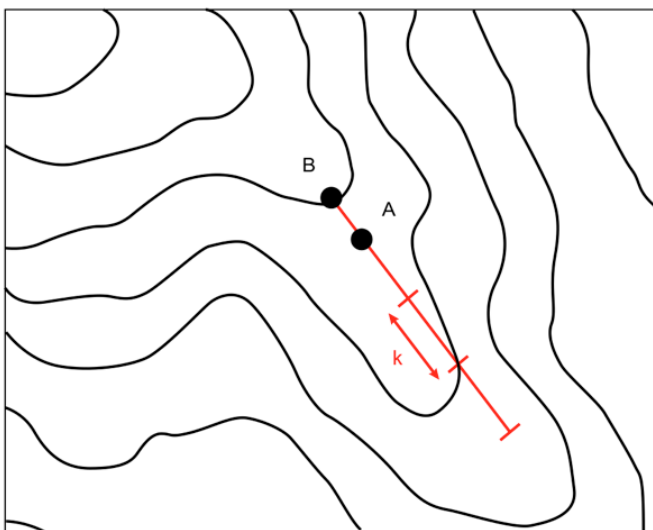


Figure 11. Intersection point finding method in programming.

### 3. Experiments and discussion

#### 3.1. Experimental data and preprocessing

In the present study, it was validated a method using a surface contour line map for the Dayang coal mine in Shanxi Province, China. The original contour map for this area is shown in Figure 12. The original contour interval is 5 m, and the output DEM data is in the form of an ASCII grid text file with a grid cell size of 2 m. The original contour map was cut into 16 sub-maps to test the results of the proposed method (Figure 12b), and those maps were used to verify the accuracy of interpolation. Then, it was generated the DEM data for each subarea using the “Topo to Raster” function of ArcGIS, the regional interpolation method of Yu and Tan (2002), and the method proposed in this study.

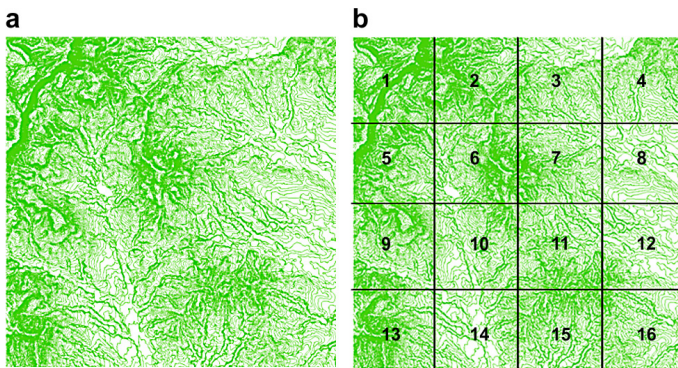


Figure 12. The original contours.

3.2. Results and discussion

It was used a stretched color ramp to display the DEM results. Obvious errors (i.e., abnormal colors, indicated by red color in Figure 13) were found in the results achieved using the method of Yu and Tan (2002). However, neither the proposed method, nor the ArcGIS method produce obvious errors. In fact, the results obtained using the “Topo to Raster” function of ArcGIS are very similar to the results obtained with this method; thus, they are illustrated in Figure 13.

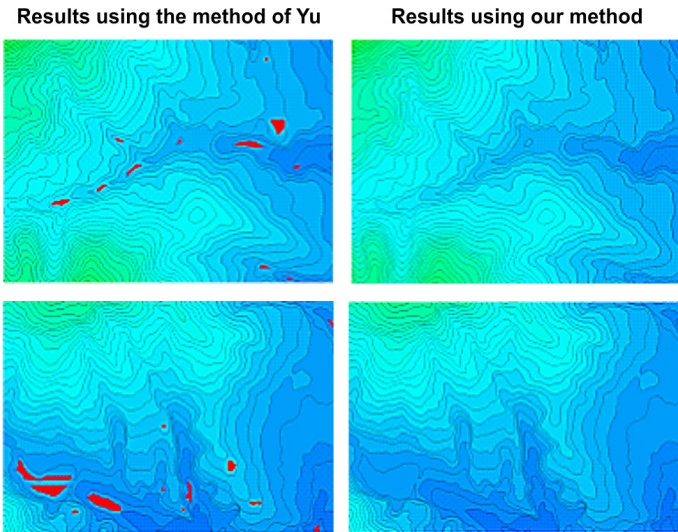


Figure 13. Comparison of DEMs generated using the method of Yu and Tan (2002) and our method in ArcMap. Red color indicates the obvious error.

The DEM results were transformed into contour line maps to compare the results in more detail, and to set the intervals and baselines of these maps to be the same as those of the original contour map (Figure 14). It was found that, in most cases, the contour lines generated by the proposed DEM fit the original contour lines very well. Moreover, in some areas, the results agree more closely with the original contour lines than the contours generated using the ArcGIS method. In fact, the ArcGIS method is found to produce obvious errors (e.g., Figure 14d, in which a closed contour line was generated according to the ArcGIS method), suggesting that the proposed method provides more accurate DEMs that can reflect geomorphic features more closely. It was noted that the smoothing effect of the contour lines is less developed in the proposed method than in the ArcGIS’s method (Figure 14). Furthermore, the proposed method generates more isolated points on the contour lines than other methods, because each DEM grid value is interpolated dynamically using intersection points and virtual control points in this approach, then smoothness is not so good.

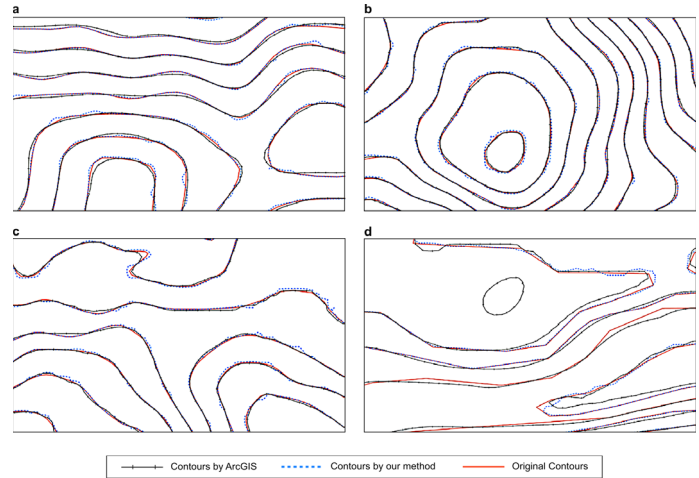


Figure 14. Comparison of contours generated using the proposed method and the ArcGIS method with original contours.

Finally, the transformed contour line maps were compared with the original map using the mean Hausdorff distance (MHD; Chen, Ma, Xu, Paul, 2010; Hung and Yang, 2004). The Hausdorff distance is a measure of the similarities between two nonempty compact (closed and bounded) sets A and B in a metric space S on their positions (Nadler, 1978). The MHD between the original and transformed contour line maps was calculated for each submap and the MHDs obtained were compared between the proposed method and the ArcGIS method (Figure 15). The results illustrate that the errors for each algorithm are similar; therefore, it was concluded that the proposed method exhibits similar accuracy to the ArcGIS process. Figure

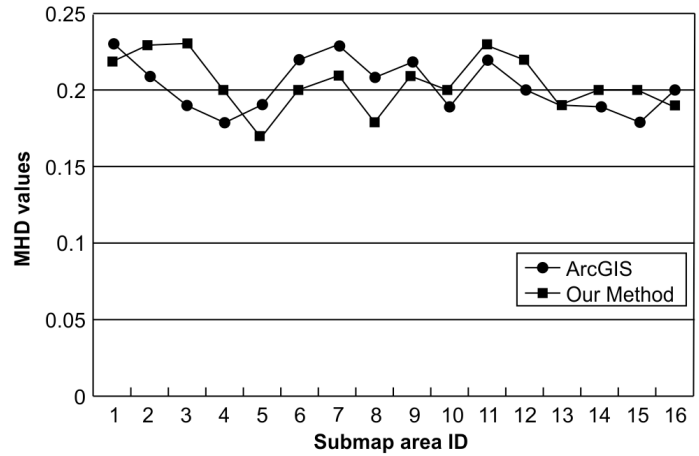


Figure 15. The difference in Hausdorff distance calculated using the two different algorithms.

4. Conclusions

Here, it was presented an improved method of generating gridded DEMs from contour line maps while taking geomorphic information into account. First, it was identified the point on a contour line that is nearest to the interpolated point; the choice of this position plays a critical role in interpolation accuracy. Then, 16 points on neighboring contour lines were obtained in eight directions from the interpolated point; these points can reflect the basic geomorphic features of the resulting DEM. For regions of complex geomorphology, it was inserted a virtual control point at a specified place in each direction according to various geomorphic features identified

from the original map, which prevents the interpolation result from exceeding the contour interval. Finally, the points with feature geomorphic information were used to construct local surface spline functions for interpolation. The method was tested using a surface contour line map of the Dayang coal mine in Shanxi Province, China, and the results were compared with those obtained using existing methods. It was concluded that the proposed method is at least as accurate as the ArcGIS “Topo to Raster” function and is more accurate than the method described by Yu and Tan (2002).

In this method, each DEM grid value is interpolated based on intersection points and virtual control points, and the spline interpolation function was constructed dynamically. Therefore, the method requires a greater analysis time than the ArcGIS method and the DEMs generated using it are not as smooth as those generated using the ArcGIS method. Improvements in this regard will form the basis of future work. The interpretation of real complex geomorphic features from contour maps remains challenging, and the objective of this study is to continue improving the methods for interpolation of gridded DEM data based on such maps.

### Funding

This work was supported by the National Science and Technology Major Project of China [No. 2011ZX05039-004], the National Natural Science Foundation of China [No. 40901191], the Strategic Priority Research Program of the Chinese Academy of Sciences [No. XDA05030200], the Hebei Province Natural Science Fund [No. D2016210008], the Social Science Foundation Project of Hebei Province [No. HB15SH015], and the Scientific Research Foundation for Doctor of Shijiazhuang Tiedao University.

### References

- Aumann, G., Ebner, H. & Tang, L. (1991). Automatic derivation of skeleton lines from digitized contours. *ISPRS Journal of Photogrammetry and Remote Sensing*, 46, 259–268. DOI: 10.1016/0924-2716(91)90043-U
- Binh, T. Q. and Thuy, N. T. (2008). Assessment of the influence of interpolation techniques on the accuracy of digital elevation model. *VNU Journal of Science, Earth Sciences*, 24(4), 176–183.
- Bonin, O., & Rousseaux, F. (2005). Digital Terrain Model Computation from Contour Lines: How to Derive Quality Information from Artifact Analysis. *Geoinformatica*, 9(3), 253–268. DOI: 10.1007/s10707-005-1284-2
- Bouillon, A., Bernard, M., Gigord, P., Orsoni, A., Rudowski, V., and Baudoin, A. (2006). SPOT 5 HRS geometric performances: Using block adjustment as a key issue to improve quality of DEM generation. *ISPRS Journal of Photogrammetry and Remote Sensing*, 60(3), 134–146. DOI: 10.1016/j.isprsjprs.2006.03.002
- Carley, J. K., Pasternack, G. B., Wyrick, J. R., Barker, J. R., Bratovich, P. M., Massa D. A., ... Johnson T. R. (2012). Significant decadal channel change 58-67 years post-dam accounting for uncertainty in topographic change detection between contour maps and point cloud models. *Geomorphology*, 179, 71–88. DOI: 10.1016/j.geomorph.2012.08.001
- Carrara, A., Bitelli, G., & Carla, R. (1997). Comparison of techniques for generating digital terrain models from contour lines. *International Journal of Geographical Information Science*, 11(5), 451–473.
- Chen, X., Ma, W., Xu, G., & Paul, J. C. (2010). Computing the Hausdorff distance between two B-spline curves. *Computer-Aided Design*, 42(12), 1197–1206. DOI: 10.1016/j.cad.2010.06.009
- Clarke, A. L., Gruen, A., & Loon, J. C. (1982). The application of contour data for generating high fidelity grid digital elevation models. *Proceedings Auto-Carto 5*, 213–222. Washington DC.
- Corral, A., & Almendros-Jiménez, J. M. (2007). A performance comparison of distance-based query algorithms using R-trees in spatial databases. *Information Sciences*, 177(11), 2207–2237. DOI: 10.1016/j.ins.2006.12.012
- Curry, H. B., & Schoenberg, I. J. (1996). On Pólya frequency functions IV: The fundamental spline function and their limits. *Journal d'Analyse Mathématique*, 17(1), 71–107. DOI: 10.1007/BF02788653
- Dinis, L. M. J. S., Natal Jorge, R. M., & Belinha, J. (2007). Analysis of 3D solids using the natural neighbour radial point interpolation method. *Computer Methods in Applied Mechanics and Engineering*, 196(13–16), 2009–2028. DOI: 10.1016/j.cma.2006.11.002
- Doytsher, Y., & Hall J. K. (1997). Interpolation of DTM using bi-directional third-degree parabolic equations, with FORTRAN subroutines. *Computers & Geosciences*, 23(9), 1013–1020. DOI: 10.1016/S0098-3004(97)00061-7
- Gofuku, S., Tamura, S., & Maekawa, T. (2009). Point-tangent/point-normal B-spline curve interpolation by geometric algorithms. *Computer-Aided Design*, 41(6), 412–422. DOI: 10.1016/j.cad.2009.02.005
- Gousie, M. B., & Franklin W. R. (2003). Constructing a DEM from grid-based data by computing intermediate contours. In *GIS 2003: Proceedings of the Eleventh ACM International Symposium on Advances in Geographic Information Systems*, 71–77. DOI: 10.1145/956676.956686
- Hearnshaw, H. M., & Unwin, D. J. (1994). *Visualization in Geographical Information Systems*. Chichester: Wiley, 168–180.
- Heritage, G. L., Milan, D. J., Large, A. R. G., & Fuller, L. C. (2009). Influence of survey strategy and interpolation model on DEM quality. *Geomorphology*, 112(3–4), 334–344. DOI: 10.1016/j.geomorph.2009.06.024
- Hickey, R., Smith A., & Jankowski P. (1994). Slope length calculations from a DEM within ARC/INFO grid. *Computers, Environment and Urban Systems*, 18(5), 365–380. DOI: 10.1016/0198-9715(94)90017-5
- Huang, F., Liu, D., Tan, X., Wang, J., Chen Y., & He, B. (2011). Explorations of the implementation of a parallel IDW interpolation algorithm in a Linux cluster-based parallel GIS. *Computers & Geosciences*, 37(4), 426–434. DOI: 10.1016/j.cageo.2010.05.024
- Huang, P. W., Lin, P. L., & Lin, H. Y. (2001). Optimizing storage utilization in R-tree dynamic index structure for spatial databases. *Journal of Systems and Software*, 55(3), 291–299. DOI: 10.1016/S0164-1212(00)00078-9.
- Hung, W., & Yang, M. (2004). Similarity measures of intuitionistic fuzzy sets based on Hausdorff distance. *Pattern Recognition Letters*, 25(14), 1603–1611. DOI: 10.1016/j.patrec.2004.06.006
- Hutchinson, M. F. (1988). Calculation of hydrologically sound digital elevation models. *Third International Symposium on Spatial Data Handling*, Sydney, Australia, August 117–133.
- Hutchinson, M. F. (1996). A locally adaptive approach to the interpolation of digital elevation models. In *Proceedings, Third International Conference/Workshop on Integrating GIS and Environmental Modeling*, January 21–25.
- Hutchinson, M. F. (2008). Adding the Z-dimension. In Wilson J.P. and Fotheringham, A. S. (Eds.) *The Handbook of Geographic Information Science*, (pp. 144–168). Blackwell. DOI: 10.1002/9780470690819.ch8
- Jones, K. H. (1998). A comparison of algorithms used to compute hill slope as a property of the DEM. *Computers & Geosciences*, 24(4), 315–323. DOI: 10.1016/S0098-3004(98)00032-6
- Kweon, I. S. and Kanade T. (1994). Extracting Topographic Terrain Features from Elevation Maps. *CVGIP: Image Understanding*, 59(2), 171–182.
- Li, Z. (1994). A comparative study of the accuracy of digital terrain models (DTMs) based on various data models. *ISPRS Journal of Photogrammetry and Remote Sensing*, 49(1), 2–11.
- Maekawa, T., Matsumoto, Y., & Namiki, K. (2007). Interpolation by geometric algorithm. *Computer-Aided Design*, 39(4), 313–323. DOI: 10.1016/j.cad.2006.12.008
- Nadler, S. B. (1978). *Hyperspaces of sets: A text with research questions*. New York: Marcel Dekker.

- Okuy, P., Ardiansyah, D., & Yokoyama R. (2002). DEM generation method from contour lines based on the steepest slope segment chain and a monotone interpolation function. *ISPRS Journal of Photogrammetry and Remote Sensing*, 57(1–2), 86–101. DOI: 10.1016/S0924-2716(02)00117-X
- Peralvo, M., and Maidment, D. (2008). Influence of DEM Interpolation Method in Drainage Analysis. Available online at [www.crrw.utexas.edu/gis/gishydro04/Introduction/TermProjects/Peralvo.pdf](http://www.crrw.utexas.edu/gis/gishydro04/Introduction/TermProjects/Peralvo.pdf).
- Rvachev, V. L., Sheiko, T. I., Shapiro, V., & Tsukanov, I. (2001). Transfinite interpolation over implicitly defined sets. *Computer Aided Geometric Design*, 18(3), 195–220. DOI: 10.1016/S0167-8396(01)00015-2
- Taud, H., Parrot, J. F., & Alvarez, R. (1999). DEM generation by contour line dilation. *Computers & Geosciences*, 25(7), 775–783. DOI: 10.1016/S0098-3004(99)00019-9
- Vieux, B. E. (1993). DEM aggregation and smoothing effects on surface runoff modeling. *Journal of Computing in Civil Engineering—ASCE*, 7(3), 310–338. DOI: 10.1061/(ASCE)0887-3801(1993)7:3(310)
- Wang, D., Tian, Y., Gao Y., & Wu. L. (2005). A New Method of Generating Grid DEM from Contour Lines. *IGARSS 2005*, 657–660. DOI: 10.1109/IGARSS.2005.1526261
- Watson, D. F. (1992). *Contouring: A Guide to the Analysis and Display of Spatial Data*. Oxford: Pergamon.
- Watson, D. (1999). The natural neighbor series manuals and source codes. *Computers & Geosciences*, 25(4), 463–466. DOI: 10.1016/S0098-3004(98)00150-2
- Werbrouck, I., Antrop, M., Van Eetvelde, V., Stal, C., De Maeyer, P., Bats, M., ... Zwertvaegher, A. (2011). Digital elevation model generation for historical landscape analysis based on LiDAR data, a case study in Flanders (Belgium). *Expert Systems with Applications*, 38(7), 8178–8185. DOI: 10.1016/j.eswa.2010.12.162
- Wise, S. (2011). Cross-validation as a means of investigating DEM interpolation error. *Computers & Geosciences*, 37(8), 978–991.
- Wise, S. (2012). Information entropy as a measure of DEM quality. *Computers & Geosciences*, 48, 102–110. DOI: 10.1016/j.cageo.2012.05.011
- Wood, J. (1994). Visualizing contour interpolation accuracy in digital elevation models. In H. M. Hearnshaw and D. J. Unwin, eds. *Visualization in geographical information systems*. Chichester: John Wiley and Sons, 168–180.
- Wood, J. D., & Fisher P. F. (1993). Assessing interpolation accuracy in elevation models. *IEEE Computer Graphics and Applications*, 13(2), 48–56. DOI: 10.1109/38.204967
- Xiao, L., & Liu, H. (2012). A novel approach for quantitative assessment of DEM accuracy using reconstructed contours. *Procedia Environmental Sciences*, 12 Part B, 772–776. DOI: 10.1016/j.proenv.2012.01.346
- Xie, K., Wu, Y., Ma, X., Liu, Y., Liu, B., & Hessel, R. (2003). Using contour lines to generate digital elevation models for steep slope areas: a case study of the Loess Plateau in North China. *Catena*, 54(1–2), 161–171. DOI: 10.1016/S0341-8162(03)00063-8
- Yu, Z. W. (2001). Surface interpolation from irregularly distributed points using surface splines, with Fortran program. *Computers & Geosciences*, 27(3), 877–882.
- Yu, Z. W., & Tan, H. Q. (2002). Regionalized interpolation: A new approach to surface map reconstruction. *Terra Nostra*, 3, 513–517.
- Zhou, Q., & Chen Y. (2011). Generalization of DEM for terrain analysis using a compound method. *ISPRS Journal of Photogrammetry and Remote Sensing*, 66(1), 38–45. DOI: 10.1016/j.isprsjprs.2010.08.005.
- Zhou, Q., & Liu X., (2004). Analysis of errors of derived slope and aspect related to DEM data properties. *Computers & Geosciences*, 30(4), 369–378. DOI: 10.1016/j.cageo.2003.07.005
- Zhu, Q., Gong, J., & Zhang, Y. (2007). An efficient 3D R-tree spatial index method for virtual geographic environments. *ISPRS Journal of Photogrammetry and Remote Sensing*, 62(3), 217–224. DOI: 10.1016/j.isprsjprs.2007.05.007





## Temporal-spatial distribution of oceanic vertical deflections determined by TOPEX/Poseidon and Jason-1/2 missions

Jin Yun Guo<sup>1,2\*</sup>, Yi Shen<sup>1</sup>, Kaihua Zhang<sup>1,3</sup>, Xin Liu<sup>1</sup>, Qiaoli Kong<sup>1,2</sup>, Feifei Xie<sup>1,2</sup>

<sup>1</sup>College of Geodesy and Geomatics, Shandong University of Science and Technology, Qingdao 266590, China

<sup>2</sup>State Key Laboratory of Mining Disaster Prevention and Control, co-founded by Shandong Province and Ministry of Science & Technology, Qingdao 266590, China

<sup>3</sup>Tianjin Survey and Design Institute for Water Transport Engineering, Tianjin 300456, China

\* Corresponding author: JinyunGuo, E-mail: jinyunguo1@126.com

### ABSTRACT

Deflections of the Vertical (DOV) are essential data in the geodetic observation reduce, the earth gravity field and geoid model refinement, and the mass earth change. The meridional and prime vertical components of global oceanic DOVs are estimated from altimetry data of TOPEX/Poseidon, Jason-1, and Jason-2, through 1992 to 2013 with the crossover method, to analyze the temporal-spatial distribution of marine DOVs. Comparing with the EGM2008-modelled DOVs, precisions of meridional and prime vertical components can be up to 0.98" and 1.02", respectively. The time series of annual mean DOVs from 1992 to 2013 are studied to get the annual variation law. Annual changes of meridional and prime vertical components are small over most oceans. But the annual changes are significant over oceans with large submarine topography undulations. The spatial distribution of oceanic DOVs is also analyzed. The absolute DOVs over oceans around lands, islands, and large oceanic trenches are greater than those over the other oceans. The meridional and prime vertical components are consistent with the longitude and latitude directions, respectively.

*Keywords: Deflection of the Vertical (DOV), satellite altimetry, temporal-spatial distribution, crossover point, marine gravity field.*

### RESUMEN

Las Desviaciones de la Vertical (DOV, del inglés Deflections of the Vertical) son información esencial en la simplificación de la observación geodésica, el campo gravitatorio terrestre y el perfeccionamiento del modelo geode, y el cambio de la masa terrestre. Se estimaron los componentes meridional y principal vertical de las desviaciones de la vertical oceánica global con la información altimétrica de TOPEX/Poseidón, Jason 1 y Jason 2, de 1992 a 2013, con un método de cruce para analizar la distribución espacio-temporal de las desviaciones de la vertical marinas. Comparadas con las desviaciones de la vertical obtenidas con el modelo EGM2008 (Modelo de Gravitación de la Tierra), la precisión de los componentes meridional y principal vertical puede aumentarse 0.98" y 1.02", respectivamente. Se estudiaron las series temporales de la media anual de las desviaciones de la vertical desde 1992 a 2013 para obtener la ley anual de variación. Los cambios anuales de los componentes meridional y principal vertical son muy pequeñas en la mayoría de los océanos. Sin embargo, los cambios anuales son mayores en aquellos océanos con una topografía submarina de grandes ondulaciones. También se analizó la distribución espacial de las desviaciones de la vertical oceánicas. Las desviaciones de la vertical absolutas alrededor de los continentes, islas y fosas oceánicas mayores son superiores que aquellas sobre los otros océanos. Los componentes meridional y vertical principal son consistentes con las direcciones de la longitud y la latitud, respectivamente.

*Palabras clave: Desviación de la vertical (DOV), altimetría satelital, distribución espacio-temporal, punto de cruce, campo de gravitación marino.*

#### Record

Manuscript received: 26/11/2015

Accepted for publication: 06/03/2016

#### How to cite item

Guo, J. Y., Shen, Y., Zhang, K., Liu, X., Kong, Q. and Xie F. (2016). Temporal-spatial distribution of oceanic vertical deflections determined by TOPEX/Poseidon and Jason-1/2 missions. *Earth Sciences Research Journal*, 20(2), H1-H5. doi:<http://dx.doi.org/10.15446/esrj.v20n2.54402>

## 1. Introduction

The Deflection of the Vertical (DOV) as one basic research topic in geodesy and geophysics can characterize the direction of gravity vector and provide one tight local tie among space geodetic techniques (Shen et al., 2015). The traditional methods to measure DOV include the astronomical geodetic surveying, gravimetry, combination of astronomical geodesy and gravimetry, and global navigation satellite system (GNSS). Based on the astronomical geodetic principle, the automatic measurement system integrating GNSS and CCD zenith telescope can precisely measure DOVs (Guo, Song, Chang, & Liu, 2011; Hirt & Seeber, 2008; Tian et al., 2014, Peng & Xia, 2015). These measurement methods of the vertical deflection are applicable to lands (Ning, Guo, B. Wang, & H. M. Wang, 2006), but are unable to measure practically the oceanic vertical deflection due to limitations of these techniques under effects of ocean dynamic environment over open oceans (Guo, Chen, Liu, Zhong, & Mai, 2013; Guo, Liu, Chen, Wang, & Li, 2014). DOVs over open oceans are commonly calculated from the Earth gravity field model at present (Jekeli, 1999; Pavlis, Holmes, Kenyon, & Factor, 2012). Ship-borne gravity data can also be used to estimate the oceanic vertical deflections. But the ship-borne gravimetry can mostly be carried out over coastal seas, and most of the oceans are short of gravity field data. With the rapid development of satellite altimetry, altimeter data can widely be used to estimate the oceanic vertical deflection (Fu and Cazenave, 2000; Guo, Hu, Wang, Chang, & Li, 2015).

With the development of satellite altimetry technique, oceanic DOVs are mainly utilized to determine oceanic gravity field model with high precision. DOVs on crossover points can be calculated from altimeter data by the crossover method (Sandwell, 1984). Altimeter data of ERS-1 and Geosat were processed to estimate DOVs of crossover points from which gravity field over Antarctic oceans was estimated by the Laplace equation (Sandwell, 1992). Sandwell and Smith (1997) used ERS-1 and Geosat altimetry data to compute DOVs of crossover points which are interpolated to get DOVs of grids and then estimated the gravity anomalies over oceans with the Fast Fourier transformation (FFT). Single differences of sea surface height along the track and corresponding track azimuths are used to calculate oceanic DOVs along the track (Olgia, Balmino, Sarrailh, & Green, 1995). Altimetry data from multi-satellite altimetry missions can be integrally processed to get DOVs along tracks which are interpolated to calculate DOVs of grids used to estimate marine gravity anomalies. Gravity anomalies along tracks with the along-track DOVs are more accurate than those determined by FFT with the inverse Stokes formula. The inverse Vening Meinesz formula is derived to calculate DOVs with the grid method (Hwang, 1998). The geoid and gravity anomalies over China seas has been calculated from oceanic DOVs with the crossover method (Li, Ning, Chen, & Chao, 2003). DOVs from the crossover method are more accurate than those from the grid method and the along track method, and the grid method is optimal to determine the high-resolution precise marine gravity field using altimeter data (Peng and Xia, 2004). DOVs over China coastal seas are calculated from Geophysical Data Records (GDR) of EnviSat with the grid method (Xing, Li & Liu, 2006). Comparing with EGM96 (Lemoine et al., 1998), precisions of the prime vertical and meridional components are 6" and 3", respectively. Multi-altimeter data are processed to calculate global DOVs with the grid method. Comparing with EGM96, precisions of the prime vertical and meridional components over global oceans are 1.97" and 1.12", respectively.

TOPEX/Poseidon (T/P) launched in 1992, Jason-1 initiated in 2002 and Jason-2 initiated in 2008 can together measure oceans. Jason-2 as Jason-1 follow on runs the same track of T/P and continuously surveys oceans. The precision of single observation is estimated to be near to 3 cm (Beckley et al., 2010; Fu and Cazenave, 2000; Tunini et al., 2010). T/P and Jason-1/2 provide altimetry data with high precision which are processed by the crossover method. Global oceanic DOVs are estimated and then the temporal-spatial distribution of global oceanic DOVs is studied in the paper.

## 2. Satellite altimetry data

GDRs version C of T/P, Jason-1, and Jason-2 released by the Physical Oceanography Distributed Active Archive Center (PO.DAAC) are processed in the paper. Time spans of T/P, Jason-1, and Jason-2 data are from October 1992 to August 2002 with cycles 2 to 364, from August 2002 to January 2009 with cycles 22 to 259, and from January 2009 to May 2013 with cycles 21 to 177, respectively. T/P starts the precise satellite altimetry era, and Jason-1 and Jason-2 follow T/P. These three altimetry satellites are in the same exact repeated orbit. Figure 1 shows global tracks and crossover points of T/P cycle 17.

The radial precision of T/P orbit determination is better than 3 cm, and the radial precisions of Jason-1 and Jason-2 orbit determination can be up to 1 cm based on the on-board satellite tracking systems. Sea surface height accuracy from these three altimeter data can be lower than 3 cm. To get more precise sea surface heights, altimetry data should be edited based on the criteria provided by AVISO (AVISO/Altimetry, 1996; Dumont et al., 2011; Picot, Case, Desai, Vincent, & Bronner, 2012; Shah, Sajeev, & Gopika, 2015).

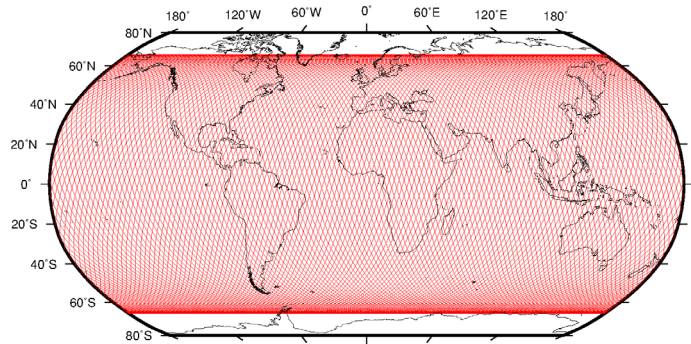


Figure 1. T/P tracks and crossover points for cycle 17

## 3. Determination of oceanic DOVs

The crossover method is one of the best ways to determine precise oceanic DOVs from satellite altimetry data. Altimetry profiles of ascending and descending arcs can be determined by the geoid gradient or the single difference of DOV along the track, and then the prime vertical and meridional components of DOV can be solved by combining the track gradients.

The meridional component  $\xi$  and the prime vertical component  $\eta$  of DOV are calculated from the two directions of geoid gradients (Heiskanen & Moritz, 1967), that is

$$\xi = -\frac{1}{R} \frac{\partial N}{\partial \varphi} \quad (1)$$

$$\eta = -\frac{1}{R \cos \varphi} \frac{\partial N}{\partial \lambda} \quad (2)$$

where  $R$  is the average radius of the Earth.  $\partial N / \partial \varphi = 1/2 |\varphi'| (N_a - N_d)$  and  $\partial N / \partial \lambda = 1/2 |\lambda'| (N_a + N_d)$  and, in which  $\varphi$  and  $\lambda$  are the directions of prime vertical and meridional speeds of nadir point respectively, is the derivative of geoid height with respect to time on the altimetry data point relative, and subscripts and denote the ascending and descending arcs respectively.  $\varphi'$  and  $\lambda'$  can be obtained by the time and location information in the altimetric data (Hwang & Parsons, 1995; Sandwell & Smith, 1997). The detailed data processing procedure is following.

1) Altimetry data preprocessing. These three-altimeter data are read with the corresponding program based on data formats. These data are edited according to the related criteria published by the data providers. All geophysical corrections are applied to altimetry data. These data including latitude, longitude, sea surface height and time are saved based on the ascending and descending arcs.

2) Determination of crossover point. The quadratic polynomials are used to fit the ascending and descending arcs on geodetic latitude and longitude based on the positioning information in altimetry data, respectively. The quadratic equations of ascending and descending arcs are combined to solve coordinates of the crossover point.

3) Unification of time and space datum. There exist systematic biases between different altimeter data under effects of a different ellipsoid, time-varying sea surface height, satellite orbit determination error, altimeter error and geophysical correction error. Corrections of coordinate frame biases for different altimetry data are calculated to unify the time and space datum for T/P, Jason-1, and Jason-2.

4) Sea surface height of crossover point. Sea surface height of crossover point is interpolated from the ascending and descending arcs' data based on coordinates with the distance weight method.

5) DOV determination of crossover point. 8-10 altimetry points around crossover point are selected based on the position of the crossover point. The quadratic polynomial on latitude and longitude, and the quadratic curves of latitude and longitude with respect to time are fitted based on information about sea surface height, latitude, longitude and time of altimetry point, respectively. Then derivatives of these quadratic polynomials are made to get  $\dot{\lambda}$  and  $\dot{\phi}$ , which are substituted for equations (1) and (2) to calculate the prime vertical and meridional components of DOV on crossover point.

6) Repeat step 5) to calculate all DOVs of all crossover points. The same pass may be different for all cycles and the farthest distance of crossover points for the same ascending and descending arcs may be up to 1 km for T/P, Jason-1 and Jason-2 (Fu and Cazenave, 2000; Luz Clara, Simionato, D'Onofrio, & Moreira, 2015). So the mean position of crossover point for the same ascending and descending arcs should be determined.

7) Reduce DOVs of crossover points to the mean position with the inverse distance weighted interpolation method within the studied time span. We can get oceanic DOVs of crossover points from altimetry data from 1992 to 2013. So the temporal-spatial distribution of oceanic DOVs can be obtained.

Altimetry data should be edited and corrected before DOV calculation because of contamination of many kinds of errors. The same editing criteria are used to modify and correct altimetry data to get precise results. To check the precision of oceanic DOVs from altimetry data, it was selected T/P data of cycle 17 to compute oceanic DOVs of crossover points in the global area (-60°S~60°N, 0°~360°), which are compared with the modeled DOVs from EGM2008 (Pavlis, Holmes, Kenyon, & Factor, 2012). Table 1 lists the statistical results. From Table 1, it can be seen that the precisions of prime vertical and meridional components are 1.02" and 0.98" comparing with EGM2008-modelled components, respectively, which indicates that oceanic DOVs of crossover points from altimetry data are reliable.

**Table 1.** Statistical results of oceanic DOVs from T/P, Jason-1, and Jason-2

Component	Max (")	Min (")	Mean (")	STD (")	RMS (")
Meridional	4.89	-4.86	0.07	0.98	0.98
prime vertical	4.98	-4.99	0.00	1.02	1.02

**4. Temporal variations of oceanic DOVs**

The earth gravity field not only changes in space but also changes in time. The temporal-spatial variation of the earth gravity field is one important part of geodynamics (Ding, Li, & Ding, 2006). The gravity field change containing the abundant geophysical information of interior earth can be studied through the DOV variations.

Oceanic DOVs of crossover points for each cycle are calculated from altimetry data of T/P, Jason-1, and Jason-2 with the crossover method. The mean position of crossover point is determined by averaging positions of crossover points from the same ascending and descending arcs in one year. DOVs from the altimetry data of about 37 cycles in one year are used to get the mean DOV of the average position with the inverse distance weighted interpolation method. So it is possible to get a group of DOVs of annual mean

crossover point on a global scale, which can make up a time series of annual mean DOVs from 1992 to 2013. The time series can be analyzed to study the interannual variations of oceanic DOVs. Figures 2 and 3 show annual variations of meridional and prime vertical components of oceanic DOVs determined by the crossover method, respectively.

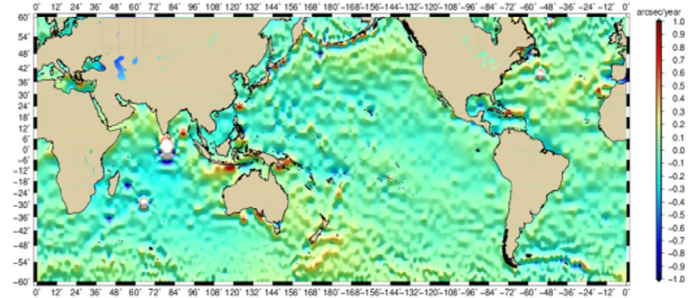


**Figure 2.** Annual change rate of meridional component of DOV

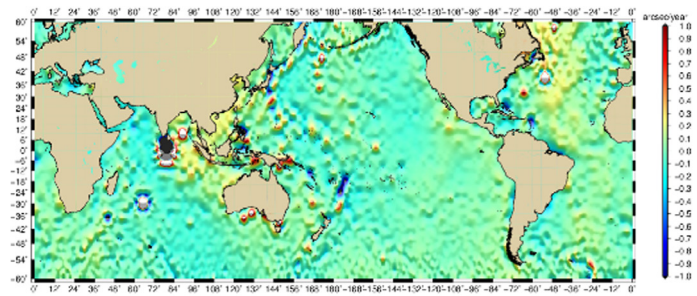


**Figure 3.** Annual change rate of prime vertical component of DOV

From figure 2, it can be found that the annual change of meridional component over most oceans is slight in 1992-2013, and the annual change in most oceans in the north hemisphere is greater than that in the south region. The annual change over open oceans far away from islands and lands is small and apt to convergence, such as the middle Pacific Ocean and the Middle Indian Ocean. The annual variation over coastal seas is great, such as the Bering Sea, the Indonesian Sea, the New Zealand Sea, and the Caribbean Sea. On the one hand, the mass over these coastal seas changes greatly. On the contrary, the variation can reflect the lower altimetry data quality over coastal seas than that over open oceans.

Figure 3 shows the annual changes in prime vertical components. Annual variations are small and apt to convergence over most oceans except for the eastern oceans of the North American, the Bengal Bay, and the China coastal seas. Also, the annual variation is significant over some oceans around islands in the Pacific Ocean.

**5. Spatial distribution of oceanic DOVs**

The Marine gravity field is mainly determined by the oceanic lithosphere and the deep mass distribution and geological structure. It shows the basic geographic information of oceanic lithosphere structure and the submarine topography (Chao, Yao, Li, & Xu, 2002). The uneven distribution of vast oceanic gravity affects the direction of the marine plumb line, which makes the spatial distribution of marine DOVs inconsistent. The marine gravity field can be analyzed by studying the spatial distribution of global oceanic DOVs. DOVs of crossover point for the same ascending and descending arcs in all cycles are interpolated to the mean position with the inverse distance weighted interpolation method. So the average DOV of each crossover point in 1992-2013 can be obtained. Figures 4 and 5 show the global distribution of oceanic DOVs.

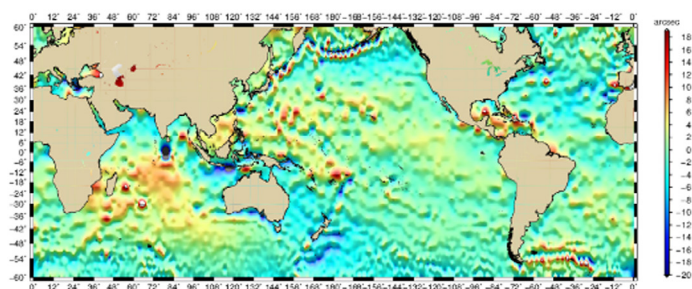


Figure 4. Spatial distribution of meridional component of DOV

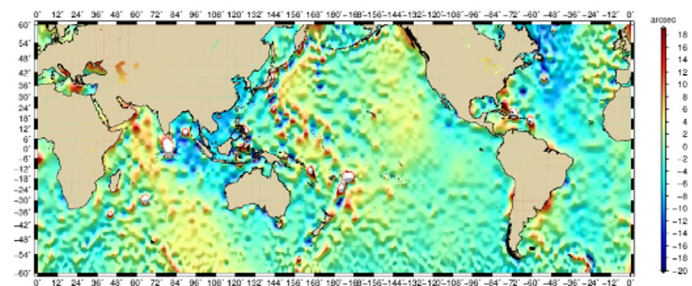


Figure 5. Spatial distribution of prime vertical component of DOV

From figure 4, it can be found that the absolute meridional components of DOV are comparatively large over the coastal oceans. The meridional components are large over the west Pacific Ocean and the Middle Indian Ocean. It is also large over the seas around islands and large oceanic trenches, such as the Bering Sea, the Japan seas, the Indonesian seas, and the Caribbean Sea. The significant meridional components over these oceans are mainly caused by the obvious marine mass changes. The meridional components are positive over the most Indian Ocean, the north-central Pacific Ocean, and the Caribbean Sea. Most meridional components over the other oceans are negative. The meridional components tend to be consistent along the longitude direction over most oceans.

From figure 5, it can be found that the spatial distribution of prime vertical components of oceanic DOVs is approximately consistent with the distribution of meridional components over most oceans. The absolute prime vertical components are large over the China seas, the west Pacific Ocean, the Indian Ocean, and the northwest Atlantic Ocean. It is also large over the oceans around islands and oceanic trenches, like the Bering Sea, the Japan seas, the Indonesian seas, the Caribbean Sea, and the ocean around the Mariana Trench. The large prime vertical components over these oceans may be mainly caused by the visible change of marine gravity field. The prime vertical components over the most Indian Ocean, the north-central Pacific Ocean and the Caribbean Sea are positive, and these are more negative over the other oceans. In contrast to the meridional component, the prime vertical components tend to be consistent along the latitude direction over most oceans.

## 6. Conclusions

Marine DOVs are determined from altimetry data of T/P, Jason-1, and Jason-2 in 1992-2013 with the crossover method. The temporal-spatial distribution of oceanic DOVs is studied. Comparing with the EGM2008-modelled DOVs, the precisions of prime vertical and meridional components determined from one-cycle altimetry data of T/P, Jason-1, and Jason-2 can be up to 0.98" and 1.02", respectively, which indicates that DOVs of crossover points estimated from altimetry data are very reliable.

Annual changes of meridional and prime vertical components of DOVs over most open oceans are small. But the annual variations over most coastal seas are significant because mass changes over coastal ocean may be

large and the altimetry precision over coastal seas may be lower. Absolute DOVs over oceans around lands, islands and vast oceanic trenches are bigger than those over the other oceans. This is mainly due to the obvious gravity change of interior earth and the severe submarine topography undulation. The meridional and prime vertical components of DOVs are consistent with the longitude and latitude directions, respectively.

The spatial resolution of oceanic DOVs determined from altimetry data with the crossover method is limited by the exact repeating period of altimetry satellite. The combination of more satellite altimetry missions can improve the resolution of oceanic DOVs.

## Acknowledgments:

This study is supported by the National Natural Science Foundation of China (Grant No. 41374009), the Shandong Natural Science Foundation of China (Grant No. ZR2013DM009), the Public Benefit Scientific Research Project of China (Grant No. 201412001), and the SDUST Research Fund (Grant No. 2014TDJH101).

## References:

- AVISO/Altimetry (1996). AVISO user handbook: merged TOPEX/Poseidon products (GDR-Ms). AVI-NT-02-101-CN, CLS & CNES
- Beckley, B., Zelensky, N. P., Holmes, S. A., Lemoine, F. G., Ray, R., Mitchum, G. T., ... Brown, S. (2010). Assessment of the Jason-2 extension to the TOPEX/Poseidon, Jason-1 sea-surface height time series for global mean sea level monitoring. *Marine Geodesy*, 33(1), 447-471. DOI: 10.1080/01490419.2010.491029
- Chao, D. B., Yao, Y. S., Li, J. C., & Xu, J. S. (2002). Interpretation on the tectonics and characteristics of altimeter-derived gravity anomalies in China South Sea (in Chinese). *Editorial Board of Geomatics and Information Science of Wuhan University*, 27(4), 343-347.
- Ding, Y. F., Li, Y. F., & Ding, X. B. (2006). Deflection of vertical in modern geodesy (in Chinese). *Journal of Geodesy and Geodynamics*, 26(2), 115-119.
- Dumont, J. P., Rosmorduc, V., Picot, N., Desai, S., Bonekamp, H., Figa J., ... Scharroo, R. (2011). OSTM/Jason-2 Products handbook. Edition 1.8. SALP-MU-M-OP-15815-CN, EUMETSAT/CNES/NOAA/NASA/JPL.
- Fu, L. L., & Cazenave, A. (2000). *Satellite altimetry and Earth Sciences: handbook of techniques and applications*. San Diego, Academic Press.
- Guo, J. Y., Chen, Y. N., Liu, X., Zhong, S. X., & Mai, Z. Q. (2013). Route height connection across the sea by using the vertical deflections and ellipsoidal height data. *China Ocean Engineering*, 27(1), 99-110. DOI: 10.1007/s13344-013-0009-9
- Guo, J. Y., Hu, Z., Wang, J., Chang, X., & Li, G. (2015). Sea Level Changes of China Seas and Neighboring Ocean Based on Satellite Altimetry Missions from 1993 to 2012. *Journal of Coastal Research: Special Issue*, 73: 17-21. DOI: 10.2112/SI73-004.1
- Guo, J. Y., Liu, X., Chen, Y., Wang, J., & Li, C. (2014). Local normal height connection across sea with ship-borne gravimetry and GNSS techniques. *Marine Geophysical Research*, 35(2):141-148. DOI: 10.1007/s11001-014-9216-x
- Guo, J. Y., Song, L. Y., Chang, X. T., & Liu, X. (2011). Vertical deflection measure with digital zenith camera and accuracy analysis (in Chinese). *Geomatics and Information Science of Wuhan University*, 36(9), 1085-1088.
- Heiskanen, W. K., & Moritz, H. (1967). *Physical geodesy*. San Francisco: Freeman.
- Hirt, C., & Seeber, G. (2008). Accuracy analysis of vertical deflection data observed with the Hannover Digital Zenith Camera System TZK2-D. *Journal of Geodesy*, 82(6), 347-356. DOI: 10.1007/s00190-007-0184-7
- Hwang, C. (1998). Inverse Vening Meinesz formula and deflection-geoid formula: applications to the predictions of gravity and geoid over the South China Sea. *Journal of Geodesy*, 72(5), 304-312. DOI: 10.1007/s001900050169

- Hwang, C., & Parsons, B. (1995). Gravity anomalies derived from Seasat, Geosat, ERS-1 and TOPEX/POSEIDON altimetry and ship gravity: a case study over the Reykjanes Ridge. *Geophysical Journal International*, 122(2), 551–568. DOI: 10.1111/j.1365-246X.1995.tb07013.x
- Jekeli, C. (1999). An analysis of vertical deflections derived from high-degree spherical harmonic models. *Journal of Geodesy*, 73(1), 10–22. DOI: 10.1007/s001900050213
- Lemoine, F. G., Kenyon S. C., Factor, J. K., Trimmer, R. G., Pavlis, N. K., Chinn, D. S., & Olson, T. R. (1998). The Development of the Joint NASA GSFC and the National Imagery and Mapping Agency (NIMA) Geopotential Model EGM96. NASA/TP-1998-206861
- Li, J. C., Ning, J. S., Chen, J. Y., & Chao, D. B. (2003). Geoid determination in China Sea Areas (in Chinese). *Acta Geodaetica et Cartographica Sinica*, 32(2), 114–119.
- Luz Clara, M., Simionato, C. G., D'Onofrio, E., & Moreira, D. (2015). Future sea level rise and changes on tides in the Patagonian Continental Shelf. *Journal of Coastal Research*, 31(3): 519–535. DOI: 10.2112/JCOASTRES-D-13-00127.1
- Ning, J. S., Guo, C. X., Wang, B., & Wang, H. M. (2006). Refined determination of vertical deflection in China mainland area (in Chinese). *Geomatics and Information Science of Wuhan University*, 31(12), 1035–1038.
- Olgati, A., Balmino, G., Sarraillh, M., & Green, C. M. (1995). Gravity anomalies from satellite altimetry: comparison between computation via geoid heights and via deflections of the vertical. *Bulletin Géodésique*, 69(4), 252–260. DOI: 10.1007/BF00806737
- Pavlis, N. K., Holmes, S. A., Kenyon, S. C., & Factor, J. K. (2012). The development and evaluation of the earth gravitational model 2008 (EGM2008). *Journal of Geophysical Research*, 117, B04406. DOI: 10.1029/2011JB008916
- Peng, F. Q., & Xia, Z. R. (2004). Vertical deflection theorem of satellite altimetry (in Chinese). *Hydrographic Surveying and Charting*, 24(2), 5–9.
- Picot, N., Case, K., Desai, S., Vincent, P., & Bronner, E. (2012). AVISO and PODAAC User Handbook-IGDR and GDR Jason-1 Products. Edition 4.2. SALP-MU-M5-OP-13184-CN, CNES & NASA.
- Sandwell, D. T. (1984). A Detailed View of the South Pacific Geoid From Satellite Altimetry. *Journal of Geophysical Research*, 89(B2), 1089–1104.
- Sandwell, D. T. (1992). Antarctic marine gravity field from high-density satellite altimetry. *Geophysical Journal International*, 109(2), 437–448. DOI: 10.1111/j.1365-246X.1992.tb00106.x
- Sandwell, D. T., & Smith, W. H. F. (1997). Marine gravity anomaly from Geosat and ERS1 satellite altimetry. *Journal of Geophysical Research*, 102(B5), 10039–10054. DOI: 10.1029/96JB03223
- Shah, P., Sajeev, R., & Gopika, N. (2015). Study of Upwelling along the West Coast of India - A Climatological Approach. *Journal of Coastal Research*, 31(5): 1151 - 1158. DOI: 10.2112/JCOASTRES-D-13-00094.1
- Shen, Y., You, X., Wang, J., Wu, B., Chen, J., Ma, X., & Gong, X. (2015). Mathematical model for computing precise local tie vectors for CMONOC co-located GNSS/VLBI/SLR stations. *Geodesy and Geodynamics*, 6(1), 1–6. DOI: 10.106/j.geog.2014.12.001
- Tian, L. L., Guo, J. Y., Han, Y. B., Lu, X. S., Liu, W. D., Wang, Z., ... Wang, H. Q. (2014). Digital zenith telescope prototype of China. *Chinese Science Bulletin*, 59(17), 1978–1983. DOI: 10.1007/s11434-014-0256-z
- Tunini, L., Braitenberg, C., Ricker, R., Mariani, P., Grillo, B., & Fenoglio-Marc, L. (2010). Vertical land movement for the Italian coasts by altimetric and tide gauge measurements. *Procedures ESA Living Planet Symposium*, Bergen, Norway.
- Xing, L. L., Li, J. C., & Liu X. L. (2006). Study on ocean vertical deflection of ENVISAT satellite altimetry along-track geoid gradient (in Chinese). *Science of Surveying and Mapping*, 31(5), 48–49.





## Compaction and Collapse Characteristics of Dune Sand Stabilized with Lime-Silica Fume Mix

Mohammed Y. Fattah<sup>1</sup> Hasan H. Joni<sup>2</sup> and Ahmed S. A. Al-Dulaimy<sup>3</sup>

<sup>1</sup> Professor, Building and Construction Engineering Department, University of Technology, Baghdad, Iraq.

<sup>2</sup> Assistant Professor, Building and Construction Engineering Department, University of Technology, Baghdad, Iraq.

<sup>3</sup> Formerly graduate student, Building and Construction Engineering Department, University of Technology, Baghdad, Iraq.

Email: myf\_1968@yahoo.com

### ABSTRACT

The purpose of this research is to assess the suitability of dune sands as construction materials, moreover, such a purpose is considered beneficial in assessing appropriate methods for soil stabilization or ground improvement and to assess the suitability of dune sands as subgrade layer for carrying roads and rail foundation. Dune sand samples were collected from a region in Baiji area in Salah-Aldeen governorate, North of Iraq. A grey-colored densified silica fume (SF) and lime (L) are used. Three percentages are used for lime (3%, 6% and 9%) and four percentages are used for silica fume (3%, 6%, 9% and 12%) and the optimum percentage of silica fume is mixed with the percentages of lime. Unsoaked CBR on compacted dune sands treated dune sands with L-SF by mixing and cured for a period of 1 day. The increasing in CBR ranged between 443 – 707% at 2.54 mm penetration and 345 – 410% at 5.08 mm penetration.

*Keywords: Dune sand, lime, silica fume, stabilization, CBR, strength.*

## Características de compactación y de colapso de arena de dunas estabilizada con una mezcla de óxido de calcio y óxido de silicio

### RESUMEN

El propósito de esta investigación es evaluar el uso de arena de dunas como materiales de construcción. Además, este objetivo permite determinar los métodos apropiados para la estabilización del suelo, el mejoramiento del terreno y la evaluación de pertinencia de la arena de dunas en capas subbase para carreteras y cimientos féreos. Se recolectaron muestras de arena de dunas en el área de Baiji, del comisionado Salah-Aldeen, al norte de Irak. Se utilizó vapor de óxido de silicio (SF, en inglés), grisáceo y densificado, y óxido de calcio (L). Se utilizaron tres porcentajes para el óxido de calcio (3 %, 6 % y 9 %), y cuatro para el óxido de silicio (3 %, 6 %, 9 % y 12%) y el máximo porcentaje del óxido de silicio se mezcló con las proporciones de óxido de calcio. Se realizó en seco el Ensayo de Relación de Soporte de California (del inglés California Bearing Ratio, CBR) en arena de dunas compactada y tratada con la mezcla L-SF curada durante un día. El incremento en el ensayo CBR osciló entre 443-707 % en la penetración de 2.5 mm y 345-410 % en la penetración de 5.08 mm.

*Palabras clave: Arena de dunas, óxido de silicio, óxido de calcio, estabilización, Ensayo de Relación de Soporte de California.*

*Record*

Manuscript received: 20/05/2015

Accepted for publication: 13/05/2016

*How to cite item*

Fattah, M. Y., Joni, H. H., & Al-Dulaimy, A. S. A. (2016). Compaction and Collapse Characteristics of Dune Sand Stabilized with Lime-Silica Fume Mix. *Earth Sciences Research Journal*, 20(2), 11-18.

doi:<http://dx.doi.org/10.15446/esrj.v20n2.50724>

## Introduction:

Ground improvement refers to any procedure undertaken to increase the shear strength, decrease the permeability and compressibility, or otherwise render the physical properties of soil more suitable for projected engineering use. The improvement may be accomplished by drainage, compaction, preloading, reinforcement, and grouting, electrical, chemical or thermal methods. Among the various soil stabilization procedures, the most suitable one is selected depending upon the type of soil available, time, cost involved etc. (Kumar, 2010).

One of the most dramatic depositional landforms, which occupy large areas all over the world, is sand dune. Sand dunes in various forms cover large areas of the world. Extensive efforts have been made to understand their origin (Shearid, 1989) physical and mineralogical properties, environmental impacts. Some studies have also been directed towards dune sand stabilization (Al-Soud, 2000). There is, however, scarcity in the literature concerning the geotechnical characteristics of these soils.

A single dune can be defined as a mound or hill of sand, which rises to a single summit. They are accumulations of windblown sand, which change their position or their shape due to wind action as long as their surface consists of loose granular material of appropriate size.

Some of typical properties of sand dunes are as follows (Das, 2007):

1. Grain size distribution of the sands at any particular location is uniform. The uniformity can be attributed to the sorting action of the winds.
2. The general grain size percentages decrease with distance from the source, because the wind carries the small particles farther than the large ones.
3. The relative density of sand deposited on the windward side of the dunes is as high as (50-65) % and decreases to about (0-15) % on the leeward.

Collapse is a typical feature of unsaturated, loose and low plasticity soils, which are typical features of dune sand. The behavior of collapsible soil is often quantified by conducting a Collapse Potential Test. However, these test interpret the soil behavior in terms of total stress, while it is well known that the behavior of soil is governed by its effective stress. Also the collapse is defined as the significant volume reduction observed when wetting an unsaturated sample under load. The collapsing behavior of this type of soil generally occurs when the water is introduced into the soil.

Collapsing cause damage too many civil engineering structures such as: spread footing, buildings, roads, highways, and earth dams leading to high economic losses. There are many factors affecting collapse behavior of compacted and soils which are: initial dry unit weight, initial water content, percentage of fines, and the method used in compaction, (Al-Juari, 2009).

To measure the collapsing potential of this type of soil, it may use an oedometer/consolidation ring to prepare an undisturbed sample (similar preparation as consolidation test). When water is introduced to this specimen, the sample may start to collapse, i.e. change in height( $dh/h$ ) or change in initial void ratio ( $e/e_0$ ) may be used as the degree of collapse of the soil.

Janning and Knight discussed the problem in 1957. Then, in 1963, they proposed a test method by which they determined the collapse potential for one specimen under an applied vertical stress of 200kPa, after one day of soaking, (Albusoda and Salem, 2012 and Mansour et al., 2008).

Abbeche et al., 2010 have studied the soil collapse and listed the factors contributing to the occurrence of this phenomenon. The main factors are summarized as follows:

1. An open unstable structure and partially saturated.
2. A high total stress is applied.
3. The presences of cementing agent in the soil, for example calcium carbonate ( $CaCO_3$ ), in unsaturated conditions contribute to stabilize the soil. A moistening the soil will reduce the suction and destroy the liaison officer. Albusoda and Salem (2012) used cement kiln dust (CKD) to stabilize Affek dune sand The effectiveness of adding different percentages of (CKD) was studied. Time of curing effect, was also considered. It was found that stabilization of collapsible soils with CKD can provide tremendous advantages. ading of 8% CKD, for example, increased the ultimate bearing

capacity of shallow foundation to 250%. The variation in shear strength parameters became almost constant after fourteen days of curing.

Vegetation cover on sand dunes mainly depends on wind power (drift potential—DP) and precipitation. When this cover decreases below a minimal percentage, dunes will start moving. It is therefore necessary to study the effects of DP and precipitation on contemporary dune activity in order to predict likely future dune mobility in the coming decades. Ashkenazy et al. (2012) concentrated on the future activity of the currently fixed dune fields of the Kalahari and the Australian deserts. These sand seas include the largest areas of stabilized dunes in the world, and changes in their mobility have significant economic implications. Global maps of DP are introduced, based on real and reanalysis data. Analyses of two global circulation models (GFDL and CGCM3.1) provide future predictions under the SRES-A1B IPCC scenario, which is a moderate global warming scenario. According to the GFDL model, both the Australian and Kalahari basin dunes will apparently remain stable towards the end of the 21st century because the DP will stay small, while the rate of precipitation was expected to remain much above the minimal threshold necessary for the vegetative growth that leads to dune stabilization. The CGCM model predicts insignificant changes in DPs and shows that the precipitation rate is above 500 mm/year for almost the entire Kalahari basin. The central-northern part of Australia is predicted to have larger DPs and greater precipitation than the southern part. Since the predicted changes in DP and precipitation are generally not drastic, both the Australian desert and Kalahari basin dunes are not likely to become active. Still, the Australian dunes are more likely to remobilize than the Kalahari ones due to some decrease in precipitation and an increase in wind power.

The research work carried out by Bouziani et al. (2012) dealt with the effect of dune sand, available in huge quantities in these regions, on the properties of flowing sand-concrete (FSC) prepared with different proportions of dune and river sands. Mini-cone slump test, v-funnel flow-time test and viscosity measurements were used to characterize the behaviour of FSC in fresh state. The 28-day compressive strength was also determined. Test results showed that an optimal content of dune sand, which makes satisfied fresh and hardened properties of FSC, is obtained. Moreover, the obtained flow index (constant b) calculated by the help of power-law viscosity model is successfully correlated to the experimental results of v-funnel flow time.

Jackson et al. (2014) stated that seven types of coastal dune are identified on KwaZulu-Natal coast: estuary barrier dunes; mainland beach foredunes; prograded beachridge dunes; headland bypass dunes; transverse dune fields; parabolic/migrating dunefield; and climbing dunes. The development and distribution of the various dune forms is more strongly controlled by the geological setting, than the aerodynamic regime.

Ciccarelli (2014) tried to assess the conservation status of coastal dune systems in Tuscany (Italy). Emphasis was given to the presence and abundance of plant communities identified as habitat in accordance with the Directive 92/43/EEC. Twenty transects perpendicular to the shoreline were randomly positioned on the whole coastal area (30 km in length) in order to sample the full spectrum of plant communities. Vegetation zonation and relationships with the most frequent disturbance factors in the study area—beach cleaning, coastline erosion, presence of paths and roads, bathing settlements and trampling—were investigated through principal coordinate analysis and canonical correspondence analysis. Natural factors, such as distance from the sea and total length, were also considered. Differences in the conservation status of the sites were found, ranging from the total disappearance of the foredune habitats to the presence of the complete psammophilous (sand-loving) plant communities. Erosion, trampling, and paths were found to be closely correlated with degradation and habitat loss. Furthermore, the overall plant species diversity of dunes was measured with NHDune, a modified version of the Shannon index; while the incidence of invasive taxa was calculated using N, a naturalness index. However, these diversity indices proved to be a weaker bioindicator of ecosystem integrity than habitat composition along transects. A possible strategy for the conservation and management of these coastal areas could be

to protect the foredunes from erosion and limit trampling through the installation of footbridges or the use of appropriate fences.

The purpose of this research is to assess the suitability of dune sands as construction materials. The tests include field density, moisture content, classification, compaction, relative density and CBR test. The effectiveness of adding different percentages of lime-silica fume mix was studied.

**Experimental Work:**

Dune sand samples were obtained from Baiji area in Salah-Aldeen governorate – North of Iraq. Three disturbed samples were taken from the surface at a depth of 0.4 m. The consistency and other physical properties of the dune sand were studied by a series of tests. Lime-silica fume mix is suggested to overcome the problems of dune sands. The physical and chemical properties of these materials are determined. The specification of each material is as follows:

In situ field density ( $\rho_{field}$ ) was obtained by sand-cone test according to (ASTM D 1556-00). The moisture content (%w.c) for the soil studied was determined according to (ASTM D 2216-00).

Grain size distribution was determined by sieve analysis and hydrometer tests conducted on dune sands samples in accordance with (ASTM D 422-00). The grain size distribution of the soil used reveals that the soil is composed of 91% sand, 3% silt and 6% clay.

Table 1 summarizes the physical properties of dune sand.

The minimum and maximum dry densities,  $\rho_{d,min}$  and  $\rho_{d,max}$ , were determined according to (ASTM D 4254-00) and (ASTM D 4253-00), respectively.

**Table 1.** Summary of Baiji dune sand properties.

Soil properties		Baijisand dunes
Total Density, (gm/cm <sup>3</sup> )	$\rho_t$	1.629
Water Content, %	%w	1.23%
Atterberg Limits on Passing No. 40	L.L.	–
	P.L.	–
	P.I.	NP
Group Index	G.I.	0.0
Specific Gravity	$G_s$	2.66
Particle Size Distribution by Wet Sieving	%Gravel	0.00
	% Sand	91.0
	% Fines	9.00
Coefficient of Uniformity	$C_u$	2.56
Coefficient of Curvature	$C_c$	1.60
Classification of Soil	USCS	SP
	AASHTO	A-3
Max. of dry Density, ( $\rho_{d,max}$ ) (gm/cm <sup>3</sup> )	Standard compaction	1.682
	Modified compaction	1.785
Optimum Moisture Content, %(O.M.C)	Standard compaction	13.6%
	Modified compaction	11.0%
Relative Density, %( $D_r$ )	$\rho_{d,min}$ , (gm/cm <sup>3</sup> )	1.485
	$\rho_{d,max}$ , (gm/cm <sup>3</sup> )	1.706
	$e_{max}$	0.795
	$e_{min}$	0.562
	% $D_r$	59.5%
Direct Shear Test	$\phi$ , degree	32°
	c, kPa	0

**The lime material (L):**

Calcium hydroxide (slaked lime) is most widely used for stabilization. Calcium oxide (Hydrated lime) may be more effective in some cases. Chemical and physical tests were carried on the lime material in the National Center for Construction Laboratories and Research (NCCLR) in Iraq. The results of chemical and physical properties of the lime used are shown in Table 2.

**Table 2.** Results of hydrated lime tests.

Physical and Chemical Properties	Results
Chemical Composition, %	
Loss on Ignition (L.O.I)	26.74
Silicon Dioxide (SiO <sub>2</sub> ) + Grays	5.62
Iron Oxide (Fe <sub>2</sub> O <sub>3</sub> )	0.44
Aluminum Oxide (Al <sub>2</sub> O <sub>3</sub> )	0.46
Calcium Oxide (CaO)	66.08
Magnesium Oxide (MgO)	0.10
Sulfur Trioxide (SO <sub>3</sub> )	0.72
Physical Properties	
Specific Gravity, $G_s$	2.30
Density, gm/cm <sup>3</sup>	0.60

**Silica fume material (SF):**

A grey-colored densified silica fume is used. It is a pozzolanic material which has a high content of amorphous silicon dioxide and consists of very fine spherical particles. Silica fume was used as an additive material to improve soil properties. The presence of this substance gives greatly improved internal cohesion, water retention and increased density when set. Chemical and physical tests were carried on the silica fume material in the National Center for Construction Laboratories and Research (NCCLR) in Iraq. The results of the chemical analysis of this material are presented in Table 3.

**Table 3.** Results of silica fume tests.

Physical and chemical properties	Composition
Chemical composition, %	
SiO <sub>2</sub>	> 85%
Fe <sub>2</sub> O <sub>3</sub>	< 2.5%
Al <sub>2</sub> O <sub>3</sub>	< 1%
CaO	< 1%
K <sub>2</sub> O + Na <sub>2</sub> O	< 3%
C (free)	< 4%
S	< 1%
Cl	< 0.2%
L.O.I	< 6%
Physical properties	
Specific gravity, $G_s$	2.25
Density, gm/cm <sup>3</sup>	0.75
Moisture, %	< 2%
Specific surface, m <sup>2</sup> /gr	~20 m <sup>2</sup> /gr

**Compaction test:**

Moisture-density relationship was determined by means of the standard and modified Proctor compaction test. The tests were performed in accordance with (ASTM D 698-00, method A) and (ASTM D 1557-00, method A) standards, respectively. The moisture density relationships are shown in Figure 1.

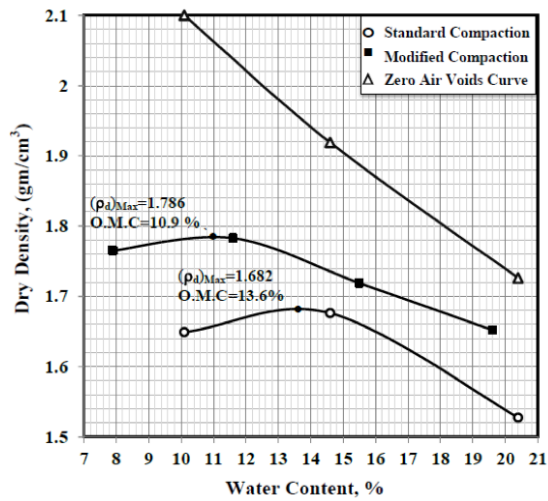


Figure 1. Standard and modified compaction curves for the dune sand.

**California Bearing Ratio (CBR) test:**

CBR-value is used as an index of soil strength and bearing capacity. A series of tests were conducted on each dune sand sample as unsoaked samples. The preparation of specimens and testing procedure were generally in accordance with ASTM D 1883-99 and ASTM D 1557-00. The specimens were prepared at 95% of maximum dry density of the modified compaction test, and compacted in five layers using 4.5 kg hammer dropped from a height of 45 cm. Fifty six blows per layer were used for compacting the two specimens.

California Bearing Ratio values were determined and calculated as follows (ASTM D 1883-99):

$$\% CBR = \frac{\text{Stress for 5.08 mm penetration for soil}}{\text{Stress for 5.08 mm penetration for standard crushed stone}} \times 100 \quad (1)$$

CBR value was measured after 1 day curing for the soil stabilized with L-SF. The test was performed on samples prepared at 95% of optimum moisture content and compacted to various densities.

**Collapse Test:**

Collapse test of soil the soil studied was determined according to (ASTM-D5333-03). The magnitude of one-dimensional collapse that occurs when the soil inundated with water.

The test method consists of placing a compacted soil specimen at the desired water content in an oedometer, applying a predetermined applied vertical stress to the specimen and inundating the specimen with distilled deionized water to induce the potential collapse in the soil specimen. The test method follows these steps.

The one-dimensional response-to-wetting test, which is performed using conventional consolidation equipment represents the frequently used laboratory collapse test for determining the collapse potential of the soil. Pressure was applied until the stress on the sample was equal to (or greater than) that expected in the field or up to 200 kPa as suggested by Jennings and Knight (1975) and as standardized by ASTM D-5333 (2003). According to ASTM D5333 (2003), collapse: indicates a decrease in the height of confined soil following wetting at a constant applied vertical stress.

A standard oedometer ring of 75 mm diameter specimen was prepared in steel ring. After careful placing. The effective vertical stresses used were: (25, 50, 100, 200 and 400) kPa.

The collapse potential ( $I_c$ ) denotes the percent-relative magnitude of collapse determined at any stress level as follows (ASTM D-5333-03):

$$I_c = \frac{\Delta h}{h_o} \times 100 \quad (2)$$

where:  $\Delta h$ = the change in specimen height resulting from wetting, mm, and  $h_o$ = the initial specimen height, mm.

Equation (2) may be rewritten in terms of void ratio as follows:

$$I_c = \frac{e_B - e_1}{1 + e_o} \times 100 \quad (3)$$

where:  $e_B$ ,  $e_1$  = the void ratio at the appropriate stress level before wetting,  $e_1$ ,  $e_2$  = the void ratio at the appropriate stress level after wetting, and  $e_o$  = the initial void ratio.

The collapse index ( $I_e$ ), which is the wetting induced strain measured at a reference stress level of 200 kPa. The classification of collapse index is listed in Table 4, (ASTM D5333-03).

Table 4. Classification of collapse index ( $I_e$ ), (ASTM D5333-03, Table 1).

Collapse Index ( $I_e$ ), %	0	0.1 – 2	2.1 – 6.0	6.1 – 10	> 10
Degree of Specimen Collapse	None	Slight	Moderate	Moderately Severe	Severe

**Results and Discussion:**

Table 5 shows the maximum density, minimum density and relative density values of the soil mixed with different percentages of lime-silica fume mix. The table shows the increase in relative density of soil with increasing of L-SF content due to the low values of the density of lime (0.60 gm/cm<sup>3</sup>) and silica fume (0.75 gm/cm<sup>3</sup>). This indicates that the additives (lime and silica fume) are fine materials and these materials relatively filled the voids of dune sands about on executing maximum density test (ASTM D 4253), which led to the increase in maximum density for soil and thereby increase the relative density. This difference may be attributed to the round - shape of sand particles tested, (Lambe and Whitmen, 1979).

Table 5. Maximum and minimum dry densities and relative densities of soil mixed with different percentages of L-SF.

%L	0				3				6				9			
	3	6	9	12	3	6	9	12	3	6	9	12	3	6	9	12
$\rho_{d,max}$ gm/cm <sup>3</sup>	1.687	1.650	1.624	1.596	1.725	1.683	1.636	1.612	1.773	1.731	1.698	1.604	1.713	1.664	1.637	1.615
$\rho_{d,min}$ gm/cm <sup>3</sup>	1.399	1.373	1.343	1.314	1.351	1.321	1.292	1.276	1.370	1.328	1.307	1.270	1.347	1.308	1.283	1.254
$\rho_{d,max}$ / $\rho_{d,min}$	1.206	1.202	1.209	1.215	1.277	1.274	1.266	1.263	1.294	1.303	1.299	1.263	1.272	1.272	1.276	1.288
%D <sub>r</sub>	76	87	96	100	74	83	94	99	65	75	82	100	76	87	94	99

**Results of compaction test:**

Table 6 and Figure 2 show the moisture-dry density relationship for stabilized soil. By examining the results, the following points could be noticed:

1. For small percentage of silica fume, (3%) and any percentage of lime, there is a decrease in the optimum water content with slight increase in maximum dry density.

2. The soils stabilized with (6%, 9% and 12%) of silica fume and any percentage of lime (which are fine materials) were compacted at lower maximum dry density and higher optimum water content. The increase in optimum moisture content due to addition of lime and silica fume may be caused by the absorption of water by L-SF mix.

3. The percentage (6% L + 3% SF) revealed the maximum dry density.

4. The shape of curves became more flat with increase of the L-SF percentage.

Similar finding was reported by Parsons et al., (2004) and Al-Jobouri, (2013).

**Table 6.** Results of Proctor compaction tests of soil mixed with different percentages of L-SF.

%L	0				3				6				9			
	3	6	9	12	3	6	9	12	3	6	9	12	3	6	9	12
$\rho_{d,max}$ gm/cm <sup>3</sup>	1.700	1.639	1.623	1.602	1.717	1.691	1.658	1.618	1.722	1.708	1.693	1.680	1.713	1.687	1.685	1.660
OMC %	13.7	14.4	15.4	15.5	14.4	14.2	15.0	15.0	13.4	13.9	14.0	14.2	13.3	14.0	14.2	14.3

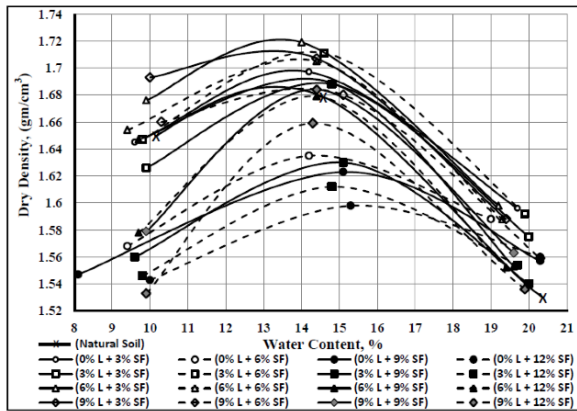


**Figure 2.** Variation of the dry density with moisture content of standard Proctor compaction for soil mixed with different percentages of L-SF.

**Results of California bearing ratio (CBR) tests:**

The values of stresses are plotted against depth of penetration in Figure 3. Stress and penetration curves for Baiji dune sands consist of an approximately straight portion for about 3 mm penetration in which stress and penetration are directly proportional, then tend to become a horizontal at further penetration.

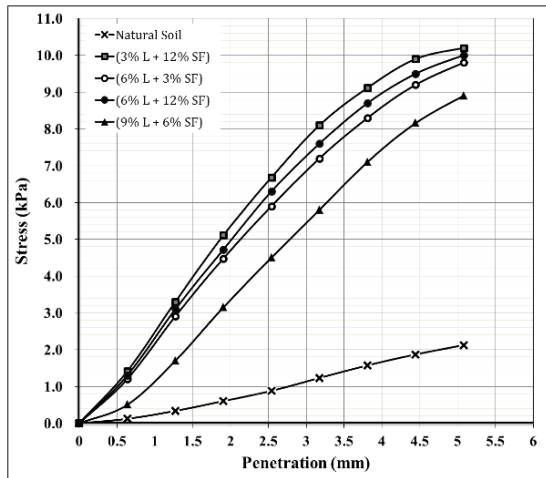


**Figure 3.** Stress-penetration curves from CBR test for natural dune sand and selected soils stabilized with different percentages of L-SF by mixing.

Unsoaked CBR values at 2.54 and 5.08 mm penetration are plotted in Figure 4 and summarized in Table 7. The higher CBR values are obtained at 5.08 mm penetration for Baiji dune sands, where the soil is sand and containing lower percentage of material passing the No. 200 sieve.

**Table 7.** Results of CBR test a chosen soils stabilized by mixing with L-SF.

Dune sands with L-SF mix		California Bearing Ratio test (4.5 kg Hammer), %		Increasing in CBR, %	
% L	% SF	At 2.54 mm penetration	At 5.08 mm penetration	At 2.54 mm penetration	At 5.08 mm penetration
0	0	12.0	19.4	—	—
3	12	96.8	99.0	707	410
6	3	85.5	95.1	613	390
	12	91.3	97.1	661	401
9	6	65.2	86.4	443	345

The results of Figure 4 show that when stabilizing the soil with L-SF after curing for 1 day, there is an increase in CBR due to the increase in the angle of internal friction ( $\phi$ ) or cohesion (c) or both. The added materials of L-SF play the major role in stabilization. Using this type of material is reflected in the improvements in terms of bearing capacity which is directly proportional to CBR.

CBR-value increase with increasing silica fume but this increasing reduces with increasing lime. The increase in CBR ranged between (443–707)% at 2.54 mm penetration and (345–410) % at 5.08 mm penetration as illustrated in Table 7 and this increase is calculated as follows:

$$\% \text{ increase in CBR} = \frac{\text{CBR of treated soil} - \text{CBR of natural soil}}{\text{CBR of natural soil}} \times 100 \quad (4)$$

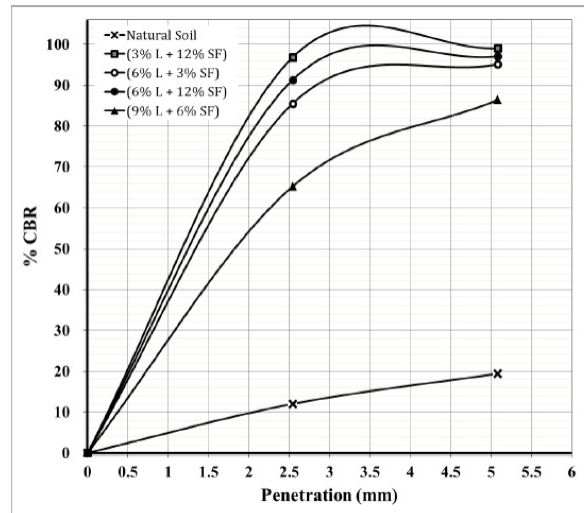


**Figure 4.** CBR-value of natural dune sand compacted and stabilized with different percentages of L-SF by mixing at different penetrations.

**Results of Collapse Test:**

Single oedometer test is selected for the collapse test for disturbed and undisturbed samples. This test is carried out according to the procedure recommended by ASTM D5333.

Collapse potential (Ic) and collapse index (Ic) magnitude are determined according ASTM D5333-03 by using the conventional oedometer device in a constant temperature and humidity environmental at different stress level. It shows high values when flooding the specimens by water during primary consolidation. It is concluded that there is an increases in collapsibility due to removal of bonding between particles upon wetting due to stress release and leaching of soil during



The calculated collapse index ( $I_c$ ) gives an indication that degree of specimen collapse for soil. Baiji dune sands undergo only small collapse. The degree of collapse of this natural soil is classified as “Slight” under different soaking pressure. This result coincides with the results found by (Al-Taiet et al., 2013). Also degree of collapse for treated soils by mixing with L-SF mix are classified as “Slight” as shown in Table 8.

**Table 8.** Results of collapse potential test a chosen soils stabilized by mixing with L-SF.

Dune Sands with L-SF mix		Collapse Index ( $I_c$ ), %	Decreasing in ( $I_c$ ), %	Degree of Specimen Collapse
% L	% SF			
0	0	1.66	Natural soil	Slight
3	12	1.29	22.4	Slight
6	3	1.37	17.2	Slight
	12	1.06	36.0	Slight
9	6	1.31	21.0	Slight

Figure 10 gives the collapse percent versus percent of lime and silica fume, diagrams obtained from one dimensional consolidation. It is clear that there is a slightly decrease in collapse with increasing stabilizers content. L-SF is effective in reducing the collapse potential of the soil. On the other hand, add L-SF decrease void ratio of soil. This indicates that the additives (lime and silica fume) are fine materials and these materials relatively filled the voids of dune sands about on executing compaction, which led to the increase in relative density for soil and thereby decrease the collapse index.

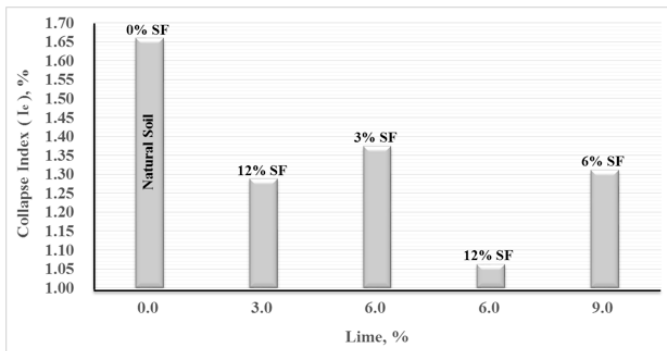


**Figure 10.** Effect of additives (lime and silica fume) on collapse potential for natural dune sand and selected soils stabilized with different percentages of L-SF by mixing.

**Conclusions:**

1. The mix of L-SF allowed compaction of the soil at higher maximum dry density. The treatment with L-SF shows a general increase in the maximum dry density from (1.609 to 1.722) gm/cm<sup>3</sup> of standard compaction, and from (1.609 to 1.834) gm/cm<sup>3</sup> of modified compaction at (6% L + 3% SF).

2. The optimum water content increases from 13.6% to 15.5% at 12% SF of standard compaction, the increase in the optimum moisture content is due, in spite of the reduced surface area caused by flocculation and agglomeration, to the additional fine contents to the samples which requires more water in addition to the free lime and silica fume that needed more water for the pozzolanic reactions to take place.

3. Unsoaked CBR on compacted dune sands treated with L-SF by mixing and cured for a period of 1 day, exhibited higher CBR values than compacted untreated dune sands. Moreover, the 5.08 mm penetration CBR of the treated dune sands is higher than the 2.54 mm penetration CBR. The increasing in CBR ranged between 443 – 707% at 2.54 mm penetration and 345 – 410% at 5.08 mm penetration.

4. The degree of collapse of natural Baiji dune sands and treated soils by mixing with L-SF mix are classified as “Slight” under different soaking pressure.

5. The difference in collapse potential between some percent of L-SF becomes very little. This means that any additional amount of L-SF does not improve considerably the control of collapse. Collapse potential and collapse index decreased with stabilizers content and drop to ( $I_c = 1.06%$ ) at (6%L + 12%SF). Finally, L-SF treatment in dune sands generally reduces collapse. The decreasing in collapse index ranged between (17.2–36)% at 200 kPa for treated soils.

**References:**

Abbech, E. K., Laouar, M. S., & Messaoud, F. (2010). Prediction of collapsible soils by cone penetrometer and ultra-sonic tests. *Studia Geotechnica et Mechanica*, vol. XXXII, no. 2.

Albusoda, B. S. & Salem, L. A. (2012). Stabilization of dune sand by using cement kiln dust (CKD). *Journal of Earth Sciences and Geotechnical Engineering*, 2(1), 131-143.

Al-Jobouri M. M. (2013). Strength and compressibility characteristics of soft soil stabilized with lime silica fume mix. M.Sc. thesis, Civil Engineering Department, University of Baghdad, Iraq.

Al-JuariKh A. (2009). Volume change measurement of collapsible soil stabilized with lime and waste lime. *Civil Engineering, Tikrit Journal of Engineering Sciences*, 16(3), 38-54.

Al-Soud, M. S. (2000). Stabilization of Baiji sand dunes by petroleum residues. M.Sc. thesis, Civil Engineering Department, University of Baghdad, Iraq.

Al-Taie, A. J., Al-Shakarchi, Y. J., & Mohammed, A. A. (2013). Investigation of geotechnical specifications of sand dune soil. A case study around Baiji Iraq. *Civil Engineering, International Journal of Advanced Research*, 1(6), 208-215.

Ashkenazy, Y., Yizhaq, H., & Tsoar, H. (2012). Sand dune mobility under climate change in the Kalahari and Australian deserts. *Climatic Change*, 112, 901–923, DOI: 10.1007/s10584-011-0264-9.

ASTM D1883-99 (1999). Standard test methods for CBR (California Bearing Ratio) of laboratory-compacted soils. American Society for Testing and Materials.

ASTM D5333-03 (2003). Standard test methods for measurement of collapse potential of soils. American Society for Testing and Materials.

Bouziani, T., Bederina, M., Hadjoudja, M. (2012). Effect of dune sand on the properties of flowing sand-concrete (FSC). *International Journal of Concrete Structures and Materials*, 6(1), 59-64. DOI 10.1007/s40069-012-0006-z.

Ciccarelli, D. (2014). Mediterranean coastal sand dune vegetation: influence of natural and anthropogenic factors. *Environmental Management*, 54, 194–204. DOI: 10.1007/s00267-014-0290-2.

Cooke, R. U., & Warren, A. (1973). *Desert geomorphology*. London: B. T. Batsford Ltd., 374 pp. 1st. Edition.

Das, B. M. (2007). *Principles of foundation engineering*. Adapted International Student Edition, Nelson a Division of Thomson Canada Limited. Sixth edition.

Jackson, D. W. T., Cooper, J. A. G., & Green, A. N. (2014). A preliminary classification of sand dunes of the KwaZulu-Natal coast. In: Green, A. N. & Cooper, J. A. G. (eds.), *Proceedings 13th International Coastal Symposium (Durban, South Africa)*, *Journal of Coastal Research, Special Issue 70*, 9, pp. 718-722, ISSN 0749-0208. DOI: 10.2112/SI70-121.1.

- Jannings, J. E., & Knight, K. (1975). A guide to truction on or with materials exhibiting additional settlement due to collapse of grain structure. Proceedings, sixth regional conference for Africa on soil mechanics and foundation engineering Johannesburg, SouthAffrica, pp. 99-105.
- Kumar, S. (2010). A study on the engineering behaviour of grouted loose sandy soils. Ph.D. thesis, Division of Civil Engineering, Cochin University of Science and Technology, India, 2010.
- Lambe, T. W. & Whitman, R. V. (1979). Soil mechanics. John Wiley and Sons Inc., New York.
- Mansour, Z., Chik, Z., & Taha, M. R. (2008). On soil collapse potential evaluation. University Kebangsaan Malaysia, ICCBT 2008 -E- (03), pp. 21-32.
- Parsons, R. L., Kneebone, E., & Milburn, J. P. (2004). Use of cement kiln dust for subgrade stabilization. Final Report, Kansas Department of Transportation, USA.
- Shearzid, M. F. (1989). Sediment wind and its impact on the design of human settlements. M.Sc. thesis, Department of Architectural Engineering, University of Technology, Baghdad, Iraq.



## Classification of cut slopes in weathered meta-sedimentary bedrocks

Johnbosco Ikenna Nkpadobi, John Kuna Raj and Tham Fatt Ng

### ABSTRACT

In order of abundance, the meta-sedimentary rocks along Pos Selim Highway in Perak state Malaysia comprise quartz mica schist, graphitic schist and quartzite layers. Field investigations revealed that these meta-sedimentary rocks have gradational weathering profile based on differences particularly in textures, hardness, lateral changes in colour, and consistency of material extension. The results from uniaxial compressive strength tests confirmed field observations whereby failure occurred mostly on outcrops having joints almost perpendicular to foliation. From the kinematic analyses, the investigated cut slopes are unstable with possibilities of wedge and planar failures. Application of rock mass classification schemes including Rock Quality Designation (RQD) and Rock Mass Rating (RMR) yielded almost similar poor to good quality ranges for each investigated rock mass. While Slope Mass Rating (SMR) classified the cut slopes from stable to unstable slopes, this study categorized them into one actively unstable, four marginally stable and five stable slopes.

*Keywords: Weathering, Uniaxial Compressive Strength, Slope stability, Rock Quality Designation, Rock Mass Rating, Slope Mass Rating.*

## Clasificación de Taludes de Corte en Sustratos Rocosos Metasedimentarios Meteorizados

### RESUMEN

En orden de abundancia, las rocas metasedimentarias a lo largo de la carretera Pos Selim, en el estado Perak de Malasia, se componen de esquistos de cuarzo mica, esquistos de grafito y capas de cuarzo. Las investigaciones de campo revelan que estas rocas metasedimentarias tienen perfiles de meteorización progresiva basados en diferencias particulares como textura, dureza, cambios laterales de color y consistencia del material de extensión. Los resultados de los ensayos uniaxiales de esfuerzo de compresión confirmaron las observaciones de campo por las cuales se estableció que las fallas ocurrieron mayormente en los afloramientos con coyunturas perpendiculares hacia la foliación. De los análisis cinemáticos se desprende que los taludes de corte investigados son inestables con posibilidades de fallas planas y de cuña. La utilización de esquemas de clasificación rocosa como el índice RQD (del inglés Rock Quality Designation) y la clasificación geomecánica de Bienawski o RMR (del inglés Rock Mass Rating) evidencia rangos similares de baja y buena calidad para cada masa rocosa estudiada. Mientras que el índice de taludes SMR (del inglés Slope Mass Rating) clasificó los taludes de corte de estables a inestables, este estudio los categorizó de uno activamente inestable, cuatro marginalmente estables y cinco estables.

*Palabras clave: Meteorización, esfuerzo de compresión uniaxial, estabilidad de talud, Designación Cualitativa de Roca, Clasificación Geomecánica de Bienawski, índice de SMR.*

*Record*

Manuscript received: 30/08/2015

Accepted for publication: 04/03/2016

*How to cite item*

Nkpadobi, J. I., Raj, J. K., & Ng, T. T. (2016). Classification of cut slopes in weathered meta-sedimentary bedrocks. *Earth Sciences Research Journal*, 20(2), J1-J9.

doi:<http://dx.doi.org/10.15446/esrj.v20n2.52781>

**1. Introduction**

Information gathered from field investigations by geologists and engineers is insufficient to predict geotechnical behaviour of rocks and rock masses, which calls for laboratory investigations to ascertain the response of rocks under a wide variety of disturbances. The uniform definition of geotechnical engineering by Murthy (2002), Venkatramaiah (2006), and Das and Sobhan (2013) is that it deals with the application of the principles of soil and rock mechanics to the design of foundations, retaining structures, and earth structures. In this investigated area, previous studies by Mohd Asbi & Associates (2005) and Andrew Malone Ltd (2007) classified the stability of the cut slopes using kinematic analyses. To ensure further understanding of the characterization of the slopes, this study carried out field observations, laboratory and computational analyses of the geotechnical properties of the rocks and then utilized the recorded and derived data for rock mass and slope mass classifications.

**2. Geological setting of investigated area**

The study area is along Pos Selim Highway in Perak State Malaysia. It traverses through the Titiwangsa Main Range mountainous terrain reaching highest altitude of 1587m above sea level at Gunung Pass and terminating at 1420m above sea level at Perak/Pahang states boarder. This study begins at latitude 4° 33' 44" and longitude 101° 18' 86" extending to 17.7km and terminating at latitude 4° 35' 95" and longitude 101° 20' 80". Granite and schist are the two major Formations covering 60% and 40% of the area respectively (Fig. 1). This investigation focused on the schist, which according to Tajul (2003) might probably be of Upper Palaeozoic. In order of abundance the schist consists of quartz mica schist, graphitic schist and quartzite layers. Petrographic analyses by Mohd Asbi & Associates (2005), Andrew Malone Ltd (2007), Nkpadobi (2014) and Nkpadobi et al. (2015) classified the schist as quartz-mica schist, graphitic schist, phyllite and quartzite, and photomicrographs confirm that most of the quartz mica schist are mylonitized.

The major identified failure types in the area include planar sliding, wedge failure, and complex failures characterized by slump and earth flow which occurred along the Gunung Pass axis. The geometrical properties of failed slopes are shown in Table 1. However, the plausible triggering factors for these different types of failures varied. Figs. 2(a) - (c) represent these planar, wedge and complex failures in the area respectively.

**Table 1.** Geometrical properties of failed slopes.

Slope location / Chainage	Slope orientation		Type of failure	Failed zone		Slip angle (Deg)	Slip direction (Deg)
	Slope angle (Deg)	Slope direction (Deg)		Failure height (m)	Lateral extent (m)		
003 / 14350	45	228	Planar	6	15	35	100
004 / 14800	63	236	Wedge	8	18	Various angles	Various directions
006 / 17800	63	110	Planar	6	-	48	100
007 / 18400	63	100	Planar	6	12	50	100
010 / 21200	68	60	Planar	6	-	53	130
014 / 24400	63	250	Complex	40	200	Complex	Complex



**Figure 2.**  
(a) Planar failure. (b) Wedge failure. (c) Complex failure.

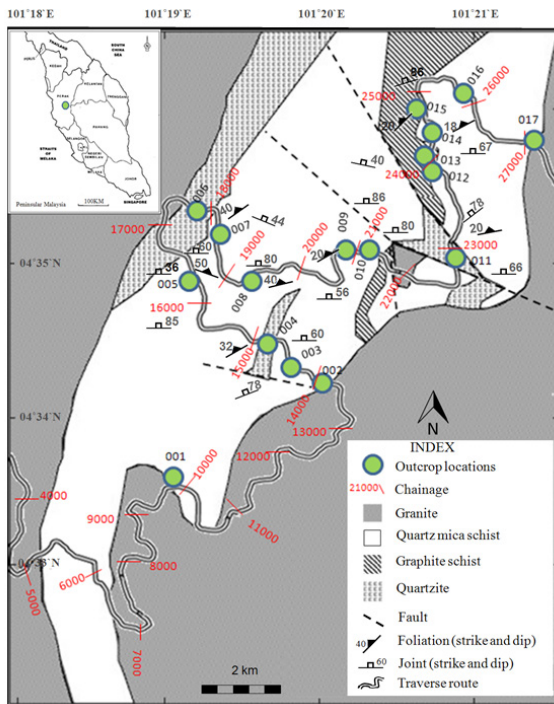


**Figure 1.** Geological map of the study area.

**2.1 Description of weathering profile over quartz mica schist**

Since the failures in quartz mica schist occurred in the weathered zones, the characteristics of these weathered earth materials were studied in order to interpret the features of the morphological zones. The photograph and schematic diagram of weathering profile of location 010 shown in Fig. 3 is typical of quartz mica schist units. Employing BSI (1981) code of practice for site investigations, the weathering profile was graded. By identifying the lateral changes in colour, texture, hardness, and consistency of material extension, the weathering profiles over the quartz mica schist are broadly differentiated into three zones; pedological soil zone, intermediate zone and bedrock zone corresponding to zones I, II and III respectively. Based on differences particularly in textures and structures of original bedrock as well as degree of preservation of the constituent minerals, these three broad zones are further differentiated into thinner characteristic horizons.

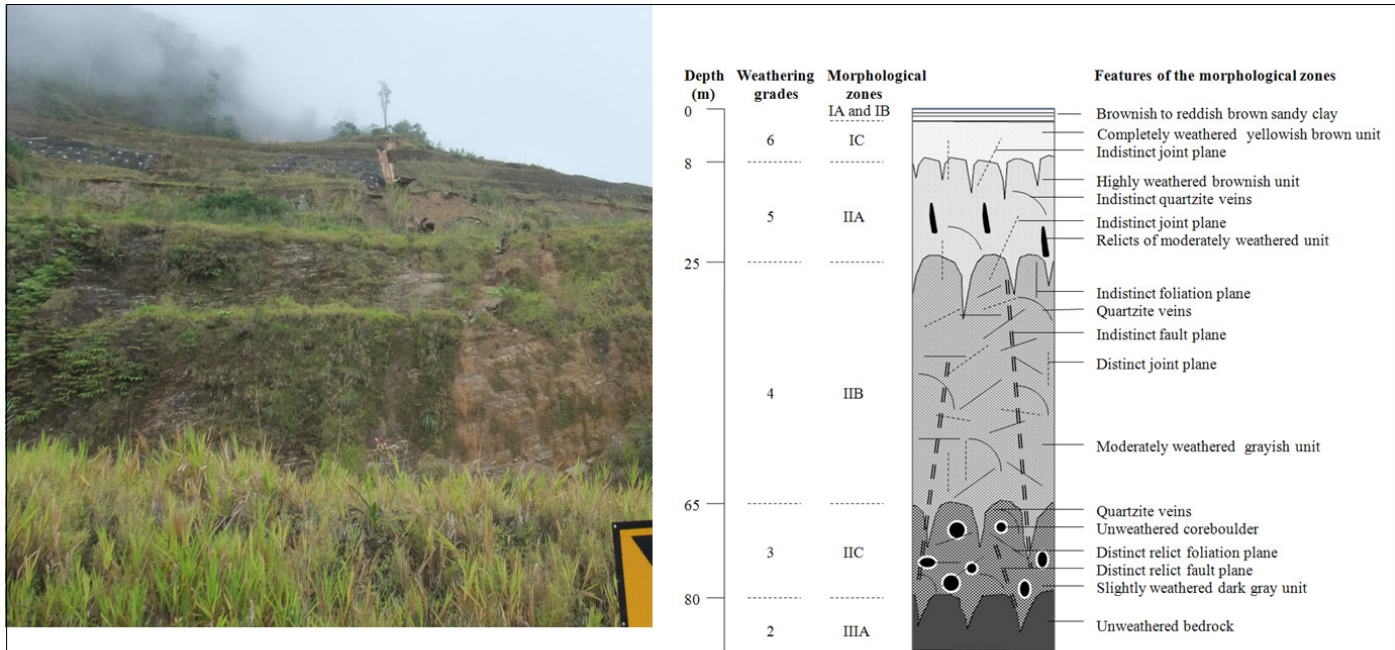


Figure 3. Field photograph and schematic diagram of weathering profile over quartz mica schist at location 010.

Zone I with vertical thickness of less than 8m which corresponds to grade 6 is further sub-divided into IA, IB, and IC. Horizons IA and IB are brownish to reddish brown pedological soil profile, whereby IA which is less than 1m is friable sandy clay, whereas IB which is less than 2m is firm sandy clay. Horizon IC is completely weathered, stiff yellowish brown sandy clay devoid of any distinct discontinuity plane. Greater attention is focused on zone II because of its extensive thickness, complexity, and easy accessibility. With vertical thickness measuring up to 72m, this zone II comprises about 24% vertical thickness of higher horizon IIA (corresponding to grade 5) of highly weathered brownish unit devoid of distinct discontinuity plane, but with intercalations of relicts of moderately weathered units. The lower horizon IIB is about 55% vertical thickness of the entire zone II, comprising moderately weathered grayish coloured quartz mica schist. It corresponds to grade 4, exhibits conspicuous quartzite veins, and distinct joint and foliation planes, but indistinct fault plane. Horizon IIC is the lowest horizon of zone II, and it corresponds to grade 3. With vertical thickness of about 21% of the entire zone II, this slightly weathered dark gray unit comprises distinct relict discontinuity planes and unweathered core-boulders which are very prominent. Zone III which is schematically represented only by morphological zone IIIA is unweathered bedrock which experiences the effect of weathering only along and between structural discontinuity planes.

3. Materials and methodology

3.1 Measurement of rock mass jointing

To ensure adequate representation of the joint parameters, the joint orientations were recorded using scanline and random survey techniques. Joint spacing and persistence were measured with ruler and tape while the aperture was measured with caliper. According to Palmström (2005), joint frequency is defined as the number of joints per meter length, and this was calculated as the inverse of joint spacing. The variations of joint spacing and frequency of joint sets are shown in Table 2. The average volumetric joint count  $J_v$  was calculated as the sum of the average frequency of the joint sets while field recording of the conditions of the joints include their hydraulic conditions, material infill and roughness. The general characterization of the rock mass jointing for the investigated slopes is presented in Table 3 and these data shall be applied in rock mass and slope mass classifications.

Table 2. Summary of spacing and frequency of individual joint sets.

Cut slopes	Joint sets	Dip dir. /Dip (Deg)	Variation of joint set spacing and frequency				Average spacing (m)	Average frequency
			Min. spacing (m)	Max. spacing (m)	Max. frequency	Min. frequency		
Location 004	J1	192/60	0.02	0.4	50	2.5	0.21	4.76
	J2	182/78	0.1	0.6	10	1.67	0.35	2.86
Location 005	J1	210/60	0.2	0.6	5	1.67	0.4	3.34
	J2	306/36	0.2	0.4	5	2.5	0.3	3.75
	J3	352/85	0.2	0.4	5	2.5	0.3	3.75
	J4	270/46	0.2	0.4	5	2.5	0.3	3.75
Location 006	J1	232/62	0.2	0.6	5	1.67	0.4	3.34
	J2	210/78	0.2	0.6	5	1.67	0.4	3.34
	J3	332/66	0.4	0.6	2	1.67	0.5	1.84
	J4	310/48	0.4	0.6	2	1.67	0.5	1.84
Location 007	J1	260/44	0.02	0.6	50	1.67	0.31	3.23
	J2	328/80	0.02	0.6	50	1.67	0.31	3.23
	J3	322/58	0.02	0.6	50	1.67	0.31	3.23
Location 008	J1	260/74	0.06	0.2	16.67	5	0.13	7.7
	J2	334/80	0.1	0.15	10	6.7	0.13	8.35
	J3	320/64	0.1	0.15	10	6.7	0.13	8.35
Location 009	J1	260/56	0.06	0.2	16.67	5	0.13	10.84
	J2	295/66	0.06	0.4	16.67	2.5	0.23	9.6
Location 010	J1	308/86	0.2	0.6	5	1.67	0.4	2.5
	J2	130/86	0.2	0.6	5	1.67	0.4	2.5
	J3	230/88	0.4	0.6	2.5	1.67	0.4	2.5
	J4	340/80	0.2	0.4	5	2.5	0.3	3.33
	J5	260/66	0.2	0.4	5	2.5	0.3	3.33
Location 011	J1	36/78	0.2	0.6	5	1.67	0.4	3.34
	J2	312/66	0.2	0.4	5	2.5	0.3	3.75
	J3	190/78	0.2	0.4	5	2.5	0.3	3.75
Location 014	J1	145/82	0.2	0.6	5	1.67	0.4	3.34
	J2	180/67	0.2	0.6	5	1.67	0.4	3.34
	J3	240/88	0.2	0.6	5	1.67	0.4	3.34
	J4	20/40	0.3	0.5	3.33	2	0.4	2.65
Location 015	J1	147/80	0.2	0.6	5	1.67	0.4	2.5
	J2	238/86	0.2	0.6	5	1.67	0.4	2.5
	J3	18/38	0.2	0.4	5	2.5	0.3	3.33

**Table 3.** General characteristics of the rock mass jointing.

Cut slopes	Maximum persistence (m)	Aperture (mm)	Average volumetric joint count Jv	Infilling	Hydraulic condition	Condition of discontinuity
Location 004	8	2 - 10	7.62	Clayey	Dripping	Slightly rough surface
Location 005	1	0.25 - 5	14.6	Shrubs and clayey	Damp	Slightly rough surface
Location 006	3	0.1 - 0.25	10.36	None	Damp	Slightly rough surface
Location 007	2	0.25 - 0.5	9.7	Shrubs and clayey	Wet	Slightly rough surface
Location 008	1	0.1 - 0.5	24.4	Clayey	Damp	Slightly rough surface
Location 009	0.8	0.1 - 0.25	20.44	Clayey	Damp	Slightly rough surface
Location 010	0.6	0.1 - 0.25	14.16	None	Dry	Slightly rough surface
Location 011	1	0.1 - 0.25	10.84	Shrubs	Flowing	Slightly rough surface
Location 014	0.6	0.1 - 0.25	12.67	None	Dry	Slightly rough surface
Location 015	1	0.1 - 0.25	8.33	None	Dry	Smooth

**3.2 Kinematic stability assessment**

Kinematic stability assessment method was applied in order to identify critical planes of weakness in the rock slopes and outline potential danger and likely modes of failure. Measurements of discontinuities were carried out with the use of both scanline and random survey techniques. The slope face orientation was also measured. These analyses were based on Markland's test as described in Hoek and Bray (1981). Pole intensity greater than 4% was regarded as a major discontinuity and assumed friction angle along the discontinuities in the rocks is averaged at 25°. Table 4 shows the summary of the orientations of the major discontinuity planes and slope face orientations.

**Table 4.** Summary of the orientations of slope locations and major discontinuities.

Summary of the investigated discontinuities								Slope face orientation	
Cut slopes	Elevation (m)	Discontinuity data	Dip (Deg)	Dip Direction (Deg)	Discontinuity Set	Intensity	Remark	Slope angle (Deg)	Slope direction (Deg)
Location 004	1003	115	32	110	J1	>8%	Foliation	63	236
			60	192	J2	>8%	Joint		
			78	182	J3	>4%	Joint		
Location 005	1061	120	50	98	J1	>8%	Foliation	63	246
			60	210	J2	>8%	Joint		
			36	306	J3	>4%	Joint		
			85	352	J4	>4%	Joint		
			46	270	J5	>4%	Joint		
Location 006	1114	119	40	100	J1	>8%	Foliation	63	110
			62	232	J2	>8%	Joint		
			78	210	J3	>8%	Joint		
			66	332	J4	>4%	Joint		
			48	310	J5	>4%	Joint		
Location 007	1129	120	40	100	J1	>8%	Foliation	63	100
			44	260	J2	>4%	Joint		
			80	328	J3	>4%	Joint		
			58	322	J4	>4%	Joint		
			40	102	J1	>8%	Foliation		
Location 008	1155	110	74	260	J2	>8%	Joint	63	98
			80	334	J3	>4%	Joint		
			64	320	J4	>4%	Joint		
			56	260	J1	>8%	Joint		
Location 009	1206	105	20	190	J2	>4%	Foliation	63	250
			66	295	J3	>4%	Joint		
			86	308	J1	>8%	Joint		
Location 010	1214	117	86	130	J2	>8%	Joint	68	60
			88	230	J3	>4%	Joint		
			80	340	J4	>4%	Joint		
			66	260	J5	>4%	Joint		
			20	228	J1	>8%	Foliation		
Location 011	1275	120	78	36	J2	>8%	Joint	70	250
			66	312	J3	>4%	Joint		
			78	190	J4	>4%	Joint		
			82	145	J1	>8%	Joint		
Location 014	1348	102	18	335	J2	>8%	Foliation	63	250
			67	180	J3	>8%	Joint		
			88	240	J4	>8%	Joint		
			40	20	J5	>4%	Joint		
			80	147	J1	>8%	Joint		
Location 015	1366	101	20	337	J2	>8%	Foliation	70	250
			86	238	J3	>8%	Joint		
			38	18	J4	>4%	Joint		

**3.3 Uniaxial compressive strength test**

Very large rock blocks were collected in the field with use of sledge hammer and chisel for this very test, and the laboratory determination of the strength of the rock samples was carried out using ISRM (1981a) standard. As shown in Fig. 4(a), the rock samples were prepared into right circular cylinders ranging from 12.5 to 15cm in height and 5cm in diameter using diamond embedded rock core drilling machine while Fig. 4(b) shows the set up of this test. The uniaxial compressive strength of the samples was then determined under dry condition which is their ultimate strength.



**Figure 4.**

(a) Some of the rock core samples. (b) Set up of uniaxial compressive strength test.

**4. Results and discussions**

**4.1 Uniaxial compressive strength (UCS)**

It was observed that the tested samples failed axially following joint trends and fissures, almost perpendicular to foliation. This confirmed field observations whereby failure occurred mostly on outcrops having joints almost perpendicular to foliation. Although some metamorphic rocks tested by Horino and Ellickson (1970) and Broch (1974) showed that uniaxial compressive strength of the rocks are almost the same at different orientations of foliation, but in these tested quartz mica schist samples, there are significant differences in the strength in different orientations of the well developed foliations. Where the orientation of the foliation to the horizontal is less than 45° in some quartz mica schist samples, failure occurred along the foliation plane. Several tests showed consistency of failure modes in graphitic schist, whereby majority of the failures occurred along orientations of foliations at 45° with minimal oblique joint trends. The determined uniaxial compressive strength of quartz mica schist samples shown in Table 5 ranges from 56MPa to 117MPa, while graphitic schist has value of 87MPa. According to classification of the uniaxial compressive strength of rocks by Deere and Miller (1966), Bieniawski (1978), ISRM (1978 and 1981b), the rocks of the study area fall within medium to high strength. This gives insight into the observed failure mechanisms whereby most of the failures were controlled by discontinuities.

**Table 5.** Uniaxial compressive strength (UCS) and Rock Quality Designation (RQD).

Cut slopes location number	Chainage	Rock type	UCS (MPa)	Jv	RQD (%)	Rock quality
004	14800	Quartz mica schist	110	7.62	90	Good
005	16400	Quartz mica schist	117	14.6	66.8	Fair
006	17800	Quartz mica schist	76	10.36	80.8	Good
007	18400	Quartz mica schist	89	9.7	83	Good
008	19300	Quartz mica schist	84	24.4	34.5	Poor
009	20900	Quartz mica schist	56	20.44	47.6	Poor
010	21200	Quartz mica schist	61	14.16	68.3	Fair
011	22750	Quartz mica schist	97	10.84	79.2	Good
014	24400	Quartz mica schist	76	12.67	73.2	Fair
015	24780	Graphitic schist	87	8.33	87.5	Good

#### 4.2 Rock mass classification

Rock mass classification has been developing over the years and various classification schemes have considered a lot of factors such as water content, discontinuities and rock strength. In this study, the considered rock mass classification schemes include Rock Quality Designation (RQD) and Rock Mass Rating (RMR).

##### 4.2.1 Rock Quality Designation (RQD)

Rock Quality Designation (RQD) index was developed by Deere (1963). It is defined as the percentage of intact rock mass length that are 10cm or longer from borehole drill cores. In absence of drill core logs but where discontinuity traces are visible in rock surface exposures, Palmström (1982) suggested that Rock Quality Designation (RQD) might be estimated from the number of discontinuities per unit volume using below equation:

$$RQD = 115 - 3.3J_v \quad (1)$$

Where  $J_v$  known as the volumetric joint count is the sum of the number of joins per unit length for all joint sets. Using already determined

values of  $J_v$  and applying equation 1, the RQD values for the rock masses are presented in Table 5. According to Deere (1968) relationship between RQD and the engineering quality of rock mass, the RQD values determined in this work range from 34.5% to 90% covering a broad range of poor, fair and good quality rocks. In view of non-consideration of joint orientation, joint condition, type of joint, infilling and stress condition by RQD index, Singh and Goel (1999) advised that its sole consideration for classification is insufficient to provide adequate description of a rock mass.

##### 4.2.2 Rock Mass Rating (RMR)

Rock Mass Rating (RMR) or Geomechanics classification was initially developed by Bieniawski (1976). The system has evolved due to a better understanding of the importance of the different parameters and increased experience leading to changes to the ratings of parameters. As a result of these advancements, the Bieniawski (1989) version was employed in this study. This scheme uses six parameters: Uniaxial compressive strength of rock material, rock quality designation (RQD), spacing of discontinuities, condition of discontinuities, groundwater conditions and orientation of discontinuities. As explained in Bieniawski (1989), estimation of RMR is the sum of the total ratings of each of the above listed six parameters. Considering the dip angles of the joints in these high cut slopes, -5 rating adjustment for discontinuity orientations was used. As presented in Table 6, the discontinuity condition is the sum of joint persistence, aperture, roughness, infilling and weathering ratings. This RMR scheme has five rock mass classes determined from total ratings ranging from very poor rock to very good rock.

In order to determine the RMR for the investigated extended cut slope, the already determined values of the six parameters were substituted with their individual ratings and the rock masses range from fair to good rocks. The estimation of the RMR of the investigated rock masses are presented in Table 7. Unlike in RQD index where quartz mica schist at location 004 yielded highest value of 90%, in this RMR only quartz mica schist at locations 010 and 014 and graphitic schist at location 015 yielded highest value of 62 and designated good rocks. Although the remaining cut slopes are in quartz mica schist and designated fair rocks, the quartz mica schist at locations 008 and 009 maintained the lowest RMR values of 43 and 44 respectively. The advantage of rock mass classification using RMR is that it incorporates geological, geometric and engineering parameters in arriving at a quantitative value of the rock mass quality.

**Table 6.** Determination of condition of discontinuities.

Cut slopes locations / Chainage	Persistence		Aperture		Roughness		Infilling		Weathering range		Conditions of discontinuities
	Max. value (m)	Rating	Range (mm)	Rating	Condition	Rating	Condition	Rating	Condition	Rating	
004 / 14800	8	2	2-10	2	Slightly rough	3	Soft filling <5 mm	2	Slightly weathered	5	14
005 / 16400	1	4	0.25-5	1	Slightly rough	3	Soft filling <5 mm	2	Slightly weathered	5	15
006 / 17800	3	4	0.1-0.25	4	Slightly rough	3	None	6	Moderately weathered	3	20
007 / 18400	2	4	0.25-0.5	1	Slightly rough	3	Soft filling <5 mm	2	Moderately weathered	3	13
008 / 19300	1	4	0.1-0.5	1	Slightly rough	3	Soft filling <5 mm	2	Slightly weathered	5	15
009 / 20900	0.8	6	0.1-0.25	4	Slightly rough	3	Soft filling <5 mm	2	Highly weathered	1	16
010 / 21200	0.6	6	0.1-0.25	4	Slightly rough	3	None	6	Moderately weathered	3	22
011 / 22750	1	4	0.1-0.25	4	Slightly rough	3	Soft filling <5 mm	2	Slightly weathered	5	18
014 / 24400	0.6	6	0.1-0.25	4	Slightly rough	3	None	6	Moderately weathered	3	22
015 / 24780	1	4	0.1-0.25	4	Smooth	1	None	6	Moderately weathered	3	18

**Table 7.** Rock Mass Rating (RMR) of investigated rock masses.

Cut slopes locations / Chainage	Rock type	UCS rating	RQD rating	Spacing of discontinuities rating	Condition of discontinuities rating	Groundwater condition ratings	Adjustment for discontinuities orientation	RMR	Rock mass classes
004 / 14800	Quartz mica schist	12	20	10	14	4	-5	55	Fair rock
005 / 16400	Quartz mica schist	12	13	10	15	10	-5	55	Fair rock
006 / 17800	Quartz mica schist	7	17	10	20	10	-5	59	Fair rock
007 / 18400	Quartz mica schist	7	17	10	13	7	-5	49	Fair rock
008 / 19300	Quartz mica schist	7	8	8	15	10	-5	43	Fair rock
009 / 20900	Quartz mica schist	7	8	8	16	10	-5	44	Fair rock
010 / 21200	Quartz mica schist	7	13	10	22	15	-5	62	Good rock
011 / 22750	Quartz mica schist	7	17	10	18	0	-5	47	Fair rock
014 / 24400	Quartz mica schist	7	13	10	22	15	-5	62	Good rock
015 / 24780	Graphitic schist	7	17	10	18	15	-5	62	Good rock

**4.3 Slope stability analysis of the rock cuts**

The kinematic analyses of the discontinuity sets revealed the possibility of both wedge and planar failures. At location 004, analysis shows intersection of J2 and J3 along 267°/27° line orientation. Four intersections within the critical zone were recorded at location 005; J2 and J3 intersected along 280°/34°, J3 and J4 intersected along 265°/30°, J2 and J4 intersected along 266°/46°, and J3 and J5 intersected along 136°/54° line orientations. Location 006 recorded three intersections; J1 and J4 intersected along 49°/29°, J1 and J3 intersected along 128°/37°, while J1 and J2 intersected along 155°/27°. At location 007, only one intersection between J1 and J3 along 53°/31° was recorded. The same single intersection was also recorded at location 008 between J1 and J3 along 58°/32°. J1 and J3 intersected along 242°/54° at location 009. There was also only one intersection between J2 and J4 at location 010 along 48°/65°. Only J3 and J4 intersected along 262°/56° at location 011, while J1 and J3 intersected along 222°/61° at location 014. Analysis on the graphitic schist at location 015 yielded only one intersection between J3 and J4 having orientation of 326°/28° line of intersection. As shown in Fig. 5(a), there are possibilities of only wedge failures at locations 004, 010, 011, 014 and 015, while Fig. 5(b) shows possibilities of wedge and planar failures at locations 005, 006, 007, 008 and 009. Based on the kinematic analysis of these discontinuity sets, it is anticipated that all cut slopes in this investigated area are unstable.

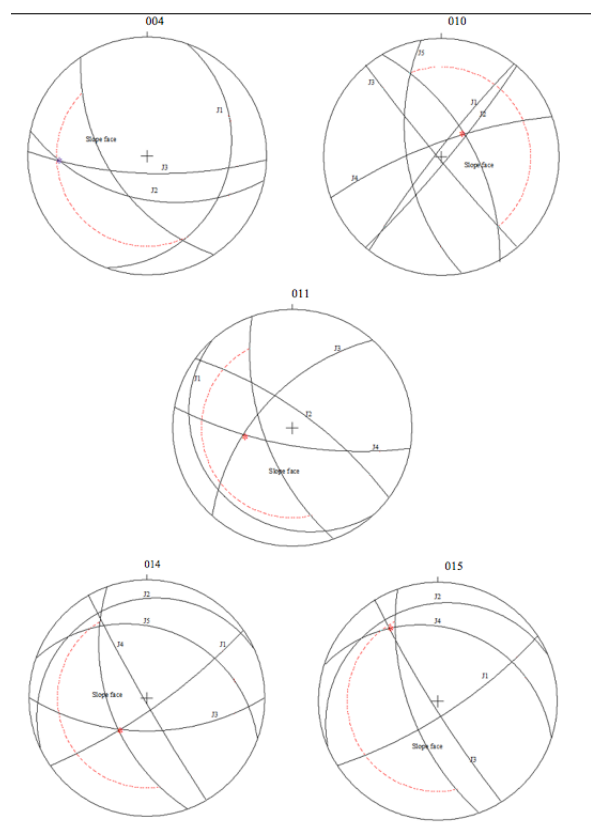


**Figure 5a.** Stereographic projections showing possibilities of wedge failures.

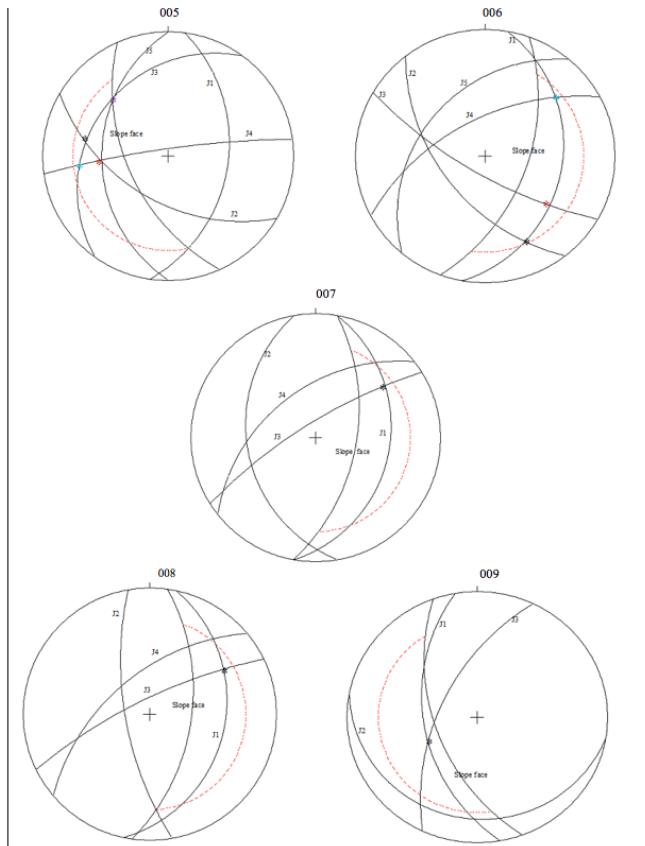


**Figure 5b.** Stereographic projections showing possibilities of wedge and planar failures.

**4.4 Classification of the rock cut slopes**

It may be useful to visualize slopes as existing in one of the following three stages:

- i. Stable - The margin of stability is sufficiently high to withstand all destabilizing forces.
- ii. Marginally stable - Likely to fail at some time in response to destabilizing forces reaching a certain level of activity.
- iii. Actively unstable - Slopes where destabilizing forces produce

continuous or intermittent movements.

Slope Mass Rating (SMR) proposed by Romana (1985) is a method to access the stability of both natural and cut slopes. According to Romana (1993) and Romana et al. (2003), SMR is obtained from RMR of Bieniawski (1989) as shown in equation 2 by adding a factorial adjustment factor which depends on the relative orientation of joint and slope and by adding another factor depending on the method of slope excavation. Rating adjustment for discontinuity orientations in RMR is not considered and this basic RMR is designated RMR<sub>b</sub>.

$$SMR = RMR_b + (F_1.F_2.F_3) + F_4 \tag{2}$$

Whereby F<sub>1</sub> ranges from 1.0 to 1.5 and depends on the parallelism between discontinuity and it fits into the relationship:

$$F_1 = (1 - \sin A)^2 \tag{3}$$

and A = the angle between the dip directions of the slope and joint.

F<sub>2</sub> depends on the joint dip angle (β<sub>j</sub>).

For toppling failure, this parameter maintains 1.0 value and F<sub>2</sub> thereby fits into the relationship:

$$F_2 = (\tan \beta_j)^2 \tag{4}$$

F<sub>3</sub> depends on the relationship between dips of slope (β<sub>s</sub>) and joint (β<sub>j</sub>).

F<sub>4</sub> is a correction factor that depends on the excavation method used and it is fixed empirically.

In Table 8, P represents plane failure, as represents slope dip direction, while α<sub>j</sub> represents joint dip direction and T represents toppling failure. As proposed by Romana (1993), the adjustment ratings of these factors are presented in Table 8 while the classes of SMR are presented in Table 9. The SMR was carried out using the independent joint sets from each investigated cut slope and finally applying equation 2. By analyzing the joint sets as shown in Table 10, SMR classified the stability of slopes as completely stable, stable, partially stable, unstable and completely stable. Using these five categories of SMR stability by Romana (1993), this study categorized the slopes as existing in three stages: Stable, marginally stable and actively unstable as presented in Table 10.

**Table 8.** Adjustment rating of F<sub>1</sub>, F<sub>2</sub>, F<sub>3</sub> for joints and method of slope excavation (Romana, 1993).

Joint Orientation	Very favourable	Favourable	Fair	Unfavourable	Very unfavourable
P  α <sub>j</sub> - α <sub>s</sub>	>30	30-20	20-10	10-5	<5
T  (α <sub>j</sub> - α <sub>s</sub> ) - 180	>30	30-20	20-10	10-5	<5
F <sub>1</sub> (for P & T)	0.15	0.40	0.70	0.85	1.00
P  β <sub>j</sub>	<20	20-30	30-35	35-45	>45
F <sub>2</sub> (for P)	0.15	0.40	0.70	0.85	1.00
F <sub>2</sub> (for T)	1.00	1.00	1.00	1.00	1.00
P β <sub>j</sub> - β <sub>s</sub>	>10	10-0	0	0--10	<-10
T β <sub>j</sub> + β <sub>s</sub>	<110	110-120	>120	--	--
F <sub>3</sub> (for P & T)	0	-6	-25	-50	-60
Method	Natural slope	Presplitting	Smooth blasting	Blasting/Ripping	Deficient blasting
F <sub>4</sub>	+15	+10	+8	0	-8

**Table 9.** Classification of slope according to SMR (Romana, 1993).

SMR	Class	Description	Stability	Failure	Support
81~100	I	Very good	Completely stable	None	None
61~80	II	Good	Stable	Some blocks	Spot
41~60	III	Fair	Partially stable	Some joints or many wedges	Systematic
21~40	IV	Poor	Unstable	Planar or large wedges	Important / Corrective
0-20	V	Very poor	Completely unstable	Large wedges or circular failure	Re-excavation

**Table 10.** Slope Mass Rating of the investigated cut slopes.

Cut slopes	RMRb	Slope dip dir. /Dip (Deg)	Joint sets	Joint dip dir. /Dip (Deg)	F1	F2	F3	F4	SMR	SMR Stability	Stability by this study
Location 004	60	236/63	J1	192/60	0.15	1	-50	+8	61	Stable	Stable
			J2	182/78	0.15	1	0		68	Stable	
Location 005	60	246/63	J1	210/60	0.15	1	-50	+8	61	Stable	Marginally stable
			J2	306/36	0.15	0.85	-60		60	Partially stable	
			J3	352/85	0.15	1	0		68	Stable	
			J4	270/46	0.4	1	-60		44	Partially stable	
Location 006	64	110/63	J1	232/62	0.15	1	-50	+8	65	Stable	Stable
			J2	210/78	0.15	1	0		72	Stable	
			J3	332/66	0.15	1	-6		71	Stable	
			J4	310/48	0.15	1	-60		63	Stable	
Location 007	54	100/63	J1	260/44	0.15	0.85	-60	+8	54	Partially stable	Marginally stable
			J2	328/80	0.15	1	0		62	Stable	
			J3	322/58	0.15	1	-50		55	Partially stable	
Location 008	48	98/63	J1	260/74	0.15	1	0	+8	56	Partially stable	Marginally stable
			J2	334/80	0.15	1	0		56	Partially stable	
			J3	320/64	0.15	1	-6		55	Partially stable	
Location 009	49	250/63	J1	260/56	0.7	1	-50	+8	22	Unstable	Actively unstable
			J2	295/66	0.15	1	-6		56	Partially stable	
Location 010	67	60/68	J1	308/86	0.15	1	0	+8	75	Stable	Stable
			J2	130/86	0.15	1	0		75	Stable	
			J3	230/88	0.15	1	0		75	Stable	
			J4	340/80	0.15	1	0		75	Stable	
			J5	260/66	0.15	1	-50		68	Stable	
Location 011	52	250/70	J1	36/78	0.15	1	-6	+8	59	Partially stable	Marginally stable
			J2	312/66	0.15	1	-50		53	Partially stable	
			J3	190/78	0.15	1	-6		59	Partially stable	
Location 014	67	250/63	J1	145/82	0.15	1	0	+8	75	Stable	Stable
			J2	180/67	0.15	1	-6		74	Stable	
			J3	240/88	0.7	1	0		75	Stable	
			J4	20/40	0.15	0.85	-60		67	Stable	
Location 015	67	250/70	J1	147/80	0.15	1	-6	+8	74	Stable	Stable
			J2	238/86	0.7	1	0		75	Stable	
			J3	18/38	0.15	0.85	-60		67	Stable	

## 5. Conclusion

The field and laboratory tests, computation of results and schematic representations were aimed at classifying the stability of the investigated cut slopes. From the uniaxial compressive strength tests, it was observed that the combination of joints and foliations induced structurally controlled failures in the tested samples. RQD and RMR schemes utilized for rock mass classification yielded almost similar poor to good quality ranges for each investigated rock mass. While the RQD values range from 34.5% to 90% covering a broad range of poor, fair and good quality rocks, RMR yielded values from 43 to 62 which cover only fair and good quality rocks. RMR applied in this study is very useful as a tool for the preliminary assessment of slope stability whereby it classified seven of the slopes cut into fair rocks and only three slopes cut into good rocks. Although based on the kinematic analyses carried out in this study, it is anticipated that the entire cut slopes are unstable with possibilities of wedge and planar failures, SMR gave comparative stability classes among these cut slopes, categorizing them actively unstable, marginally stable and stable slopes. Considering the determined unstable slopes, there is need for the use of expensive and wider in-situ and laboratory testing equipment in order to reasonably predict the stability of these cut slopes before any further infrastructural development in the area is carried out.

## Acknowledgement

Special thanks to University of Malaya for sponsoring this research through Postgraduate Research Fund, grant number: PS362/2010B.

## References

- Andrew Malone Ltd. (2007). Landslide study at Ch 23+800 Simpang Pulai Lojing Highway, Malaysia. Report to minister of works of Malaysia.
- Bieniawski, Z. T. (1976). Rock mass classification in rock engineering. In: Z. T. Bieniawski eds. Proceedings of the symposium on Exploration for Rock Engineering. Cape Town: Balkema. 1, 97-106.
- Bieniawski, Z.T. (1978). Rock mass rating systems in engineering practice. Symposium on Rock Classification Systems for Engineering Purposes, ASTM, STP; 984: 17-34.
- Bieniawski, Z. T. (1989). Engineering rock mass classifications. Wiley and Sons, New York, 251 pp.
- Broch, E. (1974). The influence of water on some rock properties. Proceedings of the Third Congress of the International Society for Rock Mechanics, Themes 1-2: Advances in Rock Mechanics, Reports of Current Research. 2(A), 33-38.
- BSI (British Standards Institution) (1981). Code of practice for site investigations. BS 5930:1981, BSI London.
- Das, B. M. & Sobhan, K. (2013.) Principles of geotechnical engineering. 8th Edition. Cengage Learning, Stamford, CT 06902, USA, 726 pp.
- Deere, D. U. (1963). Technical description of rock cores for engineering purposes. Rock Mechanics and Rock Engineering, 1, 16-22.
- Deere, D. U. (1968). Geological considerations. In: Rock Mechanics In: Engineering Practice. R.G. Stage and D.C. Zienkiewicz eds. Wiley. New York, 1-20.
- Deere, D. U. & Miller R.P. (1966). Engineering classification and index properties of rock. Technical Report No. AFNL-TR-65-116. Albuquerque, NM: Air Force Weapons Laboratory.
- Hoek, E. & Bray, J. W. (1981). Rock slope engineering. The Institute of Mining and Metallurgy, London, England, 358 pp.
- Horino, F. G. & Ellickson, M. L. (1970). A method of estimating strength of rock containing planes of weakness. US Bureau of Mines Report of Investigation 7449, 26 pp.
- ISRM (International Society for Rock Mechanics) (1978). Standardization of laboratory and field tests. Int. Jour. Rock Mech and Min. sci. and Geomech. Abst. 15, 348 pp.
- ISRM (International Society for Rock Mechanics) (1981a). Suggested methods for rock characterization testing and monitoring. Brown E. T.(ed), Oxford Pergamon Press, 211 pp.
- ISRM (International Society for Rock Mechanics) (1981b). Basic technical description of rock masses. International Journal of Rock Mechanics and Mining Sciences and Geomechanics Abstracts, 18, 85-110.
- Mohd Asbi & Associates Sdn Bhd. (2005). Surface investigation report on proposed cut slope between Ch 23+000 and Ch 24+560 Simpang Pulai – Gua Musang – Kuala Berang package 2, Malaysia. Report to Ministry of works Malaysia.
- Murthy, V. N. S. (2002). Geotechnical Engineering, Principles and Practices of Soil Mechanics and Foundation Engineering. Marcel Dekker, New York, 1029 pp.
- Nkpadobi, J. I. (2014). Geotechnical properties of meta-sedimentary bedrock and the stability of cut slopes along the Pos Selim highway in Perak State, Malaysia, PhD Thesis, University of Malaya, Kuala Lumpur, Malaysia.
- Nkpadobi, J. I., Raj J. K. & Ng T. F. (2015). Failure mechanisms in weathered meta-sedimentary rocks. Environmental Earth Sciences. Springer Berlin Heidelberg. 73 (8), 4405-4418.
- Palmström, A. (1982). The volumetric joint count - a useful and simple measure of the degree of rock jointing. Proceedings of the 4th congress on International Association Engineering Geology., Delhi. 5, 221-228.
- Palmström, A. (2005). Measurements of and Correlations between block size and Rock Quality Designation (RQD). Tunnelling and Underground Space Technology, 20, 362-377.
- Romana, M. R. (1985). New adjustment ratings for application of Bieniawski classification to slopes. Proceedings of International Symposium on Role of Rock Mechanics in Excavations for Mining and Civil Works. ISRM, Mexico City, 59-68.
- Romana, M. R. (1993). A geomechanical classification for slopes: Slope mass rating. In: Comprehensive Rock Engineering, v. 3, ch. 23 (Hudson, J. D., ed.) Pergamon Press, Oxford, 575-599.
- Romana, M., Serón, J. B. & Montalar, E. (2003). SMR Geomechanics classification: Application, experience and validation ISRM–Technology roadmap for rock mechanics. South African Institute of Mining and Metallurgy, 1-4.
- Singh, B. & Goel, R. K. (1999). Rock mass classification: A practical approach in civil engineering. Elsevier science. 282 pp.
- Tajul, A. J. (2003). Engineering geological assessment and slope failures along the Pos Selim Cameron Highland Highway. Seminar Penyelidikan Jangka Pendek (Vot F), 11th-12th March 2003, University of Malaya.
- Venkatramaiah, C. (2006). Geotechnical engineering. Revised Edition. New Age International, 926 pp.